A novel approach to fabricate bioinspired programmable composite materials : the 3D Printing way

Simone Lantean

INSTITUT POLYTECHNIQUE DE PARIS

NNT : 2021IPPAX024

Thèse de doctorat

A novel approach to fabricate bioinspired programmable composite materials: the 3D Printing way

Thèse de doctorat de Politecnico di Torino et de l'Institut Polytechnique de Paris
Préparée à l'École polytechnique

École doctorale n°626 - Ecole Doctorale de l'Institut Polytechnique de Paris (EDIPP)
Spécialité de doctorat : Physique de la matière condensée

Thèse présentée et soutenue à Torino (Italie), le Mardi 20 Avril 2021, par

Simone Lantean

Composition du Jury :

Laurence Bodelot Professeure assistant, Institut Polytechnique de Paris (IPP), Laboratoire de Mécanique des Solides (LMS),	Président
Juergen Stampfl Professeur, TU Wien, Institut of Materials Science and Technology	Rapporteur
Sandra Schloegl Chercheur, Polymer Competence Center Loeben (PCCL)	Rapporteur
Marco Zanetti Professeur associé, Università degli Studi di Torino, Dipartimento di Chimica	Examinateur
Tara Schiller Professeur associé, University of Warwick	Examinateur
Giancarlo Rizza Chercheur, Institut Polytechnique de Paris (IPP), Laboratoire des Solides Irradiés (LSI), CEA/DRF/IRAMIS/LSI	Directeur de thèse
Marco Sangermano Professeur associé, Politecnico di Torino, Dipartimento di Scienza e Tecnologia Applicata (DISAT)	Co-Directeur de thèse
Ignazio Roppolo Chercheur, Politecnico di Torino, Dipartimento di Scienza e Tecnologia Applicata (DISAT)	Co-Directeur de thèse

Doctoral Dissertation
Doctoral Program in Materials Science and Technology (33rd Cycle)

A novel approach to fabricate bioinspired programmable composite materials: the 3D Printing way

Simone Lantean
* * * * * *

Supervisors
Prof. Marco Sangermano, Supervisor
Dr. Giancarlo Rizza, Co-Supervisor
Dr. Ignazio Roppolo, Co-Supervisor

Doctoral Examination Committee:

Prof. Laurence Bodelot, President of Jury, Ecole Polytechnique
Dr. Sandra Schloegl, Reviewer, Polymer Competence Center Loeben (PCCL)
Prof. Juergen Stampfl, Reviewer, TU Wien
Prof. Marco Zanetti, Referee, Università degli Studi di Torino
Prof. Tara Schiller , Referee, University of Warwick

Politecnico di Torino
20th of April, 2021

I hereby declare that, the contents and organisation of this dissertation constitute my own original work and does not compromise in any way the rights of third parties, including those relating to the security of personal data.

…….....

Simone Lantean

Turin, April, 2021

Acknowledgments

I would like to acknowledge the supervisors of this work Prof. Marco Sangermano, Dr. Giancarlo Rizza, and Dr. Ignazio Roppolo for the chance they gave me to work on this outstanding project. They all contribute in different ways to the realization of this work and they represented and still represents an important guide for my working and non-working life. I appreciate all the support they have given me, and I am proud to have been able to work with these wonderful persons.
I would like to thank all the LSI/CEA people, especially Prof. Marc Hayoun and Prof. Hichem Dammak for their fundamental help in developing the theoretical model used to describe the behavior of magnetic nanoparticles dispersed in low-viscous liquid media.
I would like to thank Dr. Rachid Belkhou HERMES beamline manager at SOLEIL synchrotron for the support and opportunity to characterize in situ and at the nanoscale the self-assembly processes of magnetic particles.
I would like to thank Dr. Gabriele Barrera and Dr. Paola Tiberto for performing all the magnetic tests on our samples. I would like also to acknowledge again Gabriele Barrera for sharing his knowledge in magnetism and magnetic materials.
I want to thank Dr. Sandra Schlogl and Prof. Jurgen Stampfl for finding time to review this manuscript despite their busy schedules.
Nevertheless, I need to thank my co-workers in Torino for their help and friendship demonstrated during these three years. Starting from my officemates I acknowledge Angelo, Giuseppe, Gustavo, and Parnian. Then I desire to thank all the Lab buddies: Annalisa, Andrea, Matteo, Camilla, Diana, Michael, and Lorenzo.
As well as I need to thank all the buddies from Paris, starting from the people of the most international office: Uliana, Mohamed, Muhamad, Quang, and Mariusz. Of

course, a special mention goes to my friend Pierfrancesco for the Parisian nights spent together.
During these three-years, many important things happened in my personal life. I really need to thank my family for their support and the force they always give me to face the obstacles of life.
Finally, I need to thank Lavinia for being so encouraging and patient with me. Thanks for always support and helping me make important decisions. Despite the kilometers between us, I always feel you close to me.

“Science knows no country, because knowledge belongs to humanity, and is the torch which illuminates the world.”

Louis Pasteur

Abstract

At the beginning, 3D printing was mainly conceived as an innovative manufacturing method to produce objects with complex designs. More recently, the possibility to produce innovative materials with controlled properties by 3D printing technology is emerging as a new research topic and it is predicted to boost developments in several application fields such as robotics, sensing, and biomedicine. In the 4D printing framework, 3D print objects can modify their shape and properties by the applications of external stimuli. In particular, magnetic fields, are easy to apply, they are body-harmless, and they allow to remotely control the motion of the designed objects.

In the first part of the thesis, a Digital Light Processing (DLP) was used to 3D print magneto-responsive polymeric materials containing dispersed Fe_3O_4 NPs. The magnetic properties of the materials were tailored by controlling the concentration of magnetic filler up to 6 wt.%. Furthermore, by adding a reactive diluent to the photocurable resins, the mechanical response of the materials was tuned from stiff to soft. Using this strategy, several objects were fabricated possessing different types of magneto-induced motion such as translation, rolling, bending, and folding/unfolding.

In the second part of this thesis, we took advantage of the self-assembly processes of the magnetic particles to fabricate composite materials with programmed microstructures using a modified DLP 3D printer. First, the self-assembly of magnetic particles in chain-like structures was induced by the application of a magnetic field on a thin liquid layer of photocurable resin mimicking the 3D printing process. The assembling process and the orientation of the magnetic chains were experimentally investigated by Scanning X-Ray and optical microscopy techniques. The dimension of the assembled chains was tailored by tuning the magnetic field, and by varying the viscosity and the NPs concentration

in the resins. Once the magnetic chains were formed, their direction was controlled by tilting the applied field of discrete angles. A simplified physical model based on the magnetic interactions between particles was developed to describe both the self-assembly process and the rotation of the magnetic chains. The results obtained by numerical simulations were in good agreement with the experimental observations.

To translate the programmed micro-structuration from 2D to 3D, a pre-existing DLP printer was modified adding a ball-bearing-permanent magnets system to control the application of magnetic fields during the 3D printing process. The arrangement of the chains in each printed layer was programmed by controlling the magnetic field intensity and direction during the manufacturing process. As a proof of concept, a three-level structure was 3D printed by precisely control the microstructural organization in each printed layer.

Finally, the magnetic properties of the materials were tailored by the control of their microstructure. The magnetic anisotropy and the easy magnetic-axis of the composites were tailored by controlling the magnetic field intensity and direction, and by varying the Fe_3O_4 NPs concentration. Throughout the magnetic programming of the microstructure, several devices were fabricated proving remotely controlled rotation and bending motions induced by the application of magnetic torques.

The research findings demonstrated an accessible route to 3D print magneto-responsive polymers with controlled microstructures and magnetic properties. The programming of the nanocomposite microstructure proved to enhance the control of the actuation mechanism and to widen the palette of the exploitable motion typologies.

Resume in English

Three-Dimensional (3D) Printing allows the production of complex structures and the rapid prototyping of objects. The recent advances made in additive manufacturing technology are introducing year after year new 3D printers and new strategies, enlarging the palette of processable materials. Several industrial applications of 3D printers are already reported, ranging from automotive to fashion, and new ones are just around the corner. Recently, new research trends of 3D printing are arousing, and they are predicted to enhance the development of several technological topics. In particular, 4D printing consists of the fabrication of 3D printed objects undergoing controlled temporal modification of their shape and properties upon the application of external stimuli (time is the fourth added dimension). Several stimuli (such as light, moisture, electrical field) can be exploited to induce controlled transformations in the printed materials. Among them, magnetic fields show peculiar characteristics. Indeed, they can be easily applied by the use of permanent magnets and solenoids, they are body-harmless, and they can be actuated remotely, i.e. without direct contact between the source and the material.

The easiest way to produce magneto-responsive polymers consists of incorporating magnetic fillers within the polymeric matrix. To further enhance the magneto-driven control on the fabricated composite materials, the microstructural arrangement of the embedded particles can be used to tune the macroscopic magnetic properties of the material. This can be achieved by exploiting the self-assembly processes of magnetic particles. Indeed, when magnetic fillers are dispersed in a liquid medium and exposed to a uniform magnetic field, they spontaneously assemble into chain-like structures oriented along the field lines.

In this work, we proposed an innovative 3D printing methodology to exploit the self-assembly mechanisms of magnetic particles and control the microstructures and the properties of the produced objects. This strategy allows us to produce magneto-driven devices undergoing complex actuation mechanisms. Moreover, we demonstrated that the designed objects work in closed wet/dry environments, and they can be remotely controlled by the application of magnetic fields. The fabricated objects have applications in several fields ranging from soft robotics to sensing, from drug delivery to biomedicine.

For this Ph.D. work, Digital Light Processing (DLP) was selected as the printing technology as it allows processing the materials in their liquid state. This

allows to easily disperse the fillers in the materials and to exploit the self-assembly process of magnetic particles to control the microstructure of the printed objects. DLP 3D printers are based on the photopolymerization process, which is a polymerization reaction initiated by light. In particular, in a liquid mixture of monomers and oligomers, an organic molecule called photoinitiator is added. When the photoinitiator is irradiated by light, it undergoes photobleaching generating reactive species (radicals, cations, or anions depending on the type of photoinitiator), which can initiate the curing process. In DLP technology, photopolymerization is used to rapidly cure the slices of the objects by projecting the light pattern of the layer to print on the photocurable resin. The step by step addition of several photocured layers leads to the fabrication of the object. However, the load of fillers in the photocurable resin may limit the light absorption of the photoinitiator due to a competitive absorption/scattering of light, leading to a decrease of the polymerization rate or even preventing the printing process.

In the first part of the Ph.D. work, we investigated the development of magneto-responsive polymers with randomly dispersed magnetic particles, employing a DLP 3D printer to fabricate objects. Fe_3O_4 magnetic nanoparticles (NPs) were added to a mixture of a commercial urethane acrylated resin (Ebecryl 8232) and a reactive diluent (Butyl acrylate). The addition of the reactive diluent in the system accelerated the polymerization process of the photocurable formulation counterbalancing the reactivity inhibition due to the light absorption of magnetic particles. Moreover, by increasing the amount of butyl acrylate (BA) added in the formulation we were able to decrease the glass-transition temperature and the elastic modulus of the printed material, producing softer polymers. The load of magnetic nanoparticles did not significantly alter the mechanical response of the object, while the magnetization of the composites increases linearly with the NPs concentration. The prepared formulations showed a good printability up to 6 wt.% of fillers, and the printed objects showed resolution down to 400 μm. The mechanical response of the objects was tailored by varying the Ebecryl 8232 and BA ratio in the formulations. This approach allowed us to investigate different types of motion. With the rigid polymer (i.e. 75Eb25BA) we 3D printed magnetic wheels undergoing rolling and objects undergoing translation motion in confined environments. With the softer polymeric matrix (i.e. 50Eb50BA) we exploited bending motion mimicking the opening and closing of flowers. By the combination of rigid and soft parts in the same object, we were also able to program the bending points in the printed nanocomposites proving folding and unfolding processes activated by magnetic fields.

In the second part of this Ph.D. work, we studied how to control the microstructure in the printed materials, to enhance their magneto-responsiveness. Our strategy takes advantage of the self-assembly process of magnetic particles. By applying uniform magnetic fields to the photocurable resin, we promoted the spontaneous assembling of magnetic particles in chain-like structures aligned along the field lines. Once the desired microstructural arrangement is achieved, we irradiated the formulation with light to carry out the photopolymerization process and to "freeze" the magnetic chains in the cured polymeric matrix.

By optical microscopy, we investigated both the self-assembly process of magnetic particles and the rotation of magnetic chains in 2D liquid films. Also, a simplified theoretical model was proposed to describe both the phenomena and numerical simulations were performed to characterize the system. The self-assembly process followed a power-law trend characterized by a fast increase in the length of the aggregates within the first 10 minutes of magnetic field application followed by a plateau region where the dimensions of the chains remain almost unchanged. Next, we varied the self-assembly conditions to evaluate the effect of external parameters in the dimensions of the assembled magnetic chains. Higher magnetic field intensities and higher NPs loads facilitate the self-assembly process leading to longer assembled structures. On the contrary, the use of more viscous resins leads to the formation of shorter aggregates due to the reduction of NPs mobility.

Once the chains were formed, the applied field was rotated by discrete angles to control the orientation (i.e. direction) of the assembled magnetic chains. The evolution of the systems under these conditions was experimentally evaluated by optical microscopy. The existence of a critical rotation angle (≈40°) and two different rotation regimes was observed. Below the critical angle, the magnetic chains simply rotate with the magnetic field. Above the critical angle, the magnetic chains still rotate solidly with the magnetic field, but also undergo rupture, leading to shorter aggregates. This phenomenon is well predicted by the proposed physical model, and it is ascribable to the trend of the parallel magnetic interactions depending on the angular arrangement between two particles. Above 45° the magnetic interactions become negative and this leads to chains break.

Finally, the self-assembly process and the rotation of the chains were also observed *in situ* and at the nanoscale by Scanning X-Ray Microscopy in SOLEIL synchrotron. By varying the characteristics of the applied magnetic field, several phenomena occurring at the nanoscale were observed such as the rotation of the dispersed aggregates when the field is applied, the assembling of the shorter

aggregates to the ends of already formed longer chains, and the rotation of the microstructures.

These investigations allowed us to program the microstructure of polymeric films. The dimension of the chains was tailored by controlling the intensity of the applied magnetic field and by varying the viscosity of the liquid medium and the load of NPs dispersed in the resins. Finally. the direction of magnetic chains was programmed by tilting the direction of the field. In order to control the microstructure of a bulky material in a DLP process, our strategy consisted of replicating the 2D control on magnetic chains in each printed layer of the object. Therefore, the control on the direction and size of magnetic chains in each printed layer would lead to the programming of the microstructure of the 3D printed nanocomposite materials.

To enable the production of controlled magnetic fields during the 3D printing process and to control the magnetic microstructure of objects, we modified a DLP printer. The core of the modification set-up consisted of the addition of a polymeric ball bearing acting as the new resin reservoir of the printer. By adding a couple of permanent magnets outside the ball bearing, it is possible to apply a magnetic field on the photocurable resin to induce the self-assembly processes of magnetic particles. The direction of the assembled chains was tailored by rotating the ball bearing, i.e. the permanent magnets. As a proof of concept, we printed a three-level structure varying the direction of the applied magnetic field in each level during the printing process (0°, 45°, and 90°). Optical microscopy images proved that we controlled the dimension of the embedded magnetic chains by varying the self-assembly conditions. Moreover, the direction of the assembled aggregates was consistent with the direction of the magnetic field applied in each level of the structure. Therefore, we demonstrated that the proposed DLP set-up was effective in programming the microstructure of the 3D printed composites.

The effect of the magnetic chains on the macroscopic magnetic properties of the sample was investigated by measuring the magnetization cycles along three different directions of the samples (parallel, transversal, and perpendicular). In the samples with randomly dispersed NPs, the three hysteresis loops were perfectly overlapping proving that the nanocomposites were magnetically isotropic that is, the three measured directions were magnetically equivalent. On the contrary, in samples containing oriented magnetic chains, the magnetization curve measured along the chain's direction (parallel) exhibited a higher slope compared to the transversal and perpendicular directions. Since the magnetic cycles were not overlapping, the samples were magnetically anisotropic, and they were characterized by a preferable magnetization direction called easy-magnetic axis

coincident with the orientation of the embedded micro-chains. Therefore, by the control of the microstructure, we were also able to program the magnetic properties of the fabricated materials. The magnitude of the magnetic anisotropy in the objects was tailored by varying the intensity of the printing magnetic field, and the nanoparticles load in the materials. The optimum conditions to enhance magnetic anisotropy consisted of applying a 10mT field during the printing process and increase the NPs concentration up to 6 wt.%.

The produced magneto-responsive polymers with oriented microstructure behaved as magnetic compasses. Therefore, when a uniform magnetic field was applied, the objects underwent rotation to align their easy magnetic, i.e. the major axis of the magnetic chains, along the field lines. Taking advantage of this phenomenon, we produced magneto-driven spur gears undergoing programmed rotation by the remote application of a magnetic field. Two geometrically identical spur gears were 3D printed with different microstructures. Upon the application of a uniform magnetic field (4mT), the spur gear with oriented chains underwent rotation to align its easy magnetic axis to the field. On the contrary, the spur gear with randomly dispersed NPs remained steady as it is magnetically isotropic. Then, we developed a magnetic-driven gear-train, proving that the magnetic "input gear" was effective in transferring the mechanical torque to a non-magnetic driven wheel leading to the rotation of the latter. Finally, we produced more complex mechanics based on several moving parts. In particular, we developed a gripper based on the spur gear – linear rack mechanics. We demonstrated that by the application of remote magnetic fields we were able to control the opening and closing of the gripper arms in closed wet environments.

The control on the microstructure and magnetic properties of the objects was also exploited in producing magnetic hammers-like objects. The rotation of the objects was predicted by programming the microstructure of the materials. Therefore, by the application of a magnetic field, the fabricated devices undergo predictable rotations to align the embedded magnetic chains along the field direction.

In a last set of experiments, the controlled orientation of the magnetic chains was transformed into controlled bending of hammers-like structures. This can be achieved when the magnetic torque overcomes the mechanical resistance of the material. To do so, the objects were produced with the softer polymeric matrix (50Eb50BA). Moreover, taking advantage of the characteristics of 3D printing, the design of the objects was adjusted to concentrate the mechanical stress in a programmed point of the structure. On the other hand, the contribution of the magnetic torque was tuned by varying the intensity of the applied magnetic field.

As a result, the produced objects underwent bending, and the amplitude of deformation was directly related to the magnitude of the magnetic field applied.

Throughout the pages of this manuscript, we demonstrated that a designed synthesis of the photocurable formulations, together with physical knowledge on the evolution of magnetic nanoparticles self-assembly mechanism and 3D printing can lead to the fabrication of objects with added values, in which materials characteristics synergistic play with objects design. This leads to achieve different types of motion such as rolling, translating, bending, and folding/unfolding which can be remotely controlled and exploited in closed environments. Ultimately, to fabricate complex devices which use can be envisaged in different fields such as soft-robotics, biomedical devices, and sensors.

Riassunto in italiano

La stampa tridimensionale (3D) permette la produzione di strutture complesse e la rapida prototipizzazione degli oggetti. I recenti sviluppi nella tecnologia di manifattura additiva (additive manufacturing) hanno introdotto, anno dopo anno, nuove tipologie e strategie di stampa 3D, e conseguentemente, hanno esteso il numero di materiali processabili con queste tecniche. La stampa 3D ha già diverse applicazioni industriali che variano dal settore automobilistico a quello della moda, e altre sono giusto dietro l'angolo. Più recentemente, stanno emergendo nuove tematiche di ricerca relative alla stampa 3D, ed è previsto che queste possano accelerare lo sviluppo di diversi settori tecnologici. In particolare, la stampa 4D consiste nella fabbricazione 3D di oggetti che esposti a stimoli esterni subiscono modificazione temporali controllate delle loro forme e proprietà (il tempo è la quarta dimensione aggiunta). Diversi stimoli come la luce, l'umidità e i campi elettrici possono essere utilizzati per indurre trasformazioni controllate nei materiali stampati. Tra questi, i campi magnetici possiedono caratteristiche molto interessanti. Infatti, i campi magnetici possono essere facilmente applicati attraverso l'utilizzo di magneti permanenti e solenoidi, sono innocui al corpo umano, e permettono il controllo da remoto dell'oggetto, cioè non è necessario che ci sia un contatto diretto tra la fonte del campo (magneti) e l'oggetto per controllarne il movimento.

La maniera più semplice per produrre dei polimeri sensibili ai campi magnetici consiste nell'inserire dei riempitivi magnetici all'interno della matrice polimerica. Per migliorare ulteriormente il controllo magnetico sui materiali compositi prodotti, è possibile governare la disposizione microstrutturale delle particelle magnetiche inserite così da controllare le proprietà magnetiche macroscopiche del materiale. Questo controllo della microstruttura del materiale può essere ottenuto sfruttando i processi di auto assemblaggio (self-assembly) delle particelle magnetiche. Infatti, quando i rinforzanti magnetici sono dispersi all'interno di un liquido, ed esposti a un campo magneti uniforme, essi spontaneamente si aggregano in delle strutture simili a catene allineate lungo le linee di campo.

In questo lavoro, abbaiamo sviluppato un metodo di stampa 3D innovativo per poter sfruttare i meccanismi di self-assembly delle particelle magnetiche, e quindi controllare le microstrutture e le proprietà degli oggetti prodotti. In questo modo abbiamo stampato dei dispositivi in grado di subire meccanismi di attuazione complessi quando guidati da un campo magnetico. Inoltre, abbiamo dimostrato che

gli oggetti realizzati erano anche in grado di lavorare in sistemi chiusi ed erano controllabili da remoto attraverso l'applicazione di campi magnetici esterni. Gli oggetti prodotti sono interessanti per diversi campi applicativi come la robotica e la sensoristica, o il rilascio controllato di farmaco e la biomedicina.

Per questo lavoro di dottorato, la tecnologia di stampa 3D utilizzata è stata la Digital Light Processing (DLP) siccome questa stampante processa i materiali iniziali nella loro fase liquida. Questo permette di disperdere facilmente le particelle magnetiche all'interno dei materiali iniziali e successivamente di indurre i processi di self-assembly delle particelle inserite e di controllare quindi la microstruttura degli oggetti stampati. Nelle stampanti DLP le resine liquidi sono trasformate in polimeri solidi attraverso il processo di fotopolimerizzazione, ovvero una reazione di polimerizzazione promossa dalla luce. In particolare, in una miscela liquida di monomeri e oligomeri, viene aggiunta una molecola organica detta fotoiniziatore. Quando il fotoiniziatore viene irraggiato con della luce UV/visibile, esso assorbe la luce e degrada, generando delle specie reattive (radicali, cationi, o anioni) che additivandosi sui monomeri iniziano le reazioni di polimerizzazione. Nelle stampanti DLP, la fotopolimerizzazione è sfruttata per reticolare rapidamente uno strato dell'oggetto proiettando l'immagine luminosa del layer de stampare sulla resina fotoreticolabile. La costruzione dell'oggetto finale è poi ottenuta attraverso l'addizione dei diversi strati che lo compongono. Tuttavia, l'aggiunta di particelle all'interno della resina fotoreticolabile comporta una diminuzione della velocità e del tasso di polimerizzazione che può anche del tutto impedire il processo di stampa.

Nella prima parte del lavoro di tesi, abbiamo studiato la possibilità di produrre, attraverso una stampante DLP, polimeri contenenti particelle magnetiche casualmente disperse. Delle nanoparticelle (NP) di magnetite (Fe_3O_4) sono state caricate all'interno di una miscela di una resina commerciale uretano-acrilata (Ebecryl 8232) e un diluente reattivo (acrilato di butile). L'aggiunta del diluente reattivo nel sistema ha permesso di accelerare il processo di polimerizzazione della formulazione contrastando in parte la riduzione della reattività delle resine dovuta all'assorbimento di luce da parte delle particelle magnetiche. Inoltre, aumentando il contenuto di acrilato di butile (BA) nelle formulazioni, potevamo diminuire la temperatura di transizione vetrosa e il modulo elastico dei materiali stampati, producendo quindi dei polimeri più flessibili. Il contenuto di NP non influenzato in modo particolare la risposta meccanica degli oggetti. Al contrario, la magnetizzazione dei compositi cresceva linearmente con la concentrazione di nanoparticelle magnetiche. Le formulazioni preparate hanno mostrato una buona stampabilità fino al 6% di Fe_3O_4 NP, e gli oggetti prodotti una buona risoluzione su dettagli fino a 400 μm. Il comportamento meccanico dei materiali è stato controllato

variando il rapporto tra Ebecryl 8232 e BA all'interno delle formulazioni. Questo approccio ci ha permesso di investigare diverse tipologie di movimento. Con i polimeri rigidi (75Eb25BA) sono stati stampate delle ruote che rotolavano, e oggetti che traslavano in ambienti chiusi attraverso l'applicazione di campi magnetici. Con le matrici polimeriche più morbide (50Eb50BA) abbiamo sfruttato movimenti di flessione per simulare ad esempio, l'apertura e la chiusura di un fiore. Inoltre, combinando parti flessibili e rigide all'interno dello stesso oggetto, potevamo prevedere i punti di flessione dei nanocompositi stampati dimostrando processi di ripiegamento controllato attivati da campi magnetici.

Nella seconda parte di questo lavoro di dottorato abbiamo studiato come controllare la microstruttura dei materiali stampati per incrementare la loro risposta al campo magnetico. La nostra strategia sfrutta il processo di auto assemblaggio delle particelle magnetiche. Applicando un campo magnetico uniforme alle formulazioni fotoreticolabili che abbiamo sviluppato, promuovevamo l'aggregazione spontanea delle particelle di Fe_3O_4 in strutture a catena allineate lungo le linee di campo. Una volta che la disposizione microstrutturale desiderata veniva raggiunta, irraggiavamo con luce la formulazione per promuovere il processo di fotopolimerizzazione e quindi "congelare" le catene magnetiche all'interno della matrice polimerica reticolata.

Attraverso la microscopia ottica, abbiamo studiato all'interno di film liquidi planari (2D) sia il processo di self-assembly delle nanoparticelle, che la rotazione delle catene magnetiche. Inoltre, è stato elaborato anche un modello teorico semplificato per descrivere i due fenomeni, e sono state svolte simulazioni numeriche per caratterizzare il sistema. Il processo di self-assembly seguiva una curva di potenza (power-law) caratterizzata da un rapido incremento della lunghezza degli aggregati nei primi 10 minuti di applicazione del campo magnetico, seguita da una regione di plateau in cui le dimensioni delle catene rimaneva pressoché invariata. Successivamente, abbiamo variato le condizioni di self-assembly per valutare l'effetto dei parametri esterni sulle dimensioni delle catene magnetiche assemblate. Intensità maggiori di campo e concentrazioni elevate di NP favoriscono il processo di self-assembly portando a strutture assemblate più lunghe. Al contrario, l'utilizzo di resine più viscose porta alla formazione di aggregati più corti a causa della riduzione nella mobilità delle NP.

Una volta che le catene erano formate, per controllare l'orientazione (la direzione) delle catene magnetiche, il campo magnetico applicato veniva ruotato di angoli discreti. L'evoluzione dei sistemi sotto queste condizioni è stata studiata sperimentalmente al microscopio ottico. In particolare, sono stato individuati un angolo critico di rotazione ($\approx 40°$) e due differenti regimi di rotazione delle catene.

Sotto l'angolo critico, le catene ruotano semplicemente col campo magnetico. Al di sopra dell'angolo critico, le catene magnetiche ruotano sempre solidalmente con il campo, ma allo stesso tempo si rompono, portando alla formazione di aggregati più corti. Lo stesso fenomeno è stato ben predetto dal modello fisico proposto, ed è ascrivibile alla variazione delle interazioni magnetiche parallele tra due particelle al variare della loro disposizione angolare. Sopra i 45° le interazioni magnetiche parallele diventano negative e questo porta alla rottura delle catene.

Infine, il processo di self-assembly e la rotazione delle catene sono state anche osservate in situ e sulla nanoscala attraverso la tecnica di microscopia a scansione di raggi X situata presso il sincrotrone di SOLEIL. Variando le caratteristiche del campo magnetico applicato, sono stati osservati diversi fenomeni che avvengono alla nanoscala come la rotazione degli aggregati dispersi quando il campo magnetico viene applicato, l'aggiunta degli aggregati più corti alle estremità delle catene più lunghe già formate, e la rotazione delle microstrutture.

Questi studi ci hanno permesso di programmare la microstruttura di film polimerici. Le dimensioni delle catene sono state controllate variano l'intensità del campo magnetico applicato e modificando la viscosità e la concentrazione di NP disperse nelle formulazioni. Infine, la direzione delle catene magnetiche è stata programmata girando il campo magnetico applicato. Per controllare la microstruttura di un materiale tridimensionale in un processo di stampa DLP, la nostra strategia era quella di replicare il controllo sulle catene magnetiche ottenuto già in 2D su ogni strato stampato del materiale. In questo modo, sarebbe possibile programmare la microstruttura dei materiali nanocompositi stampati 3D controllando la taglia e la direzione delle catene magnetiche in ogni layer stampato.

Abbiamo modificato una stampante DLP già esistente per permettere l'applicazione di campi magnetici controllati durante il processo di stampa 3D e quindi programmare la microstruttura magnetica degli oggetti fabbricati. Il nucleo della modifica consiste nell'inserimento di un cuscinetto a sfera polimerico che funge da nuovo recipiente di resina della stampante. Aggiungendo una coppia di magneti permanenti all'estremità del cuscinetto a sfera, è possibile applicare un campo magnetico sulla resina e indurre il processo di self-assembly delle particelle magnetiche disperse. La direzione delle catene può poi essere controllata ruotando il cuscinetto a sfera, ovvero i magneti. Per verificare l'efficacia della strategia proposta, abbiamo stampato una struttura su tre livelli variando la direzione del campo magnetico di stampa per ogni livello stampato (0°, 45°, e 90°). Le immagini ottenute al microscopio ottico hanno dimostrato che eravamo in grado di controllare la dimensione delle catene incorporate variando le condizioni di self-assembly al contorno. Inoltre, la direzione degli aggregati assemblati coincideva con la

direzione del campo magnetico applicato in ogni livello della struttura nanocomposita. Pertanto abbiamo dimostrato che il set-up di modifica della stampante DLP proposto è efficace nel programmare la microstruttura dei materiali compositi stampati 3D.

L'influenza delle catene magnetiche sulle proprietà magnetiche macroscopiche dei campioni è stata valutata misurando i cicli di magnetizzazione dei materiali lungo tre diverse direzioni del campione (parallela, trasversale, e perpendicolare). Nei campioni con nanoparticelle disperse casualmente, i tre cicli di isteresi erano perfettamente sovrapposti, dimostrando che i nanocompositi erano isotropi magneticamente; cioè, le tre direzioni misurate erano magneticamente equivalenti. Al contrario, per i campioni contenenti catene magnetiche orientate, la curva di magnetizzazione misurata lungo la direzione delle catene (parallela) era caratterizzata da una maggiore pendenza rispetto alle direzioni perpendicolari e trasversali. Dato che i tre cicli magnetici non coincidevano più, i campioni erano magneticamente anisotropi, ed essi erano caratterizzati da un asse di facile magnetizzazione in cui la magnetizzazione era favorita, il quale coincideva con la direzione di orientazione delle catene magnetiche. Per cui, attraverso il controllo della microstruttura, eravamo anche in grado di programmare la risposta magnetica dei materiali prodotti. Il grado di anisotropia magnetica degli oggetti è stato regolato variando l'intensità del campo magnetico applicato e il contenuto di nanoparticelle nel materiale. Le condizioni ottimali per massimizzare l'anisotropia magnetica consistevano nell'applicare di un campo magnetico di 10mT durante il processo di stampa, e aumentare la concentrazione di NP fino al 6%.

I polimeri stampati con microstrutture orientate si comportavano come delle bussole magnetiche. Quindi, quando veniva applicato un campo magnetico uniforme, gli oggetti ruotavano per allineare il loro asse di facile magnetizzazione, ovvero l'asse maggiore delle catene magnetiche, lungo le linee del campo. Sfruttando questo meccanismo di attuazione, abbiamo prodotto delle ruote dentate guidate dal campo magnetico che subivano rotazioni programmate attraverso l'applicazione di un campo magnetico da remoto. Due ruote dentate geometricamente identiche sono state stampate 3D controllando la loro microstruttura. Sotto l'applicazione di un campo magnetico uniforme (4mT), la ruota dentata con catene orientate ruotava per allineare il suo asse di facile magnetizzazione al campo. Al contrario, la ruota dentata con nanoparticelle disperse casualmente è rimasta ferma dato che è magneticamente isotropa. Successivamente, abbiamo sviluppato un ingranaggio riduttore di velocità guidato dal campo magnetico, e abbiamo dimostrato che la ruota motrice magnetica era efficace nel trasferire la coppia meccanica alla ruota non magnetica portando alla

rotazione di quest'ultima. Infine, abbiamo prodotto ingranaggi meccanici più complessi composti da più parti mobili. In particolare, abbiamo sviluppato una morsa basata sulla meccanica della cremagliera (ingranaggio – dentiera). Attraverso l'applicazione di un campo magnetico da remoto, abbiamo dimostrato che eravamo in grado di controllare l'apertura e la chiusura dei bracci della morsa in ambienti chiusi.

Il controllo sulla microstruttura e sulle proprietà magnetiche degli oggetti è stato anche utilizzato per produrre dei martelletti magnetici. Controllando la microstruttura degli oggetti era possibile prevedere la loro rotazione. Pertanto, attraverso l'applicazione di un campo magnetico, i dispositivi prodotti subivano delle rotazioni programmate per allineare le catene magnetiche incorporate nell'oggetto lungo la direzione del campo.

Al fine di trasformare la rotazione controllata degli oggetti in una flessione controllata, è necessario che la coppia magnetica applicata superi la resistenza meccanica del materiale. Per limitare il contributo della coppia meccanica resistente, gli oggetti sono stati prodotti con la matrice polimerica più flessibile (50Eb50BA). Inoltre, anche il disegno dell'oggetto è stato cambiato per ridurne la sezione resistente e focalizzare lo stress meccanico in un punto preciso del materiale. Dall'altra parte, il contributo della coppia magnetica è stato regolato variando l'intensità del campo magnetico applicato. Infine, fissando gli oggetti ad un fulcro, essi subivano una flessione controllata, e l'ampiezza della deformazione dipendeva dall'intensità del campo magnetico applicato.

Attraverso le pagine di questa tesi di dottorato, abbiamo prima di tutto dimostrato la possibilità di produrre dei polimeri reattivi al campo magnetico con nanoparticelle magnetiche disperse. Controllando la risposta meccanica degli oggetti abbiamo dimostrato diversi tipi di movimento come il rotolamento, la traslazione, la flessione, e i processi di ripiegamento. Per controllare la microstruttura dei materiali nanocompositi, abbiamo investigato il processo di auto assemblaggio delle NP di Fe_3O_4 applicando un campo magnetico uniforme su film liquidi delle resine fotoreticolabili. La dimensione e la direzione delle catene magnetiche assemblate sono state controllate variando le condizioni di contorno al sistema (intensità e direzione del campo magnetico, concentrazione di NP, e viscosità del mezzo).

Una stampante 3D DLP preesistente è stata modificata per sfruttare i meccanismi di self-assembly per produrre materiali con microstrutture programmabili. Attraverso il set-up proposto, abbiamo controllato la dimensione e la direzione delle catene magnetiche in ogni layer stampato portando alla microstrutturazione dell'intero materiale.

Infine, controllando la microstruttura dei materiali, abbiamo programmato la loro anisotropia magnetica. E questo è stato sfruttato per produrre molteplici dispositivi attivabili da remoto che incorrono in precise rotazioni e flessioni.

Résumé en français

L'impression 3D permet la production de structures complexes et le prototypage rapide d'objets. Les récents progrès réalisés dans le domaine de la fabrication additive ont permis, année après année, le développement de nouvelles imprimantes ainsi que de nouvelles stratégies d'impression. Cela a permis d'une part d'élargir la palette des matériaux imprimables et d'autre part de développer de nombreuses applications industrielles allant de l'automobile à la mode.

Récemment, des nouvelles tendances en recherche-développement sur l'impression 3D ont vu le jour, et on prévoit qu'elles stimuleront le développement de plusieurs sujets technologiques. Parmi celles-ci, l'impression 4D consiste à imprimer des objets dont la forme et les propriétés peuvent être modifiées de manière contrôlée (le temps étant la quatrième dimension) sous l'effet de leur environnement, c'est-à-dire la lumière, l'humidité, le champ électrique.... Parmi ces stimuli, les champs magnétiques présentent des caractéristiques particulièrement intéressantes, car ils peuvent être facilement appliqués par l'utilisation d'aimants permanents et de solénoïdes, ils ne sont pas nocifs pour l'utilisateur (dans le domaine d'utilisation), et permettent le contrôle à distance des objets imprimés. C'est-à-dire, le contact direct entre la source et le matériau n'est pas obligatoire pour induire un mouvement.

La manière la plus simple de produire des polymères magnéto-actifs consiste à incorporer des structures magnétiques de dimensions micro- ou nano-métriques dans la matrice polymère. Pour optimiser le contrôle magnétique des objets composites, l'organisation microstructurelle des particules incorporées est exploitée en ayant recours au processus d'auto-assemblage. En effet, lorsque des particules magnétiques dispersées dans un milieu liquide sont exposées à un champ magnétique uniforme, elles s'assemblent spontanément en structures filaires, c'est-à-dire elles forment des chaines de nanoparticules, orientées le long des lignes de champ.

Dans ce travail de thèse, nous proposons une méthodologie d'impression 3D innovante pour exploiter les mécanismes d'auto-assemblage des particules magnétiques et ainsi contrôler les microstructures et les propriétés magnétiques des objets imprimés. Cette stratégie nous a permis de produire des dispositifs magnéto-réactifs avec une réponse mécanique programmable et contrôlée à distance par l'application de stimuli magnétiques. De plus, nous avons démontré que les objets imprimés peuvent fonctionner indifféremment dans des environnements clos

humides ou secs. Cela permet à ces objets d'avoir des applications dans plusieurs domaines allant de la robotique-souple à la détection, de l'administration de médicaments à la biomédecine.

Pour ce travail de thèse, le traitement numérique de la lumière (DLP) a été choisi comme technologie d'impression 3D car elle permet de traiter les matériaux à l'état liquide et donc de disperser facilement les nanostructures magnétiques. Les imprimantes 3D DLP sont basées sur le concept de photo-polymérisation, c'est-à-dire une réaction de polymérisation initiée par la lumière. En particulier, en partant d'un mélange liquide de monomères et d'oligomères, un photo-initiateur, généralement une molécule organique, est ajouté. Lorsque le photo-initiateur est irradié, il subit un processus de photoblanchiment qui génère des espèces réactives (radicaux, cations ou anions) déclenchant ainsi le processus de durcissement du matériau. Dans le cadre de la technologie d'impression 3D par DLP, un objet est d'abord numériquement divisé en tranches, ensuite en projetant l'image lumineuse de la couche à imprimer sur la résine photo-réticulable, l'objet est imprimé couche par couche. Si la matrice hôte contient des micro- ou nano-structures, celles-ci vont absorber une partie de l'irradiation lumineuse en réduisant le taux de polymérisation qui peut être préjudiciable pour l'impression de l'objet. Il y a donc a compromis à trouver entre la concentration maximale de particules introduites dans la matrice et le processus d'impression.

Lors de la première année de thèse, nous avons réussi à imprimer des polymères magnéto-actifs contenant des particules magnétiques dispersées de manière aléatoire. Pour cela, des nanoparticules de magnétite (Fe_3O_4) ont été ajoutées à un mélange d'acrylique d'uréthane (Ebecryl 8232) et d'un diluant réactif (acrylate de butyle). L'ajout du diluant réactif dans le système a été utilisé pour accélérer le processus de polymérisation, et ainsi contrecarrer la réduction de réactivité due à l'absorption de la lumière par les particules magnétiques. De plus, en augmentant la quantité d'acrylate de butyle ajouté à la résine de base (acrylique d'uréthane), nous avons réussi à diminuer la température de transition vitreuse ainsi que le module d'élasticité du matériau imprimé, produisant des polymères plus souples. Nous avons aussi démontré que la concentration des nanoparticules magnétiques dispersées dans la matrice ne modifie pas de manière significative la réponse mécanique de l'objet. Au contraire, les propriétés magnétiques des composites augmentent linéairement avec la concentration en particules. Les résultats expérimentaux montrent que les formulations préparées présentent une bonne imprimabilité jusqu'à 6 % en poids de particules, avec résolution spatiale de l'ordre de 400 µm. La réponse mécanique des objets a été adaptée en faisant varier dans les formulations le rapport Ebecryl 8232 et acrylate de Butyle. Cette approche nous

a permis d'étudier différents types de mouvements. Avec le polymère rigide, c'est-à-dire 75% Ebecryl et 25 % d'acrylate de Butyle, nous avons imprimé en 3D des objets permettant de mouvements de translation ou de rotation. Avec la matrice polymère plus souple, c'est-à-dire 50% Ebecryl et 50% d'acrylate de Butyle, nous avons exploité la flexibilité de la matrice pour obtenir des de mouvement de pliage-dépliage, comme par exemple éclosion d'une fleur.

Dans la deuxième partie de ce travail, nous avons étudié comment contrôler la microstructure des matériaux imprimés pour améliorer leur réponse magnétique. Notre stratégie se base sur l'auto-assemblage des particules magnétiques soumises à des champs magnétiques.

Nous avons d'abord étudié par microscopie optique la formation de chaines de particules avec le champ appliqué. Le processus d'auto-assemblage suit une loi de type sigmoïdale caractérisée par une augmentation rapide de la longueur des chaines, suivie par un plateau où les dimensions des chaînes n'évoluent presque plus. Ensuite, nous avons montré qu'en augmentant l'intensités du champ magnétique et la concentration des particules le processus d'auto-assemblage est facilité, ce qui permet d'obtenir des chaines plus longues. Au contraire, l'utilisation de résines plus visqueuses conduit à la formation de chaines plus courts en raison de la réduction de la mobilité des particules enfouies dans la matrice. En parallèle, en collaboration avec Marc Hayon et Hichem Dammak, nous avons développé un code numérique pour simuler les résultats expérimentaux.

Une fois les chaînes formées, nous avons étudié par microscopie optique leur rotation en faisant tourner le champ magnétique appliqué. Nous avons observé l'existence d'un angle de rotation critique (≈40°) ainsi que deux régimes de rotation différents. En dessous de l'angle critique, les chaînes magnétiques tournent simplement avec le champ magnétique. Au-dessus de l'angle critique, les chaînes magnétiques se fragmentent en unités plus courtes, qui tournent solidement avec le champ magnétique. Ce phénomène est bien prédit par le modèle physique proposé et par les simulations numériques, et il est imputable aux interactions magnétiques entre particules. Au-dessus de 45°, les interactions magnétiques deviennent négatives et cela conduit à la rupture de la chaîne.

Enfin, nous avons étudié le processus d'auto-assemblage ainsi que la rotation des chaînes *in situ* et à l'échelle nanométrique par microscopie à rayons X à balayage sur la ligne Hermès du synchrotron SOLEIL (collaboration avec Rachid Belkhou).

L'ensemble de ces résultats nous a permis de programmer la microstructure des films polymères lors de l'impression 3D. Afin de contrôler la microstructure d'un matériau lors d'un processus DLP, notre stratégie a consisté à reproduire le contrôle

2D sur les chaînes magnétiques dans chaque couche de l'objet imprimé. D'une part, la longueur des chaînes a été adaptée aux besoins de la manipulation en contrôlant l'intensité du champ magnétique appliqué et/ou en faisant varier la viscosité du milieu liquide et la concentration des nanoparticules dispersées dans les résines. D'autre part, la direction des chaînes magnétiques a été programmée en faisant varier l'angle d'application du champ magnétique pour chaque couche d'impression.

Le contrôle spatial du champ magnétique lors de l'impression a été possible en modifiant une imprimante DLP (RobotFactory HD2.0+). Le cœur du dispositif consiste en l'ajout au niveau du plateau de croissance de l'imprimante d'un roulement à billes en plastique pour ne pas interagir avec le champ appliqué. Celui-ci agissant comme nouveau réservoir de résine de l'imprimante. En ajoutant des aimants permanents aux extrémités du roulement à billes, il est ainsi possible d'appliquer un champ magnétique au niveau de la résine et ainsi induire l'auto-assemblage des particules magnétiques. La direction des chaînes assemblées est contrôlée en faisant tourner le roulement à billes. Comme preuve de concept du dispositif, nous avons imprimé une structure pyramidale à trois niveaux en faisant varier la direction du champ magnétique appliqué (0°, 45° et 90°) dans chaque couche pendant le processus d'impression. Les images de microscopie optique montrent la faisabilité du dispositif pour l'impression des objets contenant des chaînes magnétiques d'orientation différentes et donc son efficacité pour programmer magnétiquement des composites polymère magnéto-actifs imprimés en 3D.

L'anisotropie magnétique des échantillons imprimés a été étudié en mesurant les cycles de magnétisation dans trois directions de l'objet. Dans les échantillons contenant des particules magnétiques dispersées de manière aléatoire, les cycles d'hystérésis se superposent parfaitement, ce qui prouve que les composites sont magnétiquement isotropes, c'est-à-dire que les trois directions mesurées sont magnétiquement équivalentes. Au contraire, dans les échantillons contenant des chaînes magnétiques orientées, les cycles de magnétisation mesurés dans la direction de chaînes de particules présentent une susceptibilité magnétique plus importante que dans les autres directions (transversale et perpendiculaire). Cela signifie que les échantillons sont magnétiquement anisotropes avec une direction aisé d'aimantation qui coïncide avec celle des microchaînes.

Nous avons exploité l'anisotropie magnétique, associée à l'orientation des microstructures, pour programmer les propriétés magnétiques des matériaux imprimés. L'intensité de l'anisotropie magnétique a été adaptée en faisant varier l'intensité du champ magnétique lors de l'impression et la concentration de

nanoparticules dans les matériaux. Les conditions optimales correspondent à l'utilisation d'un champ magnétique de 10 mT pendant le processus d'impression et à une concentration de nanoparticules de magnétite de l'ordre de 6 % en poids.

Les polymères magnéto-actifs contant des microstructures orientées se comportent comme des boussoles magnétiques. Par conséquent, lorsqu'un champ magnétique externe est appliqué, les objets subissaient une rotation pour aligner leur axe magnétique aisé, c'est-à-dire le grand axe des chaînes magnétiques, le long des lignes de champ. En tirant parti de ce phénomène, nous avons produit des engrenages magnéto-actifs qui subissent des rotations programmées par l'application à distance d'un champ magnétique. Ensuite, nous avons développé un ensemble de dispositifs à entraînement magnétique, prouvant qu'une roue dentée magnéto-active est efficace pour transférer le couple mécanique à une roue non magnétique, entraînant ainsi la rotation de cette dernière. En partant de ce constat expérimental, nous avons fabriqué des dispositifs plus complexes basés sur plusieurs pièces mobiles. En particulier, nous avons développé une pince basée sur le principe de la crémaillère linéaire et nous avons démontré que nous étions capables de contrôler l'ouverture et la fermeture des bras de la pince dans des environnements humides.

Le contrôle de la microstructure et des propriétés magnétiques des objets a également été exploité pour produire des marteaux magnétiques. La rotation des objets est prédite par l'orientation des microstructures dans les matériaux. Ainsi, par l'application d'un champ magnétique, les dispositifs fabriqués subissent des rotations dont l'angle est programmé au préalable pour aligner les chaînes magnétiques intégrées dans la direction du champ.

Pour transformer la rotation contrôlée des objets en flexion contrôlée, le couple magnétique appliqué doit surmonter la résistance mécanique du matériau. Pour ce faire, nous avons imprimé des objets plus flexibles en utilisant pour la résine la formulation 50% ebecryl et 50% acrylate de butyle. En outre, pour réduire la section résistante de l'objet et concentrer la contrainte mécanique en un point programmé de la structure, la conception de l'objet a également été modifiée. La contribution du couple magnétique a été ajustée en faisant varier l'intensité du champ magnétique appliqué. En fixant les objets à un point d'appui, les objets subissent une flexion, dont l'amplitude dépend de l'intensité du champ magnétique appliqué.

Tout au long de ce manuscrit, nous avons démontré la possibilité de produire des polymères magnéto-actifs imprimés en 3D avec une réponse mécanique programmée. En adaptant la réponse mécanique des objets, nous avons démontré différents types de mouvements tels que le roulage, la translation, la flexion et le pliage/dépliage. Pour contrôler la microstructure des matériaux nanocomposites,

nous avons étudié le processus d'auto-assemblage, par l'application de champs magnétiques uniformes de particules de magnétite (Fe_3O_4) dispersées dans des résines photo-réticulables. La dimension et la direction des chaînes magnétiques assemblées ont été adaptées en faisant varier l'intensité et la direction du champ magnétique, ainsi que la concentration des nanoparticules et la viscosité de la résine.

Contents

1.

Introduction to 4D printing

1.1 A short historical overview of the development of materials science and technologies: from the Stone Age to 3D printing

By the term "3D printing" is meant: *an automated manufacturing process driven by a virtual image of a shape, where the physical object is produced by the addition of subunits of a raw material without the use of molds or materials removal processes*. In about 30 years, additive manufacturing evolved from an academic-oriented technique, first to prototyping machines and later as proper industrial manufacturing processes until the nowadays domestic diffusion with the production of desktop 3D printers for amateur users. The fast diffusion of the additive manufacturing can be explained by the novel capabilities of the technique in terms of freedom of design, material properties, and change of the manufacturing approach. For these reasons, often 3D printing is described as the cornerstone of the new industrial revolution. Indeed, it is predicted that 3D printing will durably change the manufacturing technologies, the economic development model, and in turn the today's society. In order to understand how this single technology may transform a society in depth, the historical overview of the technological progress is a helpful tool. Thus, in the following, the evolution of the manufacturing processes and the extension of available materials will be discussed, spotlighting those inventions that produced a remarkable sign in civilization development.

Starting from Stone Age, and passing through the technological milestones, the advent of the "Digital Era" landed in the nowadays globalized world based on large-scale economics and led to the dawn of the 3D printing age.

1.1.1 From stones hitting to industrialized manufacturing processes

The clearest example of the crucial role played by materials in mankind's societies is given by the traditional way adopted to divide prehistorical eras: stone, bronze, and iron ages. A material itself is almost useless if its shape cannot be controlled, otherwise manufactured. Thus, the development of new technologies is strictly related to both the material and the corresponding manufacturing techniques. During the stone age, the *Homo habilis* (from Latin "toolmaker") produced axes, arrowheads, and agriculture tools by hitting stones and cutting woods. Later, the chance to control fire and to produce ovens led to the birth of metallurgy and the production of bronze and copper artifacts that gradually substituted stone-made tools improving, for instance, men hunting capabilities. In the material-manufacturing-application development cycle, the progress of manufacturing techniques makes the new tools available, which in turn improve the production processes [1]. The introduction of newly manufactured objects radically changed the way our ancestors faced life: for instance, the production of stone tools enabled the development of agriculture, and thus the transition from a hunter-gatherer society to the establishment of the first urban centers [1]. Later, the further improvement of the materials' properties and manufacturing techniques allowed for additional food production, and consequently the possibility of devoting oneself to intellectual occupations such as administration, legislation, science, and writing [2], changing again the socio-economical layout.

The introduction of the first writing techniques represented a pivot point in mankind's development. Indeed, writing - invented in 3000 B.C. in Mesopotamia by the Sumerian civilization - allowed an easier and broader transmission of knowledge which boosted the civilization process, material science included. After the iron age, historical periods were no longer classified according to the materials used. Indeed, witnessed by the written documents, they have been classified

according to the key events and great personalities. In the early ages, the object manufacturing was carried out by the handwork of craftsmen, resulting in slow production volumes and low-reliable goods. Thanks to the improvement of the energy generation, ensured by the watermill and the windmill, the concept of "mechanized production" was first introduced during the Middle Age. It resulted in an enhancement of the production volume, as well as of the proprieties of the manufactured tools and, in turn, of several applied fields. In particular, trip hammer and blast furnace boosted the development of metallurgy leading to a larger production of pig iron, lead, and copper. But only with the discovery of steam as a new energy source, and its exploitation in steam engines, the transition from craftsmanship to an industrialized or mechanized production will be fulfilled.

Steam power and steam engines are the milestones that lead to the First Industrial Revolution (18th century) changing the approach of production from a predominant handwork approach to mechanized factories. At this stage, the innovation brought by machines mainly influenced the textile and metallurgy sectors. Indeed, thanks to mechanization, the iron industry experienced a huge development introducing novel manufacturing processes as drilling (1774) by Wilkinson, and later by Henry Cort which invented rolling (1783) and puddling (1784) for steel production. Mechanization allowed a fast production of metallic components with improved properties and repeatable shapes substituting hammer-hit manufactures. In particular, mining took advantage of the upgraded versions of steam engines allowing to dig deeper and to extract larger volumes of minerals. The synergic boost of materials, components, machines, and application fields transformed an agricultural-artisan society to an industrial one. The development of new manufacturing processes, new available minerals, e.g. coal, electricity, and petroleum lead to the Second Industrial Revolution (1831-1901), allowing the development of a wider palette of materials and technologies, as Portland cement, large-scale production of continuous sheets of paper, large-scale synthesis of chemicals, and continuous production of plate glass for windows. With the Second Industrial Revolution, the mechanization of the manufacturing processes led to the appearance of assembly lines, electrical grid systems, and by the final economic conversion in a large-scale production system. The human effort involved in the creation of artifacts was again decreased, while the reliability and volume

production of goods increased. The impact of industrialization was enormous on human society: the emerging bourgeois class led by capitalists and industrialists overthrown the already wounded aristocracy by the French Revolution of 1848, and the new laboring class left rural regions to increase urban population and demanding civil rights. Cities faced the problem of overpopulation, and sanitation and water supply systems were implemented to prevent the spread of diseases such as the cholera epidemic that blown London in 1854. The fast urbanization and the availability of new materials changed how architecture was conceived: the Eiffel Tower, the symbol of Paris and the "Belle Epoque", is a direct example of the Industrial Revolution and of the advances of metal and glass manufacturing techniques. At the same time, the railways shortened the distances between cities and increased the number of people who could afford to travel, beginning the transition to a globalized world. The socio-economic significance of the Industrial Revolution was so tremendous, that it is considered the most important event of mankind's history after agriculture and animals' domestication [3].

1.1.2 Polymer Era and the birth of 3D printing

As a result of the Industrial Revolution and the technological advances in petroleum and chemical engineering, a new class of materials emerged: the polymers. The first example of synthetic polymer was reported in 1907 by Leo Baekeland with a thermo-setting phenol-formaldehyde resin called Bakelite [4]. Polymers completely changed the materials world. Indeed, for the first time humans were able to manufacture objects starting from synthetic, not pre-existing, materials. World War II boosted the need for new polymers to replace materials that were hard to supply such as silk and natural rubber. Nylon and synthetic rubber were discovered and later advanced polymers were introduced, as Teflon and Kevlar [5]. Nowadays, polymers are used in almost every field, since they combine lightweight with unique properties such as chemical resistance, thermal stability, electric and barrier properties [6]. The possibility to start from a synthetic material allows a large control of its properties. Due to the low processing temperatures, it is possible to add specific additives and/or constituents to the final material. For

these reasons, polymers science reached important goals, and nowadays it is almost impossible to think about a device without polymers.

The cold war and the space race between the Soviet Union and the United States boosted the research on innovative materials and technology. If materials have always been a pivotal point in human civilization progression, it is only during the Cold War that materials science began to be more widely recognized as a specific and distinct field of science and engineering. The pivot point was the document released by the US President Science Advisory Committee (PSAC) that stated materials were the bottleneck for space discovery and military technology. Thanks to both academic and industrial interests and through an interdisciplinary approach, incorporating elements of physics, chemistry, and engineering, materials science has grown rapidly since the 1950s. At the same time, major technical universities around the world created dedicated schools for its study. The first "material science and engineering" department was created in 1955 at Northwestern University (Evanston, Illinois, USA), while in Europe it was only inaugurated in the 1970s [7]. During the relatively peaceful period after World War II, several new technologies were developed such as electronics, telecommunications, and informatics, driving to the so-called "Digital Era" that, with a materials interpretation, it easy to describe as "Silicon" or "Polymer" Age, since the large make use of these materials in digital applications.

Nowadays, computer numerical control (CNC) pushes for the development of electronics. CNCs are motorized machines that can be programmed by an external computer accomplishing precisely specific instructions. CNC limited once again the role of the human being in the manufacturing process, increasing the precision and the reliability of the produced objects. Simultaneously, the development of automation techniques increased the interest for an easier approach to the CNC machines. The effort on this topic led to the release of graphical computer-aided design (CAD) software, improving the programmability and the precision of CNC. The invention of CAD software is the first step for today's manufacturing revolution: 3D printing.

Until 1980s, the manufacturing techniques were based on the concepts developed in ancient times of material removal or molding, where only the procedure evolved from a hand-made approach to a large-scale fully industrialized

production. Generally, in these processes a large amount of wasted material is produced. Moreover, not all the morphologies can be obtained, as often the intrinsic deformability of the material limits the possibility of having all shapes. The two abovementioned drawbacks have been solved by the development of the 3D printing technologies. Indeed, the ultimate object shape is no longer led by material removal, but by the addition of subunits of a row material, driven by a virtual construction of the object. Furthermore, 3D printing allows better control of materials properties, and recently, it is also opening new perspectives in materials micro/nano structuration, and programming smart and functional materials, boosting progresses in several application fields such as electronics, robotics, and biomedicine [8], [9].

Technological innovation is one of the main characters in the civilization transformation and evolution. In a synergic cycle, the availability of new materials and manufacturing processes often boosts the advances in several applications, and the last ones foster again the development of new materials. In the case of 3D printing technology, its birth was determined by the development of informatics and electronics; but the last two were possible by the progress in silicon technology.

In the next section, we will describe the historical evolution of the 3D printing technologies, their spread in industrial applications, and the potential socio-economic implications and technological trends.

1.2 Additive Manufacturing and 3D printing

3D printing, also known as Additive Manufacturing (AM), is a groundbreaking technology that is rapidly becoming popular in many applications. This section aims to faithfully painting the historical effort made to widen the palette of available materials and to improve the printing technologies. The success of AM over the conventional manufacturing approaches are discussed, and several examples of industrial applications are reported. Besides, by this historical and economic analysis, the importance of a design-free approach, and the development of advanced materials in the growth of the 3D printing technology will be underlined.

1.2.1 A problem of definition

Generally speaking, when a technological innovation arrives on the market, the term used to define this novel technology is often ambiguous and subjected to different understanding and continuous variations. Additive manufacturing does not escape to this rule. In particular, already the official definitions of 3D Printing and Additive Manufacturing reported by the American Society for Testing and Materials (ASTM) in ISO/ATM 52900:2015 [10] are unclear:

3D printing - *"fabrication of objects through the deposition of a material using a print head, nozzle, or another printer technology"*

Additive Manufacturing – *"process of joining materials to make parts from 3D model data, usually layer upon layer, as opposed to subtractive manufacturing technologies."*

However, in the current use AM is generally related to industrial and technical environments, while 3D printing is often used in non-technical contexts [11]. Here, to avoid any sort of misleading discussion, the two terms are used as synonymous.

1.2.2 3D Printing: An historical overview

The advances in graphic software as CAD, coupled with the important goals achieved in the polymers science, brought in the '80s to the introduction of the 3D printing concept. In 1986, Charles Hull from Colorado University took advantage of his expertise in photopolymerization processes, realizing and patenting the first 3D printer device, as well as the STL file format used in the stereolithography software. At the same time, he founded 3D Systems, the first company specialized in 3D printing. The first 3D printer was a stereolithography (SLA) one building the physical product by the point-by-point polymerization of a photocurable acrylate resins according to the instructions contained in the virtual shapefile (STL file). SLA technique works by selectively exposing liquid resins to a laser light source, to form layers of solid polymeric materials that stack up to create a solid object.

Owing to the large success of SLA, different printing techniques were developed by several research groups in the following years. Among them, Scott Crump in 1990 invented the Fused Deposition Modeling™ (FDM), also known as Fused Filament Fabrication (FFF), the most popular 3D printing technique, where a filament of a thermoplastic polymer is first molten and then deposited by a nozzle on a building platform according to the instruction given by the STL file. A detailed description of the operating principles of the most diffused 3D printing techniques is given in section 1.4.

Another aspect that should not be overlooked is the development of new printable materials and design solutions. For instance, at the beginning of the 3D printing era, only acrylated polymers were available for SLA, and a restricted palette of low-temperature melting thermoplastic materials were processable via FFF. Later, not only the typologies of available polymeric material were increased, but also in 1993 waxy materials were successfully 3D printed by adding clays to the starting formulations or filament [12]. The introduction on the market of Selective Laser Sintering (SLS) opened the path to the 3D printing of polymeric, metal, and ceramic powders [12], [13]. In addition, from the 2000s onwards nanocomposites [14], organic and edible materials were profitably 3D printed [12]. Nowadays, advances are made to increase the volume and speed production, or to downscale the precision of manufactured objects in the micro and nanoscale, as for the Two Photons 3D Printing (2PP) [15]. From the materials point of view, researchers are developing structural and functional materials suitable for 3D printing techniques. Indeed, the possibility to manufacture materials with unique properties with no shape-limitation can help to design new devices in several application fields such as electronics, robotics, and medicines [15], [16].

Looking at the industrial applications, due to the low reliability and accuracy of the first SLA and FDM 3D printers, as well as the small palette of available materials, their use was only intended for rapid prototyping. However, nowadays AM technologies gained an important place in the automotive and aerospace industries [17]. The birth of new based-AM starts-up and companies boosted the 3D printing economy by introducing innovative technologies and materials, and, in turn, decreasing the costs related to the printing processes. Nowadays additive manufacturing is present in other industrial fields such as architecture and civil

engineering for the realization of structural models, in medical and pharmaceutics where the clearer examples are the 3D printed dental prosthesis, and lately, fashion and food industries are just around the corner [18].

1.2.3 Economic Considerations

"A once-shuttered warehouse is now a state-of-the-art lab where new workers are mastering the 3D printing that has the potential to revolutionize the way we make almost everything" – Barack Obama, 2013

Although its fast expansion, there is still a remarkable gap between the capabilities reported by the media and the effective spread of 3D printing in industries and everyday life. The manufacturing revolution linked to 3D printing is in fact in contradiction with the general economic concept of large-scale production, and the transition may result hard.

In large-scale economies, the rate and volume production of a good has a strong impact on the costs required to manufacture it, thus on the price of the object on the market. Instead, by additive manufacturing, the volume-cost-price correlation is no longer valid, since the production costs are only linked to the materials and energy consumption. The choice of the manufacturing technique is strictly related to the number of pieces to produce. In 2012 it was estimated that additive manufacturing was competitive to conventional inject molding for productions lower than 5,000 units [19]. If in 2012 the average price for a 3D printer was 10,000$ nowadays is possible to buy a DLP printer for 5,000$ and an FFF printer for less than 1,000$ [19]. Thanks to advances in technology and new materials available the threshold limit of 5,000 pieces is going to increase. The costs related to the fabrication of a single object are doubtless lower in 3D printing than in conventional manufacturing techniques, but in an economy of scale, where the production of multiple copies of the same identical object is required, conventional manufacturing processes result by far the best option [20]. Analyzing the diffusion of additive manufacturing in industrial fields, it is no wonder that their expansion concerns those fields where

large-scale production is not a fundamental requirement: aerospace, fashion, architecture, education, and high-performance automotive [16].

Although the drawbacks of 3D printing technologies compared to large-scale production, in 2014 about 11% of the producers had already switched to volume production of 3D printed parts or products [19]. Indeed, additive manufacturing shows other advantages that traditional manufacturing techniques cannot achieve such as the reduction of inventory costs and risks. The on-demand production methodology guaranteed by additive manufacturing, avoid the storage of a large number of components and semi-finished products to assemble; moreover, the number of unsold finished goods is strongly decreased. Other advantages come from the low energetic consumption and the reduction of waste. It is estimated that with 3D printing is possible to save 40% of the waste material compared to subtractive manufacturing techniques, furthermore, almost 98% of the wasted material produced during a printing process can be recycled or even re-use [21]. In Tab. 1.1 the differences between additive manufacturing and traditional manufacturing are resumed.

As an example of the side-benefits assured by 3D printing, and their exploitation in the industrial fabrication, the General Electrics (GE) case-study, concerning the production of fuel nozzles for jet engines, is here reported. GE expects to produce more than 45,000 units of the same object by year, so by considering only the production volume, traditional large-scale production would represent the best option. However, in the conventional manufacturing process, the gear is built by assembling 20 separately cast parts, while on the counterpart, additive manufacturing allows the production of fuel nozzle in a single process. Considering the costs related to the production and shipment of the cast parts, more the storage costs, GE convinced that 3D printing technology would cut the manufacturing costs by about 75% [19].

Table 1.1: comparison between Additive and Traditional Manufacturing [22].

	Traditional Manufacturing	Additive Manufacturing
Production cost	Economies of scale can lead to very low unit-cost but require a large volume of sales of specific products	Unit cost does not vary much with scale, no cost imperative to sell large volumes of specific products
Design requirement	Strict design-for-manufacturability requirements restrict product design possibilities	Reduced design-for-manufacturability requirements allow novel designs
Specialized molds and tools	The fixed cost for product-specialized tools is distributed across all units produced	No fixed cost for product-specialized tools and molds
Production speed of order	Serial process that depends on the speed of the critical path, as well as the degree to which bottlenecks lead to queues	Parallel process that depends on the speed of a printer and the number of printers used
Delivery speed of order	Globalization of production entails long transportation lead times, reducing delivery speed	Localization of production enables fast delivery upon completion of order
Capacity utilization	Specialized equipment requires high volume in specific products to achieve adequate utilization	Flexible equipment requires volume across different products to achieve adequate utilization
Capacity expansion	Lumpy expansion opportunities imply that plants often operate at over/under capacity	Easier to adjust capacity to demand since capacity can be bought in smaller increments
Learning curve	Production process may require product-specific learning, generating economies of scale	Learning is machine-specific and applies to different products made on the machine
Forecasting	Detailed product mix forecasting can lead to insufficient statistical aggregation to make accurate predictions	Forecasting shifts to aggregate raw materials and capacity, making forecasting more accurate
Bill of materials	High parts count due to product portfolio proliferation and specialization of supply chain partners	Low parts count due to the ability to integrate parts in the printing process
Purchasing	Separate bill of materials in product portfolio can lead to a large number of suppliers and low volume in supplied components	Raw material needs reduce complexity of purchasing portfolio and allow efficient scale in purchasing with less demand volume
Transportation	Leveraging economies of scale requires aggregating global demand, increasing complexity of transportation of parts and finished goods	Localized production means less transportation of parts and finished goods; transportation needs focus on raw materials, where demand is more aggregated and transportable
Material use	Subtractive process leads to excess material and waste	Additive process leads to less excess material and waste; recycling of printed and other materials a promising possibility
Marketing	Reaching global markets requires investment in brand to create global awareness and trust	Local production allows tapping into social responsibility and local networks to create awareness and trust

The huge versatility and potential of additive manufacturing is also confirmed by the market trends. Between 2012 and 2014 3D printing experienced an annual average growth of 33% reaching a total value of $5.1 billion in 2015 and representing the strongest industry growth in 18 years. The future trends of 3D printing are even brighter and in 2018 when the current value of the market was $10.8 billion, the growth of this market segment was predicted to be $20 billion for the year 2020 [16]. The AM revolution may also change the firms balance settled in the large-scale economy. In the conventional manufacturing world, large organizations operating already in the market have a consolidated advantage compared to small companies, and they act as barriers to entry for new firms. A new industry needs a large capital investment to build large factories and increase production volume to decrease the production cost. With AM this is no longer true since the unit cost of the product is comparable with the value of the same product processed by traditional manufacturing [22].

Many speculations have been made in order to predict the future impact of additive manufacturing on society: the chance to localize the production to get closer to the costumers will drastically decrease the costs and environmental impact of the shipment services. The chance to produce the good closer to the costumers may be the turning point for the transition from a globalized economy to new localization. UPS has predicted a future shrinkage of the delivery business, and now it is investing in the foundation of world-spread 3D printing factories to manufacture products closer to their customers [22]. According to other futuristic opinions, in the future 3D printing technology will enter in family houses, allowing easy customization and production of the required goods.

In general, the choice between additive manufacturing and large-scale production is still related to the production volume, the part size, the design complexity, and the materials cost. Anyway, the advancements of 3D printing technologies are continuously promoting the spread of this technology in a variety of applications, and in the next future, they could transform the production economic model, and therefore society. Recently, a new research path is increasing the potential of additive manufacturing, and this is the chance to manufacture materials with specific and precise properties that cannot be obtained by

conventional manufacturing techniques. The new designing concept promoted by 3D printing allows a faster development of devices in many application fields. In particular, the design-freedom leads to the enhancement of the properties of smart materials, especially those focused on shape features and shape-morphing behavior. This new trend known as 4D printing will be discussed in the next unit introducing the technological background of this work.

1.3 Smart Materials and 4D Printing

1.3.1 Introduction to Smart Materials

Materials have always been developed to meet specific needs. Until the modern age, the application fields of materials were mainly linked to mechanics: tooling and construction. To materials were mainly required mechanical properties such as hardness and strength or structural specifications, i.e. they had to avoid deformation or breakage. With the advent of fields as electronics and optics, where the applied materials mainly have to fulfill specific demands and functions, hence the term "functional material", the mechanical performances of the devices became less important. Anyway, despite a less crucial role of mechanical stiffness, the materials still have to maintain their shape.

On the other hand, a living organism differs from "*synthetic matter*" by showing motion (animals) or shapeshifting (plants), which is the result of an intelligent interaction with external stimuli. For instance, the chameleon is able to change the color of its skin according to the surrounding environment, the Dionea Muscopia, a carnivorous plant, answering to a tactile stimulus can quickly move its leaves in order to capture a fly and the sunflower rotates according to sun position.

In the course of history, nature has always been a fascinating source of inspiration for scientists. Recently, the emerging topic of "advanced (functional) materials" aims to develop materials able to mimic behaviors observed in nature. This new scientific field can be divided into two main sub-topics: *bio-inspired materials* and *smart materials*. Bio-inspired materials show a high level of complexity in their micro or nanostructure, mimicking the natural world i.e. shells and shellfishes for mechanical properties, insects' wings for optical properties, but

also thorny devil (Moloch horridus) skins for water-harvesting. On the other hand, *smart materials* are intended *those materials which can modify their shape or their properties as a response to specific external stimuli* [23]. Otherwise stated, smart materials deal with the reproduction of the stimuli-responsive behavior of living organisms avoiding complex motorized motion systems. This research activity covers several topics such as self-healing materials, smart-sensing materials, and shape-changing materials [24], and represents a revolutionary procedure aiming at improving robotics and sensor technology, with a significant impact on biomedical, mechanic, and construction fields.

1.3.2 The need for 4D Printing

The enhancement of smart materials is often limited by the manufacturing techniques in terms of design freedom, microstructure properties, and processing complexity. Recently, however, the fabrication of smart materials by additive manufacturing technologies emerged as a solution to fully develop devices potentialities. This innovative concept was first introduced in 2013 by Skylar Tibbits during his TED talk and afterward named as "*4D printing*". The term of 4D printing was introduced to describe how 3D printed multi-materials were able to self-assemble in new structures when submerged in water [25].

It is worth mentioning that due to its recent development, a univocal and simple definition of 4D printing is still missing. Originally, 4D printing has been considered as a 3D printed object exhibiting time-dependent shape morphing properties, the time being the fourth dimension [26]–[28]. However, considering only shape-morphing materials is a limiting statement. Indeed, 4D printing can be also applied to 3D printed objects with programmable microstructures, or to devices undergoing complex motions without changing their shape. Thus, considering a less stringent definition, 4D printing can also be defined as a 3D printing process where smart materials responding to external stimuli are involved [23], [24].

Despite the terminology issue, it's important to point out that 4D printing is not a new technology, i.e. 4D printers do not exist, but 4D printing has to be intended as the combination of 3D printing technologies and smart materials. Thus, by

combining the previous statements, a more general definition for the 4D printing can be as follows:

4D printing is the result of a 3D printing process where the printed structure is able to change its shape in a smart and predictable manner when exposed to external stimuli. The chance to further modify the shape of the 3D printed object add time as the fourth dimension.

A graphical explanation of this concept is shown in Fig. 1.1. In geometry, dimensions are expressed as the minimum number of coordinates requested to locate any point within it. In a one-dimensional object, as a line, the position of a point is described by only specifying its distance from the origin, while in a surface two coordinates are needed (length and width), and three coordinates in a solid (length, width, and height). The same approach is applied to the volume of a real object. But if the material's properties or shape can change, time must be added as a fourth coordinate. The application of time as a new coordinate brings the system to the 4^{th} dimension. As previously claimed, only smart materials exhibit properties or shape transformations evolving with time.

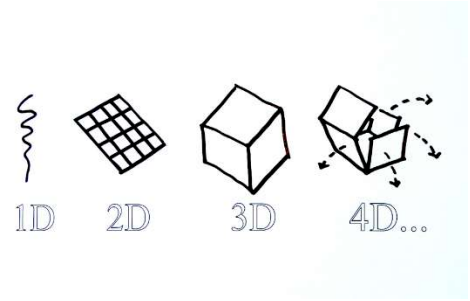

Figure 1.1: From 1D to 4D graphical representation [29].

1.3.3 Shape Morphing Materials

Focusing on materials undergoing shape-transformation, they are commonly divided into Shape Morphing Alloys (SMAs) and Shape Morphing Polymers (SMPs) according to the material's class they are made of [23], [26].

SMAs are made of metallic alloys and undergo shape-memory mechanism due to thermo-activated transformations of their crystal structure [30]. SMAs show all the advantages related to using metallic materials such as high operating temperatures and good mechanical properties [26]. However, cyclic phase

transformations often lead to microstructural defects which deteriorate the shape-memory behavior.

On the other hand, polymeric materials are affected by poor mechanical and thermal stability compared to SMAs, but they offer a larger control of the shape-morphing mechanism, and according to their chemical structure, or the presence of embedded functional particles, SMPs can be activated by several sources such as temperature [31]–[34], solvents [35], [36], pH [37], [38] light [39]. Thanks to an easier manufacturing process, it is possible to take advantage of the polymers' tunability fabrication to produce composite materials with programmable anisotropy and objects undergoing multiple and complex motions or even tailor-made properties according to the desired application, i.e. biocompatibility and biodegradation [26]. Among the available polymers, thermosets are mainly adopted since higher cyclic shape recovery capabilities than thermoplastic [26]. In Tab. 1.2 the main advantages and drawbacks of SMA and SMP are summarized, as well as the available sources.

Table 1.2: Main features and comparison of SMA and SMP.

	Advantages	**Drawbacks**	**Sources**
Shape Morphing Alloys (SMA)	• Operating temperature • Mechanical properties	• Lower strain recovery • High cost • Difficult to produce	• Temperature
Shape Morphing Polymers (SMP)	• High strain recovery • Low density • Tunable properties • Low cost • Easy to manufacture	• Lower mechanical properties • Lower thermal resistance	• Temperature • Moisture • Solvents • pH • Light • Magnetic field • Electricity

According to the type of the applied external stimuli, the SMPs devices show peculiar properties. For smart polymers reacting to temperature, glass transition temperature (T_g) covers a key role. Indeed, below T_g the polymers will maintain the original shape, while above T_g the material can be shaped by stress. On the other

hand, light-responsive polymers allow a precise activation of the material controlling the intensity, direction, and polarization of the light, avoiding heating the surrounding [40]. If thermo- and light-responsive polymers show a slow reactivity to the external impulses, electroactive polymers (EAPs) are characterized by fast reaction kinetics and high deformation. However, the remote control is not possible since they need to be connected continuously to an electric supplier [41]–[43]. Recently, magnetic polymeric nanocomposite emerged as a new class of shape-morphing materials, as they are often applied as soft-actuators. By adding magnetic fillers in the polymeric matrix, it is possible to magnetize the material making it magneto responsive. Magnetic-driven materials show several advantages: they can be remotely controlled working in several environments. Moreover, the magnetic sources are in general cheap and safe, thus not well-controlled laboratory environments are requested to operate with these materials. The reactivity of magnetic-driven actuators is generally fast, and the magnitude of the deformation depends on the amount of magnetic particles embedded in the matrix. In Tab. 1.3 the main advantages and drawbacks of the applied sources are summarized.

Table 1.2: Characteristics of the 4D printed polymeric materials according to the exploited external stimuli.

	Control	Deformation Magnitude	Deformation rate	Sources	Application flexibility
Temperature	**Remote** NO directional	**Medium**	**Low**	Heaters	**Low**- Limited by a controlled environment
Light	**Remote** NO directional	**Medium**	**Low**	Lamps with controlled intensity and polarization	**Medium** – Limited only in environments where light can be applied
Moisture	**Remote** NO directional	**Medium**	**Low**	Environment	**Low** - Limited by a controlled environment
Solvent	NO remote NO directional	**Medium**	**High**	Liquids	**Pour** - Only in liquid environments
Electric current (EAPs)	NO remote **Directional**	**High**	**High**	Electric energy suppliers	**Good** - but constantly linked to the supplier. No application in liquids
Magnetic Field	**Remote Directional**	**Medium**- limited by particles concentration	**High**	Magnets Solenoids	**Excellent** – Limited only when magnetic fields are avoided

In conclusion, the recent growing interest concerning smart materials and 4D printing is justified by considering the enormous implications that these two topics may have in several application fields. In particular, magneto responsive polymers emerged as an interesting solution for the fabrication of micro-robots, soft-actuators, and sensors by combining the advantages of polymeric materials with remote actuation control, high deformation rate, and a relatively cheap and accessible production process. The chance to freely-design magnetized polymers by the use of a 3D printer can finally develop the full potentialities of these materials. In this framework, this Ph.D. work aimed to develop a new class of 3D

printed magneto responsive polymers with enhanced properties. A further discussion about these materials is given in chapter 2 of this manuscript.

In the next sections, a technological overview of the 3D printer technologies is given, describing the operating principles and the physical and/or chemical processes involved.

1.4 3D Printing Technology

To develop an efficient printing process of polymeric magnetic composites, the choice of the 3D printing apparatus has a crucial significance. Here the main technological aspects related to 3D printing technologies are introduced, and a more detailed discussion is carried out about the 3D printers more frequently used for 4D printing applications (FFF, DIW, SLA, and DLP). Moreover, since this Ph.D. work focused on the production of magneto-responsive polymers, an overview of the main strategies to produce nanocomposite materials by 3D printing technologies is reported.

1.4.1 From virtual file to real object

As a common pathway, the 3D printing process starts from a "3D model data". It is generated by a Computer-Aided Design (CAD) software describing the geometries and dimension of the object. In order to print a real object from the CAD file, it is first converted into a stereolithography (STL) file. STL file, also known as "Standard Tessellation Language", allows to convert the continuous shape of the CAD file as a set of triangles and coordinates. The STL file also withstand a slicing process, where the graphic model is subdivided as a multiple sequence of layers. Lately, the STL file is converted by the 3D printer in a g-code file, that contains the precise information requested by the 3D printer (i.e. nozzle path, nozzle temperature) to produce the physical object (Fig. 1.2) [15].

The approximations introduced by the STL file and slicing process may affect the final result due to the replacement of the continuous contour of the CAD object with a discrete stepped form. Anyway, starting from a precise virtual model of the object, it is possible to manufacture complex structures that by conventional

manufacturing techniques would be hard or even impossible to achieve. Moreover, 3D printing allows the production of neat-shaper or neat-near shape artifacts that drastically decreases the costs and time involved in finishing processes [44].

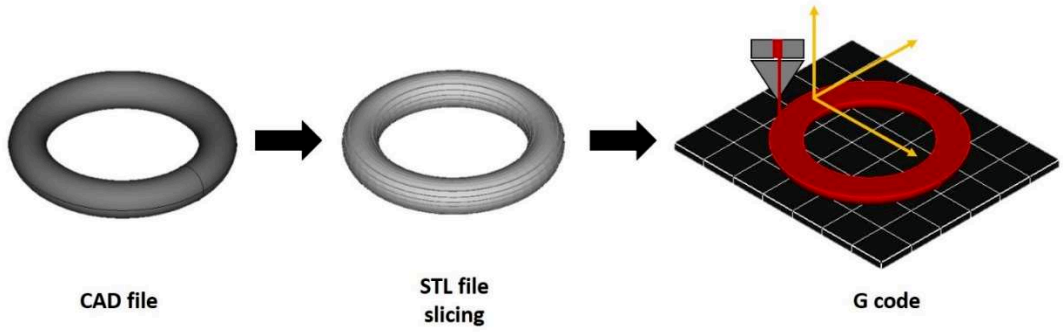

Figure 1.2: Conversion process from a CAD file to the 3D printing of a real object.

1.4.2 3D Printers Classification

Nowadays, about thirty 3D printing techniques are commercialized, but a standardized classification still does not exist. Indeed, several approaches are used to categorize additive manufacturing equipment: they can be related to i) the source of the manufacturing process (laser, temperature, or light), ii) the type of materials processed (metal, ceramics, polymers), or even the physical state of the raw materials (solid, liquid and powders) [15]. Spotlighting those 3D printing techniques most widely used for manufacturing composites materials, magneto responsive polymers included, here the attention is focused on Fused Filament Fabrication, Direct Ink Writing, Stereolithography, and Digital Light Processing. These four techniques are easily distinguished according to the printing principles and the materials applied. In DIW and FFF the raw materials are slurries or inks, and thermoplastic filaments respectively, and they are extruded from movable nozzles to fabricate the 3D printed object. On the other hand, SLA and FFF both rely on the photopolymerization process, and liquid photocurable monomers are processed producing thermoset polymers. According to these differences, the 3D printing technique are here classified as “Extrusion 3D Printers” (FFF and DIW) and “vat photopolymerization 3D Printers” (SLA and DLP).

1.4.3 Extrusion 3D Printers

Fused Filament Fabrication (FFF) 3D printers are the most popular and spread 3D printers thanks to a large palette of available materials, friendly use, and low cost. In this work an FFF 3D printer was used just as a support for the research activity, but often it is applied in 4D printing applications. FFF and DIW manufacturing processes are similar, and they are here discussed for a better understanding of the *"State of the Art - Magneto Responsive Polymers"* chapter.

Operating Principles

In FFF printers the starting materials are thermo-plastic wires or filaments, which are melted by a heated nozzle and deposited on a support according to the CAD file specifications (Fig. 1.3); the melted wire cools down quickly and solidifies on the building platform. The printing heads extrude the filament in thin wires of a diameter of about 0.25 mm [15], [45]. Because of the high thickness of the printed layer, the resolution of the printed parts is low, and often a smoothing process is needed. The layers adhesion and presence of porosity and voids in the printed object drastically decreases the mechanical performances. Anyway, the friendly-use approach and the absence of dangerous sources make FFF a perfect candidate for hobbyists and rapid prototyping.

FFF has several advantages compared to other 3D printing techniques, one of them is the multi-material printing. A single object can be built with different materials according to the number of the printing heads in the machine, but of course, a good result depends on the adhesion properties of layers from different materials. Anyway, by FFF is possible to manufacture many polymers as polylactic acid (PLA), polycarbonate (PC), acrylonitrile butadiene styrene (ABS), Polyphenuylsulfone (PPSF), and PC-ABS blends [15].

As FFF, Direct Ink Writing extrudes by nozzle slurries or highly viscous pastes. According to the composition of the pastes, three different procedures are implemented: i) for polymer solutions a drying or solvent evaporation follows the 3D printing process, ii) when polymers cured by temperature, light, or ions are processed, a rapid polymerization is requested, iii) Pastes with shear-thinning behavior do not need a curing process [46], [47]. Of course, the extrusion of slurries limits the precision of the printed parts.

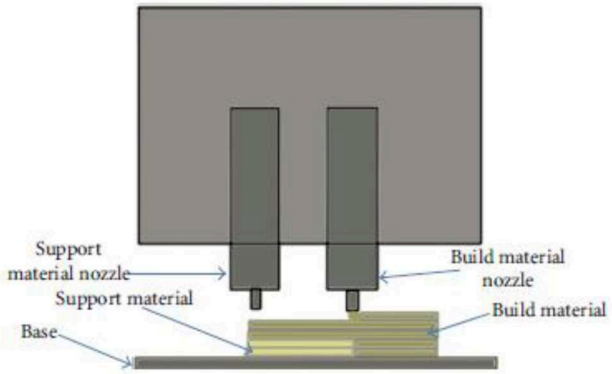

Figure 1.3: Fused Filament Fabrication set-up *[15]*.

Composite materials by FFF

In order to produce composite and nanocomposite materials by FFF, the polymeric wires are fabricated by twin-screw extruders [48] or batch mixer technology [49]. The high shear forces ensured by these techniques allow the dispersion of nanofillers. Anyway, the addition of fillers in a thermoplastic wire modifies the rheology properties and may cause nozzle clogging and/or bad resolution [14]. In order to control the viscosity, two approaches may be used: i) to increase the temperature of the printing heads, but this may deteriorate (nano)composite; ii) to add surfactants and plasticizers to decrease the viscosity and the processing temperature, but this would modify the nanocomposite mechanical properties. Besides the drawbacks discussed many examples of 3D printed nanocomposite materials are shown in the literature [14], [45], witnessing the potentiality of FFF in this field.

DIW is widely applied in the fabrication of ceramic structures due to the high amounts of fillers allowed by this technique [46]. Nevertheless, the precision and the manufactured shapes are often restricted due to bad layer-layer interfaces and ink cohesion, and this may be an issue when controlled and complex shapes are required as for 4D printing applications.

1.4.4 Photopolymerization

Stereolithography and Digital Light Processing 3D printing techniques are based on the photopolymerization process. Hereafter, a short overview will be given to describe the two technologies.

Photopolymerization is a polymerization process started by the absorption of light. By means of photopolymerization, it is possible to obtain very rapidly solid-state polymers starting from a liquid solution of monomers by light irradiation [50].

$$Monomers - Oligomers\ (liquid) \xrightarrow{light} Polymer\ (solid)$$

Photopolymerization is usually performed at room temperature, and it does not require solvents; moreover, it's a low energy-consumption technique, and its environmental impact is low [50]. By combining the advantages of photopolymerization and 3D printing (low waste material, low energy required), DLP and SLA can be considered as environmental-friendly technologies.

The key to the process is the photoinitiator, an organic molecule that absorbs light (usually between 250-450 nm) and generates reactive species which can initiate the polymerization reaction. According to the nature of the reactive species generated, photopolymerization processes are distinguished in radical, cationic, and anionic. Radical photopolymerization is the most applied one, and it is used in this work. In Figure 1.4 the common pathway of radical photopolymerization is described. The Photoinitiator (PI) absorbs light (hv), and it is promoted to an excited state ([PI]*). The excited state can eventually decay generating a free radical (R*). The free radical is now able to add and to cleave a suitable functional group (usually unsaturated C-C bonds such as vinyls, acrylate, methacrylate, etc.) present on the monomer, generating a propagating species (M*) which starts the polymerization process. During propagation, the polymer chains grow until termination following the below scheme.

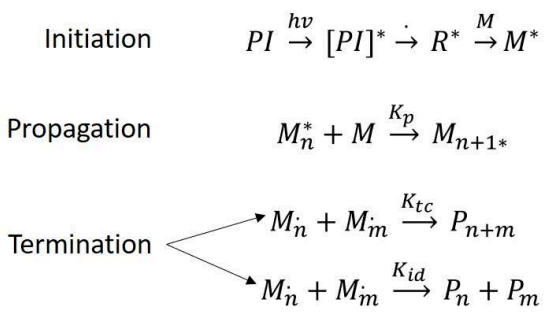

Figure 1.4: General radical photopolymerization scheme.

The efficiency of the photopolymerization process is strictly related to the yield of the photoinitiator. The first aspect to consider to have a high rate of polymerization is a good match between the light source emission spectrum and the photoinitiator absorption spectrum. Moreover, the light intensity has a central role since it can be considered as the number of photons available to excite the photosensitive molecule. As described by the eq 1.1 the light absorbed is directly dependent on the intensity of the emitted light [51].

$$I_{abs} = I_0(1 - 10^{\varepsilon cl}) \qquad \text{(eq. 1.1)}$$

Where I_{abs} and I_0 are respectively the intensity of the portion of the absorbed light and the intensity of the incident light. ε is an intrinsic optical property of the molecule and (molar extinction coefficient), while c and l are respectively the concentration of the photoinitiator and the depth in the irradiated sample.

The efficiency of the photopolymerization process is the result of two different quantum yields: the photoinitiator yield which stands for the number of reacting monomers generated per absorbed photon, and polymerization yield, or rather the number of monomeric units polymerized per absorbed photon [52], [53].

Cationic and anionic photopolymerizations are less widespread than the radical ones due to the low availability of photoinitiators in the market, and due to slower polymerization kinetics. As a fast photopolymerization process is a mandatory condition for a good Vat 3D printing process only the radical photopolymerization mechanism was here described. In the next paragraph the main ingredients used in a photocurable resin for radical polymerization are described.

Photocurable resin composition

A photocurable formulation is composed of several chemicals with a specific function. The core elements of the formulations are monomers and oligomers, photoinitiators, and dyes. Moreover, additives can be also present in order to increase the processability of the formulation (plasticizers and surfactants) or to improve the properties of the polymer (cross-linkers, toughening agents, and fillers).

Monomers are the building block of a polymer, thus their chemical structure strongly influences the mechanical and physical-chemical properties of the material. Oligomers (from ancient Greek oligo – a few) is a macromolecule composed of few repeating monomers. In a conventional photocurable resin, both monomers and oligomers are present, and according to their ratio is possible to tune the polymerization kinetics and the mechanical response of the material. For instance, an excessive amount of oligomers can delay the photopolymerization process because their high viscosity affects the photoinitiator and dye solubility. On the counterpart, an excessive presence of monomers increases the cross-linking density deteriorating the mechanical properties of the material. In 3D printing technologies based on photopolymerization, mainly acrylates and methacrylates can be processed due to their fast polymerization kinetics. However, by controlling the chemical structure of the monomers, i.e. number of moieties and the alkyl backbone, it is possible to tune the polymerization kinetics and the properties of the polymer. For instance, by increasing the number of functional groups in the monomer, and/or adding rigid groups to the alkyl backbone of the monomer, the rigidity and the hardness of the polymer is enhanced. On the other hand, to obtain softer polymers it is possible to decrease the cross-linking density of the material by limiting the number of functional groups and using long and flexible alkyl groups as the monomeric backbone. The p*hotoinitiator* does not directly influence the performances of the material, but a formulation with an optimized photoinitiating system allows to fully polymerize the monomers and oligomers improving the material characteristics. When photocurable formulations are intended for DLP and SLA 3D printers, a *dye* is usually also added. The role of the dye is to control the light penetration depth in other to prevent overpolymerization, thus improving the resolution of the printed artifacts (Fig. 1.5).

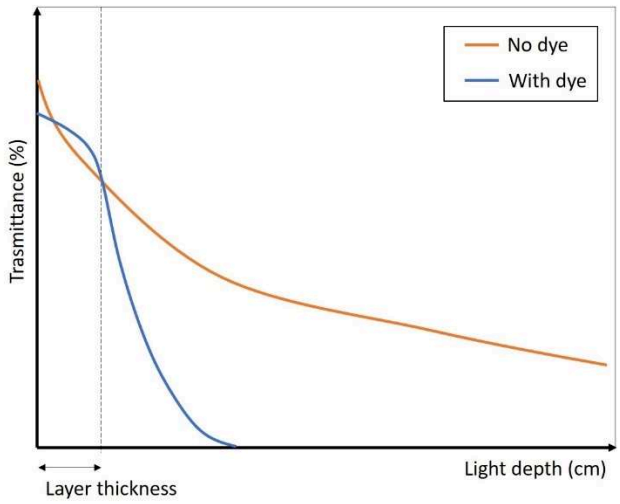

Figure 1.5: Example of the ideal effect of the addition of a dye on the light penetration depth.

1.4.5 Vat photopolymerization 3D Printers: Stereolithography and Digital Light Processing

The first 3D printer invented was based on the photopolymerization process. During the 1908's, Charles Hull realized that by photocuring by a scanning laser a photocurable resin one layer over the other, it was possible to build a 3D object. This was the founding concept for stereolithography (SLA) technology, the first 3D printer. After the patent and the commercialization of SLA, independent researchers developed SLA-based new processes, collected under the term of "vat photopolymerization" [54]. "Vat" distinguishes the photopolymerization-based 3D printers from the other, since a vat filled with photocurable resins (in liquid state) is adopted. Nowadays, we can mainly distinguish three different technologies.

- Stereolithography (SLA): where a laser scan photopolymerize punctually the liquid precursor
- Digital Light Processing (DLP): One layer is fully cured in only one step by using light projectors

- Two-photons (2PP): Higher definition is achieved by the simultaneous absorption of two photons in the near infra-red region.

Stereolithography

A typical SLA 3D printer is composed mainly of four elements (Fig. 1.6): a mobile platform, a light source (visible or UV), a scanner system, and of course a vat containing the liquid photocurable formulation [18]. In order to print the object, the mobile platform is dipped in the vat containing the resin, and the scanner system irradiates *point by point* the formulation to build the layer according to the CAD specifications. Once the first layer is cured, the platform further submerges to expose new material for the curing process, and the new resin is again photopolymerized by the scanned light. These steps are repeated until the complete formation of the 3D printed object. After the removal of the object from the platform, the object is clean and sonicated with the use of a solvent (generally isopropanol or ethanol) to get rid of the unreacted resin. According to the materials processed, a post-curing treatment may be necessary to fully polymerize the object by a UV lamp.

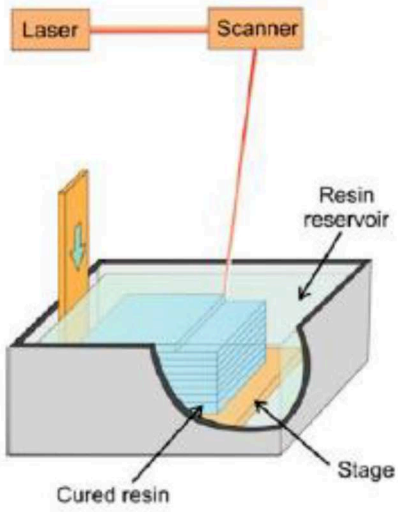

Figure 1.6: Stereolithography apparatus [18].

The definition of the printed object depends on two factors: the first one is the dimension of the enlightened spot by the scanning system, the second is the layer thickness. Typically, the spot dimension ranges from few microns to a millimeter

and the layer thickness can be varied between 5 and 200 μm. By regulating the spot dimension and the layer thickness, the user can tune the compromise between velocity and precision [18]; i.e. decreasing the layer thickness the definition of the object is improved, but also the number of layers that must be printed is increased resulting in a growing production time. In the latest years, some new technologies based on laser scanning were developed in order to increase the resolution of the printed artifacts. **Micro-stereolithography** (μSLA) allows a better definition of the printed parts thanks to an improvement on the laser scanning system which can reduce the spot size up to 2 μm [15], [55]; also the slicing is improved limiting the layer thickness up too few microns. In **two-photons** 3D printers (2PP) is possible to further decrease the focal spot achieving outstanding submicron resolution (about 50 nm) two orders of magnitude smaller than traditional SLA [56].

Digital Light Processing

Digital Light Processing (DLP) 3D printer is an evolution of SLA with an increased manufacturing velocity. The components described for SLA are almost the same as DLP, but the first remarkable difference is the set-up configuration. DLP differs by a top-down (layer) configuration form SLA which is often built in a bottom-up (bath) configuration. By a top-down configuration, the light source is placed under the vat containing the liquid formulation, while the mobile platform is suspended over the resin reservoir (Fig. 1.7). The vat sole is made of glass or polymers transparent to the emitted light allowing the photopolymerization of the resin.

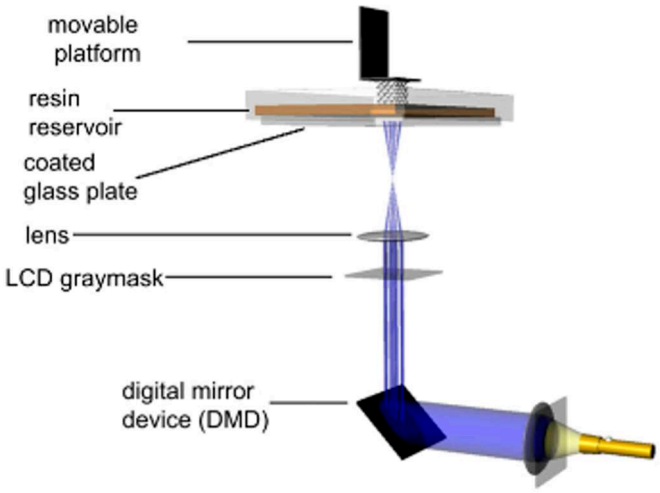

Figure 1.7: DLP set-up and components *[57]*.

The key element which distinguishes DLP printers from SLA ones are the light source and the light scanning system. First of all, the laser beam is replaced by a digital light projector equipped with a lamp or more commonly a LED emitting in the UV or visible region. Secondly, in order to focus the light on the area of interest, a Digital Mirror Device (DMD) displace the SLA's laser scanning system. DMD is a device composed of millions of mirrors that can be independently and simultaneously rotated in an on/off state selecting the light passing and inducing photopolymerization [57]. The innovation of DLP consists of the chance to fully cured one layer in a single step, changing the concept of point-by-point polymerization to a faster two-dimensional pixel patter, or layer-by-layer, control.

In conclusion, DLP slightly sacrifices printing resolution for a remarkable increase in production rate. Moreover, DLP show some advantages in terms of multi-material printing and composite material processing.

Nanocomposite materials by vat photopolymerization 3D printers

SLA and DLP technologies result suitable for 3D printing nanocomposite materials. Starting from a liquid formulation, the dispersion of fillers is easier and cheaper compared to FFF 3D printers since no expensive equipment is required as a twin-screw extruder. Many examples of 3D printed nanocomposite materials are reported in the literature [58]–[60]. Anyway, the addition of inorganic fillers in a

photo-curable formulation brings some issues in terms of viscosity and light absorption [60]. Since the manufacturing process is driven by the absorption of photons by the photoinitiator, the addition of nanoparticles decreases the yield of the process due to a light absorption competition. This can be explained by considering that nanoparticles introduce to the system additional absorption sites, thus the amount of photon absorbed by the photoinitiator is reduced and fewer reacting species are generated preventing or slowing down the polymerization kinetics.

The addition of fillers to a photocurable resin brings several issues in the processability of the resin as they impact on the viscosity of the system, the photocuring process, and the rheological behavior of the system. Nevertheless, the maximum affordable amount of particles addable to a formulation is mainly dependent on their absorption spectrum. In the case of high absorbing particles in the visible or UV range as graphene and nanotubes, the concentration achievable is low [61], [62]. Many strategies have been implemented in order to increase the amount of fillers in the nanocomposite materials:

- Optimize the photocurable formulation
- Optimize processing parameters
- In-situ nanoparticles production

To maximize the polymerization kinetics of the photocurable formulations, it's possible to minimize the overlapping of the absorption spectra by selecting the correct photoinitiator. Furthermore, high reactive monomers are preferred since they increase the photopolymerization kinetics. From the technological point of view, the choice of the light source is fundamental to move the photons light absorption in regions where the nanoparticles have a lower absorption coefficient. Nanoparticles also decrease the light penetration depth in the resin, and a reduction of the layer thickness may minimize this issue. Other strategies consist of adding particle precursors to the photocurable resin and once the object is printed, promote in-situ formation of nanoparticles by sol-gel approach [63] or by photo/thermal reduction [64], [65].

2.

Magneto Responsive Polymers: a short overview

Smart materials can be used to induce mechanical movements or to perform shape morphing, in response to external stimuli. Among those, magnetic fields have emerged as an interesting way to remotely tune both properties and morphology of magnetic responsive materials [66]–[69]. On the other hand, polymers are good candidates for this kind of application as they can undergo shape morphing, i.e. deformation, for low applied forces. Unfortunately polymers, being for the most diamagnetic, they do not show magneto-responsive behaviors. The easiest way to make a polymer magnetic-responsive is to load it with magnetic fillers. The magnetic properties of the filler are thus the key elements to influence the behavior of the composite polymers, determining in turn, their potential applications. Therefore, in this chapter, a brief overview of magnetic nanomaterials and their properties is first given. Then, the role of the polymeric matrix is introduced. Finally, it is described how the design of the object allows mustering the functional properties of the composite polymer when an external stimulus is applied, Fig. 2.1. It will be also demonstrated that the use of additive manufacturing largely facilitates this task.

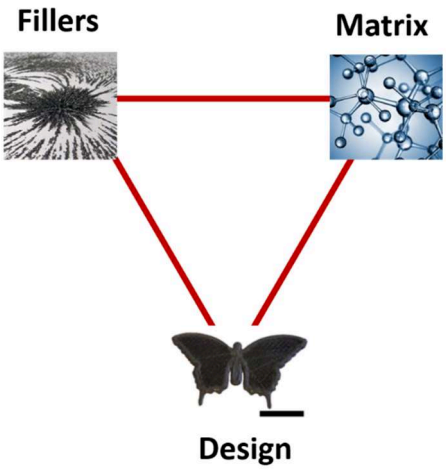

Figure 2.1: Schematic representation represents the main parameters (fillers, matrix, and design) for the fabrication of a magneto-responsive polymer.

For illustrative purposes, some typologies of magneto responsive polymeric smart composites are described: magneto-rheological elastomers, 3D printed permanent magnets, and magneto-driven soft-actuators. In each dedicated section, the materials and the preparation methods of these devices are discussed. In particular, magneto-driven soft-actuators play the leading role of this section, being the main topic of this Ph.D. work.

2.1 Magnetic fillers

To understand how magnetic fillers respond to an external magnetic field hereafter a review of some concepts of magnetism is given [70], [71]. When a material is exposed to a magnetic field **H** (A m^{-1}), the induced magnetic flux in the material, also known as magnetic induction, **B** is given by:

$$\boldsymbol{B} = \mu_0(\boldsymbol{H} + \boldsymbol{M}) \qquad \text{(Eq. 2.1)}$$

Where bold letters refer to vectors, μ_0 is the permeability of vacuum (J A^{-2} m^{-1}) and **M** is the magnetization of the material, and it represents the magnetic moment (**m**) per unit volume (V):

$$\boldsymbol{M} = \frac{\boldsymbol{m}}{V} \qquad \text{(Eq. 2.2)}$$

On the other hand, the magnetization $\boldsymbol{M}$ is linearly proportional to the magnetic field $\boldsymbol{H}$ through the magnetic susceptibility χ, which is an indicator of the responsiveness of the material to an applied magnetic field:

$$\boldsymbol{M} = \chi \boldsymbol{H} \qquad \text{(Eq. 2.3)}$$

Thus, using Eq. 2.3 in Eq. 2.1 B can be written as:

$$\boldsymbol{B} = \mu_0(1+\chi)\boldsymbol{H} = \mu_0\mu_r\boldsymbol{H} \qquad \text{(Eq. 2.4)}$$

Where $\mu_r = (1+\chi)$ is the relative permeability of the material.

Now, using the aforementioned definitions, it is possible to classify materials as a function of their magnetic properties.

Diamagnetic materials

In the absence of an external magnetic field, diamagnetic materials do not have permanent magnetic dipoles. When the magnetic field is applied, very weak dipoles are induced in the direction opposite to that of the applied field as shown in Fig. 2.2a. Diamagnetic materials have, thus, a small magnetic response and a negative value of the magnetic susceptibility which generally ranges between -10^{-6} to -10^{-3}.

Paramagnetic materials

In contrast with diamagnetic materials, paramagnetic materials show a very small positive magnetic response, i.e. they are weakly attracted, to an applied field. Paramagnetic materials reveal randomly distributed dipoles in the absence of the magnetic field which have the tendency to align along the field direction when the field is applied (Fig. 2.2b). The magnetic susceptibility of these materials is positive and varies from 10^{-6} to 10^{-5}. In Fig. 2.2c magnetization, M, of paramagnetic and diamagnetic materials are schematically shown as a function of the applied field, H.

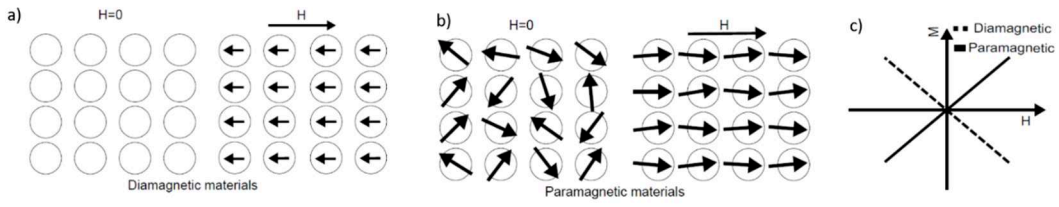

Figure 2.2: Schematic representation of the dipole behavior in absence (H=0) and presence (H≠0) of an external magnetic field for a) diamagnetic and b) paramagnetic materials. c) Magnetization versus applied field (M-H curve) for diamagnetic and paramagnetic materials.

Ferromagnetic materials

These materials exhibit a permanent magnetization at the macroscopic scale. In ferromagnetic materials, all the magnetic dipoles are pointed in the same direction, Fig. 2.3a. Ferromagnetism occurs in transition metals, iron, nickel, cobalt, and their alloys, and alloys of rare earth metals and it is originated from exchange interactions occurring in ordered magnetic solids. Depending on their capability to remain magnetized, ferromagnetic materials can be further divided into two subcategories: magnetically "soft" materials which tend to lose their magnetization, and magnetically "hard" materials, which maintain their magnetization with time.

Ferrimagnetic materials

In ferrimagnetic the magnetic moments are anti-parallel but of different amplitude as shown in Fig. 2.3b. The result is a spontaneous magnetization of the material below the Curie temperature.

Antiferromagnetic materials

They consist of two magnetic sub-lattices where magnetic moments are oriented antiparallel and coupled ferromagnetically. Thus, the net magnetization is zero, Fig. 2.3c.

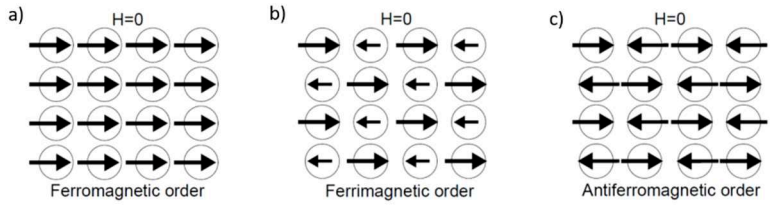

Figure 2.3: Behavior of a) ferromagnetic, b) ferrimagnetic and c) antiferromagnetic materials

2.1.1 Properties of magnetic materials

The M-H curve, also known as the magnetic hysteresis loop, allows characterizing the magnetic response of a material to an applied external magnetic field [70], [71], Fig. 2.4. The horizontal axis is usually H or the magnetizing force,

while the y axis is the projection of the considered quantity along the direction of H [e.g.: (M.H)/H].

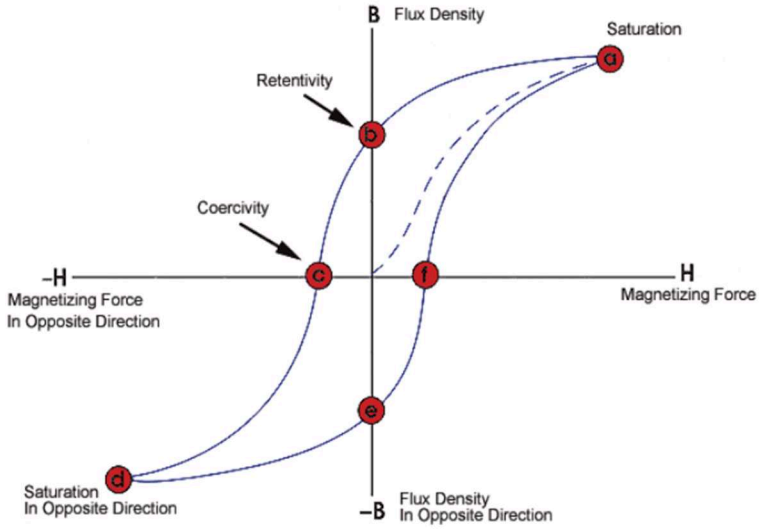

Figure 2.4: Sketch showing the typical hysteresis loop of a ferromagnetic material

When an external magnetic field H is applied, the magnetic spins of the material become aligned in the field direction. The magnetization will tend to align itself along H, which shall be attained for a sufficient magnitude of H. This process is called a magnetization process. The "a" point, also known as the saturation point, describes the situation when almost all of the magnetic domains become aligned to the magnetization. Here, an additional increase in the magnetic field will only produce very little increase in magnetic flux, i.e. a plateau is reached. When the intensity of the applied field is then reduced to zero, the curve will move from point "a" to point "b". Here, some magnetic flux remains in the material even if the value of H is zero. This is referred to as the point of *retentivity* and indicates the level of residual magnetism in the material. This point is also known as the *magnetic remanence* of the material. Physically, it corresponds to the facts that when the magnetic field is removed, statistically some spins start to relax and randomly reorient leading to the magnetization drops to a residual value. However, a residual orientation of the domains remains, as well as a residual magnetic induction (B_r) in the material. Next, when the external magnetic field is reversed, the curve moves to point "c", where the value of B is reduced to zero. This point defines the *coercivity* of the material and corresponds to the force required to remove the residual magnetism from the material. At point “c” the net flux within the material

is zero, i.e. reversed magnetizing force has flipped enough of the domains so that the net flux within the material is zero. The magnitude of the coercivity field, H_c, depends on both structural (shape, size, impurities, vacancies) and intrinsic properties of the material. Continuing to increase the magnetic field in the negative direction, the curve reaches the point “d” for which the material becomes again magnetically saturated. Reversing the field H to zero brings the curve to point "e" which, as for the point “b”, describes the residual magnetism at H=0. It is worth mentioning that as some force is required to remove the residual magnetism the curve does not return to the origin of the graph but intercepts the x-axis at the point “f”. The loop is completed when the path goes back to the saturation point “a”. The area enclosed by the hysteresis cycle represents the magnetic energy losses per magnetization-demagnetization cycle per unit of volume. These losses occur as heat, increasing the temperature of the material. [72].

The magnetization cycles are distinctive of the magnetic materials typologies [72]. Paramagnetic materials show magnetic induction values (B) several orders of magnitude lower than those observed in ferromagnetic materials. Hard ferromagnetic materials are characterized by a wide magnetization curve and high values of residual induction (Br), therefore they are applied for the production of permanent magnets. Instead, soft ferromagnetic materials have a more narrowed and sloped hysteresis cycle and a low value of Br. Combining high permeability and low hysteresis losses they are often applied in magnetic circuits.

The hysteresis loop can be thus used to determine some of the main magnetic properties of a material exposed to an external magnetic field.

- The **magnetization** (**M**) indicates the density of magnetic dipole moments produced in a material exposed to a magnetic field. Also, it is used to calculate the magnetic forces produced by the interactions between the magnetic field and the material.
- The **magnetic susceptibility** (χ), is the ratio between the magnetization (M) and the applied magnetic field (H). It indicates the responsiveness of the material when a magnetic field is applied.
- The **remanence** or *retentivity* measures the material's ability to retain a certain amount of residual magnetic field when the magnetizing force is removed (H=0) after achieving saturation.

- The **residual flux (Br)** or *residual magnetism* defines the magnetic flux density that remains in a material when H=0. It is worth noticing that the residual flux and the retentivity are equal when the material has been magnetized to the saturation point. However, when the magnetizing force did not reach the saturation level, the level of residual magnetism can be lower than the retentivity.
- The **coercive force** (**Hc**) defines the amount of reverse magnetic field which must be applied to a material to demagnetize the material, i.e. make the value of M (or B) returns to zero.
- The **permeability (μ)** indicates the ease with which a magnetic flux is established in a material.
- The **reluctance** is analogous to the resistance in an electrical circuit and indicated the opposition of a ferromagnetic material to establish a magnetic field.

In the case of permanent magnets, often **maximum energy product**, otherwise **(BH) max,** is used to describe the magnetic properties of the material. The maximum energy product is expressed as the product between the coercive magnetic field and the residual magnetic induction (Hc*Br), and in the magnetic hysteresis loops corresponds to the largest rectangle inscribable under the demagnetization curve (top left quadrant) [73]. It is the maximum magnetic energy stored within the magnet, and it is an indicator of the force of the magnets. For instance, two identical magnets for shape, dimensions, and magnetization voltage, with a different (BH) max show two different magnetic fields at their surface.

2.1.2 Magnetism at the nanoscale

At the atomic level magnetism is described by taking spin interactions into account through the overlap of electron wave functions. However, at the nanometric-scale, the description of a magnetic system becomes more complicated [74]. This is because magnetic properties are not only related to the composition of nanomaterials but also to their size. Indeed, when the dimension of the object is

increased, magnetic domains appear to minimize the internal energy, and thus microstructures becomes important. Therefore, particles of different sizes will not behave in the same way under a magnetic field.

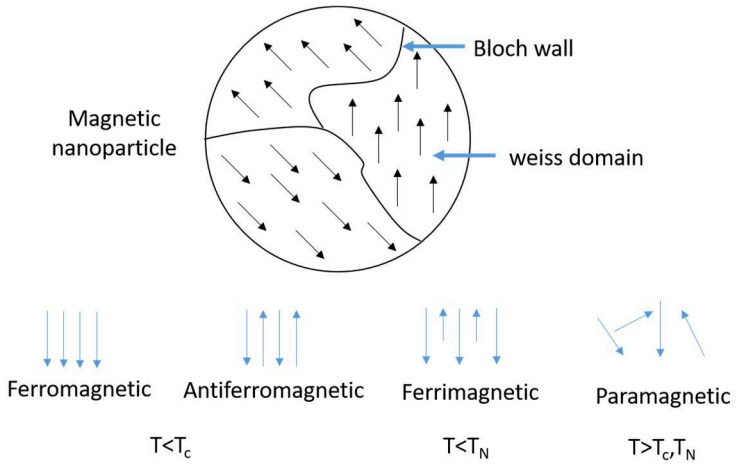

Figure 2.5: Schematic representation of the internal structure of a magnetic particle showing Bloch walls and Weiss domains. The orientation of the atomic moment as a function of the type of nanoparticle is also reported.

Generally speaking, magnetic particles larger than 100 nm are considered as bulk materials, whereas particles smaller than this size are considered to belong to the category of nanoparticles [75]. In the first category, bulks particles possess a microstructure composed of magnetic domains (Weiss domains) separated by walls (Bloch walls) as shown in Fig. 2.5. In each Weiss domain, typically smaller than 100 nm, the magnetization is uniform, and the magnetic moment of the atoms is all aligned with one another pointing in the same direction. The magnetization is uniform in each domain, but it is different from one domain to another one. The structure of Weiss domains is responsible for the magnetic behavior of both ferromagnetic materials (Fe, Ni, Co, and their alloys) and ferrimagnetic materials (ferrites) and it is at the origin of the formation of permanent magnets and their attraction to a magnetic field.

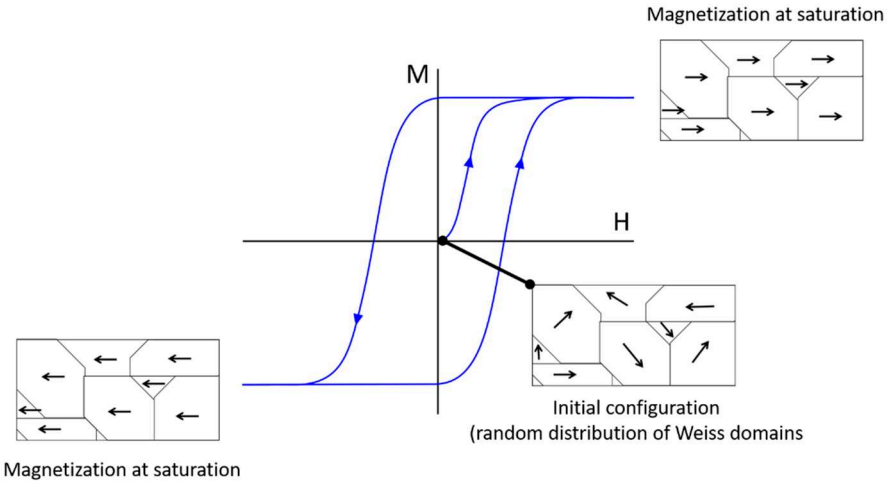

Figure 2.6: Schematic representation of the evolution of the orientation of the spins within the different Weiss domains' as a function of the applied magnetic field, H.

At room temperature and H=0, all magnetic domains within the sample present a random spin alignment (Fig. 2.6). Since Weiss domains' magnetism is balanced by neighboring domains, the bulk material is macroscopically non-magnetic or with a global magnetization near zero. When an external magnetic field is applied spin rotation or domain nucleation, is induced. At saturation, all the spins within each Weiss domain have been reoriented along a unique and same direction, that of the applied field H, and the bulk material becomes macroscopically magnetized (Fig. 2.6). On the contrary, paramagnetic materials, in which the dipoles are not spontaneously aligned, do not have magnetic domains and are macroscopically non-magnetic or with a global magnetization near zero.

Magnetic dipoles only align in response to an external field creating a uniform and finite magnetization that persists as long as the magnetic field is applied and stops right after its removal. When the size of the magnetic material is reduced, the number of domains within the material is also decreased until only a single domain remains. When the size is reduced below a certain limit the sample no longer holds any ferromagnetism, becoming superparamagnetic. Superparamagnetism occurs in nanoparticles with a diameter ranging between 3 and 50 nm, depending on the material, and composed of a single magnetic domain. Here, the magnetization of the nanoparticles is considered as a single giant magnetic moment, sum of all the individual magnetic moments of all the atoms composing the particle. Temperature (T) has also an influence on the behavior of magnetic particles. When the thermal energy becomes large enough, the thermal fluctuations destroy the microscopic

magnetic order canceling the material magnetization. For ferro- and ferri-magnetic materials, this transition is defined by the Curie temperature, T_c. Above T_c magnetic moments lose their preferential orientation and become randomly distributed (paramagnetic). For antiferromagnetic, the Curie temperature is replaced by the Néel temperature, T_N. The permanent magnetic properties of these materials are no more described by the orientation of Weiss domains but by a field-induced magnetism like in paramagnetic materials. When cooled below T_c, the material again spontaneously divides into several Weiss magnetic domains.

Magnetic Iron Oxide Nanoparticles

Magnetic iron oxide nanoparticles are in widespread use in modern technology where they have important industrial applications in, for instance, magnetic data storage, sensors, switches as well as in biotechnology and medicine.

Metallic ferrous nanoparticles are common in nature and mainly found in soil and rocks and also in air, essentially as a pollutant (automotive and industrial emissions). They can be divided into three different types: hematite (α-Fe_2O_3), maghemite (γ-Fe_2O_3) and magnetite (Fe_3O_4), which significantly differ in oxidation number, composition, crystallographic structures, and magnetic properties. Besides, the magnetic properties of the three types are also size-dependent [76].

The first type is the hematite (α-Fe_2O_3) which is kinetically and thermodynamically stable and, historically the first known iron oxide [76]. The magnetic saturation is 0.3 $A.m^2/kg$ and the Curie temperature around 1000 K. At room temperature and above 6 nm, hematite is ferromagnetic, and it does not show superparamagnetic ordering but it is able to change the magnetic ordering to antiferromagnetic below ~260 K, which is known as Morin temperature [76]. This change of magnetic ordering can be suppressed by a decrease of crystallinity and/or decrease in the size of the nanoparticle (≤10–20 nm).

The second type is the maghemite (γ-Fe_2O_3) which is a metastable mineral, that has the tendency to slowly transform into hematite, the stable form of iron oxide. This transition leads to a drastic drop in magnetization. The magnetic saturation of maghemite is 60–80 $A.m^2/kg$ and the Curie temperature around 820-980 K. Depending on the polymorphism, the α- or the γ- phase, hematite, and maghemite vary from red to brown to grey [77]. At room temperature, maghemite exhibits a

superparamagnetic behavior below 10 nm, whereas it becomes ferrimagnetic above 10 nm [77].

The third type is the magnetite (Fe_3O_4), also called Hercule stone. Magnetite was widely used in this Ph.D. work and therefore its properties are discussed more in details. Its color is generally black and, among the three, it presents the strongest magnetic behavior. Indeed, the magnetic saturation is 92–100 $A.m^2/kg$ and the Curie temperature is around 850 K. The crystal structure of magnetite is characterized by alternating octahedral and tetrahedral layers. Ferric species occupy all the tetrahedral lattice sites, and half of the octahedral sites, while the remaining octahedral sites are occupied by ferrous atoms [78]. The two lattices have different magnetic behavior: the magnetic moments in the tetrahedral sites are aligned in a ferromagnetic configuration, while the octahedral lattice show antiferromagnetic configuration (antiparallel orientation). The combination of the two lattices leads to a ferrimagnetic behavior in the bulk magnetite [78]. However, as the size of the Fe_3O_4 particle is reduced, the magnetic behavior of the material turns from ferrimagnetic to superparamagnetic below 6 nm. Being highly susceptible to oxidation, magnetite is transformed to maghemite in the presence of oxygen: $2Fe_3O_4+O_2 \rightarrow 2\gamma Fe_2O_3$.

NdFeB based alloys

The second category of fillers largely used in magneto-responsive polymers are NdFeB-based nanoparticles.

The Nd–Fe–B alloy with formula $Nd_2Fe_{14}B$ has a tetragonal crystal structure, and it shows the highest magnetic properties in nature. The $Nd_2Fe_{14}B$ belong to the category of permanent magnet-based rare earth metals, and it has been independently discovered by Sumitomo Special Metals and General Motors (GM) almost simultaneously in 1984 [79], [80]. These materials are derived from the strong magnetocrystalline anisotropy and high saturation magnetization of the compound. Indeed, $Nd_2Fe_{14}B$ has a high value of maximum energy product of about 10 - 50 MegaGaussOersteds (MGOe), a magnetic remanence of about 5 – 11 KGauss, and Curie temperature of about 583° K [81]. Thanks to the outstanding properties of this material, NdFeB alloys are the most powerful permanent magnets

available, and they are applied in several application fields such as automobile industry, office automation, electric toys, and magnetic curing products [80], [81].

2.2 Polymer matrix

The mechanical behavior of a polymer depends on many factors, among which the most important are the chemical structure and macromolecular arrangement. In particular, the type of chemical bonds and moieties in the polymer, either in the backbone or as lateral groups, strongly influence the mobility of macromolecular chains, and consequently the mechanical properties of the material [82]–[85]. Moreover, also the molecular weight, the intermolecular forces (e.g. H-bonds, π-π stacking), crystallinity, and the cross-linking density determine its mechanical response [82]–[86]. Polymers offer a wide palette of materials spanning from very stiff ones as Kevlar, to very soft ones such as polydimethylsiloxane (PDMS). Among those, it is possible to select the most suitable polymeric matrix with the appropriate mechanical properties according to the application.

2.3 Synthesis and properties of magneto responsive polymers

Composites are a class of material constituted by two or more components each of which possess different chemical and physical properties. The final properties of a composite material belong to the individual constituents as well as to their interactions [87]. Generally, in a composite it is possible to determine a continuous phase (matrix), in which a second phase is dispersed (filler). If the matrix is constituted by a polymeric material, the composite is defined as a polymeric composite. The incorporation of the fillers can be performed through a twin-screw extruder, direct mixing, and solvent mixing.

Twins screw is used when the matrix is already in a solid (polymerized) form, such as granulates, powders, or flours. In this system, pellets are directly mixed with the particles upon melting and eventually extruded by a spinning head to produce, after cooling, a composite filament or composite pellets as shown in Fig. 2.7 a.

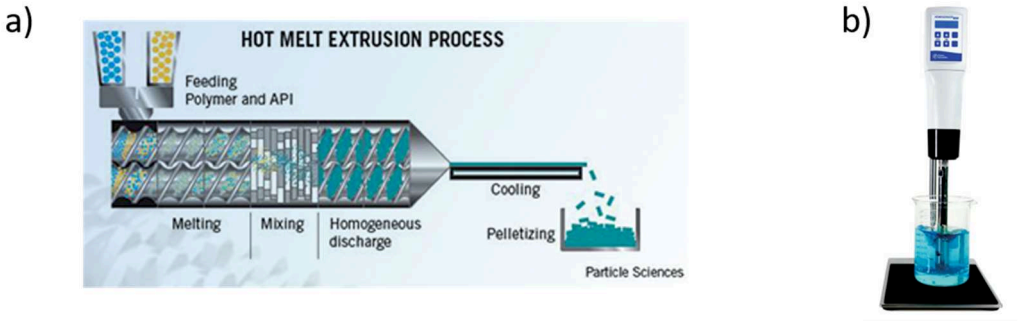

Figure 2.7: A) Schematic of the twin-screw extrusion process. A conventional mechanical homogenizer bench tool.

Alternatively, to facilitate the materials mixing step, solvents or ionic liquids are used to dissolve the polymer. In this way, nanoparticles can be dispersed into the polymeric solution. For instance, if the polymer is water-soluble, solubilization is achieved by adding water (H_20). Otherwise, stronger solvents, like acetone or chloroform, or ionic liquids are employed to improve the solubility of the fillers.

On the other hand, if the raw material is in a liquid (viscous) state, nanoparticles are simply added to the liquid mixture of monomers and oligomers and upon mechanical mixing embedded into the resin (Fig. 2.7b). Eventually, to improve the dispersion of the nanoparticles and to avoid their sedimentation compatibilizing agents are used.

Regarding the composite characteristics, if a good matrix-fillers interaction is achieved, it is possible to transfer the properties of the filler to the matrix, achieving a composite material exhibiting enhanced properties. This paradigm is also exploited for the production of magneto responsive polymeric composites. Indeed, by embedding magnetic particles within a polymeric matrix, it is possible to confer magneto responsive behavior to the material, despite the intrinsic diamagnetic characteristic of polymers.

2.3.1 The intrinsic properties of the magneto-responsive polymers

Once the particles are embedded, an easy way to improve the magnetic response of the composite is to increase the content of the magnetic powders.

Indeed, a linear dependence exists between the particle concentration and the magnetization of the polymeric composite [88], [89]. However, an excessive amount of fillers may generate defects in the composite and affect the mechanical properties of the material [90].

As aforementioned, the interactions between the embedded fillers and the matrix is another key parameter to define the mechanical response of the composite. A strong adhesion allows force transfer mechanisms through the filler-matrix interface. In the case of a properly synthetized magnetic composite, the magneto-attraction on the fillers may be transferred to the polymeric matrix. According to the mechanical properties of the matrix, the transfer of these forces will result in motion (translation, rotation, etc.) or deformation (bending) of the whole material. As a consequence, for stiff polymers, possible envisaged applications can be devices that roll or shift without deforming or even composite magnets. On the other hand, for soft polymers, a possible application is in the field of shape-morphing actuators.

It was already discussed that embedded fillers drive the magnetic properties of the composite polymer, whereas the host matrix controls its mechanical behavior. From a thermodynamic viewpoint, the influence of these parameters can be described by the Helmholtz free energy (E_H), which is expressed as the sum of two terms: magnetic energy (E_m), which promotes the deformation, and the elastic energy (E_e), which hinders the deformation [91].

$$E_H = E_m + E_e \qquad \text{(Eq. 2.5)}$$

Any distortion of the sample will result in an increase in the free energy. The shape of equilibrium of an object is thus reached by balancing the magnetic energy of the fillers with the elastic energy of the polymer and is defined by the minimum of the Helmholtz free energy [91].

$$\nabla E_H = 0 \qquad \text{(Eq. 2.6)}$$

If an external stress is applied, the free energy of the system, which is a function of the morphology of the object, is also modified and the new minimum identifies the displacement from the original equilibrium state.

2.3.2 The role of the design

In addition to their intrinsic properties (the nanostructure, the composition, the NPs loading, and the NPs-matrix adhesion), the design of the sample is another fundamental parameter to control the behavior of the magneto-responsive polymers and to drive the amplitude of the desired magneto-response. It is thus important to understand and to master, how geometrical parameters, such as aspect ratio, length, and distance from the magnetic source affect the behavior of the sample.

As the stress-strain response of a magneto-sensitive polymer is strictly related to the geometry and its distance to the magnetic field, a careful multiscale design is necessary to fully program the response of the composite polymer upon the application of an external stimulus. In literature, there are several tables summarizing the influence of the geometrical parameters [91] as well as the magnetic sources [92].

Usually, polymers are manufactured by molding techniques, which restricts the design possibility of the object. However, recently, the emergence of the 3D printing changed the history, and paved the way for the development of free-designed objects fulfilling the crucial objective to enhance the properties of the corresponding devices.

Fused Filament Fabrication (FFF), Direct Ink Writing (DIW), and vat polymerization (SLA and DLP) 3D printing technologies are the most widely used in the fabrication of magneto-responsive polymers [93]. By DIW and FFF, inks and wires containing a high load of magnetic fillers were developed to fabricate fast responding actuators [94]–[99], and calculations were performed in order to program and predict the shape transformations [90]. Unfortunately, the use of FFF and DIW techniques often lead to the production of materials with limited resolution in the order of hundred micrometers [100], owing to the intrinsic limitation of the two techniques. Furthermore, especially in FFF, the synthesis of composite wires may be complicated [100], [101]. Vat polymerization techniques, and especially Digital Light Processing, may overcome the drawbacks of FFF and DIW techniques, due to a higher resolution [102], [103], an easier dispersion of

fillers, and a low processing temperature. Conversely, due to light absorption competition issues between the photoinitiator and the fillers, DLP and SLA techniques allows a lower concentration of magnetic particles into the matrix compared to FFF and DIW [104], [105].

In the next section, a short overview of the use of the 3D printing technique in the field of magneto-responsive polymers is given.

2.4 Examples of magneto-responsive polymer composites

2.4.1 Magneto-rheological elastomers

Magneto-rheological materials are the most diffused example of smart materials driven by magnetic fields. Magneto-rheological (MR) effects are related to the modification of the rheological properties of matter by the application of external magnetic fields. For instance, a magnetorheological fluid (MR fluid) is composed of magnetic micro-particles in a carrier fluid, Fig 2.9a. When subjected to a magnetic field, the fluid greatly increases its apparent viscosity, to the point of becoming viscoelastic. Since its discovery in 1954 by Thomas Rainbow [106], MR fluids, found an important industrial interest due to their damping properties [107]. However, MR fluids present several issues such as low yield stress, limited fluid stability, and durability [108]; furthermore, they need solid confinement because of their liquid state.

In the past decades, magneto-rheological elastomers (MREs) emerged as an alternative to MR fluids. Elastomers are a class of polymeric materials that possess a peculiar mechanical behavior. Those exhibit high deformation for low applied stresses, moreover, they can recover their initial shape rapidly upon load removal (Fig. 2.8). From a macromolecular point of view, this behavior can be achieved by different strategies. The most common elastomers are high molecular weight polymers characterized by very high chains mobility (low T_g) and with very low cross-linking density (e.g. natural rubber, silicone elastomers). As an alternative, thermoplastic elastomers can be produced which present hard segments that act as physical cross-linking points (e.g. elastomeric polyurethanes).

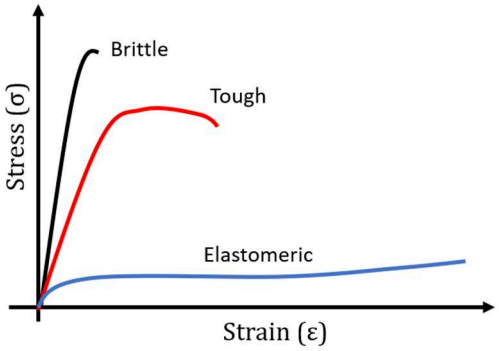

Figure 2.8: Ideal tensile test curves of brittle, tough, and elastomeric polymers

MREs are soft magneto-active rubber-like material, whose physical or mechanical properties can be altered upon the application of a magnetic field (Fig. 2.9b-c). MREs can be considered as the first example of magnetic-driven smart materials. When a magnetic field is applied, the magnetic particles are polarized and exert forces on one another that cause the material to stiffen. When the magnetic field is switched off, the MRE returns to its original, softer state. One of the most interesting characteristics of these materials is that they show a fast-magnetic response, in the order of ms [107]. Nowadays, MREs are applied in several fields such as shock absorbers, clutches, and brakes [107], [109].

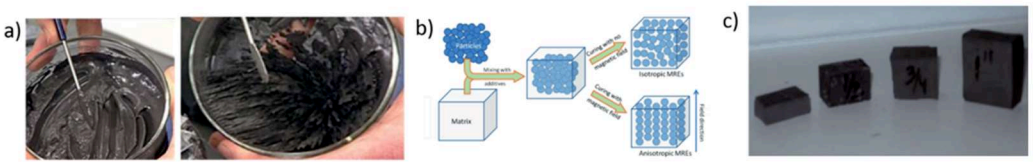

Figure 2.9: a) Magnetorheological fluids, b) illustration of the processing for preparing MREs, and c) prepared block of MREs with different thicknesses [110].

MREs consist of ferromagnetic micro-particles embedded in an elastomeric matrix. Among them, silicon rubber arises as the best choice to enhance the MR effect, even if other synthetic elastomers, as well as natural rubbers, are also employed [111]. About the filler, micro-sized ferromagnetic particles (2-5 μm) are the most frequently used. In particular, Fe and Co microparticles enhance the magneto-rheological effect due to high magnetic permeability and low hysteresis loop [107].

MREs are mainly fabricated by molding-based techniques, i.e. by dispersing the magnetic particles in the elastomeric matrix prior to the thermal curing process. Often an external magnetic field is applied during the curing process so that the magnetic particles organize in chain-like structures along the magnetic field lines, and this microstructural organization is maintained within the cross-linked material. MREs with such microstructure show enhanced magneto-rheological properties, furthermore the elastic modulus shows a higher increase compared to random-MREs, especially when the external magnetic field is applied along the micro chain direction [107], [109] improving their performances.

Recently, 3D printing techniques emerged as an interesting option to MREs manufacturing processes, eventually widen their potentialities [112]. Indeed, the possibility to improve the control of the device's shape has emerged as a new opportunity to enhance the magneto-rheological effect. However, since a high load of magnetic particles is requested to exploit MR properties [113], only Direct Ink Writing (DIW) and Fused Filament Fabrication (FFF) 3D printers afford the production of these materials [112]–[114].

In conclusion, the blossoming of new approaches to combine polymers and magnetic properties stimulated the development of MREs and in particular of magneto-driven soft actuators which is the subject of this thesis.

2.4.2 Composite Hard Magnets

Permanent magnets are an essential component in electric and electronic devices such as electric engines [115], data storage devices, and sensors [116], [117], or even in medicine like in Magnetic Resonance Imaging (MRI) [118]. In the latest years rare-earth magnets, especially NdFeB magnets, gained industrial and scientific interest since their unique magnetic properties: the highest magnetic remanence found in nature (higher than 1 Tesla), coercivity above 1000 KA/m, and maximum energy product $(BH)_{max}$ about 200 KJ/m^3 [119].

NdFeB magnets, conventionally manufactured by sintering, are fragile and hardly post machinable [120], [121]. They are thus limited to a few simple shapes, which limits the flexibility of the corresponding electric devices. The possibility to make magnets with complex-shapes would highly improve the performance of the

associated devices. Printing magnets without shape limitations is nowadays possible thanks to 3D printing technology. This technology is believed to boost the production of next-generation electrical and electronic devices. For instance, Toyota declared that by replacing conventional adjacent magnets in a rotor with a "V" shaped permanent magnet, the modification would increase the motor output power by 50% [122]. Moreover, the enhancement of power outcome would be even higher if the rotor was implemented with single curved permanent magnets [123].

Because of the remarkable industrial interest, in the past years many efforts have been done to achieve the additive manufacturing of free-designed permanent magnets. Among 3D printing techniques, Fused Filament Fabrication (FFF) demonstrated to be suitable for this goal, as it allows the additive manufacturing even at high filler load. The filaments are generally produced via twin-screw mixing of polymer beads and NdFeB particles, followed by the extrusion of the composite (Fig. 2.10a). The printed parts can consist of hollow-structures as well as 3D objects of various dimensions (Fig. 2.10b). The amount of NdFeB particles embedded in the polymeric matrix ranges between 45% and 60%, and because $(BH)_{max}$ strictly depends on the particles' concentration, the maximum energy product is about half of the conventional sintered magnets [121]. Besides, the increasing cost and environmental issues related to NdFeB particles, pushed alternative materials to be developed, like for instance Sr doped ferrite (Fe_2O_3) [124] or MnAl particles [125]. For the polymeric matrix, nylon is often preferred as it shows good rheological features that prevent nozzle clogging during the 3D printing process [120].

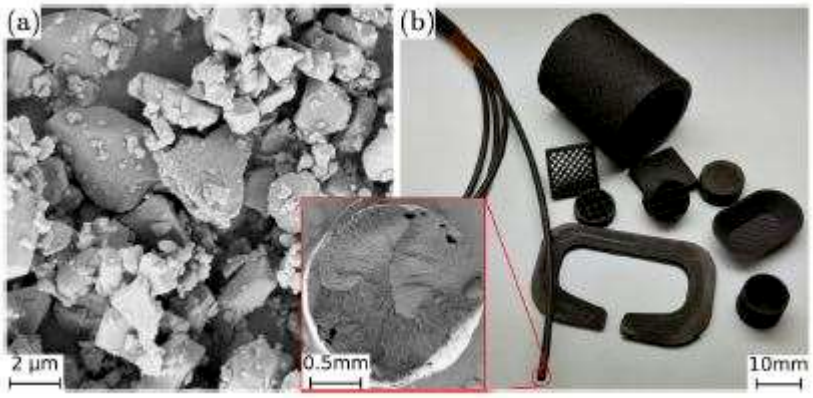

Figure 2.10: A) SEM image of Sr ferrite powder. B) Several 3D printed magnets. Inset: picture of the extruded filament containing 50 vol. % of powders. [124]

In order to improve the magnetic properties of the 3D printed composite permanent magnets, and to enhance the $(BH)_{max}$ three approaches are possible:

i) **Increase the concentration of the filler**: An easy way to improve the magnetic properties of the composites is to raise the content of the magnetic powders in the extruded filaments. Anyway, this strategy often leads to several issues in terms of the material's printability. An excessive increase of the particles' content may involve the use of plasticizers or to increase the printing temperature, generating defects in the printed structures and eventually affecting the mechanical and magnetic properties [99].

ii) **3D Printing of Metallic Structures**: As an extremization of the first point, the direct printing of fully metallic magnets emerged as an alternative to composite magnets. Starting from NdFeB powders by Selective Laser Sintering (SLS) technique does not require binders, thus it represents a promising alternative to FFF printing of composite polymers [119]. However, because of the poor thermal stability of NdFeB powder, the coercivity rapidly decreases when the temperature exceeds 100°C [126], and due to the high temperatures generated during the SLS printing process, the magnetic properties of the final object will result unavoidably deteriorated [125].

iii) **Anisotropic Magnets**: As reported in several studies, anisotropic composite magnets, characterized by the alignment of the magnetic easy axis, show higher magnetic remanence and higher maximum energy product $(BH)_{max}$ compared to isotropic magnets [125], [127]–[130]. As a drawback, the manufacturing process results expensive due to the need for homogeneous and high intensive magnetic fields (> 1.2 T) to promote anisotropy within a plasticized matrix.

2.5 Magneto-driven soft actuators

Actuation is defined as the response of an object as the result of environmental stimuli [131]. In nature, this is often observed as shape morphism, such as the blossoming of a flower, and involves a smooth deformation of the whole organism. Trying to mimic the shape morphism observed in nature, conventional robotics produce motion by the reciprocal movements of several mechanical parts, and this often leads to a jerky motion of the apparatus. Recently, smart materials emerged to bridge this gap [131] paving the way to soft robotics in which the shape morphism is produced by the smooth deformation of the whole material as a response to an external stimulus, similarly to what is observed in nature. Among the various actuation sources such as electric charges, moisture, and temperature, magnetic fields show several advantages as ease of application and remote contactless control. Moreover, Magento-responsive Polymeric Actuators (MPA) typically exhibit high strain and fast response. In addition, magnetic fields allow a wider and more precise control over the shape morphism of MPAs. In fact, since the magnetic field is a vector field, and therefore characterized by a sign and a direction, different types of actuation can be controlled within the same object by changing the direction, the intensity, and the polarity of the applied magnetic field. This is an enormous advantage compared to other actuation such as compared humidity or temperature, where the actuation mechanism can only be on/off [131].

The peculiar characteristics of MPAs and their potential applications justify an increasing interest in these materials. For instance, their possible control in remote, i.e. contactless, makes MPAs the best candidate for working in confined spaces, such as in microfluidic applications [132], [133]. Besides, the possibility to combine biocompatible polymers associated with the harmless penetration of magnetic fields in the human body [134], [135], makes magnetic-driven soft actuators the perfect candidate for biomedical applications as expandable stents [136], artificial muscles [136]–[138], targeted drug delivery systems [139] and microsurgery [140]. Other application fields include defense, aerospace, optics, and robotics [131], [133], [141].

In the next paragraphs, the preparation and production of magneto responsive polymeric actuators will be described, as well as an overview of the strategies to enhance the actuation performance will be given.

2.51. Common strategies for MPAs fabrication, and their actuation mechanisms

In general, magneto-responsive polymeric actuators are composed of two elements: a polymeric soft matrix, and magnetic micro- and nano-fillers. For the former, soft thermoset polymers and elastomers are the most used materials due to their high deformation rates. Among them, natural rubber [142]–[144], silicone rubber [145]–[147], polyurethane [148], [149], and polybutadiene [150] are among the most frequently investigated. In particular, polyurethanes are employed due to their high wear and tear resistance [151].

Concerning the magnetic fillers, their choice strongly influences the actuation mechanisms. In general, fillers can be either soft-magnets (i.e. magnetite, Fe_3O_4) or hard-magnets (i.e. neodymium alloy, NdFeB) with dimensions ranging from nanometric to micrometric sizes. In the case of soft magnets, as Fe_3O_4, particles exhibit a magnetic dipole only when exposed to an external magnetic field, while the magnetization return approximately null when the magnetic source is removed. In this case, magnetic soft actuators do not show a permanent magnetic polarity, but their magnetization can be turned into an on/off state by applying an external magnetic field. On the other hand, hard-magnet particles show a permanent magnetic polarization due to the high magnetic remanence of the particles, such that they act as proper magnets.

Regarding the synthetic strategy, although several approaches have been developed so far, the more accessible route is to mix the magnetic particles in the unreacted material and subsequently polymerize it [141]. Alternative approaches consist of the absorption of magnetic fluids by a porous polymer [152], or by particle's precipitation [153]. If the embedded particles are hard magnets, the composite material has to be magnetized by the application of a strong magnetic field [141]. According to the actuation mechanism promoted by the external magnetic source, it is possible to define three different classes of MPA:

- **Direct**: Once the magneto responsive polymer is exposed to an external magnetic field, the magnetic particles interact with the external source according to their magnetic class. On the one hand, soft magnetic particles get magnetized and attracted to the external magnetic field; on the other hand, ferromagnetic particles maintained their magnetization and are attracted or repelled by the magnetic source based on their magnetic polarization. Regardless of the type of particles, once the magnetic field is applied the embedded fillers interact with the surrounding matrix modifying the position of the polymeric chains resulting in a macroscopic shape transformation of the whole object [131].

- **Undirect**: Similar to the thermally activated shape memory polymers [154], [155], the actuation is led by heating the polymer above its glass transition temperature. In this case, the heat is not provided by a thermal source via heat conduction, but the heat is generated within the material itself via magnetic inductive heating. This is promoted by external high frequency alternating magnetic fields that provoke magnetic hysteresis losses into magnetic particles heating the whole composite material [156], [157].

- **Hybrid**: The actuation mechanism is the combination of both direct and undirect approaches. Superparamagnetic particles are added to the composite in order to heat the material via magnetic inductive heating (Undirect mechanisms). Once the heat provided is enough to soften the polymeric matrix, the actuation is performed by hard magnetic fillers according to the direct mechanism [158].

Regardless of the actuation typology, in all the cases there is an urgent need to improve several aspects of the actuation mechanism such as the deformation magnitude and rate, or even enhance the control on the shape-morphing transformation and increasing their complexity. In the next section, the main strategies attempted are taken into account focusing on the direct actuation mechanism.

2.5.2 Programmable magnetic anisotropy and microstructures

Recently, a new path to enhance the magnetic actuation of MPA and enlarge the palette of shape-morphing transformations has emerged. This innovative approach consists in controlling the microstructure of the nanocomposites during the 3D printing process, which in turn induces magnetic anisotropy in the printed composite material. According to the magnetic properties of the fillers embedded in the polymeric matrix, two main strategies are distinguished: i) control of the magnetic polarization of hard magnetic particles, ii) exploiting the self-assembly process of soft-magnetic and superparamagnetic fillers.

Controlling magnetic polarization of hard magnetic fillers

The common pathway to produce composite polymers with embedded hard magnetic particles consists of dispersing the not-yet-magnetized fillers in the polymeric precursor prior to the manufacturing process, and to magnetize the composite only after the polymerization process occurred. In fact, if the magnetic particles were magnetized before the curing process of the matrix, the magnetic interactions between particles would lead to the formation of a massive aggregate. On the other hand, when particles magnetization occurs after the polymerization process, the embedded particles cannot migrate within the polymeric matrix, preventing the formation of agglomerates. This productive solution allows to program the magnetic polarization of the ferromagnetic particles, but not to exploit self-assembly processes and the formation of complex microstructures.

Controlling the magnetic polarization of an MPA filled with ferromagnetic particles allows the exploitation of multimodal locomotion and shape-transformation by changing the parameters of the external magnetic field. The first examples of this approach are limited to millimetric rectangular-shape films developed in the micro and milli-robotics [159], [160]. *Hu et al.,* [159] embedded NdFeB microparticles in a silicone elastomer, and by a precise magnetization process they programmed a single-wavelength harmonic magnetization profile along the magnetic film, Figure 2.11. Thanks to the obtained magnetization profile, by changing in time the external magnetic field, different modes of locomotion were exploited allowing the magnetic robot to move in both wet and dry environments.

Furthermore, the authors demonstrate the magnetic robot's ability to overcome obstacles by jumping, and to choose between rolling and walking motion on solid surfaces.

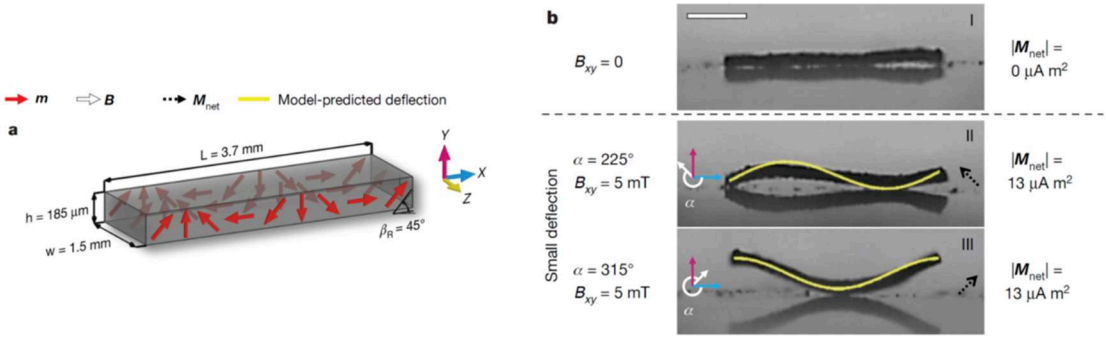

Figure 2.11. a) Design, and b) shape-charging mechanisms of magneto-elastic millirobot. [159]

Lu et al. [160] developed a similar milli-robot equipped with magnetic responsive micro-legs, Fig. 2.12. The device was fabricated by mixing polydimethylsiloxane with magnetic iron microparticle and applying an external magnetic field perpendicular to the rectangular surface to promote the formation of magnetic legs during the polymerization process. When the magnetic robot was exposed to an external permanent magnet, the magnetic feet got aligned along the magnetic flux direction showing different types of postures and movements. In both cases, the applications were limited by the limited dimension of the developed prototypes.

Figure 2.12: Locomotion mode of a bioinspired multilegged soft millirobot. [160]

In parallel, *Y. Kim et al.* [161]. developed a magnetically assisted 3D Printer for the fabrication of magnetic soft composites with programmable magnetic domains, Fig. 2.13. In this work, the authors modified the nozzle of a DIW 3D printer introducing a magnetic field to induce a magnetic polarity to NdFeB microparticles loaded into a composite ink made of silicone monomers and silica nanoparticles. The application of a permanent magnet or an electromagnet coil after the nozzle of an inkjet printer allows reorienting the magnetic dipole of the particles

within the filament along the field direction. In this way, a permanent magnetic momentum is imparted to the extruded ink filament allowing programming different ferromagnetic domains within the same composite polymer (Fig. 2.13a). As owing to their magnetic polarization the different ferromagnetic domains can attract or repel each other when exposed to magnetic fields, and a shape transformation of the object becomes possible upon the application of an external magnetic field (Fig. 2.13b). Thanks to the developed 3D printing apparatus and finite element analysis calculations, the authors were able to 3D print two-dimensional planar structures with programmed ferromagnetic domains, that once exposed to magnetic fields, rapidly transform into complex 3D shapes as a result of programmed ferromagnetic domains (Fig. 2.13c). The production of proper complex 3D structures was held back by the intrinsic limitation of DIW systems, or rather by structural instability issues related to the deposited filaments.

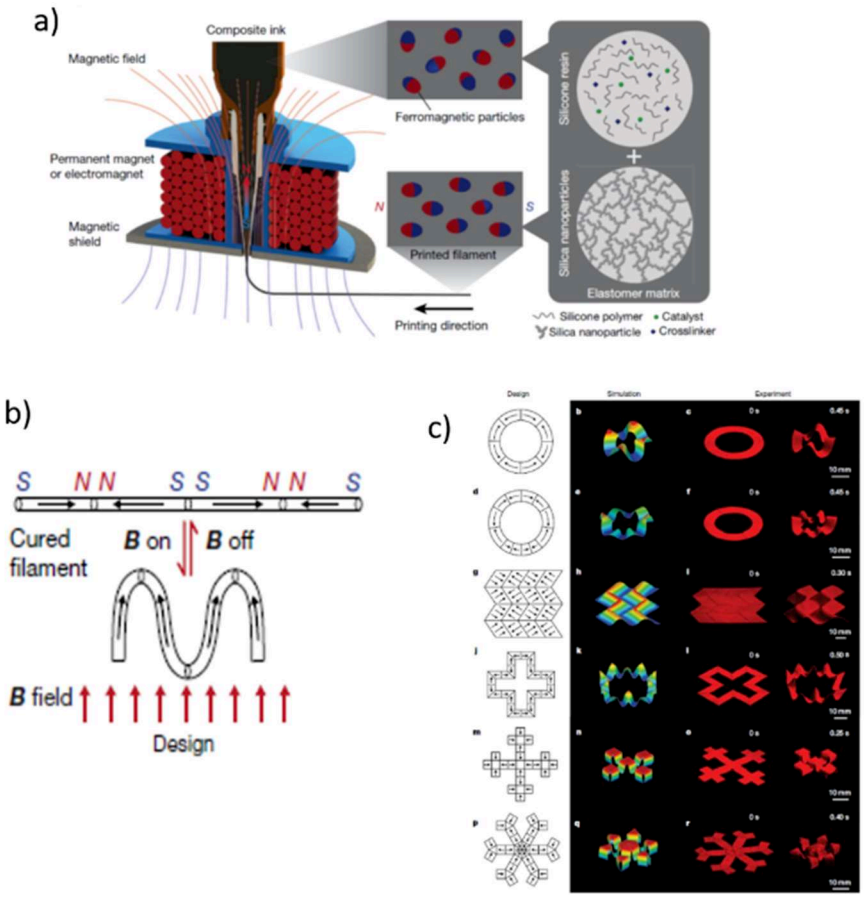

Figure 2.13: a) Set up of the printing process and the material composition, b) Schematic illustration of the actuation mechanism involving different ferromagnetic domains. c) Two-dimensional planar

structures containing several magnetic domains evolution in 3D complex structures. Design, simulation, and experimental data [161].

Exploiting Self-Assembly process

When magnetic particles dispersed in a low-viscous liquid medium are exposed to external magnetic fields they undergo a self-assembly process, and the system rapidly evolves from a random and disordered configuration toward organized structures and patterns [162], [163]. Self-assembly is a thermodynamically driven process of organization where nanostructures are stabilized against thermal fluctuations through forces generated by external fields. For superparamagnetic nanoparticles, the self-assembly process is mainly governed by magnetic dipole-dipole interactions that promote the alignment of the particles along the external magnetic field lines [164]–[166]. The dipole-dipole energy of interaction represents the work required to bring two particles from the infinity to the distance *r* and writes:

$$U_{12} = \frac{\boldsymbol{m_1 m_2} - 3(\boldsymbol{m_1}\cdot r)(\boldsymbol{m_2}\cdot r)}{4\pi\mu_0 r^3} \qquad \text{(Eq 2.5)}$$

Where m_1 and m_2 are the magnetic dipole moments of the two particles connected by the vector r. It results that the energy for a single particle submitted to an external magnetic field H is $U=-\mu_0 mH$ and the force acting on it is described by the gradient of the energy: $F=\nabla(mH)$.

However, the process is also influenced by Van der Waals forces, thermal fluctuations, and nanoparticles-solvent interactions [166]. According to the applied external electromagnetic forces, different self-assembled configurations have been observed, such as chains [164]–[172], rings [169]–[172], and 2D patterns [170], [171].

Among them, the formation of magnetic chains is by far the most investigated process and the easiest to obtain. An accessible and fast route for promoting the formation of assembled magnetic chains consists of exposing the liquid dispersion of particles to an external magnetic field generated by the interaction of two parallel permanent magnets. The dipole-dipole interactions between particles lead to a spontaneous alignment along the lines of the applied external magnetic field [170],

[171] (Fig. 2.14). When the magnetic chains are aligned in the system, a favorite magnetic axis is produced, and magnetic anisotropy is established. Once the chains are aligned along the magnetic field lines, and the external magnetic field direction is changed, the chains feel the magnetic torque and undergo a rotational motion realigning along the new magnetic field lines. The magnetic torque can also be exploited to induce actuation motion in soft materials as an alternative to traditional magnetic forces, enlarging the control and the typologies of shape-morphing transformations [172]–[174]. In order to maximize the effect of magnetic torque, it is fundamental to predict the system evolution and the dimensions of the magnetic chain. Despite a large scientific production describing the influence of magnetic field intensity [165], [166], [168], [169], particle size and concentration [169], [172], and system viscosity [173], [174], a complete model considering the influence of all the external parameters on the dimensions of the magnetic chain does not exist as well as a complete investigation on the rotation of the assembled chains.

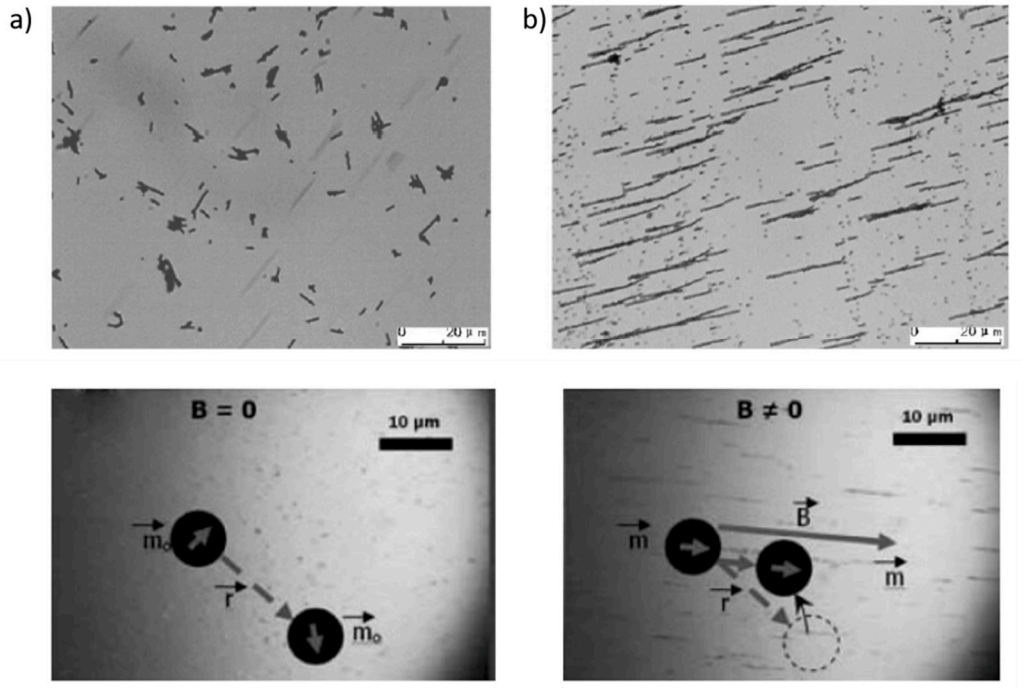

Figure 2.14: Optical microscope images of Fe3O4 nanoparticles dispersed in a liquid without a magnetic field applied (a) and with a magnetic field applied (b) [165]. Schematics of the magnetic dipole interactions of the nanoparticles occurring during the self-assembly process [166]-

The production of magnetic composite materials with controlled microstructure and magnetic anisotropy can significantly improve the features of magneto-driven

soft actuators introducing more complex transformations. Along the assembled chains, the magnetic axis of the particles is aligned accordingly to the direction of the chains bringing to the formation of a magnetic easy axis within the composite and inducing magnetic anisotropy in the system. Furthermore, by controlling the aforementioned parameters (viscosity, magnetic field intensity, particles concertation) the magnetic anisotropy of the object can be tuned, programming the chain's dimension. In particular, the anisotropic actuators are no longer ruled only by magnetic forces, but also magnetic torque plays a role through the interaction with the assembled chains embedded in the polymeric matrix.

Several examples of the exploitation of magnetic anisotropy to produce innovative soft-actuators are already found in the literature. Kim *et Al.* were able to program several anisotropic magnetic domains within the same composite materials by taking advantage of photopolymerization processes [175]. In particular, the authors dispersed iron oxide superparamagnetic nanoparticles in uncured polyethyleneglycol diacrylate (PEGDA) resin containing a photoinitiator, and they exposed the formulation to an external magnetic field promoting the formation of self-assembled magnetic chains. By initiating photopolymerization via light irradiation, it was possible to fix and freeze the assembled microstructure in the cured polymeric matrix in a tenth of a second.

This approach was extended to a maskless lithography process: by changing the direction of the applied magnetic field and by selecting the area to irradiate, it was possible to locally control the magnetic anisotropy in multiple regions of the object. The control achieved in the microstructure brought to a complex and programmable magnetic anisotropy of the whole material. When the object was exposed to a magnetic field, the generated magnetic torque forced each magnetic domain to rotate in order to re-align the chains along the external magnetic field direction, leading to the exploitation of multiple complex actuation mechanisms within the same object (Fig. 2.15). By an analytical model, the microstructure and the design aspects were combined predicting the deformation magnitude promoted by changing the external magnetic field intensity [175]. The robot was limited to flat 2D structures of hundreds of micrometers in size, due to the lithography process.

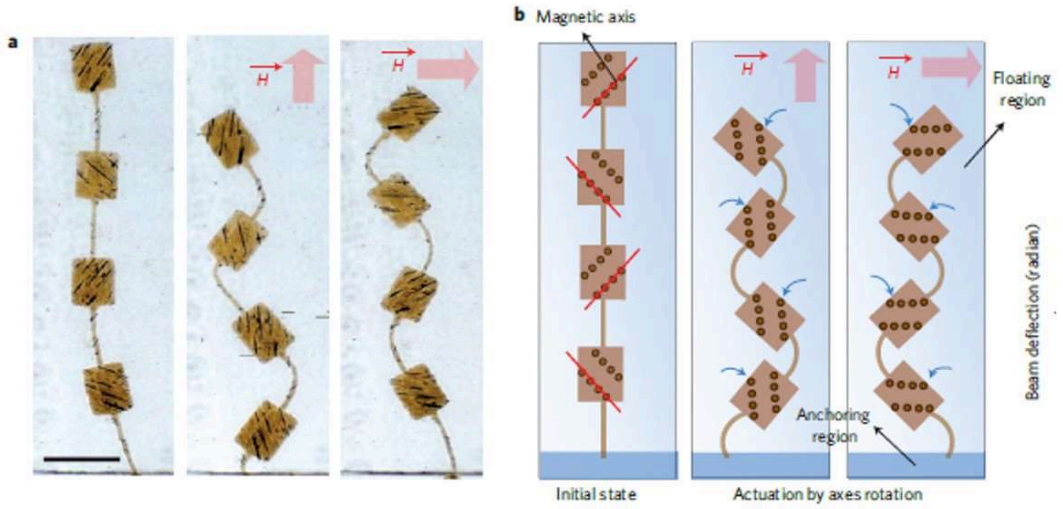

Figure 2.15: a) A microactuator undergoing several bending motions by changing the direction of the magnetic field (scale bar is 100 um). B) Scheme of the actuator describing the easy magnetic axis of each part and the possible actuation mechanisms. [175]

The aforementioned self-assembly process was never developed during a 3D printing process. Nevertheless, in the literature, there are several examples of 3D printing processes assisted by an external magnetic field, and one example was already discussed in the previous section [161]. Anyway, vat polymerization 3D printing appears as the most suitable approach for the fabrication of nanostructured magnetic objects via self-assembly process. This is because these 3D printers operate with low-viscosity resins enabling nanoparticles self-assembly upon magnetic field application and rapid object production via a rapid photopolymerization process which "freeze" the assembled magnetic microstructure within the printed layers.

2.5.3 Magnetically Assisted Vat Photopolymerization 3D Printers

The first example of a DLP 3D printer assisted by magnetic fields was recently proposed by Martin *et Al* [176]. Thanks to the application of rotating magnetic fields in the resin reservoir, the authors were able to control the axial orientation of alumina platelets decorated with magnetic nanoparticles (Fig. 2.16a). The rotating magnetic field generated a magnetic torque on the alumina platelet making them to orient along the magnetic rotational plane. The orientation process was governed

by the dimensions of the microparticles and by the magnetic field parameters: i) the alumina platelets need to have an ellipsoidal shape and a length of 10 μm, ii) the magnetic field intensity has to be few mT, rotating and alternating. If the contour-conditions were not respected, the orientation process was ruled by thermal or gravity considerations (Fig. 2.16b). Thanks to this approach, the authors were able to manufacture composites with enhanced impact resistance ensured by bio-inspired programmable microstructures (Fig. 2.16c). In this case, the magnetically-assisted 3D printer was not developed in order to produce magneto-responsive materials, and thermodynamics aspects limited the plethora of processable materials.

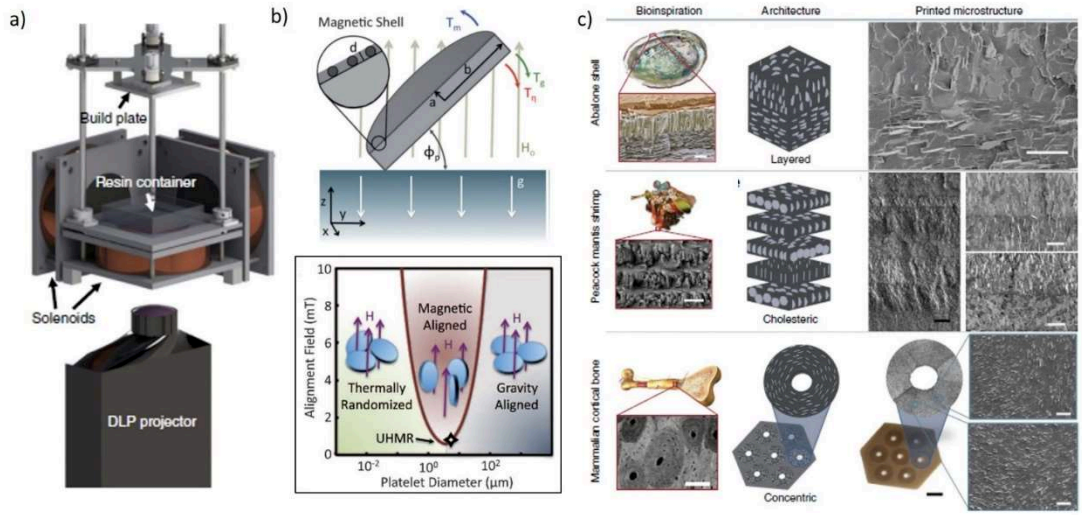

Figure 2.16: A) 3D printing set up with solenoids allowing the production of rotating magnetic fields. B) Magnetic drive orientation of alumina platelet decorated with magnetic nanoparticles and platelet diameter vs magnetic field orientational diagram. C) Complex microstructure in nature, architecture design of the microstructure, and bio-inspired microstructure in the 3D printed samples [176].

The latest example of a magneto-assisted 3D printing processed was proposed by Joyee *et Al* introducing a magnetic-assisted projection stereolithography process able to 3D print a multi-material object in a single process [105]. In this case, the 3D printer was equipped with a micro nozzle and a movable magnet under the resin reservoir applied to spatially-localize magnetic nanoparticles dispersed in a photo-curable resin (Fig. 2.17a). In order to print a layer containing magnetic fillers, the micronozzle feeds the resin reservoir with the magnetic particles, and the magnets spatially localized them according to the CAD instructions. The authors exploited

this innovative 3D printing apparatus to produce a multi-material soft robot mimicking the movements of an inchworm when remotely activated by two permanent magnets (Fig. 2.17b).

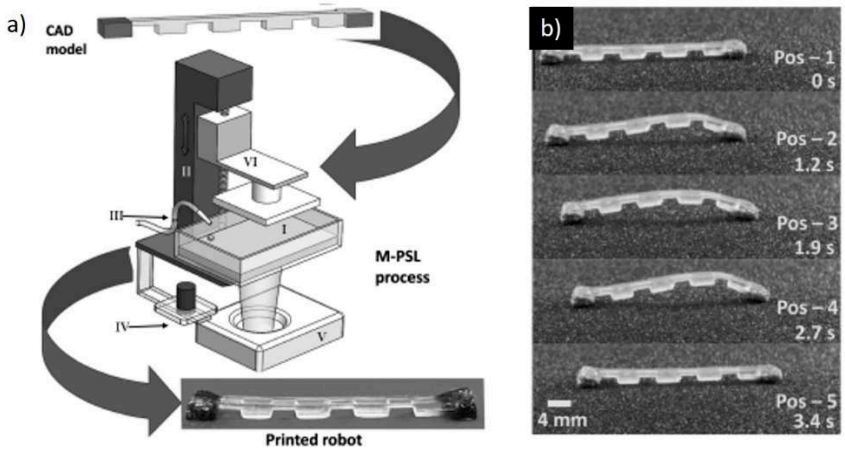

Figure 2.17: A) set-up of the magnetic-assisted stereolithography 3D printer. B) 3D Printed bio-inspired soft robot [105].

2.6 Final Remarks

Magnetic composite polymers are an intriguing class of smart materials with unique properties. The interest in enabling a quick and remote-activated control over the shape and the motion of objects by the application of an external magnetic field is rapidly growing in the scientific community. Magnetic driven soft actuators are the core of these investigations. The full development of these materials is predicted to radically transform several fields as electronics, robotics, sensors and biomedicine, and eventually every-day life. Anyway, several issues have to be resolved in order to fully exploit the unique features of magnetic driven soft actuators. 3D printing technology boosted the development of these devices avoiding design-limitation and allowing a larger control in materials properties. Furthermore, in the 4D printing trend, several attempts are made in order to improve the tuning and the reliability of these materials by controlling their microstructure and inducing magnetic anisotropy.

This Ph.D. work lays in the 4D printing and magneto responsive polymers topics by proposing a novel 3D printing process that produces an innovative class of magnetic composite materials with controlled microstructure and magnetic

anisotropy in each layer of the printed composite. This was made possible by assisting a DLP printer with tunable magnetic fields taking advantage of the self-assembly behavior of magnetic particles dispersed in liquid photocurable resins. Specifically, by tuning the magnetic field intensity and direction in each printing step, the photocured layers had an independent microstructure made by the assembled magnetic chains with controlled length and direction. Thanks to the obtained microstructures in the printed layers it was possible to exploit both magnetic force and magnetic torque in the shape-transformations, enabling movement of the printed magneto composite materials.

In order to clearly describe the structure of this research, the experimental part of this manuscript is organized as follows:

- Chapter 3 "3D and 4D printing with randomly dispersed magnetic nanoparticles"- describes the 3D printing process of isotropic polymeric composite with randomly dispersed magnetic particles.

- Chapter 4 "Magnetic nanoparticles self-assembly and magnetic chains orientation" – here the self-assembly behavior of magnetic particles dispersed in photocurable resins is described underlining the parameters that rule the assembly process and how to control their shape, thus the anisotropy in the cured composite. Once the chains are formed, the control over their direction is also explained.

- Chapter 5 "Set-up of a novel magneto-assisted DLP printer" – The modifications made on the 3D printer to apply magnetic fields during the printed process are here shown. Moreover, it is underlined how it was possible to control the chains and size direction in the whole printing space.

- Chapter 6 "4D printing of magneto responsive polymeric composites materials with programmable microstructures" – The 3D printing process and properties of the printed composite materials are shown, and several examples of devices exploiting their magnetic anisotropy are introduced.

3.

3D Printing of Magneto-Responsive Polymers with Randomly Dispersed Magnetic Nanoparticles

3.1 Motivations of the work

In this chapter, a strategy to 3D print magneto-responsive polymers with randomly dispersed magnetic nanofillers is described. The first step consists in optimizing the initial photocurable formulation to obtain the desired reactivity, mechanical properties, and functional response. The second step concerns the printing of magneto-responsive objects using Digital Light Printing (DLP) technology, focusing on maximizing the content of magnetic nanoparticles embedded within a photo-curable resin. The final step is the design of the printed objects such that these will respond in a controlled way to the application of an external magnetic field. The results presented in this chapter have been published in the peer-reviewed Journal "*Advanced Materials Technologies" with the following title "3D printing of magnetoresponsive polymeric materials with tunable mechanical and magnetic properties by digital light processing*" [177].

3.2 Optimization of the Photocurable Resin Containing Magnetic Nanofillers

3.2.1 Selection of the photocurable formulation: the urethane-acrylate resin

Elastomers are commonly used for the fabrication of soft-actuators because of their flexibility and fast deformation rates. However, in vat 3D printing, usually multifunctional acrylates are employed, in order to have faster printing processes and higher precision [178]. This, on the other hand, usually results in the printing of stiffer materials compared to elastomers. To mitigate this effect and to tune the mechanical properties of the printed polymers, several approaches have been developed so far such as the use of additives, oligomers with large molecular weight, or the addition of different functional groups in the polymeric structure [178]–[180]. In this context, urethane-acrylate resins emerged as a valid option to produce pseudo-elastomeric materials through photopolymerization [181], [182]. These materials uphold the properties of urethane rubbers and owing to the presence of multiple acrylic functionalities, can be eventually photocured using DLP or SLA 3D printers.

To develop a photopolymerizable matrix suitable to produce magnetic driven soft polymers, three urethane-acrylate resins were tested: Ebecryl 8254, Ebecryl 8232, and Ebecryl 4740 all kindly provided by Allnex. Those urethane-acrylate resins were commercially developed as photopolymerizable coatings [183]. Thus, the possibility to 3D print these resins with the DLP technique is first investigated. In addition to pristine urethane-acrylate resins (Ebecryl 8254, 8232, and 4740), phenylbis(2,4,6-trimethylbenzoyl)phosphine oxide (BAPO), purchased from Merck, was added as radical photoinitiator at 1 wt.%, and reactive Orange 16 (RO16), purchased from Merck, was added as a dye at 0.2 wt.%. The composition of all the tested resins are summarized in the *Appendix 1* of this thesis. Finally, a RobotFactory HD 2.0 was used as Digital Light Processing (DLP) 3D printer (Fig. 3.1a). The DLP apparatus has a broadband projector emitting light in the visible region (400-700 nm) with an intensity of 10 mW cm^{-2}. The nominal resolution of the 3D printer was equal to 50 μm in the x-y plane and ranging from 10 to 200 μm

in the z-axis, depending on the set layer thickness. After the printing step, the objects were first cleaned with ethanol or acetone and eventually sonicated, and successively submitted to a UV post-curing to complete the polymerization process using a medium-pressure mercury lamp also from RobotFactory.

Complex objects were successfully 3D printed with all the tested resins (see for instance the printed colosseum in Fig. 3.1 b). The printing parameters were similar for all the used resins, although for Ebecryl 8232 the process was slightly faster compared to the others (Tab. 3.1).

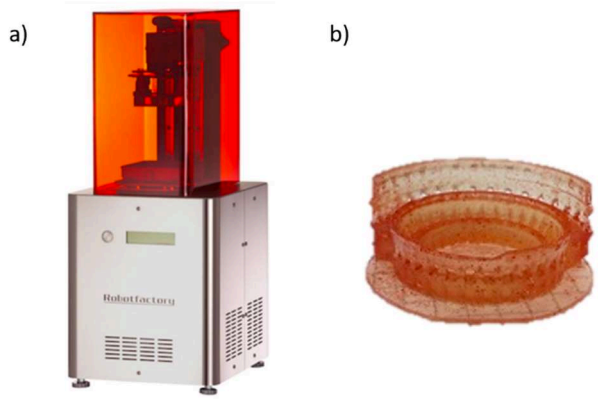

Figure 3.8: A) The RobotFactory HD 2.0 DLP 3D printer used in this work. B) example of complex structure 3D printed with Ebecryl 8232 formulation.

Table 3.3: Printing parameters and glass transition temperatures of Ebecryl 8254, Ebecryl 8232, and Ebecryl 4740 samples.

Sample	Base exposing time (s)	Object exposing time (s)	Tg 1st DSC run (°C)	Tg 2nd DSC run (°C)
Ebecryl 8254	2	1.4	-2	36,5
Ebecryl 8232	2	1.2	-12	-10
Ebecryl 4740	2	1.8	-12	16

FT-IR analysis was performed to study the photopolymerization kinetics by following the evolution of acrylic bounds conversion upon visible light irradiation. *When a molecule is exposed to infrared (IR) rays, it absorbs photons at specific frequencies which are characteristics of the compound. During a conventional FT-IR measurement, the sample is scanned with an IR beam, and when a frequency match with the vibration energy of a bond or a group of atoms of the sample, a*

photon is absorbed. Thus, the IR spectrum contains several peaks associated with the chemical bonds present in the tested sample. As a correlation between the area of the peak and the number of bonds in the sample exist, FT-IR can be used to follow the kinetics of a chemical reaction. In particular, as the polymerization process involves chemical reactions within the functional groups of a monomer, it is possible to follow the appearing (or disappearing) of a chemical group by analyzing the evolution of a specific peak associated with the reacting group. The FT-IR spectra were collected using a Nicolet 50 FT-IR (Thermo Scientific), Fig. 3.2a. The samples were prepared by pouring the formulation on a silicon wafer, the film thickness was controlled by a wire wound bar to be 12 µm. Samples were irradiated with visible light for 0, 10, 20, 30, and 60 seconds by a Hamamatsu LC8 visible lamp with a cut-off filter below 400 nm, and with an intensity of 10 mW cm^{-2}. The acrylic group conversion was followed by monitoring the trend of the double bond peak area located in the 1630-1650 cm^{-1} region. The decreasing area of this peak was normalized with the aromatic peak area at 1505-1575 cm^{-1}, which was not changing upon irradiation. As an example, the evolution of the spectra collected for the Ebecryl 8232 are reported in Fig. 3.2b.

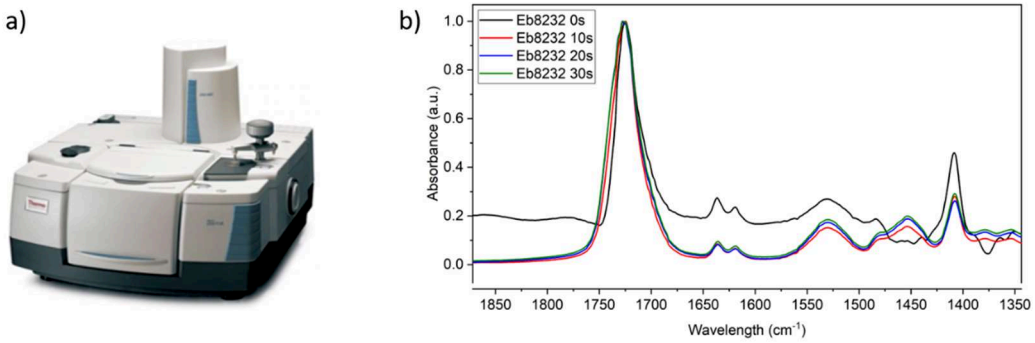

Figure 3.9: a) Nicolet 50 FT-IR (Thermo Scientific) used to collect the FT-IR b) Example of FT-IR spectra collected for Ebecryl 8232 formulation after 0s, 10s, 20s, and 30s of visible light irradiation.

The time evolution of double bonds conversion extracted from FT-IR spectra are shown in Fig. 3.3 for the three studied urethane-acrylate formulations, Ebecryl 8254, 8232, 4740. Among them, Ebecryl 8232 is the more reactive resin, reaching a conversion of about 80% of acrylic group after 30 seconds of light irradiation. On the contrary, Ebecryl 8254, and Ebecryl 4740 show both a conversion lower than 70% as well as slower polymerization rates, i.e. initial slope of the curves.

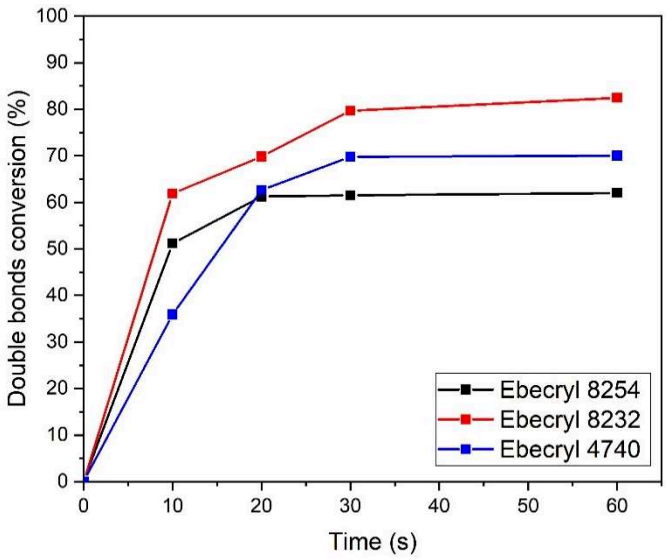

Figure 3.10: Double bonds conversion vs time kinetics of Ebecryl 8254, Ebecryl 8232, and Ebecryl 4740. Date were elaborated from FT-IR collected spectra.

Differential Scanning Calorimetry (DSC) is typically used to follow the thermal processes occurring in a sample varying the temperature. In particular, by testing simultaneously a sample and a reference (typically an alumina crucible), the amount of heat required to maintain the sample and the reference at the same temperature is measured. During the measurement, heat flux vs temperature curve is acquired. Every change in the heat flux can be associated with transformations occurring in the sample, these can be either endothermic and exothermic reactions depending if the system absorbs or releases heat respectively, due to any chemical/physical change. In polymers, DSC is used to follow several processes such as crystallization (exothermic reaction), crystalline zone melting (endothermic reaction), and thermal activated polymerization or curing (exothermic). In this work DSC1 STARe System (Fig. 3.4a) was used to detect the glass transition temperature (T_g) of 3D printed samples after the post UV curing process. Glass transition is a second-order transformation consisting of a variation of the specific heat capacity (C_p) of the material related to the change in macromolecules mobility [83], this process is not characterized by a peak but by an inflection in the enthalpy vs temperature curve. Conventionally, the flex is defined as glass transition temperature (T_g) and it is given as a characteristic of a material. During the tests, two runs were performed on every sample, and T_g was measured in the second run. The thermal cycles were a 5 minutes isothermal -70°C, followed by a heating stage up to 150°C with a

heating ramp of 10 °C/min, and ending with a cooling stage down to -70°C with a cooling ramp of -10°C/min. The second run followed the same routine. All the tests were performed under nitrogen flux (30 ml/min), where the glass transition temperature coincides with the inflection point of the characteristic DSC curve as shown in Figs. 3.4 b-d.

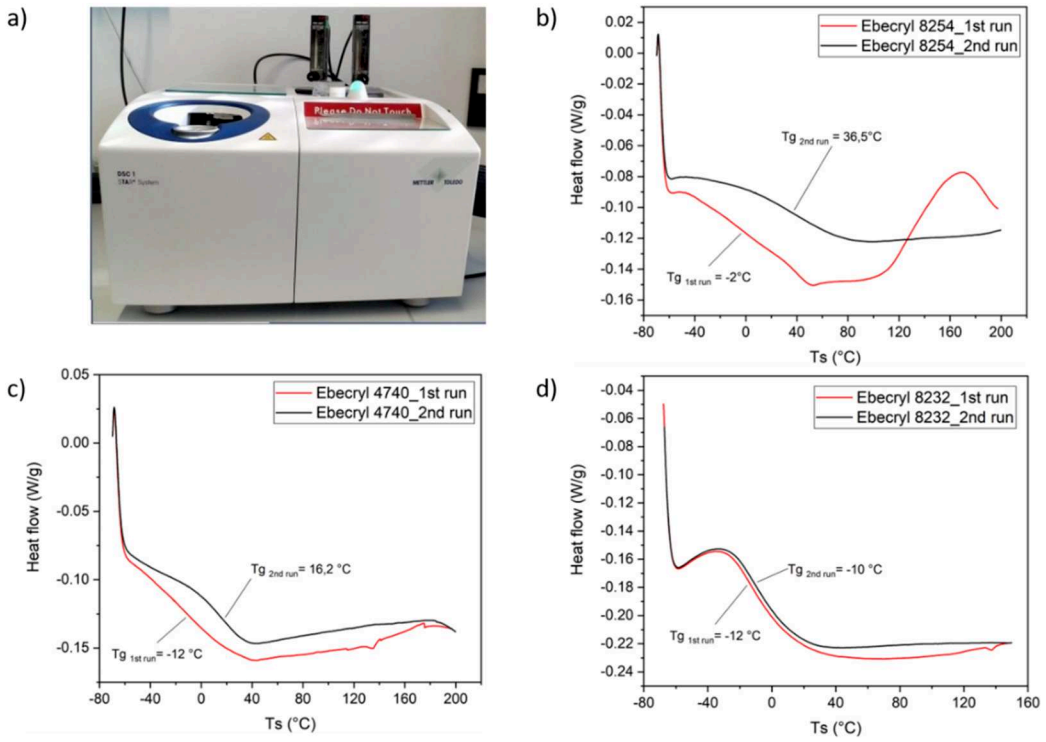

Figure 3.11: a) Differential Scanning Calorimetry DSC1 STARe System used in the experiments. DSC curves obtained for b) Ebecryl 8254 formulation, c) Ebecryl 4740 formulation, and d) Ebecryl 8232 formulation.

Glass transition temperature can be considered as an index of the softness of the polymer. Indeed, the lower the T_g, the higher the macromolecules mobility at room temperature, and thus the softer and the more flexible the polymer. During the first run of Ebecryl 8254 and Ebecryl 4740 an exothermic peak was observed. It has been associated with the thermal curing of residual unreacted moieties after the 3D printing procedure induced by the heat introduced into the system during the first heating ramp (Fig. 3.4b, c respectively). This effect was also confirmed by a shifting of T_g toward higher temperatures between the first and the second run. This is associated with the production of a higher cross-linked network that, in turn, reduces the mobility of the polymeric chains. These results are in good agreement

with FT-IR experiments. On the other hand, DSC curves associated with Ebecryl 8232 do not show any exothermic peak linked to post-curing, indicating that the UV treatment after 3D printing was enough to fully polymerized the samples (Fig. 3.4 d). Moreover, no significant difference was observed among the T_g determined in the first and in the second DSC run.

Among the three tested resins, Ebecryl 8232 presents a higher reactivity and flexibility (i.e. lower T_g) if compared to Ebecryl 8254 and Ebecryl 4740. In addition, post-UV-curing was sufficient to complete the polymerization of the material, which avoids the need for any additional thermal post-curing. Thus, for further investigations, this resin was selected. In the next section is described the strategy to enhance the reactivity of the formulation and to tune the mechanical properties of the printed polymers using reactive diluents.

3.2.2 Optimization of the formulation: the effect of the reactive diluent

Ebecryl 8232 was selected as the optimum photocurable formulation. Here, its reactivity and viscosity have been tuned by adding two monofunctional monomers, Butyl Acrylate (BA) and 2-hydrixyethyl acrylate (HEA), whose chemical structures are reported in Fig. 3.5. Those chemicals are expected to participate in the reaction due to the presence of reactive groups and, at the same time, decrease the viscosity of the system, thus they are defined as reactive diluents [184].

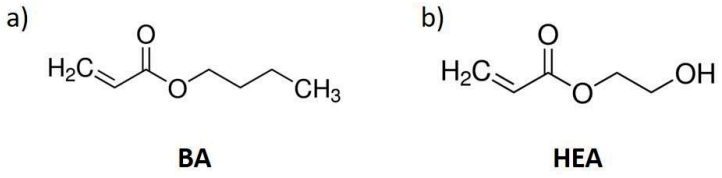

Figure 3.12: Chemical structure of a) Butyl Acrylate (BA), and b) 2-hydroxyethyl Acrylate (HEA).

The addition of a reactive diluent is expected to decrease the cross-linking density of the polymer, and thus to decrease the glass temperature of the sample (T_g), which, in turn, may result in the fabrication of a softer material. The

polymerization kinetics were evaluated by following the conversion of acrylic double bonds during visible light irradiation for different concentrations of BA and HEA (0%, 25%, and 50%). Five different formulations were tested:

i) 100 wt% Ebecryl 8232 (100Eb)
ii) 75wt% Ebecryl 8232 and 25 wt% BA (75Eb25BA)
iii) 50 wt% Ebecryl 8232 and 50 wt% BA (75Eb25BA)
iv) 75wt% Ebecryl 8232 and 25 wt% HEA (75Eb25HEA)
v) 50 wt% Ebecryl 8232 and 50 wt% HEA (50Eb50HEA)

As expected, the addition of reactive diluents produces an increase in the polymerization rate, i.e. the initial slope of the curve in Fig. 3.6. ln addition, the amount of conversion was increased passing from 80% for pure Ebecryl 8232 up to 95% for the formulations containing the reactive diluents (Fig. 3.6). Indeed, the addition of a low-viscous reactive diluent postpones the gelation point and accelerates the polymerization kinetics, and increases the acrylic group conversion [185].

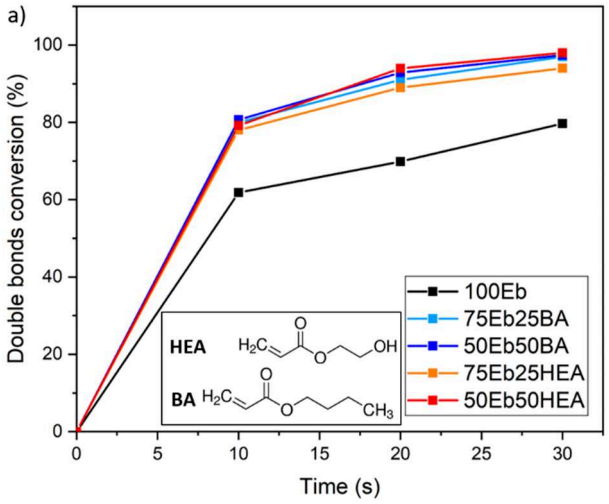

Figure 3.13: polymerization kinetics of the 100Eb, 75Eb25BA, 50Eb50BA, 75Eb25HEA, and 50Eb50BA samples. In the insert the chemicals structure of Butyl Acrylate and 2-hydrixyethyl acrylate used as reactive diluents.

The thermo-mechanical properties of UV cured films were investigated by Dynamic mechanical thermal analysis (DMTA). During this test, a sinusoidal strain (ε) is applied to the specimen, the force - and thus, the stress (σ) – necessary to achieve the fixed displacement is then measured with regard to a temperature ramp.

Polymers typically behave as viscoelastic materials thus they exhibit both viscous and elastic behavior. By DMTA it is possible to follow the elastic behavior of the material through the thermal evolution of the *in-phase* Storage Modulus (E') as well as its viscous component by the thermal evolution of the *out-of-phase* Loss Modulus (E''). Moreover, due to the viscous component of the material, a phase shift between stress and strain is observed and it is registered by the DMTA as the phase angle δ, whose tangent (Tan δ) is expressed as the ratio of the loss to the storage moduli (i.e. E''/E'). In a DMTA analysis, the moduli and the Tan (δ) curves offer significant indications about the rigidity of the material. In particular, a decrease of storage modulus is associated with the transition for the material from the glassy to the rubbery behavior. During the transformation, the phase angle (Tan δ) exhibits a peak, whose maximum is conventionally fixed as the value of T_g. As an example, the curves obtained for the 75Eb25BA sample are reported in Fig. 3.7b. It is important to highlight that the T_g measured with DSC and with DMTA usually are different since they are based on the measurement of two different characteristics of the material (thermal capacity and mechanical properties respectively).

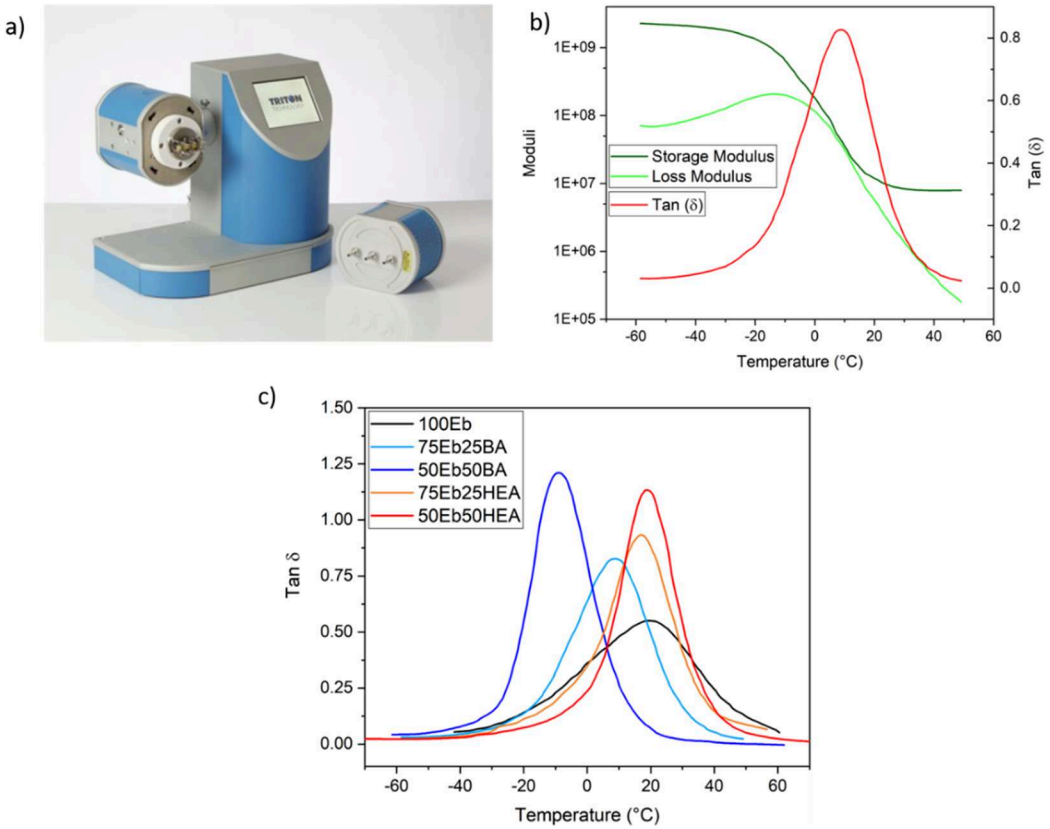

Figure 3.14: Triton dynamic mechanical thermal analysis (DMTA) setup used in the experiments, b) Storage modulus, loss modulus, and Tan (d) curves obtained for 75Eb25BA sample, c) Tan (δ) curves of all the samples tested by DMTA.

UV cured polymeric films (400 μm thickness) were used as samples to check the effect of BA and HEA monofunctional diluents. Tests were performed with a Triton Technology TTDMA (Fig. 3.7a) in strain control (0.02 mm) and with a constant frequency of 1Hz, and a heating ramp of 3 °C/min. The glass transition temperature (T_g) values reported in Tab 3.2 corresponded to the peak of the tan (δ) curve of the tested samples (Fig. 3.7c). As expected, the peak of Tan (δ) is higher in samples containing HEA or BA compared to pristine Ebecryl 8232 resin (Fig. 3.7 c), indicating that the addition of a reactive diluent in the urethane-acrylic formulations provokes a reduction of the cross-linking density in the polymeric matrix [184], [185]. Furthermore, as the amount of reactive diluent increases, the peak of Tan (δ) curves shift to lower temperatures, indicating the decrease of the glass transition temperature in the relative system.

However, the effect on the T_g is different for the two reactive diluents. Butyl acrylate reduces the T_g of the material proportionally to the amount of the added diluent: for instance, the T_g of the pristine formulation (100Eb), which was measured to be 19.7°C, drops to 8.3°C when BA was added at 25 wt% (75Eb25BA) and to -9°C when the concentration of BA was further increased up to 50 wt% (50Eb50BA). This effect has a twofold explanation: on one hand, it is associated with the reduction of the cross-linking density and, on the other hand, to the addition of a low T_g phase which is about -51°C for the Butyl Acrylate. Conversely, the addition of HEA does not significantly affect the T_g of the material (17°C for 75Eb25HEA, and 19°C for 50Eb50HEA samples). This is explained by considering the different chemical structures of HEA and BA (Fig. 3.5). The presence of -OH groups on the HEA chains leads to the creation of hydrogen bonds within the polymeric chains that harden the material counterbalancing the softening effect of the reduction of the crosslinking density.

Table 3.4: Glass transition temperature, gel content, and Elastic modulus of the tested samples varying the amount of the reactive diluent.

Sample	T_g (°C)	Gel content (%)	E (MPa)
100Eb	19.7	96	8.5±0.2
75Eb25BA	8.3	97.5	7.7±1.1
50Eb50BA	-9	97.5	5.5±0.5
75Eb25HEA	17	96.5	8.2±0.1
50Eb50HEA	19	97.5	6.0±0.9

On the cured sample, insoluble fraction (gel%) tests were performed, by extraction in chloroform for 24 hours. This solvent can swell the polymeric matrix and solubilize the unreacted monomers, which leave the sample remaining in the solution. After the specimens were dried in an oven (60°C, 12 hours), and then weighted, comparing the weights of the samples before and after the test. The results showed that the gel fraction, i.e. the insoluble part, slightly increases when BA and HEA were added to the photocurable resin (tab. 3.2). This demonstrates that besides the decrease of the cross-linking density produced by the reactive diluents, the conversion of the groups increased, confirming FT-IR tests. Furthermore, this indicates that the reactive diluent effectively reacted with the acrylate urethane, becoming part of the cross-linked network.

To characterize the mechanical behavior of the UV cured samples, the same Triton Technology TTDMA apparatus was used to perform stress vs strain analysis (Fig. 3.7a). Runs were carried out at room temperature and in load control (1 N/min), measuring the strain in the material (Fig. 3.8). Four samples for each formulation were tested and the elastic modulus values were reported as arithmetical average.

The addition of BA and HEA results in an important decrease of the elastic moduli which is related to the weakening of the cross-linked network and a more flexible material (Tab. 3.2). Besides, owing to the absence of hydrogen bonds within the polymer chains and a lower T_g, the effect on the moduli is more evident in samples containing BA than in those with HEA.

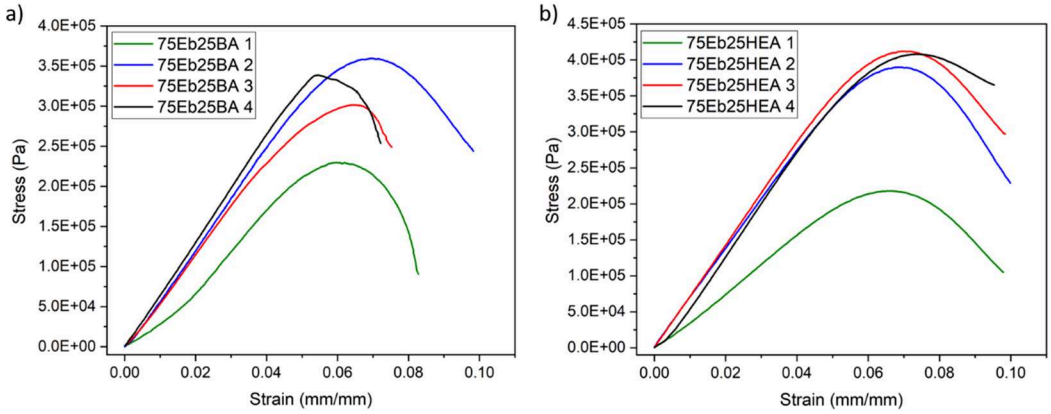

Figure 3.15: Stress vs strain curves of a)75Eb25BA samples, and b) 75Eb25HEA samples.

To conclude this section, two different diluents for Ebecryl 8232 resin were tested, and Butyl Acrylate emerged as the best option. Indeed, samples containing BA showed improved flexibility and softness, maintaining, at the same time, the desirable high polymerization kinetics required for a 3D printing process. On the other hand, also HEA promotes the reduction of cross-linking density but this effect was counterbalanced by the presence of hydrogen bonds that harden the polymeric matrix, while no significant improvements were observed in terms of elasticity and thermomechanical properties.

3.2.3 Optimization of the formulation: the effect of the magnetite nanoparticles

In previous sections, Ebecryl 8232 was selected as photocurable resin and Butyl Acrylate was added as a monofunctional monomer to optimize the reactivity of the formulation and to produce a pseudo-elastomeric material. In this section, the strategy to integrate magnetite nanoparticles in the resin to obtain a vat-printable magneto-responsive polymer is discussed. Magnetic nanoparticles have a crucial role in the production of magneto-responsive soft polymers as they drive the magnetic response of the material. As reported in the literature, the effect of the magnetization is linearly dependent on the amount of magnetic fillers embedded in the polymeric matrix [88], [89], thus high contents of magnetic fillers are desirable. Conversely, the addition of fillers has detrimental effects on materials' reactivity

and mechanical properties as they absorb part of the impinging light reducing/modifying the curing processes.

First, the influences of BA and magnetite nanoparticles on the viscosity of the formulations was investigated by rheological tests using an Anton Paar rheometer Physica MCR 302 (Fig. 3.9a). The plates gap was set at 200 µm and the shear rate was ranging from 0.1 to 100 s^{-1}. Following the behavior of the formulation under increasing shear rates, it was possible to collect data about the viscosity of the system (Fig. 3.9 b). Besides, the same instrument was used to run photorheological tests, by equipping the rheometer with the Hamamatsu LC8 visible lamp with a cut-off filter below 400 nm, and with an intensity of 10 mW cm^{-2}. The light was switched on after 60s to stabilize the system. The shear frequency was set to 1 rad s^{-1} and the temperature was maintained constant at 25°C.

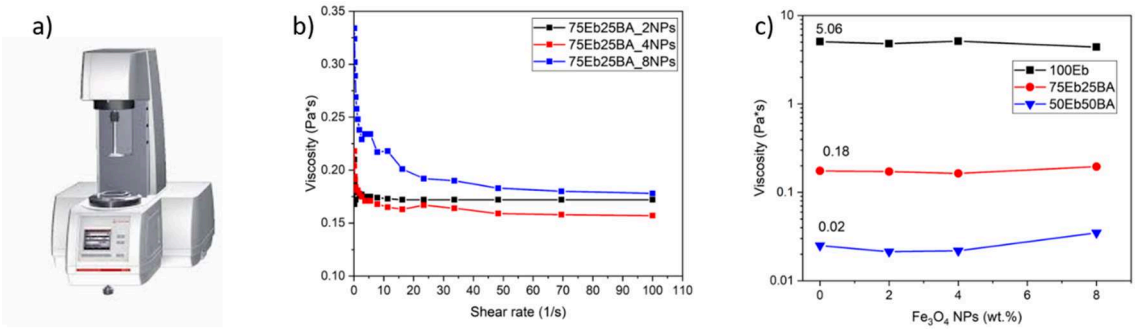

Figure 3.9: A) Anton Paar rheometer Physica MCR 302 used to perform rheology and photorheology tests in this work. B) Viscosity vs shear rate curves of 75Eb25BA formulation with increasing content of NPs. C) Influence of BA and Fe_3O_4 NPs concentration on the viscosity of the formulations.

As reported in the previous section, the addition of the Butyl Acrylate drastically decreases the viscosity of the system of two orders of magnitude for the 50Eb50BA formulation, i.e. from 5.06 to 0.02 Pa s. On the contrary, the addition of Fe_3O_4 nanoparticles (solid phase) does not significantly affect the final viscosity of the system (Fig. 3.9c). Indeed, for the three studied formulations viscosity values remain nearly constant for nanoparticle concentration up to 8 wt.%. The reason for this trend is related to the spherical shape of Fe_3O_4 NPs, which act as lubricant and compensates for the increase of the viscosity due to dispersion of the powder into the formulation [99]. However, the stability of the dispersed fillers is strongly influenced by the viscosity of the resin. Indeed, when the concentration of BA overcomes 50 wt.%, segregation/sedimentation of fillers is observed to occur very

quickly, making the prepared formulations unsuitable for 3D printing. Inversely, formulations having a concentration of BA up to 50 wt% and a loaded content of nanofillers up to 6 wt% have been checked to be stable for at least one hour, which is compatible with a common printing process (Fig. 3.10).

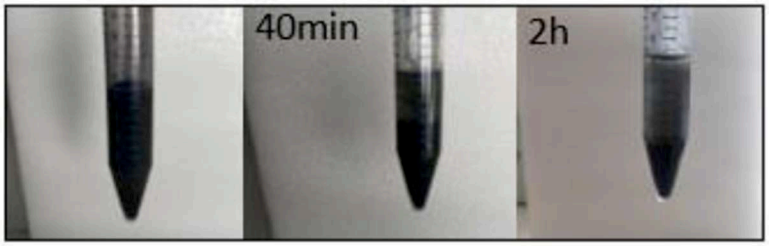

Fig. 3.10: Stability of 50Eb50BA_6NPs formulation after 40 minutes and 2 hours.

The effect of the addition of Fe_3O_4 NPs on the polymerization kinetics was studied by Photorheological tests by following the evolution of the storage moduli during light irradiation (Fig. 3.11). As previously reported by FT-IR analysis, the addition of Butyl Acrylate to the two studied formulations, i.e. 75Eb25BA and 50Eb50BA, enhances the polymerization process. However, when the fillers were embedded a significant delay in the start of the photocuring process was observed. Experimentally this corresponds to the delay between the shining on of the light and the actual increase of the storage modulus. This effect - that was observed to scale with the NPs concentration as shown in Fig. 3.11b and Fig. 3.11d- is ascribed to the competition in absorbing the light of the lamp between the photoinitiator and the magnetic fillers. Indeed, magnetite nanoparticles, acting as additional light-absorption sites, decrease the number of photons available for the photoinitiator. This, in turn, results in a reduction of the generated reactive species (radicals), and thus in the slowing down of the curing photoreactions.

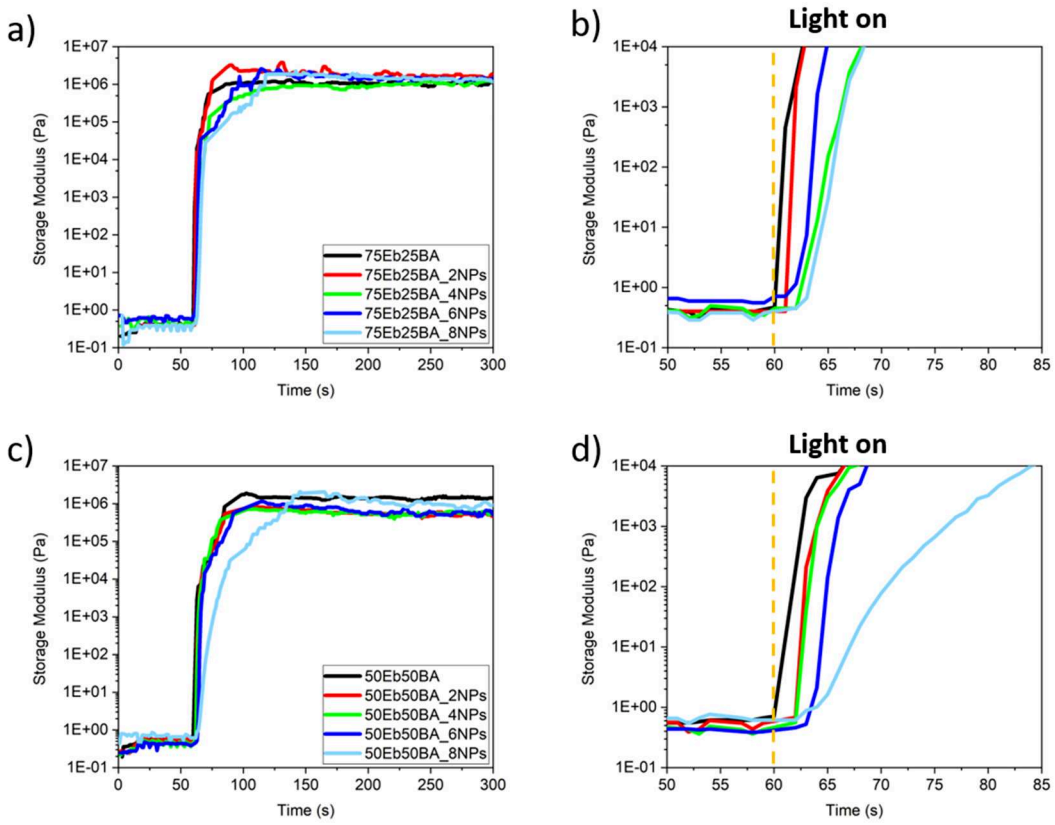

Figure 3.11: Storage modulus versus time curves obtained by photoreology tests. A) 75Eb25BA formulations. B) Zoom in the first seconds of irradiation of 75Eb25BA formulations. C) 50Eb50BA formulations. D) Zoom in the first seconds of irradiation of 50Eb50BA formulations.

3.3 Optimization of the 3D printing parameters

Despite the photo-reactivity of the formulation decreases with the content of embedded fillers, the necessity to print composite materials with a high concentration of magnetic particles remains a mandatory condition for producing high reactive magnetic soft actuators. However, the existing literature reports that the maximum load of magnetic particles in polymers printed by DLP is of the order of 1 wt% [104]. In this section, the strategy developed to increase the amount of dispersed particles in the printable formulations is described. This has been done by using a RobotFactory HD 2.0 as Digital Light Processing (DLP) 3D printer (see section 3.2.1 for the DLP printer characteristics).

First, to facilitate the adhesion between the printing platform and the magneto-responsive composite, a 20 to 50 µm layer of polymer without nanofillers was preprinted. Then, the formulations 75Eb25BA and 50Eb50EA containing up to 8

wt% of Fe_3O_4 NPs were added to the vat and processed maintaining a constant thickness of the layer of 20 μm. The processing parameters are reported in Tab 3.3, where the base exposing time (BET) and object exposing time (OET) represent the processing time for the base and for the object, respectively.

Table 3.3: Processing parameters and glass transition temperature of the 3D printed samples

Sample	Slicing (μm)	Base exposing time (s)	Object exposing time (s)	Tg (°C)
100Eb	50	2.2	1.6	19.7
100BA		*Not Printable*		-51.5[57]
75Eb25BA	50	2	1	4.3
75Eb25BA_2NPs	20	2.9	1.6	3.1
75Eb25BA_4NPs	20	4.4	2	3.3
75Eb25BA_6NPs	20	5.8	2.4	1
75Eb25BA_8NPs	20	9.5	3	-11
50Eb50BA	50	2	1	-6.2
50Eb50BA_2NPs	20	2.9	1.4	-8.4
50Eb50BA_4NPs	20	4.2	1.8	-7
50Eb50BA_6NPs	20	5.5	2.2	-10.7
50Eb50BA_8NPs	20	9.5	3	*Not measured*

As shown in Figures 3.12 a-b, the irradiation time scales with the concentration of added nanoparticles, and the dataset can be fitted with an exponential law:

$$y = y_0 + Ae^{x/t} \quad \text{(Eq. 3.1)}$$

Knowing that the maximum irradiation time per layer is 20 seconds, equation 3.1 can be used to determine the maximum amount of fillers that can be introduced into the resin during the processing step, i.e. up to 12 wt% of Fe_3O_4 nanoparticles. The gap between the extrapolated maximum NPs concentration and the experimental value is not solely related to the competition in absorbing the light between particles and photoinitiator, but also to the deterioration of the mechanical properties of composites as the particle load is increasing.

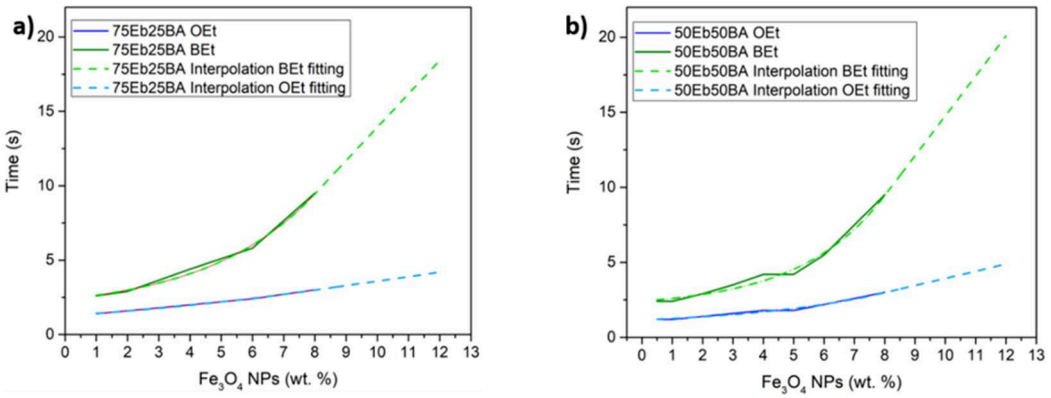

Figure 3.12: 3D printing parameters and interpolation curves by varying the NPs amount of a) 75Eb25BA formulations and b) 50Eb50BA formulations.

Stress-strain tests were performed to evaluate the mechanical properties of the nanocomposites using pure Ebecryl sample (100Eb) as reference. Figure 3.13 shows the evolution of Elastic modulus (E) of the printed samples for the two used formulations: 75Eb25BA and 50Eb50BA. For samples without fillers, the addition of the monofunctional diluent (BA) reduces the value of the elastic modulus from 5.5 to 4.5 MPa. On the other hand, the addition of fillers, up to 6 wt%, results in a slight decrease of E, of the order of 10%, for both the composite samples (75Eb35BA and 50Eb50BA). For larger fillers content, i.e. at 8 wt%, sample 75Eb25BA_8NPs shows a strong reduction of E, probably due to defects produced during the printing process. On the other hand, we did not succeed to print sample 50Eb50BA_8NPs. This is probably due to the poor mechanical properties of the material that prevent the self-standing of the printed objects. For the abovementioned reasons, we fixed the maximum amount of loaded magnetic nanofillers for a 3D printable object to be 6 wt%. Nonetheless, it is worth mentioning that this value is 600% larger than those previously reported in the literature [104].

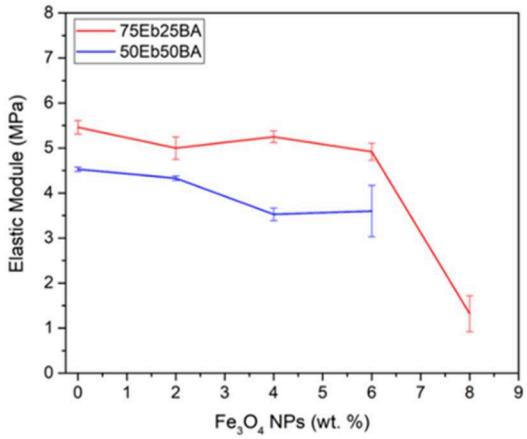

Figure 3.13: Evolution of the Elastic modulus with the NPs concentrations.

The effect of magnetite nanoparticles on the thermo-mechanical properties of the printed object was investigated by dynamic mechanical thermal analysis (DMTA) on rectangular samples (50 x 5 x 2 mm^2). As reported in Tab 3.3 and in Fig 3.14, the T_g of the composite remains nearly constant up to 4 wt% of Fe_3O_4 powders, while above this value the T_g starts to decrease. This effect is due to the reduction of the double bond conversion related to the competitive light absorption between fillers and photoinitiators.

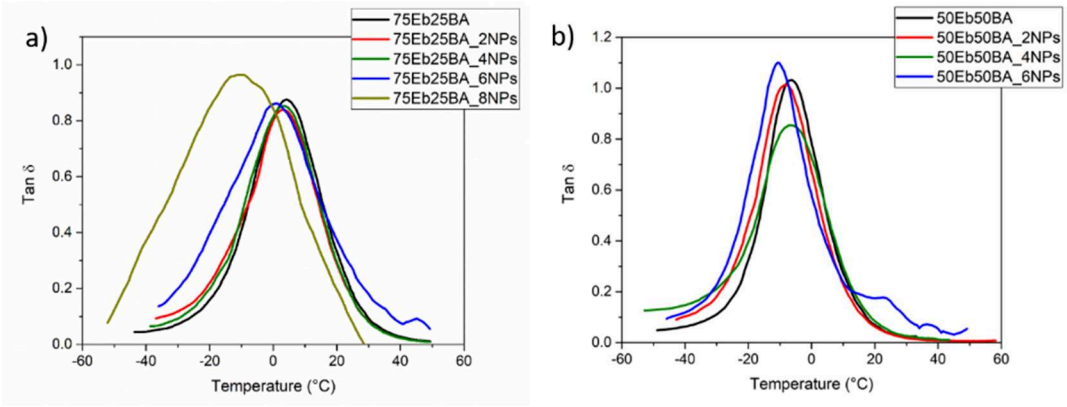

Figure 3.14: Thermal evolution of tan(δ) curves for a) 75Eb25BA and b) 50Eb50BA formulations for increasing amount of Fe_3O_4 nanoparticles

To develop magneto-responsive polymers with a homogeneous magnetic response, a good dispersion of the embedded magnetic particles within the polymeric matrix is the key factor. Thus, the surface topography of a 12 µm thick polymeric films coated on a microscope glass slide by a wire wound bar has been checked using an Olympus BX 53 M optical microscope equipped with 2.5x, 10x, and 50x ocular lenses. In addition, the dispersion, distribution, and agglomeration of the embedded Fe_3O_4 nanoparticles has been studied using a Field Emission

Scanning Electron Microscopy (FESEM) on cryo-fractured 3D printed samples. Four systems have been analyzed with different concentration of BA diluent and magnetic particles: 75Eb25BA_2NPs, 75Eb25BA_8NPs, 50Eb50BA_2NPs, and 50Eb50BA_6NPs, Fig. 3.15. All the tested systems present a good dispersion of nanofillers. However, for sample 50Eb50BA small aggregates were observed, which is probably due to the lower viscosity of the resin making it hard to homogenize the dispersion of the particles.

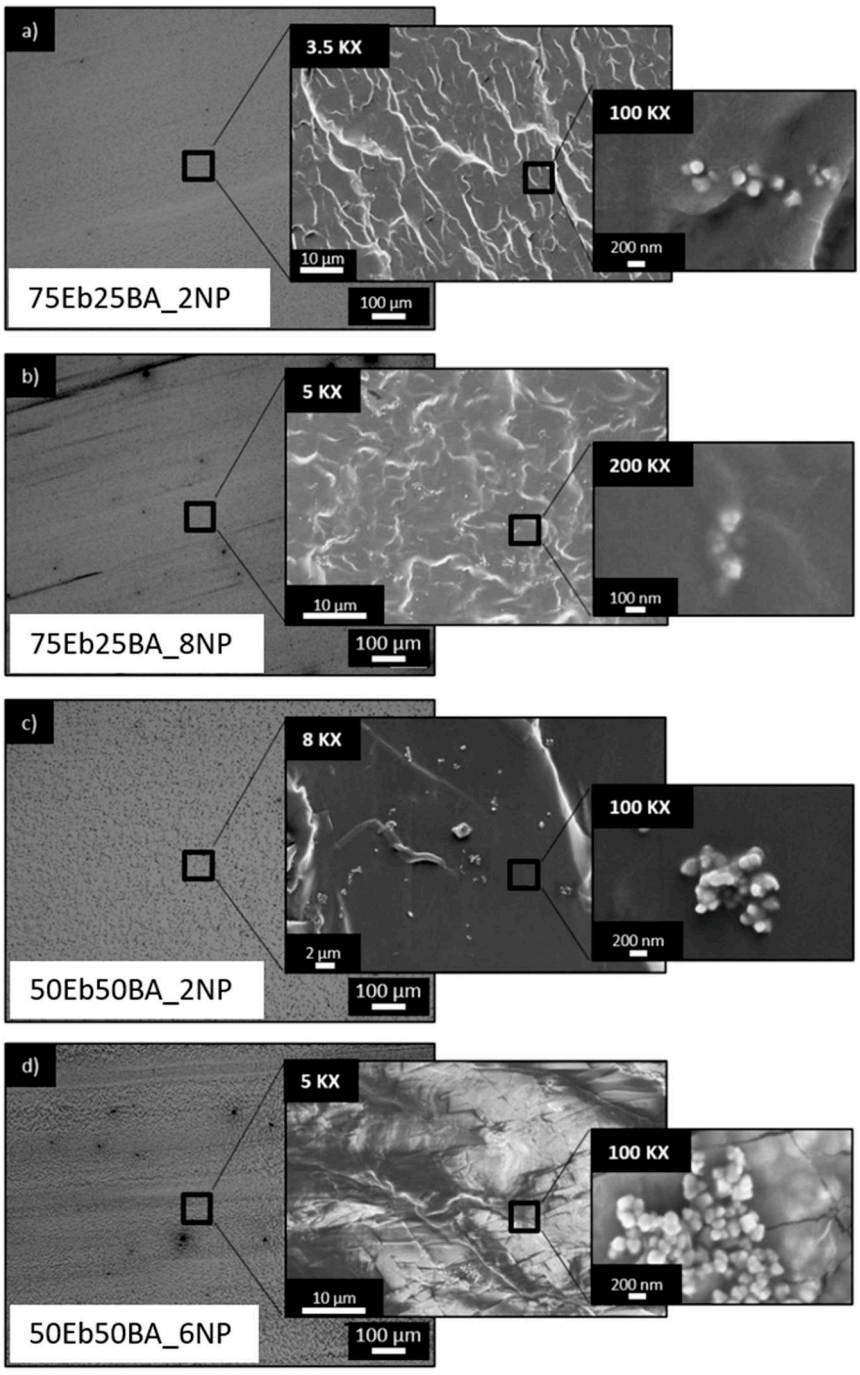

Figure 3.15: Optical microscope images taken of a) 75Eb25BA_2NPs, b) 75Eb25BA_8NPs, c) 50Eb50BA_2NPs, and d) 50Eb50BA_6NPs formulations. In the insets, FESEM images at different magnification values are reported.

Table 3.3 summarizes the experimental conditions used to optimize both the properties of the photocurable resin and the process parameters for 3D printing. In particular, the high concentration of magnetic particles, up to 6 wt%, in 3D printed objects was obtained by exploiting two features: i) the use of Butyl Acrylate as

reactive diluent allows to enhance the photo-reactivity of the resin and, in turn, to introduce higher concentration of magnetic fillers within the printable formulation. ii) the use of a light projector emitting in the visible range allows to reduce the absorption coefficient, of Fe_3O_4 nanoparticles, Q_{Fe2O3}. Indeed, the value of Q_{Fe2O3} in the visible range of the optical spectrum is much lower (about 2 x 10^5 cm^{-1}) than in the UV range (about 5 x 10^5 cm^{-1}) [186]. This increases the amount of light that is available for the photoinitiator to set in the curing process.

3.4 Magnetic properties of 3D printed samples

When magneto-responsive polymers are exposed to an external magnetic field, the magnetic force exerted on the sample is proportional to the volume of the material (V), its magnetization (M), and the magnetic field gradient (H). The magnetic force can be written as:

$$F_{mag} = MV(\nabla H) \quad \text{(Eq. 3.2)}$$

Hysteresis curves can be used to describe the magnetic response of the material as a function of the applied external magnetic field. Thus, the magnetic properties of 3D printed 75Eb25BA and 50Eb50BA samples were measured by investigating hysteresis loops at room temperature as a function of the load of magnetic particles, whose values have been measured using the thermogravimetric (TGA) analysis. TGA experiments were performed testing 20 mg of material with a TGA/SDTA-851 (Mettler) (Fig. 3.16a). During the experiment, the samples were exposed to air atmosphere (50 mL/min) to a heating ramp of 10°C/min varying from 25°C to 800°C. During the test, the material was constantly weighted, to investigate the effect of the thermo-oxidation induced by the high temperatures. After the measurement, pristine polymeric samples show approximately 100% loss of their weight (black curves Fig. 3.16 b and c) which is due to the evaporation of the degradation products. On the contrary, samples containing Fe_3O_4 NPs always showed a residual weight at the end of the curve which is proportional to the NPs content. This indicates that the residual weight measured is due to the presence of the NPs which have not been degraded during the test. By measuring the residual mass of the sample, it was possible to estimate the amount of NPs embedded in the

polymeric specimen, and a good correlation was found between the nominal NPs concentration and those measured by TGA analysis.

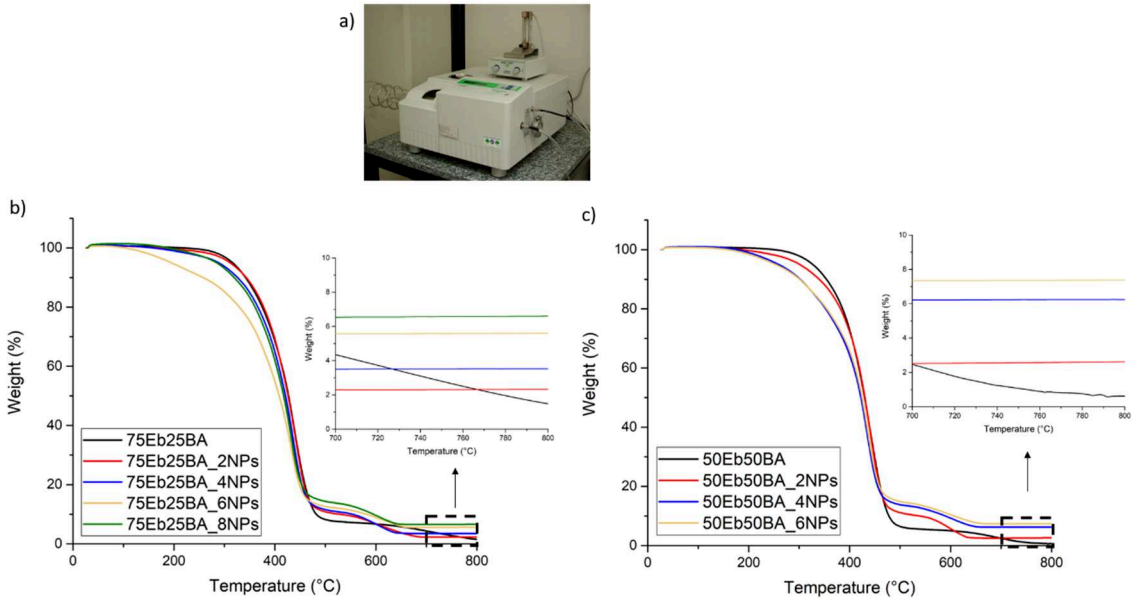

Figure 3.16: A) DSC apparatus used in this work. Thermogravimetric (TGA) curves of b) 75Eb25BA and c) 50Eb50BA samples. The inserts are the zoom of TGA curves in 700°C-800°C range.

Hysteresis loops were obtained by using a vibrating sample magnetometer (Lakeshore 7400) where the specimens were mounted on a quartz holder and exposed to a magnetic field ranging between -17 kOe and 17 KOe. These experiments were performed in collaboration with Dr. Paola Tiberto and Dr. Gabriele Barrea from Istituto Nazionale di Ricerca Metrologica (INRIM). The measured magnetization, M, of the 3D printed magneto-responsive polymers was determined by normalizing the magnetic momentum of the sample to its mass. Magnetization curves of Figs. 3.17a-b show the same features in terms of hysteretic and reversal behavior. This is compatible with the presence of magnetic fillers having a size between 50 nm and 100 nm and presenting a multi-domain configuration. As expected, the magnetization of the material (M) increased with the content of the magnetic filler and the polymeric matrix did not play any role in the magnetization (Fig. 3.17c). Indeed, for both the matrices M scales with the concentration of Fe_3O_4, (75Eb25BA squares and 50Eb50BA circles), in agreement with the existing literature [88], [89], a linear correlation between the measured magnetization M, taken at the maximum applied field (H = 17 kOe), and the fillers concentration was observed. Moreover, magnetic coercivity was measured to be about 120 Oe in all the printed samples. This result indicates that for the two 3D

printed matrices, the magnetic volume responds coherently to the application of an external magnetic field [187]. This result is in agreement with optical and FESEM analyses showing that the distribution of nanoparticles in the polymeric matrix is nearly homogeneous, with only a small fraction of visible aggregates.

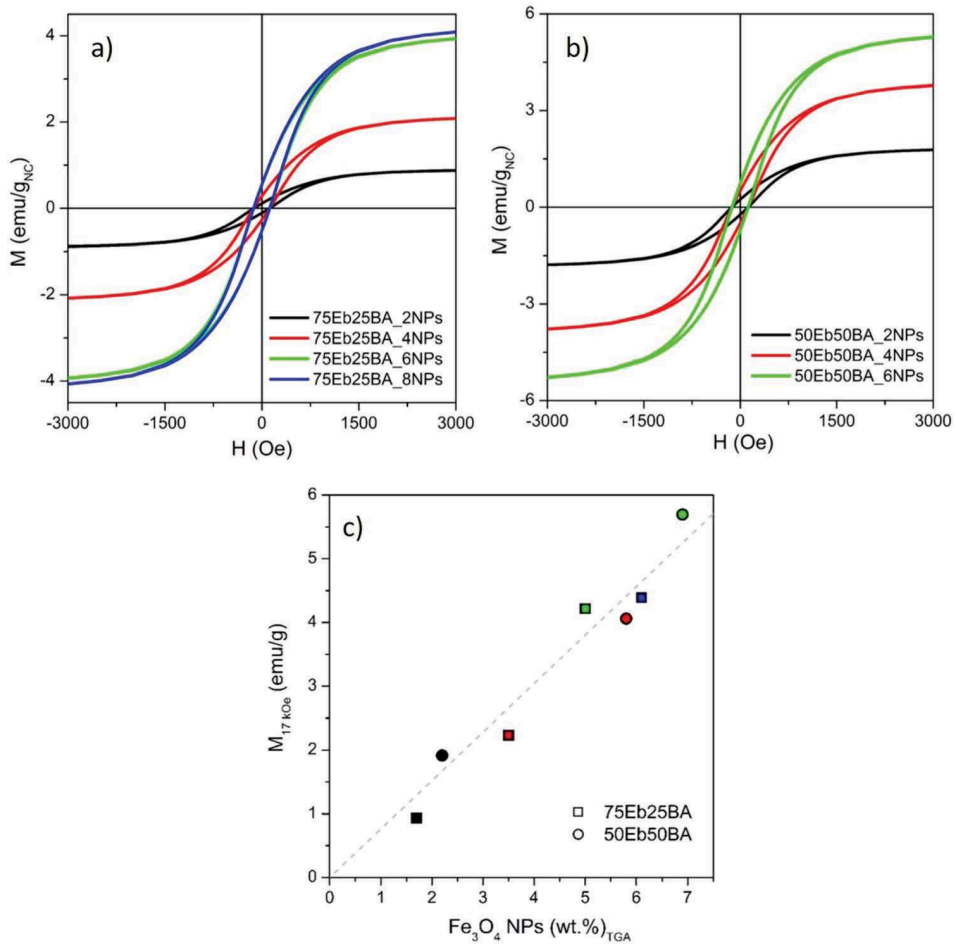

Figure 3.17: Room temperature hysteresis loops for a) 75Eb25BA and b)50Eb50BA samples with several magnetic particles concentrations. C) Magnetization vs NPs concentration trend observed for 75Eb25BA (squares) and 50Eb50BA (circles) samples. The nanoparticles concentrations were measure by TGA. The dotted line is a guide to the eyes.

3.5 3D printing of magneto-responsive nanocomposite polymers with dispersed Fe_3O_4 nanoparticles

Before starting the printing of magneto-responsive nanocomposites, the achievable x-y plane resolution for the optimized formulations was determined using the RobotFactory HD 2.0 DLP. This was done by printing holes and pillars structures of progressively smaller dimensions from 4 mm to 0.2 mm (Fig. 3.18 a). The physical dimensions of the printed objects (Fig. 3.18 b-c), were measured by

optical microscopy and compared with the elements of the CAD file. On the other hand, the possibility to obtain complex-shaped objects and hollowed structures was evaluated by 3D printing honeycomb structures as shown in Fig. 3.18 d-g. From the inspection of the optical images, a good CAD fidelity was observed in the printed objects, and a resolution of about 400 µm was found for the formulations loaded with the highest amount of magnetite nanoparticles.

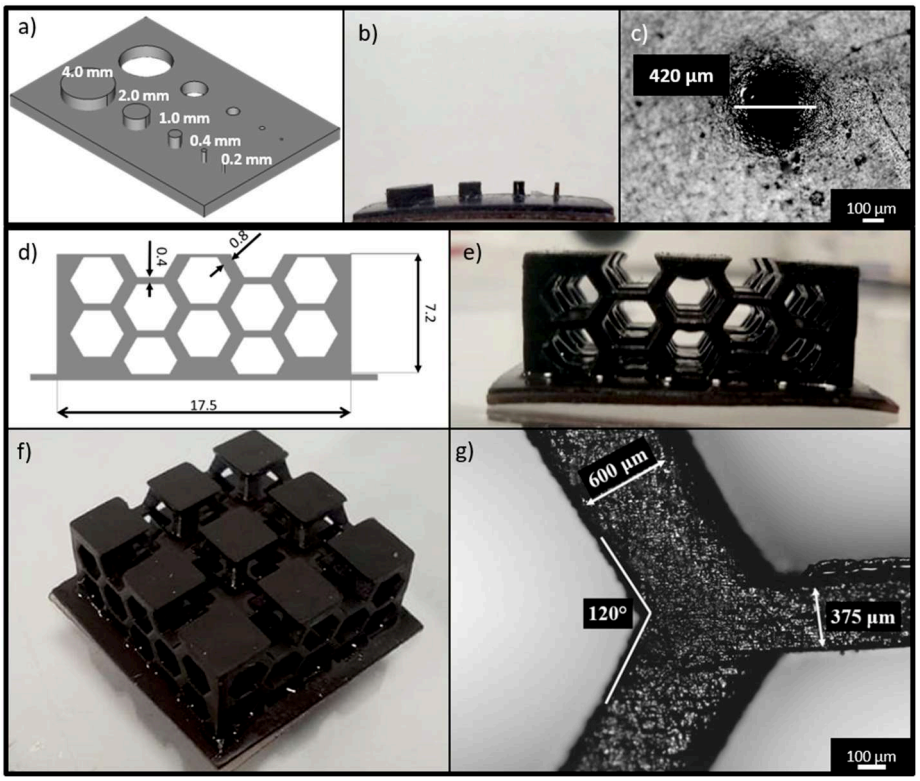

Figure 3.18: a) CAD file of the pillars-holes structure and its dimensions, b) pillars-holes 3D printed abject and c) particular of the smallest 3D printed hole (scale bar is 100 µm). d) Lateral CAD face of the honeycomb structure and its dimensions, and e) corresponding lateral face of the 3D printed objects. f) Whole 3D printed honeycomb structure, g) optical image and dimensions of a honeycomb section taken by optical microscopy (scale bar is 100 µm).

Besides, a first estimation of the flexibility and toughness of the material was checked on a 500 µm thick 3D printed film by submitting the film to cyclic bending and twisting as shown in Fig. 3.19. The printed materials demonstrate good flexibility and toughness without showing any failure or damages, regardless of BA diluent or Fe_3O_4 fillers concentration.

Figure 3.19: Cyclic bending and twisting to check the resistance to damage of the printed film.

Finally, to validate the proposed approach, several magneto-responsive polymers were printed showing different types of movements when exposed to magnetic fields. In particular, as a proof of concept we investigated: (i) rolling, (ii) translation, (iii) stretching, (iv) shape-shifting, and (v) folding/unfolding.

Motions, like rolling and translation, do not involve shape transformation as the movement is associated with the object as a whole. As the mechanical properties of the composite polymer are not a critical issue, these structures are easy to be obtained. Although 50Eb50BA and 75Eb25BA formulations can both be used to print objects to perform translation and rotation movements, the stiffer formulation, i.e. 75Eb25BA, gave better results in terms of field-induced motion.

The rolling response was investigated by 3D printing wheels and spheres (Fig. 3.20 a,b) and exposing them to external magnetic fields whose intensity has been measured to be 300 mT at the surface of a permanent NdFeB magnet. It is observed that already a content of 2 wt% of Fe_3O_4 NPs is sufficient to activate and control the roll motion of the wheels and spheres.

The translation motion has been demonstrated in a wet environment, by immerging a cone-like object in a tube filled with water (Fig. 3.20 c). Again, specimens containing 2 wt% of magnetic fillers were remotely controlled using a permanent magnet external to the pipeline.

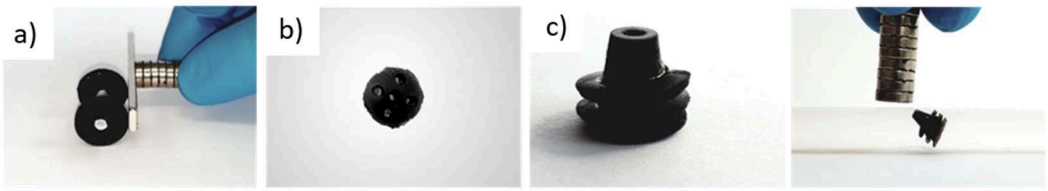

Figure 16: Examples of rigid magneto responsive objects: a) wheels, b) sphere, and c) cone-like object remotely controlled when immersed in a water pipeline.

On the other hand, more complex transformations, such as shape-morphing and folding/unfolding, require deformation of the printed object itself, thus the softness and flexibility of the polymeric matrix play a crucial role. For this reason, 50Eb50BA formulation was selected because compared to 75Eb25BA formulation presents lower values of T_g and elastic moduli, and a reduced cross-linking density, leading to softer printed objects.

First, planar springs were 3D printed to analyze the effect of nanoparticles content on the magnetic driven transformations. As shown in Fig. 3.21 a and Fig.

3.21 b the magnitude of deformation is much higher in specimen 50Eb50BA_6NPs than in 50Eb50BA_2NPs one. If the main reason for this different behavior is doubtless the higher magnetization in the 50Eb50BA_6NPs sample, due to the enhanced concentration of Fe_3O_4 NPs, other effects must be considered. As previously discussed, NPs do not only affect magnetic properties, but also the mechanical performance of the composite material. In particular, high concentrations of magnetite nanoparticles lead to a significant reduction of the elastic modulus and T_g resulting in a softer polymer. Thus, the higher load of nanoparticles enhances both the magnetization and the softness of the spring.

Shapeshifting and folding/unfolding motions have been studied considering 50Eb50BA_6NPs formulation. Indeed, the printed material possesses the appropriate toughness and magneto-mechanical response.

Fig. 3.21 c shows a blossom-like behavior of a 3D printed flower when exposed to an external magnetic field represented by 6 stacked cylindrical magnets. This example resumes several actuation modes exploited in engineering applications such as clamps and holders which have proven to be interesting in industrial design and soft-robotics [104].

In the last example, a cross-like planar structure able to shape-shift through folding/ unfolding movements into a 3D cube was printed Fig. 3.21 d. The sample was obtained by stacking pristine polymer elements (without NPs) to the magneto-responsive cross-like base printed with 50Eb50BA_6NPs formulation. This solution allowed to strengthen the walls of the cube during the folding/unfolding processes.

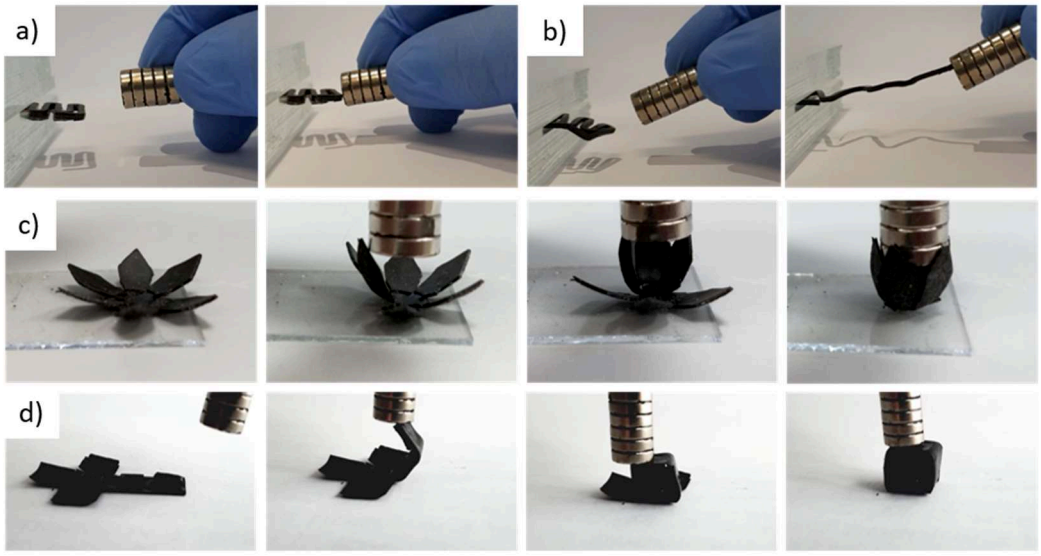

Figure 17: Different shape transformation of a nanocomposite spring exposed to a magnetic field according to the polymer matrix a) 75Eb25BA_6 NPs, and b) 50Eb50BA_6 NPs. Examples of objects undergoing complex shape transformations, c) flower with a blossom-like behavior, and d) planar multi-material structure folding in a 3D cube.

3.6 Conclusions

In this chapter, we described the fabrication of magneto-responsive polymers with randomly dispersed magnetic fillers through DLP 3D printing. The formulations used were based on urethane-acrylate resins loaded with Fe_3O_4 nanoparticles. The mechanical properties and the photopolymerization kinetic of the photocurable formulation have been adjusted by diluting the urethane-acrylate resin with monofunctional butyl acrylate; while the load of NPs has been used to control the magnetic response of the specimen, which is simply proportional to the NPs concentration and only slightly affected by the formulation. We demonstrated that the optimum formulation is suitable for 3D printing and that the printed objects present a resolution of 400 mm up to 6 wt% of fillers and a good fidelity compared to the CAD file. However, for larger load values of fillers, i.e., 8 wt%, the reactivity of the photo-polymerization process is strongly reduced due to the competition between the photoinitiator and the nanofillers in absorbing the impinging light. This results in poor mechanical properties of the final object which are not compatible with the 3D printing process. Finally, as a proof of concept, several types of magnetic-driven movements have been probed: (i) rolling, (ii) translation, (iii) stretching, (iv) shape-shifting, and (v) folding/unfolding.

4.

Self-assembly of Fe_3O_4 NPs dispersed in photocurable resins and investigations on the rotation of the assembled chains

4.1 Introduction & motivation of the work

In the previous chapters, we demonstrated the fabrication of magneto-responsive polymers by a DLP 3D printing technique. The produced devices exhibit shape-morphing behavior when exposed to external magnetic fields, showing elongation, bending, and folding/unfolding movements. Despite the important goal achieved, we wanted to improve the control and the programming of the actuation motion of the composite materials. This can be achieved by programming the microstructure of the nanocomposites during the 3D printing process, which in turn may induce magnetic anisotropy in the material. Recently, the exploitation of self-assembly processes typical of magnetic particles emerged as an accessible route to fabricate composite materials with programmable microstructural organizations [175], [188]–[192].

As a generical consideration, the term "self-assembly" is intended for all those processes that spontaneously bring a disordered system into an organized structure due to the local interactions between the components [193], [194]. In material science, this is promoted by the reduction of the free-energy of the system which

leads to the self-construction of the microstructure. It is important to note that the assembled configuration must have a grade of order higher than the starting configuration, thus spontaneous aggregation processes as the precipitation cannot be considered as a self-assembly process.

With regards to soft-magnetic nanoparticles, such as the Fe_3O_4 NPs used in this work, we exploited here a specific example of the self-assembly process, in which magnetic particles spontaneously organize in chain-like structures. As in a common laboratory experience, when magnetic powders are placed nearby a magnet, they spontaneously arrange along the magnetic field lines (Fig. 4.1a). The same experience performed between two magnets evidences an organization of the magnetic particles along the lines of the magnetic field, forming parallel chains (Fig. 4.1b). A magnetic chain is composed of several lined-up particles with aligned magnetic moments [164], [166], [169], [195], [196]. This configuration produces a favorable magnetic axis along the major axis of the chain inducing a strong magnetic anisotropy in the aggregate [197].

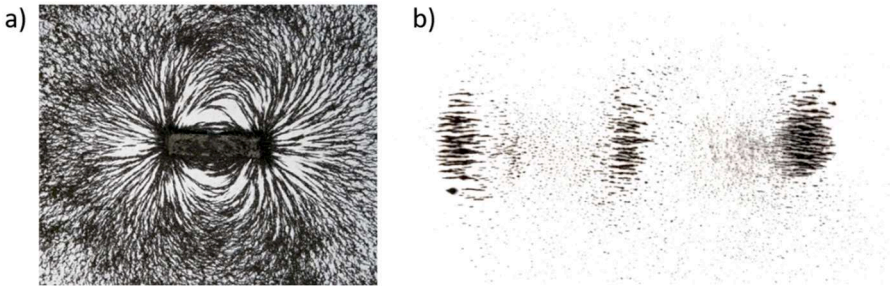

Figure 4.18: a) Distribution of magnetic powders along the magnetic field lines generated by a permanent magnet. B) scheme of the distribution of magnetic particles in the case of a couple of permanent magnets.

This assembling process is indeed known for many centuries, but recently it was investigated in detail by several research groups. As the driving force for these researches was the production of electronic and spintronics devices, many studies focused only on the fabrication of superparamagnetic mono-atomic chains [164]–[167], [169], [173], [195]–[201]. More recently, the interest in magneto-responsive composite materials further boosted these investigations. The idea is to incorporate the assembled magnetic structures within a polymeric matrix so that the obtained composite possesses a programmable microstructure consisting of the magnetic

chains and a controlled magnetic anisotropy derived from the easy magnetic axis of the chains [175], [190], [191].

The most investigated approach to embed the magnetic chains in a soft-polymer consists of a three-step procedure (Fig. 4.2). i) Dispersing the magnetic particles in a liquid photocurable resin. ii) Expose the mixture to an external magnetic field to produce the magnetic chains, and iii) activate the photopolymerization processes to freeze the microstructure within the polymer matrix.

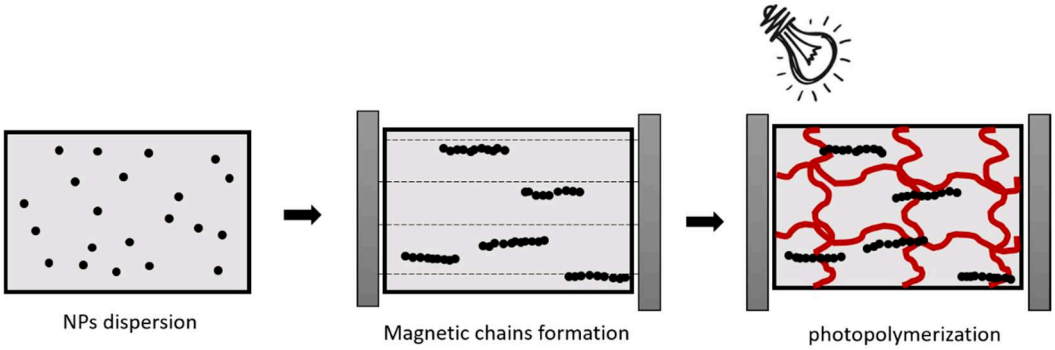

Figure 4.19: Procedure to incorporate self-assembled magnetic chains in a photocurable polymer.

Up to now, this procedure was mainly applied to produce polymeric films with controllable magnetic anisotropy [175], [192]. When a magnetic field is applied to an anisotropic magnetic material, the magnetic chains are forced to re-orient along the magnetic field lines; according to the magnitude of the exerted magnetic torque, the whole composite is subjected to forces that may produce rotation or bending motions to re-align its magnetic easy-axis to the external field. Example in literature shows that exploiting the local magnetic properties of the films, it was possible to produce magnetic torques on the material and control its rotation and bending applying uniform magnetic fields (Fig. 4.3).

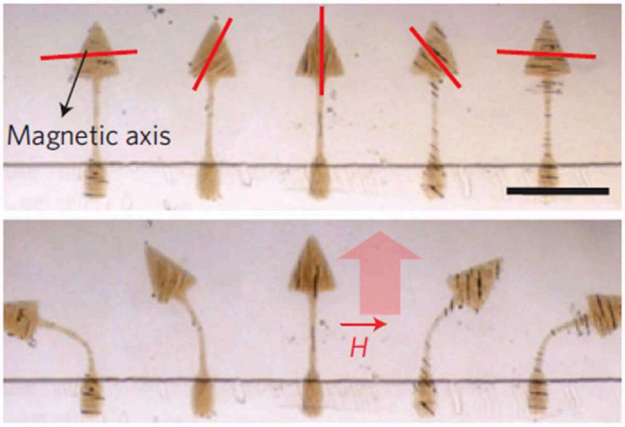

Figure 4.3: Examples of bending control in magnetically anisotropic soft-actuators [175].

The strategy proposed in this Chapter aims to take advantage of the self-assembly of magnetic particles to 3D print composite materials with programmable microstructures and magnetic anisotropy. Because 3D printing is a layer by layer technology, this goal can be achieved by controlling in every layer the chain formation, repeating the aforementioned control over them in 2D. To predict the obtainable microstructures, both experimental tests and physical models were developed. In particular two phenomena were investigated: i) The magnetic chains formation via self-assembly, and ii) The rotation of magnetic chains when the direction of the applied field is varied. First, the mechanisms of self-assembly were investigated at the nanoscale by means of Scanning Transmission X-Ray Microscopy (STXM). Then, the average behavior of the magnetic particles' dispersion was observed at the microscale via optical microscopy, investigating the influence of external parameters such as the magnetic field intensity, the nanoparticles concentration, and the viscosity of the photocurable monomers on the size of the assembled magnetic chains. In the second part of this chapter, the rotation of the magnetic chains was investigated by optical microscopy, and the results obtained were compared with the proposed theoretical model varying the direction of the applied field was studied.

This approach allows to have a deeper control over the self-assembly process of magnetic nanoparticles dispersed in photocurable resins. By implementing this approach in a DLP 3D printing process it may be possible to control the magnetic microstructure of each printed layer leading to the fabrication of magneto composite

materials with programmable microstructural organizations and tunable magnetic properties, as it will be discussed in Chapters 5 and 6.

4.2 Physical considerations of the self-assembly process

First, the main physical aspects governing the self-assembly process of magnetic particles will be described.

For the sake of clarity, a graphical explanation of the self-assembly process is given in Fig. 4.4. When magnetic nanoparticles are dispersed into a liquid medium, the particles remain isolated or form clusters due to Van der Waals interactions (Fig. 4.4 a). However, when a magnetic field is applied (H≠0), the particles get magnetized, and their magnetic dipoles arrange in the same direction as the applied magnetic field (Fig. 4.4 b). Lately, due to the magnetic interactions produced by this new configuration, the particles start to migrate within the medium to assemble in chain-like structures (Fig. 4.4 c) minimizing the free-energy of the system.

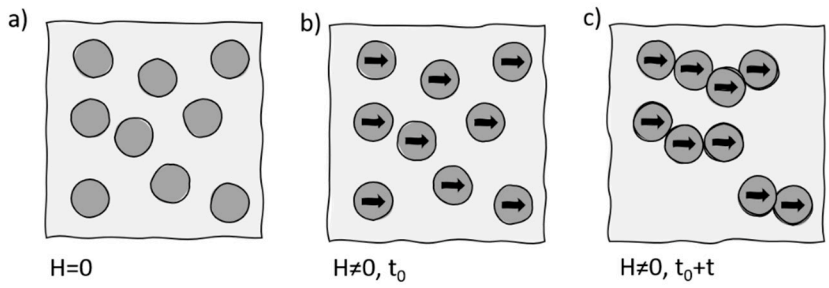

Figure 4.4: Formation of self-assembled magnetic chains starting from magnetic particles.

For a correct description of the process, in addition to the magnetic interactions between particles, also Brownian motion, Van der Waals forces, and electrostatic repulsions should be taken into account. However, the self-assembly process can be simplified as the competition between magnetic dipolar interactions and thermal fluctuations. In particular, the dipolar interactions must overcome the contributes of the thermal fluctuations, limiting the Brownian motion of the particles which opposes the formation of ordered chain structures [166]. An analytical representation of this competition is given in eq. 4.1, where the dipole coupling constant (λ) is expressed as the ratio between the magnetic and the thermal

contribution. This must be higher than 2 to obtain a head-to-tail configuration of the magnetic moments necessary to the chains assembling [166].

$$\lambda = \frac{\mu_0 m^2}{(4\pi k_B T \sigma^3)} > 2 \qquad \text{(eq. 4.1)}$$

Where μ_0= 4x10^{-7} JA^{-2}m^{-1}, m is the magnetic moment, k_B is the Boltzmann constant, T is the temperature (K), and σ is the diameter of the particle.

As shown by equation 4.1 the magnetic moment of the particles has a crucial role in the self-assembly process, and the higher the magnetic moment, the greater will be the magnetic interactions between the particles. The magnetic moment depends both on the general magnetic properties of the material and on the diameter, the grade of crystallinity, and the size distribution of the particles [201]. However, considering a magnetic particle as a magnetic dipole, its magnetic moment can be written as the product of the saturation magnetization (M_s) and volume of the particle (V) (eq. 4.2).

$$m = M_s \cdot V \qquad \text{(eq. 4.2)}$$

Thus, the interaction energy between two particles (U_{dd}) can be written as the interaction energy of two magnetic dipoles $\mathbf{m_1}$ and $\mathbf{m_2}$ placed at a distance of $\mathbf{r_{12}}$ (eq. 4.3). Bold letters are vectors.

$$U_{dd} = \frac{\mu_0}{4\pi|\boldsymbol{r_{12}}|^3}\left\{\boldsymbol{m_1}\cdot\boldsymbol{m_2} - \frac{3}{|\boldsymbol{r_{12}}|}(\boldsymbol{m_1}\cdot\boldsymbol{r_{12}})(\boldsymbol{m_2}\cdot\boldsymbol{r_{12}})\right\} \qquad \text{(eq. 4.3)}$$

The magnetic interaction between two particles inversely depends on their distance as it scales as r^3, so the closer the particles are, the greater their magnetic interaction will be. Nevertheless, also the magnetic moments of the particle play a crucial role, and not only in terms of their modulus but also in terms of their direction. In fact, in eq. 4.3 a dot product of the magnetic moment vectors is reported ($\boldsymbol{m_1}\cdot\boldsymbol{m_2}$), which value is maximum when the two vectors have the same direction. In the presence of an external magnetic field, the magnetic moments of the particles are parallel and aligned, and this condition enhances the magnetic interactions between neighboring particles favoring self-assembly.

4.2.1 Physical models of the self-assembly process in the Literature

Owing to the complexity of the system and the large number of competitions involved in the process [166], [197], [198], there is not a rigorous theoretical model that can completely describe the magnetic-induced self-assembly behavior. However, several physical models of the self-assembly process of magnetic particles are reported in the literature [167], [173], [198], [201] describing specific phenomena occurring during the self-assembly of magnetic particles.

In particular, Bertoni et Al [167] developed a theoretical model to describe the self-assembly process of superparamagnetic nanoparticles of diameter d_0 and capped with a steric layer of thickness δ dispersed in a liquid medium and exposed to an external magnetic field. The simulations were performed with the Monte Carlo method based on the Metropolis algorithm by calculating the sum of four different energetic terms for a system of N particles dispersed in a 2D box.

1) The single-particle energy (U_i^H) was expressed as follows (eq. 4.4):

$$U_i^H = -KT\xi_i n_i \cdot \boldsymbol{H}/H + K_i(1 - (\mathbf{n_i} \cdot \mathbf{a_i})^2) \quad \text{(eq.4.4)}$$

Where K_i is the anisotropy barrier, a_i is the easier magnetization direction, and ξ_i is a dimensionless parameter.

2) The dipolar magnetic interactions U_{ij}^m between particles was described as (eq. 4.5):

$$U_{ij}^m = KT\lambda_{ij}\frac{d_0^3}{r_{ij}^3}\{\mathbf{n_i} \cdot \mathbf{n_j} - 3(\mathbf{n_i} \cdot \mathbf{t_{ij}})(\mathbf{n_j} \cdot \mathbf{t_{ij}})\} \quad \text{(eq. 4.5)}$$

Where λ_{ij} is a dimensionless parameter which takes into account the dipole coupling constant (λ) reported in eq. 4.1.

3) The particles repulsion due to the capping layers U_{ij}^v (eq. 4.6):

$$U_{ij}^v = \frac{2\lambda_{vi}KT}{2}\left(2 - \frac{2C_i}{t_{\delta i}} ln\left(\frac{t_{\delta i}+1}{C_i}\right) - 2\frac{C_i - 1}{t_{\delta i}}\right) + \frac{2\lambda_{vi}KT}{2}\left(2 - \frac{2C_j}{t_{\delta i}} ln\left(\frac{t_{\delta i} + d_j/d_i}{C_j}\right) - 2\frac{C_j - d_j/d_i}{t_{\delta i}}\right) \quad \text{(eq. 4.6)}$$

Where λ_{vi} is a dimensionless parameter that considers the number of nanoparticles in the system and their dimensions. C_i and C_j are also constants deriving from the dimension of the particles and referred to particle *i* and *j* respectively. And $t_{\delta i}$ is the ratio of the steric layer thickness on the particle radius ($t_{\delta i} = 2\delta/d_i$).

4) The last energetic contribution was given by the attractive forces of Van der Waals interactions (U_{ij}^{VdW}), and it was described as follows (eq.4.7).

$$U_{ij}^{VdW} = \frac{A}{6}\left(\frac{2R_iR_j}{r_{ij}^2-(R_i+R_j)^2} + \frac{2R_iR_j}{r_{ij}^2-(R_i-R_j)^2} + ln\left(\frac{r_{ij}^2-(R_i+R_j)^2}{r_{ij}^2-(R_i-R_j)^2}\right)\right) \qquad \text{(eq.4.7)}$$

A is the Hamaker constant, and R_i and R_j are the radius of the particles *i* and *j* respectively.

This physical model did not take into account the viscosity of the system, but fixing the NPs concentration at 0.1, the authors qualitatively evaluated the effect of the dimension of the particles and the capping layer on the assembled magnetic chains by varying the intensity of the applied magnetic field [167]. However, also other parameters are expected to influence the dimensions of the assembled chains, and these are discussed in the next paragraph.

4.2.2 The effect of external parameters

In the next parts of this chapter, the influence of several parameters on the self-assembly process was experimentally investigated. In particular, we investigated three aspects that may influence the mobility and the spontaneous aggregation of the particles: i) magnetic field intensity, ii) NPs concentration, and iii) viscosity of the medium.

The **magnetic field** can be considered as the driving force of the entire self-assembly process because it induces the magnetization of the particles and the alignment of their magnetic moments. The linear relationship between the magnetization of the material (*M*) and the magnetic field applied (*H*) is reported in (eq. 4.8):

$$M = \mu_0(1+\chi)H \qquad \text{(eq. 4.8)}$$

μ is the magnetic permeability in vacuum, and χ is the magnetic susceptibility of the material. Eq. 4.8 shows that the higher the magnetic field, the higher is the

magnetization of the material. Thus, using this expression of the magnetization on equation 4.2, it is possible to define the magnetic moment of the particle as:

$$m = \mu_0(1 + \chi)H \cdot V \qquad \text{(eq. 4.9)}$$

Equation 4.9 shows that the magnetic moment of the material is proportional to the applied magnetic field. Thus, varying the intensity of the external magnetic field is possible to modify the values of the magnetic dipoles. As the magnetic interaction energy U_{dd} is proportional to the magnetic moments of two particles (m_1 and m_2 in eq. 4.3), the intensity of the external magnetic field has a strong influence on the self-assembly process.

The **NPs concentration** indirectly influences the average distance between two particles (r_{12}) reported in eq. 4.3. Andreev et Al. [199] estimated that the mean distance between the centers of two particles (r) in a randomly distributed system can be written as (eq. 4.10):

$$r = \Gamma\left(\frac{4}{3}\right) 4\pi N_0^{-1/3} = 0{,}5540 N_0^{-1/3} \qquad \text{(eq. 4.10)}$$

Where $\Gamma(4/3)$ is the value of gamma function for an argument of (4/3) and N_0 is the numerical density of particles that expresses the number of particles per unit of volume of the system. As the average distance between particles is related to the concentration of fillers, the latter influences the magnetic interaction between particles because U scales with r^3 (see eq. 4.3).

Finally, the **system viscosity** is not present in the magnetic dipolar contribution *Udd* (eq. 4.3), but it is intuitive that it affects the mobility of nanoparticles, and therefore their self-assembly process. The mobility of particles dispersed in a liquid medium (b) can be express as the ratio between the diffusion coefficient (D) and the temperature of the liquid (T) [200]:

$$b = \frac{D}{T} \qquad \text{(eq. 4.11)}$$

In turn, the diffusion coefficient is defined by the Stokes-Einstein relation as:

$$D = \frac{K_B T}{6\pi R\eta} \qquad \text{(eq. 4.12)}$$

Where R is the radius of the particle and η is the viscosity of the liquid medium. By substituting eq 4.12 in eq 4.11, the mobility of the particles can be written as:

$$b = \frac{K_B}{6\pi R\eta} \qquad \text{(eq. 4.13)}$$

Equation 4.13 shows as the mobility of the particles is inversely proportional to the viscosity of the liquid in which they are dispersed. Thus, the viscosity of the liquid medium also influences the mobility of the particles and plays a role in the self-assembly process.

In the next section, the physical model used to describe the self-assembly in this work is discussed.

4.3 Physical model for self-assembly description

In this work, a simplified physical model was developed to describe the self-assembly process and to interpret the experimental results. This work was realized in collaboration with Hichem Dammak and Marc Hayoun from Laboratorire des Solides Irradiés (LSI) of Ecole Polytechnique de Paris (France). The novelty brought by the proposed theoretical model consisted of the chance to describe the self-assembly process of magnetic NPs only considering the magnetic interactions within the particles, therefore using a reduced number of parameters. Furthermore, the same model also well described the rotation of the assembled chains.

In this model, nanoparticles are considered superparamagnetic and approximate to spheres of equal diameter *d* and magnetic susceptibility χ. Considering **B** as the magnetic induction and **H** as the magnetic field, the particles magnetization **M** can be defined as follows (bold letters stand for vectors):

$$\boldsymbol{M} = \frac{1}{\mu_0}\frac{\chi}{\chi+1}\boldsymbol{B} \qquad \text{(eq. 4.14)}$$

For superparamagnetic materials $\chi >> 1$, thus eq. 4.14 can be written as:

$$\boldsymbol{M} = \frac{1}{\mu_0}\boldsymbol{B} \qquad \text{(eq. 4.15)}$$

The magnetic moment of a particle can be so written as:

$$\boldsymbol{m} = \frac{\pi d^3}{6}\boldsymbol{M} = \frac{\pi d^3}{6}\,\frac{1}{\mu_0}\,\frac{\chi}{\chi+1}\boldsymbol{B} \qquad \text{(eq. 4.16)}$$

Approximating the magnetic particles to magnetic dipoles, the potential energy derived from the magnetic interaction ($\mathbf{V_m(i,j)}$)between two magnetic dipoles $\mathbf{m_i}$ and $\mathbf{m_j}$ can be written as:

$$\boldsymbol{V_m(i,j)} = \frac{\mu_0}{4\pi}\frac{\mathbf{m_i}\cdot\mathbf{m_j}-3(\mathbf{m_i}\cdot\mathbf{u_{ij}})(\mathbf{m_j}\cdot\mathbf{u_{ij}})}{r_{ij}^3} \quad \text{(eq. 4.17)}$$

Where r_{ij} = $|r_j-r_i|$and u_{ij} = $(r_j-r_i)/r_{ij}$

Thus, the magnetic force produced by the nanoparticle i on the nanoparticle j is:

$$\mathbf{F_m}(i,j) = \frac{3\mu_0}{4\pi r_{ij}^4}\left[(\mathbf{m_i}\cdot\mathbf{u_{ij}})\mathbf{m_j} + (\mathbf{m_j}\cdot\mathbf{u_{ij}})\mathbf{m_i} + \left(\mathbf{m_i}\cdot\mathbf{m_j} - 5(\mathbf{m_i}\cdot\mathbf{u_{ij}})(\mathbf{m_j}\cdot\mathbf{u_{ij}})\right)\mathbf{u}_{ij}\right] \quad \text{(eq. 4.18)}$$

The magnetic field applied to a particle j (B_j) corresponds to the external magnetic field B_{ext} more the additions of all the magnetic fields produced by the other particles in the system:

$$\mathbf{B}_j = \mathbf{B}_{ext} + \Sigma_{i\neq j}\mathbf{B}(\mathbf{m}_i, \mathbf{r}_{ij}) \quad \text{(eq. 4.19)}$$

Where

$$\mathbf{B}(\mathbf{m}_i, \mathbf{r}_{ij}) = \frac{\mu_0}{4\pi}\frac{3(\mathbf{m_i}\cdot\mathbf{u_{ij}})\mathbf{u}_{ij}-\mathbf{m}_i}{r_{ij}^3} \quad \text{(eq. 4.20)}$$

The numerical value of the magnetic moments $\mathbf{m_i}$ and $\mathbf{m}$j are obtained by a self-coherent loop that converges after 3 or 4 interactions. Instead, the total magnetic energy of the system was obtained considering the following relation:

$$U_m = -\Sigma_j \mathbf{m}_j \cdot \mathbf{B}_j \quad \text{(eq. 4.21)}$$

Simulations were run-up until the minimization of the magnetic energy U_m in the system.

Five different parameters were selected to scale the problem:

1) $B_0 = B_{ext}$ is the magnetic field,
2) r_0 = d is the particle dimension,
3) $m_0 = 4\pi d^3(B_0/\mu_0)$ is the magnetic dipole,
4) $E_0 = m_0B_0$ is the energy,
5) And to = $(Md^2/E_0)^{1/2}$ is the time, and M is the mass of the nanoparticle.

By changing these five parameters it was possible to change the contour conditions investigating how the modeled self-assembly process was changing and how this was reflected in the modelized assembled chains.

By using the reduced parameters which are defined as r'= r/r_0, B'=B/B_0 … The reduced magnetic force applied by a nanoparticle *i* on a nanoparticle *j*, and the reduced total magnetic energy can be written as:

$$\mathbf{F'_m}(i,j) = \frac{3}{r'^4_{ij}}\left[\left(\mathbf{m'}_i \cdot \mathbf{u}_{ij}\right)\mathbf{m'}_j + \left(\mathbf{m'}_j \cdot \mathbf{u}_{ij}\right)\mathbf{m'}_i + \left(\mathbf{m'}_i \cdot \mathbf{m'}_j - 5\left(\mathbf{m'}_i \cdot \mathbf{u}_{ij}\right)\left(\mathbf{m'}_j \cdot \mathbf{u}_{ij}\right)\right)\mathbf{u}_{ij}\right] \quad \text{(Eq. 4.22)}$$

$$U'_m = -\Sigma_j \mathbf{m'}_j \cdot \mathbf{B'}_j \quad \text{(Eq. 4.23)}$$

By summing the magnetic contributions of each particle in the system it was possible to simulate the self-assembly process of magnetic particles. The Evans and Beeler dumping was used to follow the system relaxation when the magnetic field was applied or rotated. Compared to other theoretical models, the one proposed here is simplified because it does not take into account the Van der Waals interactions nor the repulsive potential of the particles, however the simulations well described the system evolution both in terms of magnetic particles self-assembly, and magnetic chains rotation.

4.4 Investigations of the self-assembly process of magnetic particles at the nanoscale

The self-assembly process of magnetic particle dispersions was studied at the nanoscale by Scanning Transmission X-Ray Microscopy (STXM). The experimental tests were performed at Synchrotron of Soleil (France) at the HERMES beamline (for High Efficiency and Resolution Beamline dedicated to X-ray Microscopy and Electron Spectroscopy) with the precious support of Professor Rachid Belkhou. This technique allows to obtain images with spatial resolution below 20nm and on an energy range varying from 70eV to 2.5 KeV.

Electronic microscopy techniques such as Scanning Electron Microscopy (SEM) and Transmission Electron Microscopy (TEM) were already used to investigate already-assembled magnetic chains [165], [195]–[197]. However, the intrinsic difficulties to work with liquid-phase samples and to apply magnetic fields during TEM and SEM observations prevented the chance to follow the entire self-

assembly process of magnetic particles over time. On the contrary, thanks to the apparatus designed by the HERMES research group, we were not only able to characterize liquid samples but also to apply controlled magnetic fields during the observations. This experimental set-up allowed us to investigate the growth of the magnetic chains in-situ and at the nanoscale, contributing to a better understanding of this process.

In a first attempt to imitate 3D printing conditions, Fe_3O_4 nanoparticles were added to photocurable monomers mixtures. Unfortunately, during testing the monomers were undergoing degradation due to the interactions with X-rays, preventing a good image acquisition. Fort this reason photocurable resins were substituted with silicon oil. This solution represented the best compromise to avoid the degradation of the liquid medium and to not alter the self-assembly conditions of the magnetic particles.

Samples were prepared by sonicating for 10 minutes the NPs dispersion and encapsulating a drop of the formulation (≈0.75 μL) within two 50 nm thick membranes of Silicon nitride (Si_3N_4) transparent to the X-rays. The space between the two membranes was about 5 μm, and the observable window area was proximately 1x1 mm. The two membranes were then glued with an epoxy resin and fixed on a sample holder by double-sided adhesive tapes (Fig. 4.5). Due to the reduced spacing between the two membranes, the friction exerted on the magnetic particles limited their mobility, conditioning the self-assembly process. For this reason, high magnetic fields were applied to compensate for the friction forces and to accelerate the self-assembly process. The magnetic fields were controlled by two couple of electromagnets able to produce not-simultaneous magnetic fields in the X or Z direction of the sample, with intensity spanning between -180 and 180 mT. Unfortunately, due to the experimental set-up configuration, when the sample is mounted in the STXM, it passes nearby the electromagnets, being subjected to their magnetic field. This caused an unintentional activation of the self-assembly processes and the formation of the magnetic chains. For this reason, it was not possible to follow the self-assembling kinetics starting from zero condition (dispersed NPs system), but only an evolution of the chains partially formed.

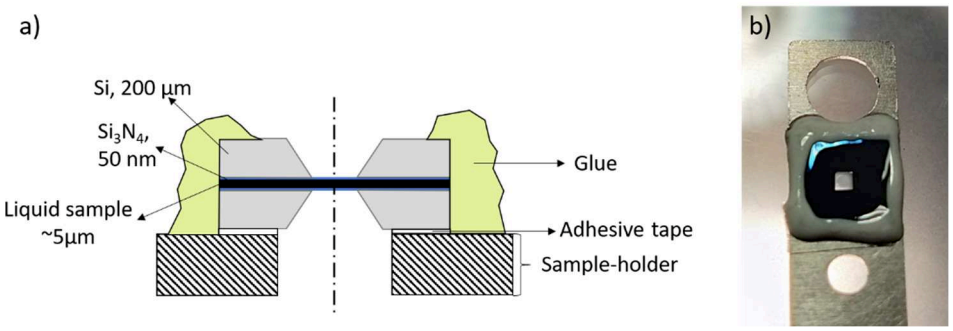

Figure 4.5: Sample holder and Si_3N_4 membranes used in the STXM experience.

Regardless of the technical difficulties encountered in performing the experiments, this technique allowed to observe several features characteristic of the self-assembly process, (Fig. 4.5).

First of all, the first instants of the self-assembly process were investigated by turning the planar magnetic field from 0mT to 100mT. Fig. 4.6 a shows the assembling of a small aggregate (in the red circle) to a pre-existing magnetic chain. The application of the external magnetic field caused the rotation of the smaller aggregate provoked by the alignment of its magnetic moment along the field lines leading to the production of a longer chain.

In a second experiment, the mechanisms occurring during the self-assembly process were investigated by maintaining the planar magnetic field intensity fixed at 75mT. It was observed that the assembling of the magnetic units was occurring at the ends of already assembled chains (Fig. 4.6 b) and this was in agreement with the interpretation of the self-assembly as magnetic dipoles interactions. In fact, as already shown in eq. 4.3, the magnetic dipoles interactions are higher when two magnetic dipoles are in the head-to-tail configuration. This particular condition may be more likely to occur at the ends of the chains, where an isolated particle is free to rotate to align its magnetic moment without being affected by the footprint of the chain.

The influence of the field intensity on an assembled chain was investigated progressively decreasing the magnetic field from 180 mT, to 25mT, and finally to 15 mT (Fig. 4.6c). A reduction of the chain length was observed decreasing the magnetic field, despite no disassembling processes were detected. Based on these observations, some hypotheses can be proposed: assuming that disassembling does not occur, the number of particles per chain can be considered constant. Thus, the

reduction of the chain's length may be ascribable to the mean interparticle distance of the particles composing the chain which was varying with the applied magnetic field [202]. A possible explanation of this phenomenon can be given by considering the Van der Waals interactions. As the dipole-dipole interactions are proportional to the magnetic moment of the particles (eq. 4.3), and the latter is proportional to the applied magnetic field (eq. 4.5), for low magnetic field the dipole-dipole contribution is lower, thus Van der Waals interactions are more relevant and this leads to shorter interparticle distances, so to shorter chains. Therefore, the dimension of a magnetic chain is not only dependent on the number of aligned particles but also on the interparticle distance in the aggregate.

Furthermore, the rotation of the chains was investigated by firstly orient the magnetic chain in the plane (Bx=100mT), then switch off the magnetic field in the plane and activating the field in the z-direction (Bz=100mT), and again switch off the transversal magnetic field and re-activating the magnetic field in the plane (Bx=100mT). The images reported in Fig. 4.6 d show that the magnetic chains perfectly follow the external magnetic field direction and eventually assembles with other aggregates during the rotation motion.

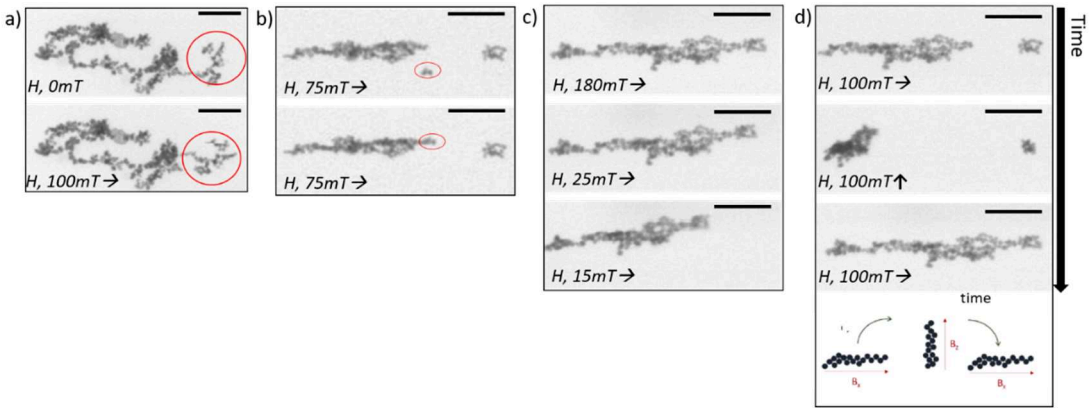

Figure 4.6: STXM images obtained by a) applying a magnetic field of 75 mT in time, b) switching on the magnetic field from 0 to 100 mT, c) decreasing the magnetic field from 180 mT to 25 and 15 mT, and d) tilting the magnetic field from the x-direction to the z-direction and back again to the x-direction.

The simulations of the self-assembly mechanisms physical model are in good agreement with the experiments performed by STXM (Fig. 4.7). Starting from a randomly dispersed system of aggregates (Fig. 4.7a), the application of a horizontal magnetic field causes the rotation of the aggregates along the x-axis (Fig. 4.7b),

similarly to what is observed in Fig. 4.6a. As the self-assembly process proceeds, the formation of chains mainly occurs by the addition of aggregates at the ends of the chains (circles in Fig.4.7b-d), as also experimentally witnessed in Fig. 4.6b.

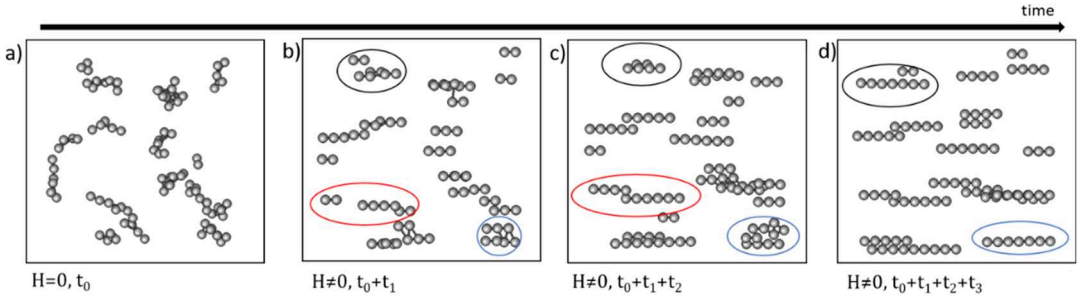

Figure 4.7: Simulations based on the simplified theoretical model of the self-assembly process of magnetic particles.

These investigations can give a better understanding of the phenomena beyond the self-assembly process of magnetic nanoparticles, and the results obtained were coherent with the physical model described in section 4.3. Furthermore, the possibility to control the direction of the magnetic chains by varying the external magnetic field was also demonstrated at the nanoscale. In the next parts of this chapter, the self-assembly mechanism was investigated at a larger scale via optical microscopy, analyzing the average behavior of dispersed nanoparticle systems, and mimicking the 3D printing conditions of photocurable resins.

4.5 Optical microscopy investigations on the self-assembly process of Fe_3O_4 NPs

Optical microscope observations were conceived as a tool to program the microstructure of nanocomposite polymers during the 3D printing process. Thus, not only the generic self-assembly process was studied, but also the possibility to control the chains dimension by varying external parameters.

To simulate a DLP printing process, Fe_3O_4 NPs (Sigma-Aldrich, diameter 50-100 nm) were added to photocurable resins obtained by different ratios of Ebecryl 8232 and Buty acrylate. After mixing and sonication (10 minutes in an ultrasonic bath), few drops of the formulation were placed on a microscope slide and stretched out by a wire wound bar to obtain a liquid layer of about 200 µm thickness and

approximately 5 mm of radius. A Leica DM 2500 m optical microscope (Fig. 4.8a) was used to perform the optical microscopy investigations of all the tested samples. The observations were taken by the transmitted light microscopy method to enhance the contrast and avoid light reflection. Image J software was used to carry out the image analysis. In particular, the observed aggregates were approximated to ellipses, and their lengths and widths were measured. The errors on the average values were calculated as the product of the standard deviation σ_s and the square root of the reciprocal of the number of the measured aggregates (eq. 4.24) [203]. An exhaustive discussion of the image analysis method is reported in the *Appendix 2* of this thesis.

$$\sigma_m = \sigma_s \sqrt{\left(\frac{1}{N}\right)} \qquad \text{(eq. 4.24)}$$

The experiments were run by applying a controlled magnetic field and placing the sample between a couple of permanent magnets. Two typologies of magnets were used: A magnets (60x10x2mm), and B magnets (40x10x4mm), exerting a magnetic field at the surface of 120 mT and 310 mT respectively. By changing the combination of the magnets and their mutual distance it was possible to control the intensity of the applied magnetic field, distinguishing the two magnetic field intensities used to run these characterizations: 6 mT, and 30mT (red circles in Fig. 4.8 b).

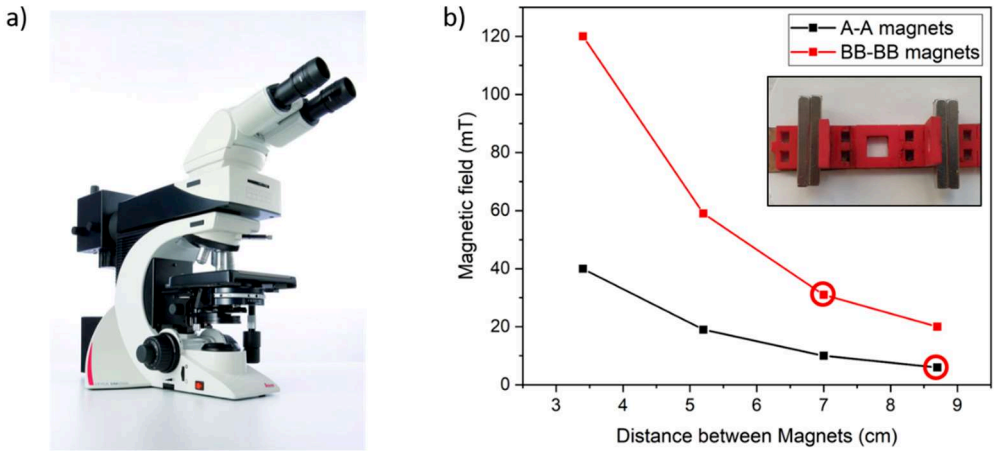

Figure 4.8: a) Leica DM 2500 m optical microscope used in this work, and B) Magnetic field intensities measured by changing the mutual distance between different couples of magnets. Inset: apparatus used to control the magnetic field intensity during the tests.

Regarding the optical microscopy evaluation of the self-assembly mechanism, the first tests were performed on the 3D printed formulations which present the highest content of NPs (6% wt) described in Chapter 3. Unfortunately, the images were unclear and with low contrast, therefore it was not possible to distinguish the assembled chains and to perform a correct evaluation of the aggregates dimensions. For this reason, the best experimental conditions to observe the phenomena, i.e. good image contrast, and a large number of well-defined chains were sought. After several trials, we selected the optimum by dispersing the 3wt.% of NPs in a liquid of 0.05 Pa*s, which corresponded to 60Eb40BA formulation. Thus, the study on the general self-assembly mechanism was performed on 60Eb40BA_3NPs formulation as reference (REF). This formulation was employed to investigate the effect of magnetic field intensity, NPs concentration, and system viscosity on the size of the magnetic chains.

Thus, the complete kinetics of the self-assembly process was followed on the REF formulation by applying a magnetic field of 30 mT and observing the evolution of the system up to 110 minutes. Thanks to the application of the magnetic field the system rapidly evolved from a random particle dispersion to an organized system composed of magnetic chains aligned along the magnetic field lines (Fig. 4.9a). The growth process of the chains seemed to slow down after 10 minutes of magnetic field exposure, reaching a plateau with no significant differences up to 110 minutes. The evolution of the chains dimensions (length and width) with the magnetization time was evaluated to further investigate the kinetics of the self-assembly process. The kinetics curves reported in Fig. 4.9b show a rapid increase of the length within the first 10 minutes of magnetization, followed by a plateau region characterized by small variations in the average length of the aggregates. The simulations well predicted the evolution of the microstructures (Fig. 4.9c) and, as already reported in the literature, this trend is typical of a power-law growth [168], [173]. On the contrary, after an instantaneous reduction of the width of the chains, the average width value remained constant for all the duration of the self-assembly process. These results agree with the STXM observations (section 4.4), and further evidence that the self-assembling process mainly involves the addition of NPs at the ends of the chains.

Based on these experiments, the next tests were performed at 10 minutes of magnetic field exposure since at this time the microstructural organization of the reference remains constant. Furthermore, this time is considerably lower than the sedimentation time for these formulations (about 2h, see chapter 3) and thus may be compatible with a 3D printing process.

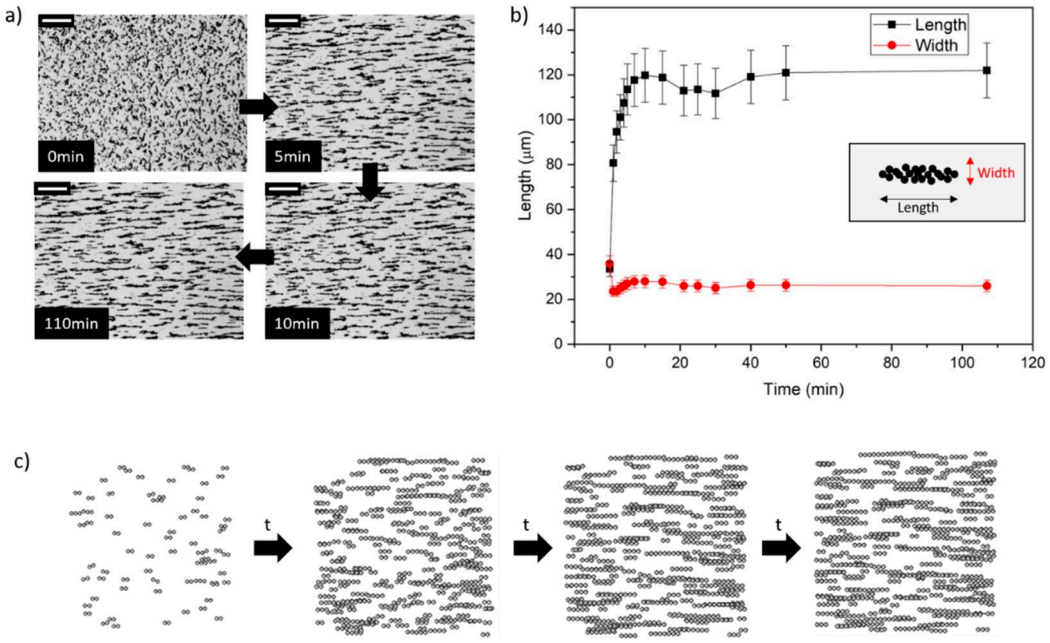

Figure 4.9: A) Optical microscopy images taken for 60Eb40BA_3NPs exposed to a magnetic field of 30mT after 0, 5, 10, and 110 minutes (scale var is 500 µm). B) kinetics of the self-assembly process related to the average dimensions of the assembled chains. Inset: definition of chains length and width. C) Evolution of the assembled chains observed by the simulations based on the developed theoretical model.

The length distribution of the chains during the self-assembly process was investigated, reporting the relative frequency of the number of aggregates present in the system along with time (Fig. 4.10a). The distribution is compatible with a Lognormal distribution, with a peak for short aggregates and a long tail corresponding to the longer chains. Over magnetic exposure time, it was observed that the number of the smaller aggregates reduces while the relative frequency of longer chains increases; this is reflected in a reduction of the peak height and to an increase of the tail of the distribution curves (rectangles in Fig. 4.10a). Likewise, the total number of aggregates drastically decreases within the first minutes of application of the magnetic field, reaching a plateau after 5 minutes of exposure (Fig. 4.10b). This trend was already reported in previous works in the literature [168]. The combination of these results can give further elements to describe the

mechanism of self-assembly at the microscale: as soon as the magnetic field is applied, the energetic contribution of the magnetic dipoles is at its maximum, and the nanoparticles rapidly assemble in chains. This leads to a decrease in the number of aggregates in the system, which in our test drop from 2500 to 1000 unities in 30 seconds, as well as to a strong increase of the average length of the aggregates. Considering that the driving force of the self-assembly is the energy associated with the dipolar interactions of the particles U_{dd} (see eq. 4.3), the assembling of magnetic chains over time decreases the magnetic potential energy in the system. Therefore, the formation of chains still occurs even at longer times, but the magnetic energy in the system is lower, and the self-assembly process is characterized by lower kinetics (i.e. small reduction of the number of the aggregates, and small increase in chains length) and it is mainly related to the incorporation of shorter aggregates in longer chains as witnessed experimentally.

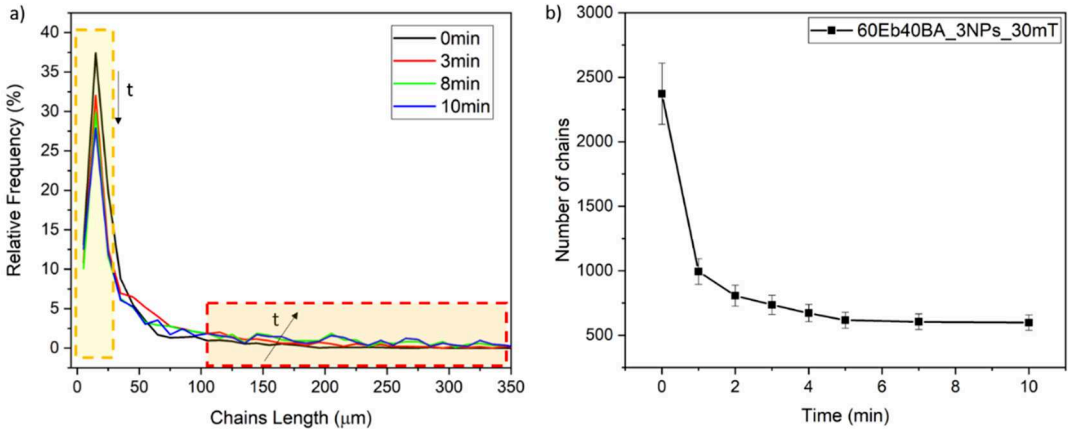

Figure 4.10: A) Evolution of the chains length distribution with time observed for 60Eb40BA_3NPs formulation exposed to a magnetic field of 30mT. B) Evolution of the number of aggregates in 60Eb40BA_3NPs formulation after exposure to a magnetic field of 30 mT.

The optical microscopy observations described how the self-assembly process proceeds at the microscale. In order to program the magnetic microstructure of composite polymers during a DLP 3D printing process, the effect of several parameters on the size of the assembled chains must be investigated. In particular, the magnetic field intensity, the NPs concentration, and the viscosity of the formulations were taken into account. To facilitate the comparison between the tested samples, in the next paragraphs the nomenclature of the systems evidences the changed parameter.

4.5.1 Effect of the magnetic field intensity

The magnetic field is predicted to strongly influence the self-assembly process. In fact, it is responsible for the magnetization – magnetic dipoles formation – of the Fe_3O_4 NPs. To investigate the effect of the magnetic field intensity, the REF formulation was tested, comparing the results previously obtained at 30mT (REF_30mT) with the observation performed applying a magnetic field of 6mT (REF_6mT). Differently from the case at 30mT (Fig. 4.11a), in the case of 6mT system, the magnetic chains were not evident by optical microscopy (Fig. 4.11b). For a quantitative comparison of the two systems, in addition to the length kinetics growth of the chains (Fig. 4.11c), also the aspect ratio of the chains (expressed as Length/Width) was evaluated and compared (Fig. 4.11d). The curves show that for REF_6mT only a tiny increase in the average length of the chains was measured. Furthermore, REF_30mT reached an average aspect ratio of the chains about 4 after 10 minutes, while on the contrary, REF_6mT only reached an aspect ratio value of 1.2. This means that while in the first case it is possible to state that anisotropic chains are formed, in the latter the aggregates remain almost isotropic. These trends are in good agreement with other studies reported in the literature [204], evidencing the strong influence of the magnetic field intensity on the self-assembly process of the magnetic particles. In fact, as the magnetic field (H) is the driving force of the process, for low applied fields the induced magnetic moments in the particles (m) are not strong enough to push the system to evolve in an organized manner (m is proportional to H, see eq. 4.9), thus limiting the self-assembly process.

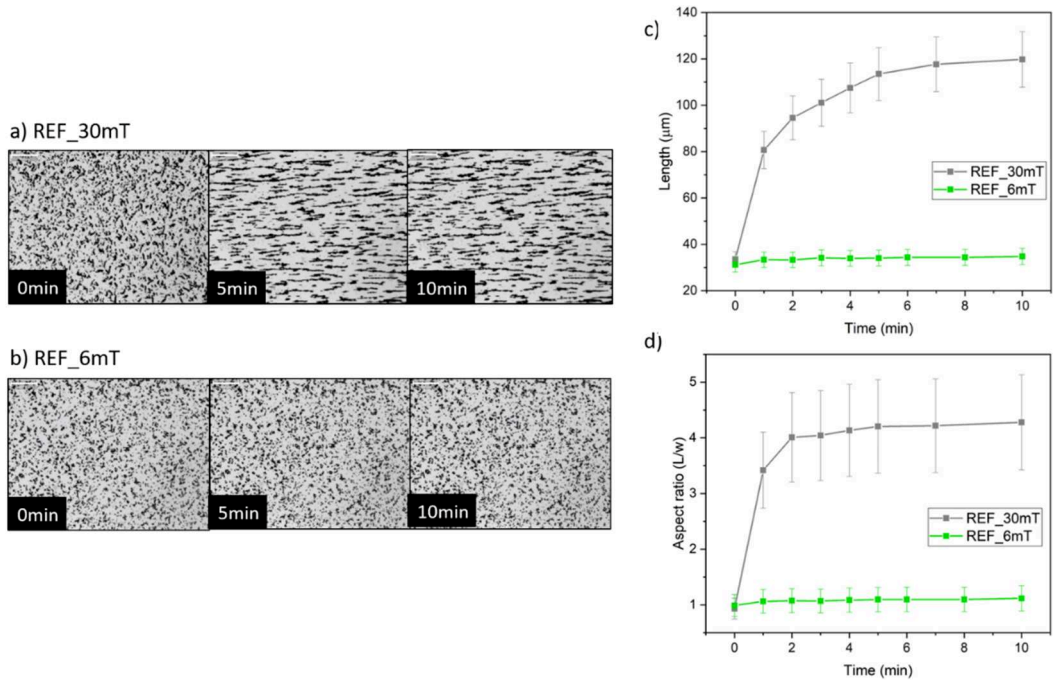

Figure 4.11: Optical images taken at 0, 5, and 10 minutes after exposure to an external magnetic field of a)40Eb60BA_3NPs_30mT, and b) 40Eb60BA_3NPs_6mt. c) Chain length evolution with time upon magnetic field exposure, d) evolution of the average aspect ratio of the assembled chains.

4.5.2 Effect of the nanoparticles concentration

Similarly, the effect of nanoparticles concentration was evaluated, performing experiments in the 60Eb40BA_0.5NPs formulation (REF_0.5NPs) under a magnetic field of 30mT. The two systems evolved differently: chains assembled in the 60Eb40BA_3NPs_30mT system (REF_3NPs) are longer and thicker than those observed in the REF_0.5NPs system (Fig. 4.12). Additionally, as the REF_0.5NPs system starts from tiny aggregates, small increments in chain length lead to a significant increase in the average aspect ratio of the chains (Fig. 4.12d). The experimental results suggested that high concentrations of magnetic NPs in the system foster the formation of long chains, and this trend was in agreement with the literature [168], [169]. The effect of the NPs concentration may be related to the mean interparticle distance in the system (r). Since magnetic dipoles interactions scale with r^3 (eq. 4.3), in diluted systems the average space between two neighboring particles is higher than in loaded systems (eq. 4.10), thus statistically the chance for two particles to magnetically interact is lower. This leads to a lower number of magnetic interactions within the system which is translated into shorter

assembled chains. On the other hand, it is also important to highlight that for this investigation we can take into account only aggregates bigger than a few µm due to the limitation of the technique and further experiments may be necessary for having a complete evaluation of the microstructure evolution.

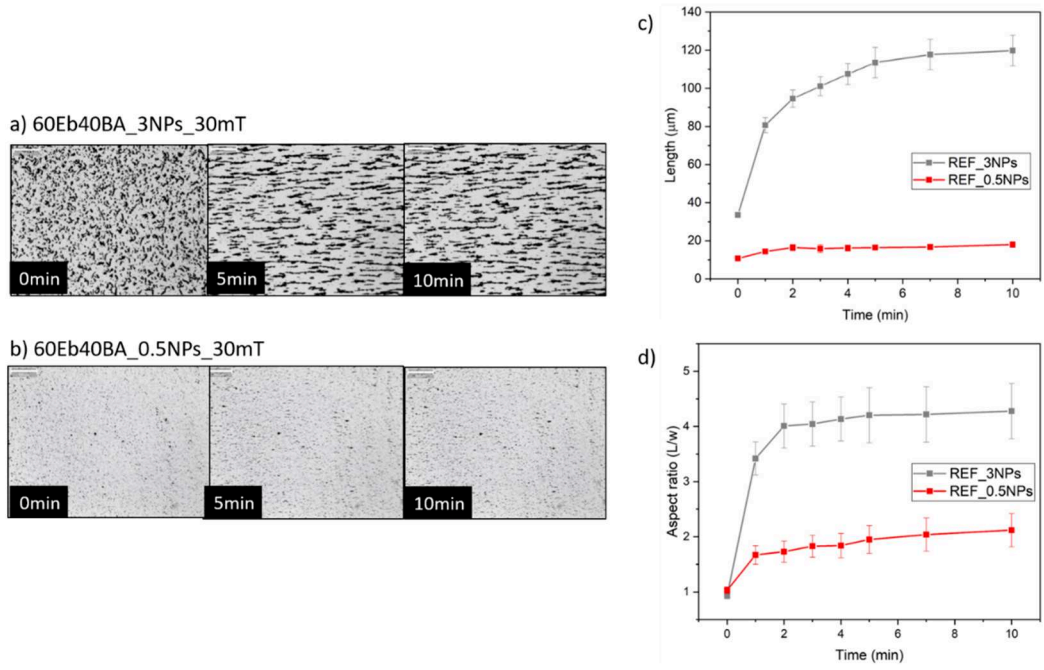

Figure 4.12: Optical images taken at 0, 5, and 10 minutes after exposure to an external magnetic field of a)40Eb60BA_3NPs_30mT, and 60Eb40BA_0.5NPs_30mT. c) Chain length evolution with time upon magnetic field exposure, d) evolution of the average aspect ratio of the assembled chains.

4.5.3 Effect of the viscosity of the liquid medium

To investigate the effect of the viscosity of the liquid medium, the Ebecryl/Butyl acrylate ratio in the formulation was varied. In particular, 67Eb33BA_3NPs formulation was prepared which has a viscosity of 0.078 Pa*s (REF_0.078 Pa*s) which is almost doubled compared to the formulation used as a reference (REF_0.048 Pa*s). On the other hand, the two other investigated parameters, i.e. magnetic field intensity and NPs concentration, were the same for the two samples. Despite the different viscosities, in both systems the initial dimensions of the aggregates were similar, however their evolutions differ (Fig.4.13a,b). The chains obtained for REF_0.078 Pa*s formulations were shorter than those observed in the REF_0.048 Pa*s, moreover the kinetic growth of the chains in the more viscous formulation was slower, reaching the plateau only for longer exposure times (Fig. 4.13c).

This effect is even more evident in the aspect ratio curves (Fig. 4.13d), where the REF_0.078system shows a low slope and it reaches a plateau-region after 5 minutes of exposure, while the REF_0.048 Pa*s curve reach it already after 2 minutes (Fig. 4.13d). The data suggests that viscosity may slow down the growth process of the chains, and according to a previous study reported in the literature [173], two systems differing only by the viscosity of the medium may reach the same equilibrium-configuration but at different times. This effect can be explained considering eq. 4.9 which introduces the effect of viscosity on the mobility of the aggregates. As the mobility of the particles is inversely proportional to the viscosity of the liquid medium (see eq. 4.9), with the same intensity of magnetic interactions, the more viscous system evolves slowly at its equilibrium state due to the reduced mobility of its aggregates [173].

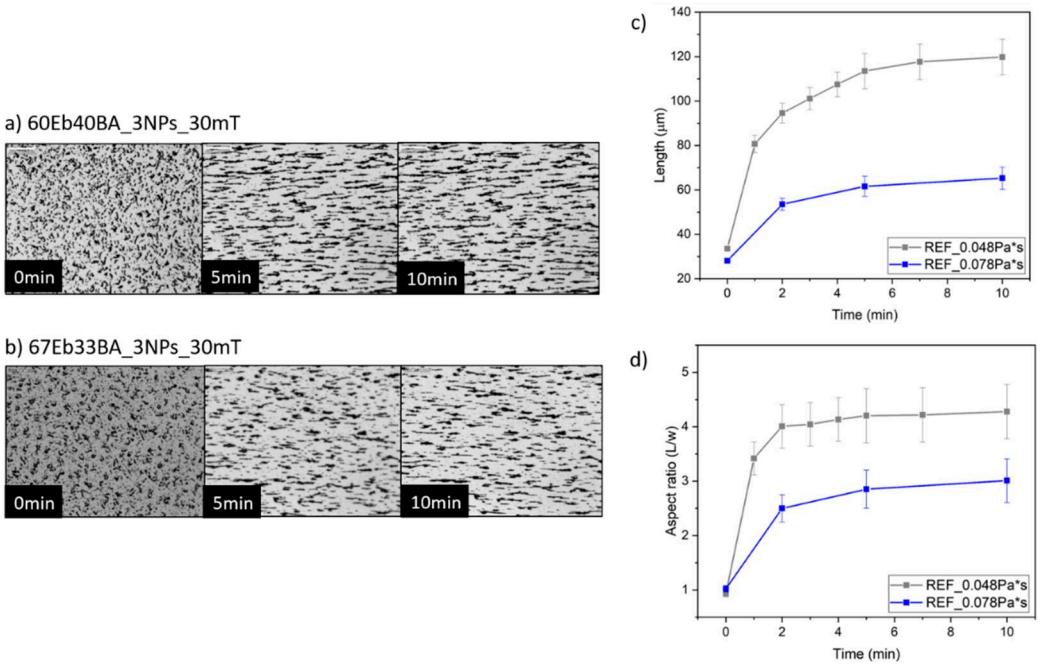

Figure 4.13: Optical images taken at 0, 5, and 10 minutes after exposure to an external magnetic field of a)40Eb60BA_3NPs_30mT, and b) 67Eb33BA_3NPs_30mT. c) Chain length evolution with time upon magnetic field exposure, d) evolution of the average aspect ratio of the assembled chains.

4.5.4 Final remarks on the self-assembly process of Fe_3O_4 nanoparticles

The observations performed allowed to deeply investigate the self-assembly process of Fe_3O_4 NPs dispersed in photocurable resins. The experience made at SOLEIL synchrotron has provided information at the nanoscale, and it represents an innovative investigative approach. By optical microscopy, the same phenomena were studied on a larger scale, introducing also additional parameters. The results evidenced that by tuning the intensity of the applied magnetic field, the NPs concentration, and the liquid medium viscosity, it was possible to control the average dimensions of the assembled chains. This part of the work was fundamental in order to control the formation of the chains during the 3D printing process. Nevertheless, to achieve full control of the microstructures of the printed composite materials, it is also necessary to study the evolution of the chains when the magnetic field vector changes direction. This will be discussed in the next paragraph.

4.6 Rotation of the assembled magnetic chains

Besides the control of the size of the magnetic chains, also the control of their direction is a prerequisite necessary to fabricate composite magnetic materials with programmable microstructures. In a 3D printing process, the combination of size and direction control of the magnetic chains would allow to predict the microstructure of each printed layer, leading to full freedom in the whole material design. At a first sight, the control of the direction of the magnetic chains seems a trivial problem, as it seems achievable simply by changing the magnetic field direction on a dispersed formulation layer. However, this solution is not practicable during a 3D printing process as it is not possible to disperse randomly the NPs after each layer printing step. On the contrary, more likely the formed chains will be subjected to several changes of the magnetic field direction during the printing process.

4.6.1 Physical considerations about magnetic chains rotation

When the direction of an applied magnetic field is changed, the NPs composing the chain rotate their magnetic moments, and consequently the chain rotates to realign its magnetic moment to the direction of the field [205]–[210]. The rotation of monodispersed magnetic chains exposed to rotating magnetic fields can be exploited to produce labeling, sorting, transporting, and mixing systems for nanotechnology and Lab on a Chip applications [190], [205], [206]. This boosted the development of several theoretical models describing the behavior of individual monoatomic magnetic chains in the presence of continuously rotating magnetic fields [205]–[210].

In particular, two rotational regimes of the chains were observed according to the frequency of the rotating field, and for high rotation speeds the chains break [205]–[210]. This behavior was explained as the competition between magnetic dipole forces which aim to rotate the chains with the magnetic field, and a viscous drag opposed to their rotation [205]–[210]. Many studied focused on developing theoretical models able to predict the critical frequency value for the two regimes [205]–[210], and this was achieved by computing the ratio of viscous forces on magnetic forces. According to S. Melle et Al. [210] this ratio corresponded to the Mason number (*Ma*) expressed as follows (eq. 4.25):

$$Ma = \frac{12^2 \eta \omega}{\mu_0 \mu_s M^2} \qquad \text{(eq. 4.25)}$$

Where η is the viscosity of the solvent, ω the frequency of the magnetic field, μ_0 and μ_s the magnetic permeability of the vacuum and of the solvent respectively, and M the particle magnetization. Thus, for low frequencies, i.e. Ma<<1, the magnetic forces prevail on the viscous ones, and the chains remain intact and turn solidly with the magnetic field. On the contrary, for high frequencies i.e. Ma>>1, the viscous forces are dominant and the chains brake-up.

Simulating the magnetic-assisted 3D printing process, the contour conditions differ from the above-mentioned studies, as the magnetic field is rotated instantaneously of a discrete angle rather than continuously rotated. However, the existence of two rotational regimes has to be investigated as it may affect the control of the magnetic chains during the 3D printing process. Therefore, further investigations were required both experimentally and theoretically to characterize

this system. In particular, we focused on the kinetic rotation of the chains and the evolution of their dimensions. The same theoretical model described in section 4.3 was used to describe the magnetic chains rotation, and although the model did not take into account the viscosity of the liquid medium, the results of the simulations were in good agreement with the experimental observations.

4.6.2 Preliminary studies on the rotation of magnetic chains

The experimental set-up adopted was similar to that described in Chapter 4.5. 60Eb40BA_3NPS formulation was used as the reference for the entire rotational process. The magnetic particle dispersions were exposed for 10 minutes to a magnetic field generated by a pair of magnets to reach the plateau-region of the self-assembly process. Afterwards, the magnetic field direction was changed by rotating the permanent magnets and the evolution of the magnetic chains was followed using a Leica DM 2500 m optical microscope (Fig. 4.8a). The physical model used to describe the self-assembly process was here again used to explain theoretically the rotation of the magnetic chains.

After promoting the self-assembly process for 10 minutes by applying a horizontal magnetic field (θ_B=0) of 30mT, the magnetic field was rotated to reach different rotation values. After 2 minutes from each field rotation, the microstructure obtained was observed through the optical microscope. The collected images witnessed that the magnetic chains were free to rotate in the photocurable resin and to re-orient their magnetic moment along the applied magnetic field (Fig. 4.14). Nevertheless, it was observed that the amplitude of the angle variation ($\Delta\theta_B$) influences the evolution of the microstructure, with a rupture of the present chains over a certain value. In particular, two rotational regimes were observed:

- **I regime** ($\Delta\theta_B < 40°$): The magnetic chains are able to rotate following the magnetic field without breaking.
- **II regime** ($\Delta\theta_B > 40°$): Chains are not able to follow the rotation and undergo breakage (red rectangle in Fig. 4.14)

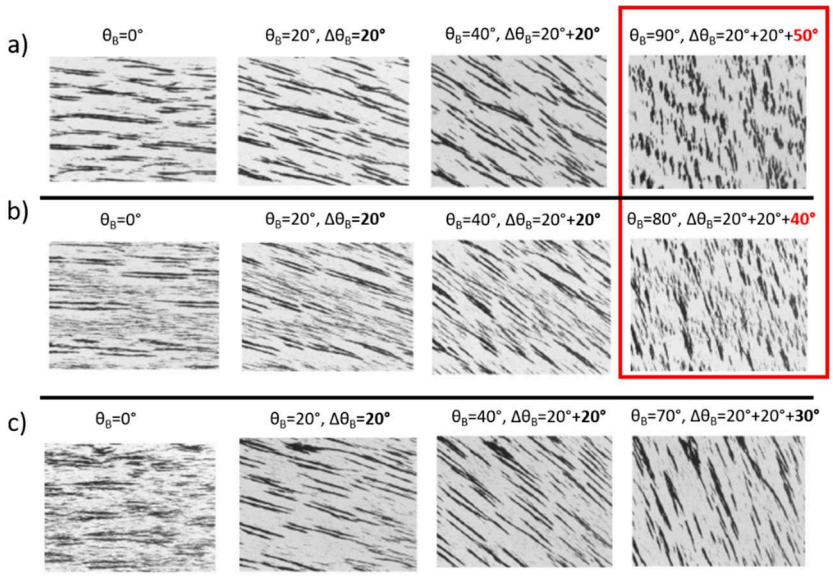

Figure 4.14: Optical microscopy investigations of the rotation of the chains in the 60Eb40BA_3NPs formulation for different angles of the applied magnetic field. A) subsequent rotations of 20°, 20°, and 50° (waiting 2 minutes after each rotation), b) subsequent rotations of 20°, 20°, and 40° (waiting 2 minutes after each rotation), and c) subsequent rotations of 20°, 20°, and 30° (waiting 2 minutes after each rotation)

Thus, a relationship was found between the two rotational regimes reported in the literature for rotating magnetic fields [205]–[210], and the two regimes observed for discrete magnetic field rotations. In fact, as the frequency of rotation of the magnetic field increases, the angular speed increase as well as the angle that the chains have to span. Therefore, high magnetic field rotation frequencies correspond to high $\Delta\theta_B$, and thus to the II chains rotational regime in our system.

4.6.3 Limit cases $\Delta\theta_B$=30° and $\Delta\theta_B$=40°

To further investigate the two regimes, the limit cases $\Delta\theta_B$=30° and $\Delta\theta_B$=40° were studied by analyzing the ratio between the angle of the chains θ_{exp} and the angle of the magnetic field θ_B and evaluating the ratio between the initial chains length (L_0) and their length (L) during the rotation. Furthermore, also the evolution over time of the distribution of the chains lengths was investigated.

For the I regime, i.e. $\Delta\theta_B$=30°, the length of the chains remained almost constant for the whole experiment except for a small decrease (≈ -10%) at the beginning of the process (red curve in Fig, 4.15a). A similar trend was observed also in the analysis of the chains length distributions taken before and after 5

minutes from the magnetic field rotation: in fact, the two distributions were overlapping, indicating that the size of the chains was not varying (Fig. 4.15b). Instead, the average magnetic chains angle increased according to a sigmoidal trend characterized by a rapid shift in the first seconds of the experiment followed by a plateau-region (black curve in Fig. 4.15a). However, the chains angle never reached the nominal magnetic field rotation, with a difference of approximately 5°. This aspect will be discussed more in details in section 4.6.4.

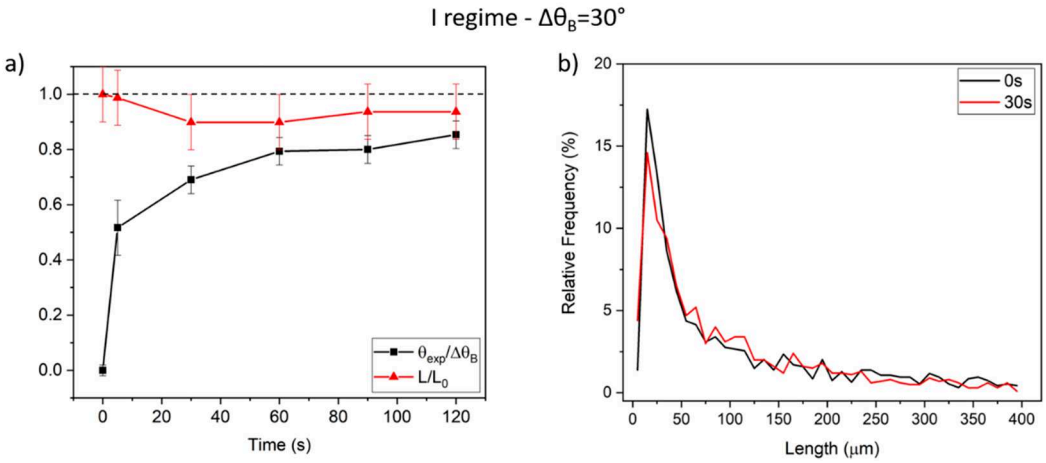

Figure 4.15: a) θ/θ_B and L/L_0 trends for $\Delta\theta_B$ =30°. B) Distribution of the length of the chains prior to the rotation of the external magnetic field and after 30 seconds for $\Delta\theta_B$ =30°.

For the II regime, i.e. $\Delta\theta_B$=40°, as soon as the magnetic field was rotated, the magnetic chains underwent breakage. This is observed in Fig. 4.16a where the L/L_0 curve dropped by 50% within the first 30 seconds of rotation. After, the average chains length increases due to the self-assembly processes occurring during the rotation, however magnetic force was not enough to reach their initial length (red curve in Fig. 4.16a). This was also observed in the chains length distribution curves (Fig. 4.16b): after 30 seconds from magnetic field rotation, the peak of the distribution increased and shifted to the left of the graph evidencing that the number of short aggregates drastically increased. Comparing the rotation kinetics of the I and II regimes (black curves in Fig. 4.15a, and 4.16a respectively): the rotation rate (slope of the first segment of the curve) is higher in the II regime, and the chains angle reaches the magnetic field angle already after 30 seconds from the beginning of the rotation.

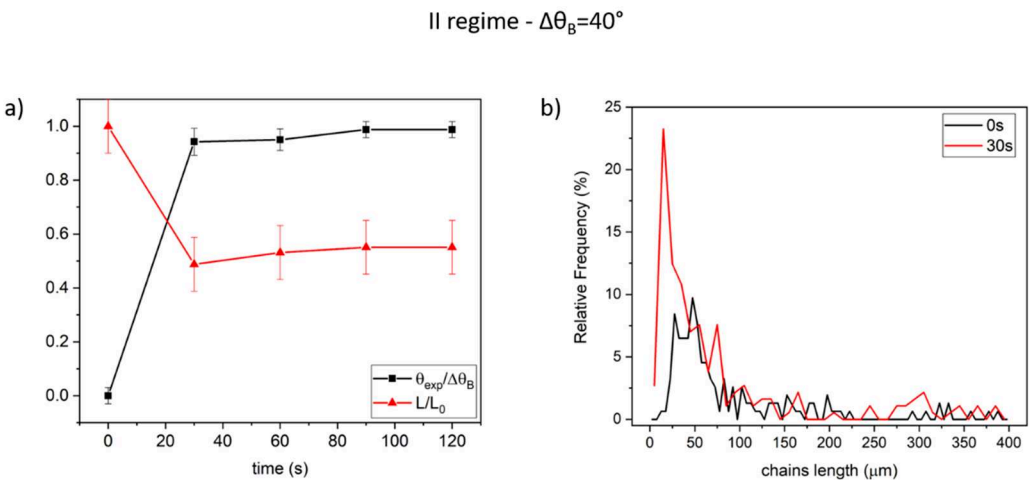

Figure 4.16: a) θ/θ_B and L/L_0 trends for $\Delta\theta_B$ =40°. b) Distribution of the length of the chains prior to the rotation of the external magnetic field and after 30 seconds for $\Delta\theta_B$ =40°.

The proposed physical model well described the phenomena observed experimentally by only considering the magnetic interactions within the assembled particles (Fig. 4.17). Subdividing the magnetic interaction between two particles in the parallel and perpendicular components, the module and the direction of the two components varies according to the magnetic field angle ($\Delta\theta_B$). In particular, when $\Delta\theta_B$ is approximately 45°, the parallel magnetic forces produced by the two particles are opposite and therefore cause the chain to break.

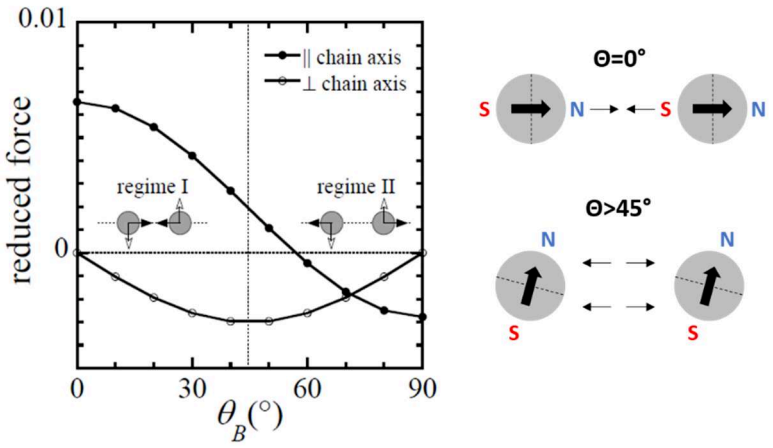

Figure 4.17: Theoretical description of the existence of two rotational regimes considering only the magnetic dipoles interactions.

Thus, the existence of two regimes in the rotation motion of the magnetic chains was well predicted by the physical model (Fig. 4.18a). The simulations showed that

for angles up to 30°, the chains follow the magnetic field rotation with a certain time delay (fig. 4.18b) without a significant decrease in their length (Fig. 4.18c). On the contrary, for larger rotations, the chains follow nearly instantaneously the field angle, but with abrupt length decrease (Fig. 4.18b, c). This behavior is more clearly shown in the insets of Fig. 4.18b, c. The angle difference between the orientation of the chains and nominal field direction ($\Delta\theta$) linearly increases up to 30°, this behavior will be related to the experimental results in section 4.6.4. It is important to observe the abrupt change in this trend for angles larger than 40°: in these cases, the chains follow perfectly the field orientation ($\Delta\theta$=0°) but with a strong reduction of their initial length ($\Delta L/L_0$).

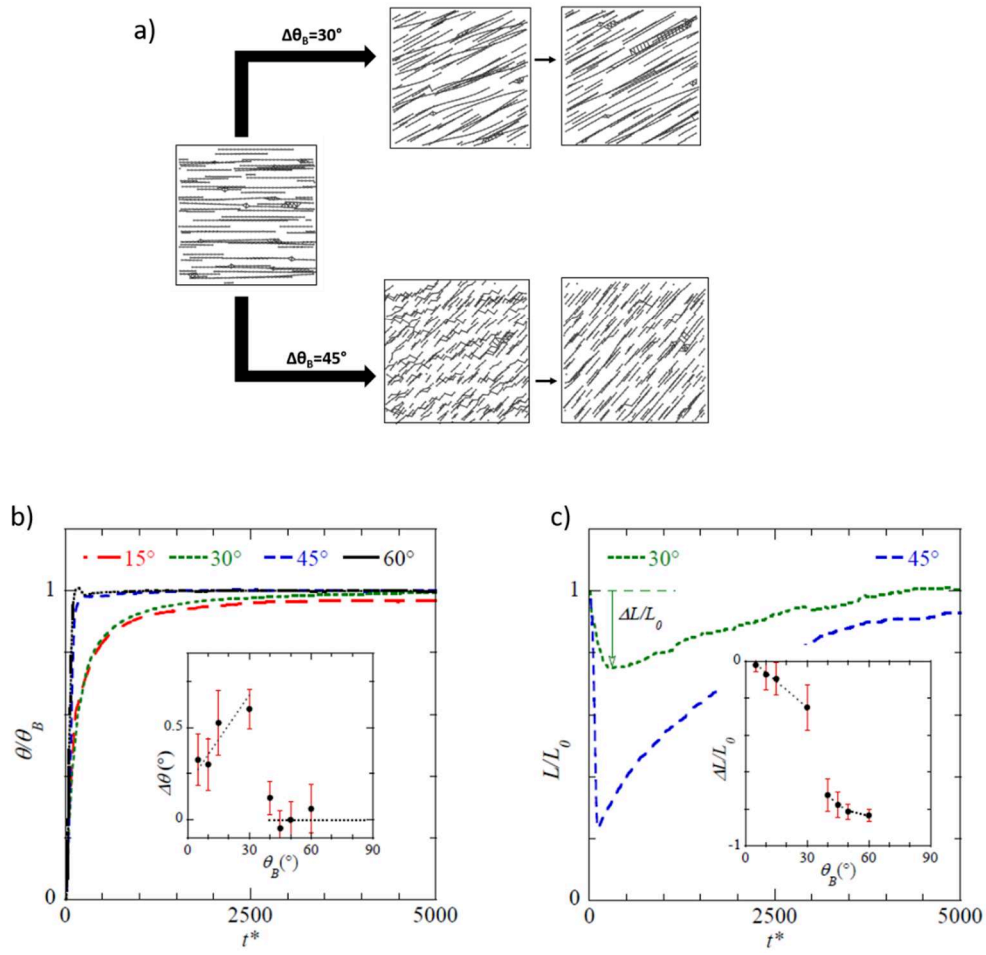

Figure 4.18: A) Images obtained by the simulations of the theoretical model for $\Delta\theta_B$ =30° and $\Delta\theta_B$ =45°. B) θ/θ_B trends obtained by the simulations based on the physical model for several values of $\Delta\theta_B$: 15°, 30°, 45°, 60°, and 60°. F) L/L_0 trends obtained by the simulations based on the physical model for $\Delta\theta_B$= 30°, and $\Delta\theta_B$= 45°.

To conclude, the proposed physical model well described and predicted the phenomena observed experimentally and vice versa, evidencing the existence of

two distinctive regimes according to the rotation angle. In the next paragraph the regime I will be studied more in details.

4.6.4 Study on the I rotational regime of magnetic chains

With the same experimental set-up described above, the magnetic chains assembled by exposing 60Eb40BA_3NPs formulation to a magnetic field of 30 mT for 10 minutes were rotated by four different angles in the I regime: $\Delta\theta_B$ = 5°, 10°, 15°, and 30°. It was already reported that within regime I the chains length is not affected by the imposed angle, so the experiments will be focused only on evaluating the angle evolution. In Fig. 4.19 the rotation kinetics curves for the four tested $\Delta\theta_B$ are reported. It is possible to observe that the rotation rate of the chains (initial slope of the curves) depends on the amplitude of the magnetic field angle (Fig. 4.19a). This can be explained considering that larger rotation angles induce a higher magnetic torque to the chains, which leads to a faster rotation of the aggregates. By selecting an observation time of 120 s after rotation, which time range is compatible both with the printing process of a layer, and the time necessary to reach the plateau region in the kinetics of rotation (Fig. 4.15a), it was measured a gap between the imposed direction of the magnetic field and the orientation of the chains. As predicted by the physical model (inset of Fig. 4.18a), these differences, measured at plateau times, increase increasing the rotation angle as the chains need to fulfill longer angle paths (figure 4.19b).

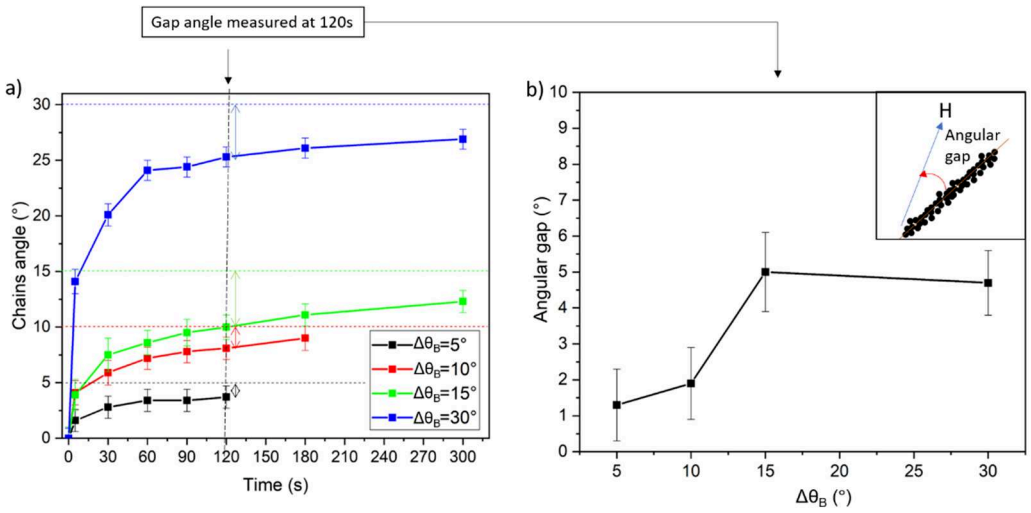

Figure 4.19: a) Chains angle vs time kinetics curve $\Delta\theta_B$ = 5°, 10°, 15°, and 30°. B) Angular gap vs $\Delta\theta_B$ at 120s. Inset: representation of the angular gap.

Comparison of the evolution of the assembled chains for a subsequent rotation of 20°+20° versus a unique rotation of 40° of the magnetic field.

The previous results demonstrated that for rotation larger than 40°, the magnetic chains break while follow the magnetic field variation. This behavior may be undesired in view of a complete control over the microstructure of a polymeric composite. A possible solution to overcome chains breaking consists in subdivide the angled path of the field in subsequent small rotations.

To prove this multi-rotation concept the REF formulation was (i) rotated of $\Delta\theta_B$=40°, or (ii) rotated by two equal and consecutive angles $\Delta\theta_B$=20° waiting 2 minutes between each rotation (Fig 4.20a). The angle of the magnetic chains in both the experiments are reported in figure 4.20b. It is evident that performing two consecutive rotations lead to achieve a total rotation angle as well of 40°. Furthermore, this experiment shows that the multi-rotation approach avoids the breakage of the chains typical of the II rotational regime (Fig. 4.20c), allowing the chains to rotate for larger angles without affecting the microstructure and in times compatible to a 3D printing process. Moreover, it can be envisaged to have a reduction of time by performing the second rotation earlier than after two minutes, as soon as the first plateau is reached.

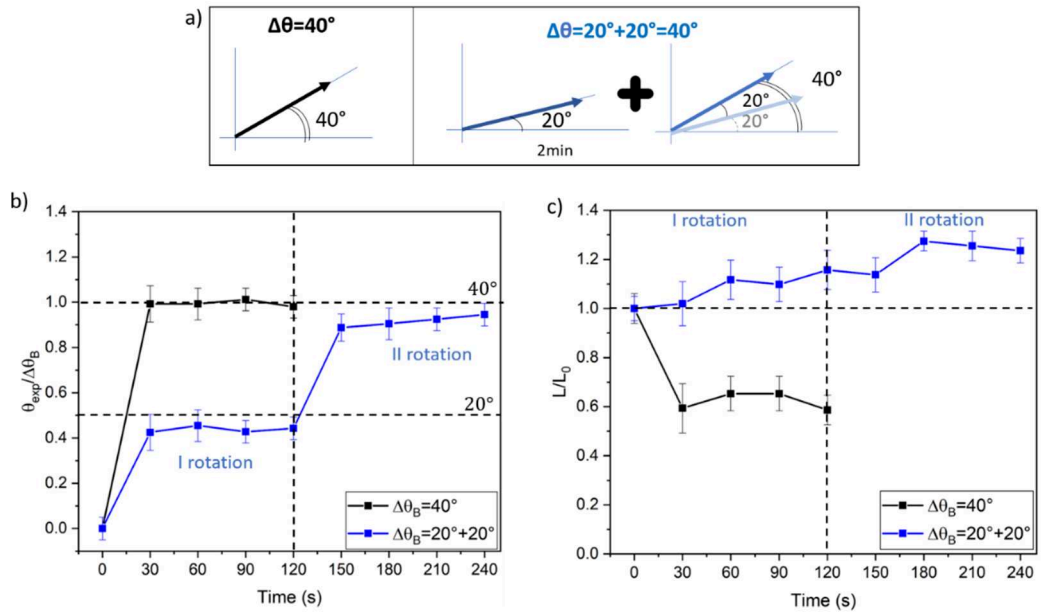

Figure 4.20: A) Experimental set-up: single rotation of 40° versus two subsequent rotations of 20°. B) evolution of the angle in the two systems. C) evolution of the length in the two systems.

The multiple-rotations solution allows to rotate the chains at any angle without changing their shape. This is a fundamental achievement in order to control the microstructure during the 3D printing process.

The role of viscosity in the I rotational regime.

As a last experimental test, the influence of the viscosity on the rotation of the magnetic chains was evaluated. In this context, it is important to remind that, as reported in section 4.2.2 an increase of viscosity leads to a decrease in magnetic chains length. Nevertheless, it is also interesting to evaluate its effect on the chains rotation. For this purpose, it was prepared a formulation with consistent higher viscosity, namely 85Eb15BA_3NPs formulation (η=0.580 Pa*s), and the results were compared with the standard formulation 60Eb40BA_3NPs (η=0.048 Pa*s). In this case, two magnetic field angles were tested: 10° and 30°. Even though the viscosity values of the two formulations differed by one order of magnitude, the rotation kinetics were similar for both the tested $\Delta\theta_B$, except for a small delay in the kinetics for the more viscous formulation, i.e. 85Eb15BA_3NPs (Fig. 4.21). This suggests that, differently from the effect on chains length, the rotation process is not strongly influenced by the medium viscosity since it does not involve the migration of NPs.

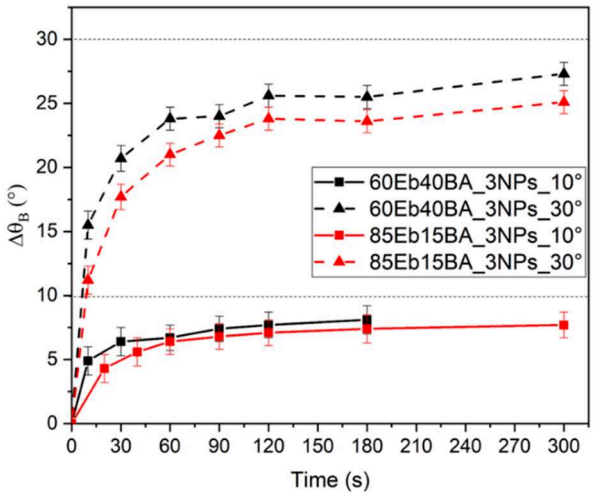

Figure 4.21: Comparison of the rotation kinetics between the 75Eb15BA_3NPs and 60Eb40BA_3NPs formulations for $\Delta\theta_B$ =10°, and 30°.

4.6.5 Final remarks about the magnetic chains rotation

The investigations made on the rotation of assembled magnetic chains were coherent with the physical model, and both witnessed the existence of two rotational regimes. In the first regime ($\Delta\theta_B$<40°) the chains rotate solidly with the magnetic field, but a gap between the magnetic chains and the magnetic field angles was always detected. In the II regime ($\Delta\theta_B$>40°), magnetic chains rapidly reach the magnetic field angle within 30 seconds, but they undergo disassembling processes that abrupt their average length. In the attempt to control the microstructure of magnetic polymeric composites by a 3D printing process, the II regime has to be avoided as it brings several issues in controlling the magnetic chains dimensions. However, by a multi magnetic field rotation approach, it is still possible to rotate the magnetic chains by large angles without affecting their size. Therefore, the I rotational regime was studied in detail focusing on the rotation kinetic of the chains and on the evolution of agglomerates length. Moreover, the influence of viscosity on the rotation of chains was also evaluated.

4.7 Conclusions

In the framework of controlling the microstructure of nanocomposite materials during the 3D printing process, the assembling in chain-like structures of Fe_3O_4

NPs dispersed liquid films of photocurable resins was here discussed. The mechanisms of the self-assembly process were observed in-situ and at the nanoscale by an innovative STXM microscopy technique. The results obtained gave a better understanding of several assembling phenomenon. In particular, we demonstrated that the application of the magnetic field leads to the rotation of the dispersed aggregates and that the assembling process mainly occurs at the ends of already formed chains.

Optical microscopy investigations were performed to evaluate the average behavior of the magnetic particles dispersed in the resin when exposed to an external magnetic field. By the analysis of the acquired images, we observed that the kinetics of the self-assembly follows a power-law growth characterized by a strong increase in the aggregates length during the first seconds of the field application, followed by a pseudo-plateau-region. Varying several process parameters, we found that magnetic field intensity and NPs concentration both facilitate the self-assembly process leading to the formation of longer magnetic chains. On the other hand, more viscous formulations slow-down the assembling process leading to shorter aggregates.

We also developed a simplified theoretical model of the self-assembly process based on the magnetic interactions produced between particles; and the numerical simulations well described the trends observed experimentally.

After we were able to predict the dimensions of the assembled aggregates, we investigated the chance to control the direction of the magnetic chains by varying the direction of application of the magnetic field. Below a critical angle of 40°, the magnetic chains rotate to align to the field lines (I regime), above the critical angle the chains break during their rotation (II regime). The existence of a critical rotational angle was also predicted by the developed physical model and its value was comparable with the experimental one. We studied more in details the I rotation regime by optical microscopy and we observed that magnetic chains exhibit a gap angle with the magnetic field linearly proportional with the amplitude of the induced rotation.

The data acquired in this work enable us to predict and program the arrangement of Fe_3O_4 NPs in the microscale. The next step for the fabrication of

nanocomposite materials with programmed microstructures consists to replicate this control in each layer of the material during the 3D printing process.

5.

Set-Up of a Magnetically Assisted DLP 3D Printer

5.1 Introduction

The formation and control of self-assembled magnetic structures in polymeric matrices during the printing process may allow the production of nanocomposite materials with complex microstructures, and programmable magnetic anisotropy [211]–[213]. However, so far, this approach was mainly developed in two dimensions (2D) and using photolithographic-like technics, which may reduce the field of practical applications to thin and small elements for micro-robotics, see for instance [175] and Fig. 5.1. To expand the palette of potential uses of magnetically-driven polymer nanocomposites, it is mandatory to scale up the process by producing larger devices exhibiting complex actuation movements. This can be obtained by implementing the photolithography-based techniques to a true 3D DLP fabrication process.

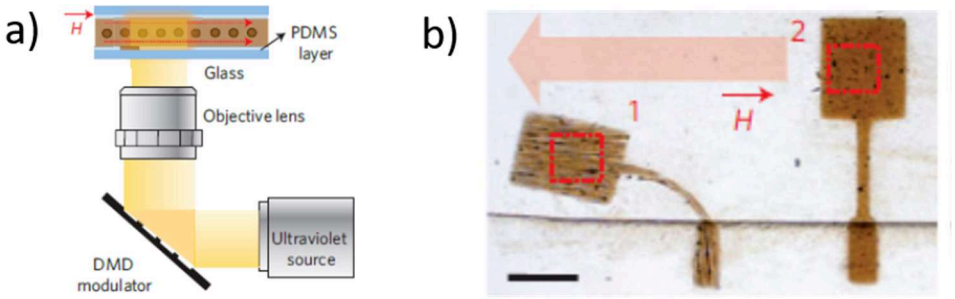

Figure 5.1: a) Maskless lithography set-up. The set-up is composed of an ultraviolet light source, a digital micromirror device (DMD) modulator, and objective lenses. The light is patterned through a DMD modulator and focused on the microfluidic channel, polymerizing the resin. B) Actuation of a simple magnetic cantilever. Under a homogeneous magnetic field the magnetic cantilever, which contains self-assembled magnetic nanoparticles (MNs), only bends towards the field line. (Scale bar 50 _m). [175]

As described in previous chapters, the low viscosity of the dispersing media is a compulsory condition to induce the self-assembly of the Fe_3O_4 fillers when a magnetic field is applied. Indeed, in this case, low magnetic fields are sufficient to promote both the formation of chain-like structures and to control their spatial orientation. As introduced in the previous chapters, if the dispersing media is a photocurable resin, the desired magnetic chains arrangement can be "frozen" by fast photo-induced curing. Repeating the same procedure for subsequent polymeric layers, as in DLP and SLA vat stereolithography techniques, should allow to print an object where each layer will present spatially oriented magnetic microstructures, and therefore programmable magnetic anisotropies.

This chapter describes the modification of a commercial DLP 3D printer (HD 2.0+ RobotFactory) introducing a magnetic field during the printing process to 3D print polymeric nanocomposites with spatially oriented chains of magnetic nanoparticles in each printed layer.

5.2 Introducing a magnetic field in a DLP printer

The application of a spatially tunable magnetic field is the first step to program the microstructure of a 3D printed composite material. Being very complex to directly control a magnetic field, **B**, in three-dimensions of the space, we exploit the fact that **B** is a vector characterized by a direction and a magnitude (or strength) and we decompose the problem into two sub-problems (Fig. 5.2). Our strategy consists of first producing a magnetic field in the X-Y plane and then add a further

component of the field in the Z direction. By using the "parallelogram" method, the combination of the two vectors allows to control the magnetic field in the X-Y-Z direction.

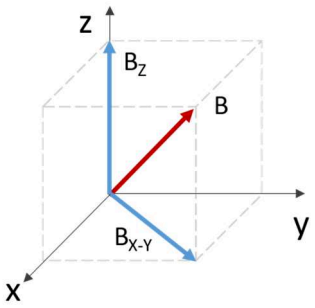

Figure 5.2: sketch of the parallelogram method allowing the decomposition of a three-dimensional vector, B, into two sub-vectors, the first one in the X-Y plane, B_{X-Y}, and the second one in the Z direction, B_Z.

Unfortunately, the modification of a DLP 3D printer is not a straightforward process and necessarily several issues need to be solved. First of all, the magnetic elements must be placed outside the light path of the projector to avoid the formation of shadow-areas on the vat. Second, the interaction among the applied magnetics elements and the metallic components of the 3D printer must be avoided, in order to not modify the magnetic fields. Last but not least, the applied magnetic fields have to be homogeneous and avoid the formation of NPs depleted regions in the resins as they may be detrimental to the final magnetic response of the printed object.

5.2.1 Introducing a magnetic field in X-Y plane

There are two ways to apply a magnetic field with a controlled direction in the X-Y plane: (i) using *Helmholtz* coils or (ii) using permanent magnets. Undoubtedly, *Helmholtz* coils (Fig. 5.3) presents the advantage of producing a region of nearly uniform magnetic field in the middle of the distance between coils. However, dimensional constraints owed by the 3D printer are barely compatible with the dimension of the coils. Besides, when a viscous resin is used, the low magnetic field intensity produced by the *Helmholtz* coils, e.g. of the order of few (3-5) mT, is not compatible with the promotion of self-assembly of magnetic NPs. Otherwise stated,

the time necessary for the formation of the chains would be longer than the printing time.

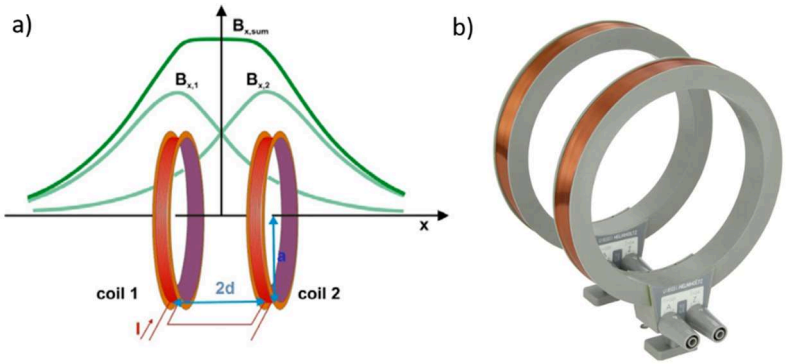

Fig. 5.3: a) Helmholtz coils showing the homogeneity of the magnetic field in the center of the system. b) Set up composed of three sets of Helmholtz coils to vectorial control the magnetic field in the X-Y-Z space (https://www.3bscientific.fr).

For the abovementioned reasons, the developed solution consists of using a couple of permanent magnets stuck on a rotating ball bearing as shown in Fig. 5.4a. To minimize the interactions between the applied magnetic field and the ball-bearing, all the components of the latter were made of non-magnetic materials, i.e. the whole cage is made of nylon, whereas the rotating balls of glass. The ball bearing, purchased from SKF (www.skf.com), is 10 mm thick with an external diameter of 70 mm, whereas the diameter of the central hole is 40 mm. On the other hand, two classes of NdFeB magnets were tested, hereafter named as A and B, and purchased from Supermagnete (www.supermagnete.fr), Fig. 5.4b. Magnet A is a 60x10x2 mm parallelepiped whose magnetic field at the surface has been measured to be 120 mT, while the magnet B is a 40x10x4 mm parallelepiped whose magnetic field at the surface is 310 mT. For both magnets the magnetization axis is along the smallest dimension of the parallelepiped. Once fixed on the ball bearing, the direction of the magnetic field in the X-Y plane is controlled by rotating the permanent magnets as indicated in Fig. 5.4c. As described in the next section, as the magnetic field scales as B~1/r, its intensity is controlled by changing the relative distance between the two magnets. Also, as the ball bearing is fixed onto the glass plate of the vat of the DLP, it becomes the new reservoir for the resin (Fig. 5.4d). Finally, Fig. 5.4e sketches the whole apparatus.

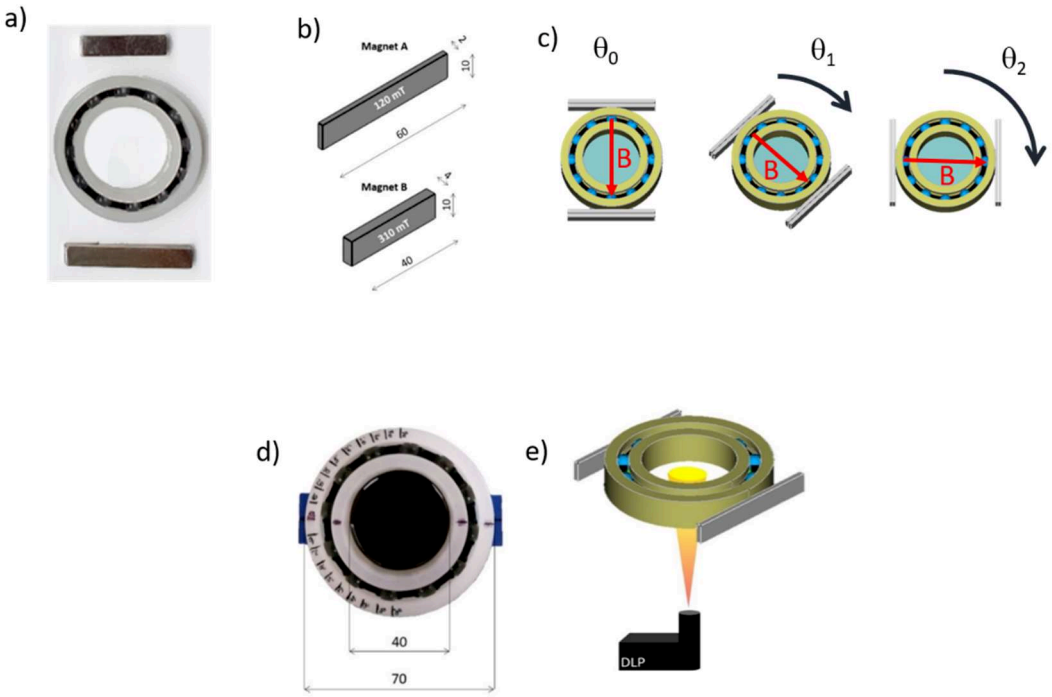

Figure 5.4: a) Non-metallic ball bearing and used NdFeB permanents magnets. b) Geometries and magnetic field of the tested magnets. c) The designed set-up of magnets and ball bearing allowing the rotation of the magnetic field. d) The adopted ball bearing and its geometrical dimension. The inner hole of the ball bearing acts as a resin reservoir. e) this set up allows the passage of the light emitted by the light projector of the DLP 3D printer.

The addition of the ball-bearing in the printing plane led to some modifications to the original set-up of the HD 2.0+ RobotFactory (Fig. 5.5). First, the metallic vat of the printer (Figs. 5.5a-b) has been removed and the ball bearing was fixed onto the bottom glass of the vat (Figs. 5.5c-e). In the HD 2.0+ RobotFactory, this glass plate is covered with a protective film (named *siligel*) which is fixed to the metallic vat through a screws system. The *siligel* is compulsory for the printing process as it ensures the detachment of the printed layers from the printing area. To maintain the *siligel* anchored to the printing glass, a PLA structure with the same dimensions as the original vat and reproducing the exact screw-holes was 3D printed using an FFF 3D printer (FlashForge Creator Pro). As it is not possible to accurately reproduce the threading of the holes, the PLA structure was fixed to the glass with a system of aluminum screws and nuts. Thanks to this solution the inner hole of the ball bearing became the new resins reservoir where the photocurable formulation can be poured. Finally, as the addition of ball bearing as a new resin reservoir limits the printing area to the dimension of the hole, a custom glass cylinder with a diameter of 25 mm and a height of 40 mm was crafted and glued to the platform

acting as growth platform (Figs. 5.5 c-e). It is worth mentioning that using this configuration, the added elements neither interfere with the projected light nor deflect the magnetic field produced by the magnets.

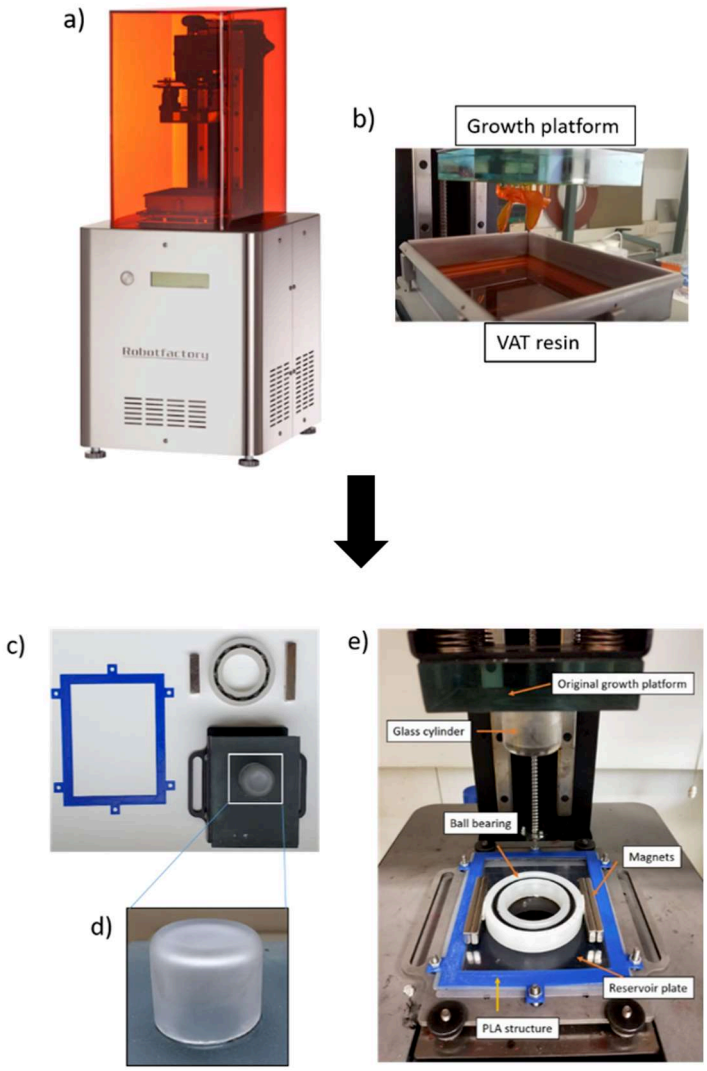

Figure 5.5: a) DLP Robotfactory (HD 2.0+), b) detail of the growth platform, and the vat resin. c) Ensemble of the modified and added pieces, d) detail of the glass cylinder used as a new growth platform. E) Modified Robotfactory 3DL HD 2.0+ to control the magnetic chains assembling and direction in the X-Y plane.

5.2.2 Mapping of the magnetic field distribution in X-Y plane

A homogeneous magnetic field distribution within the center (the hole) of the ball bearing is mandatory to ensure a proper homogeneity of magnetic fillers inside the printed object (Fig. 5.6a). On the contrary, whenever a magnetic gradient is present, it induces the migration of the fillers toward the magnets and the edges of

the ball-bearing, causing the creation of a depleted region of NPs in the center of the printing area as shown in Fig. 5.6b.

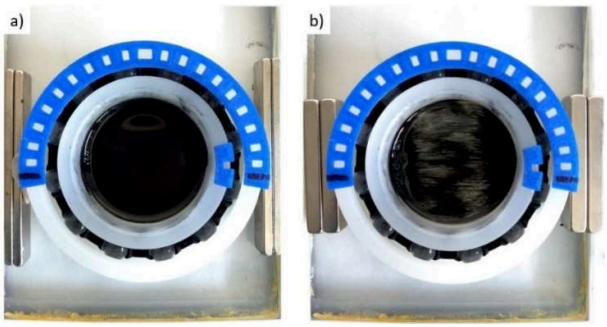

Figure 5.6: Distribution of the magnetic fillers dispersed in the photocurable resin according to the configuration of the permanent magnets: a) AA-AA, and b) BB-BB. In the latter, remarkable inhomogeneities are observed as well as depleted areas.

The homogeneity of the nanoparticles dispersion was tested by leaving the resins exposed to the magnetic fields for 30 min, a time compatible with the printing time for an object of 5 mm thickness.

First, the spatial distribution of the magnetic field in the central hole of the ball-bearing has been mapped. This has been done by evaluating with a teslameter the intensity of the field in 13 different zones of the printing area as shown in Fig. 5.7 a. For each point, 5 measurements were taken, the estimated error is 0.1 mT. The mapping has been done by considering several combinations of A and B NdFeB magnets and reported in Figs. 5.7b-f. Configurations composed of A-A and AA-AA magnets (Figs. 5.7b and 5.7c respectively) produce a quasi-homogeneous magnetic field whose intensities at the center of the printing area are 5 mT and 10 mT, respectively, and the gradient was estimated to be $\delta G_x \approx 1 \div 2$ mT/cm. In both cases, a homogeneous distribution of the nanoparticles within the printing area is observed as shown in Fig. 5.6 a.

Figures 5.7 d-f show the B-B, BB-BB, and BA-AB configurations. Here, the intensity of the magnetic field at the center of the printing area is 11 mT, 20 mT, and 15 mT respectively, whereas the field gradient has been estimated to be $\delta G_x \approx 5 \div 10$ mT/cm. This value is one order of magnitude larger than those observed for the A-A and AA-AA configurations and favors the migration of the fillers toward the edges of the ball bearing and the formation of a depleted zone within the printing area, as shown in Fig. 5.6b.

These preliminary tests have been used to choose the correct combination of magnets to be used in the 3D printer. The results indicate that only A-A and AA-AA configurations are suitable for our purpose as they guarantee an optimal distribution of the particles within the printing area.

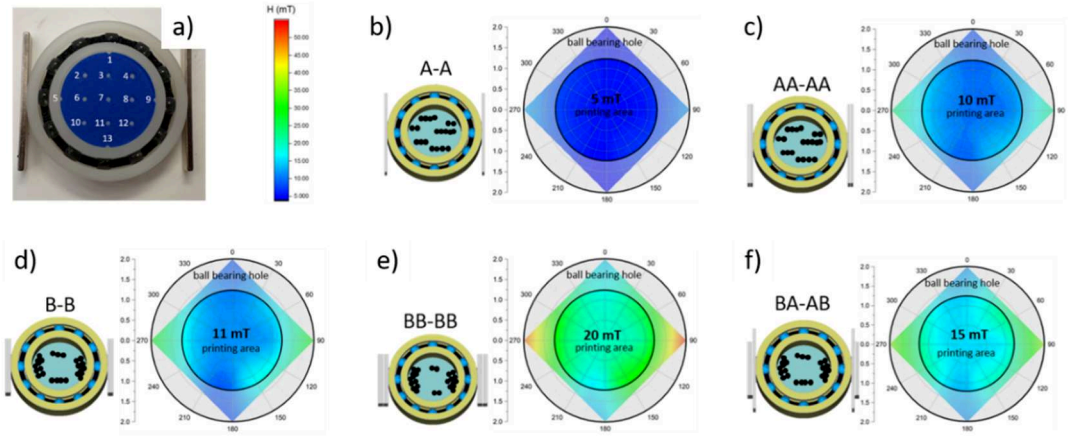

Figure 5.7: Magnetic field distribution tested for different magnets couples: a) A-A, b) AA-AA, c) B-B, d) BB-BB, and e) BA-AB.

5.2.3 Control of magnetic chains direction in the X-Y plane during the 3D printing process: a proof of concept.

To validate our experimental setup, it is necessary to investigate if the magnetic field produced by the two chosen configurations of magnets (A-A and AA-AA) is sufficient to obtain the desired magnetic microstructure in the printed objects. This was done by using the modified Robotfactory HD 2.0+ (Fig. 5.5e) to print a pyramid-like three-level object, shown in Fig. 5.8a. For each planar floor of the pyramid, the direction of the magnetic field was changed by manually rotating the external wall of the ball bearing such that three different chains orientations were obtained: respectively at 0°, 45°, and 90° (Fig. 5.8b-c). The thickness of each planar floor was chosen to be 500 µm, sliced into 10 sub-layers, each 50 µm thick, Fig. 5.8a. The microstructural organizations of the three planar levels have been investigated by optical microscopy. To facilitate the observation of the embedded chains and to minimize the absorbed light, the load of nanoparticles dispersed within the resin has been limited to 0.5 wt.%.

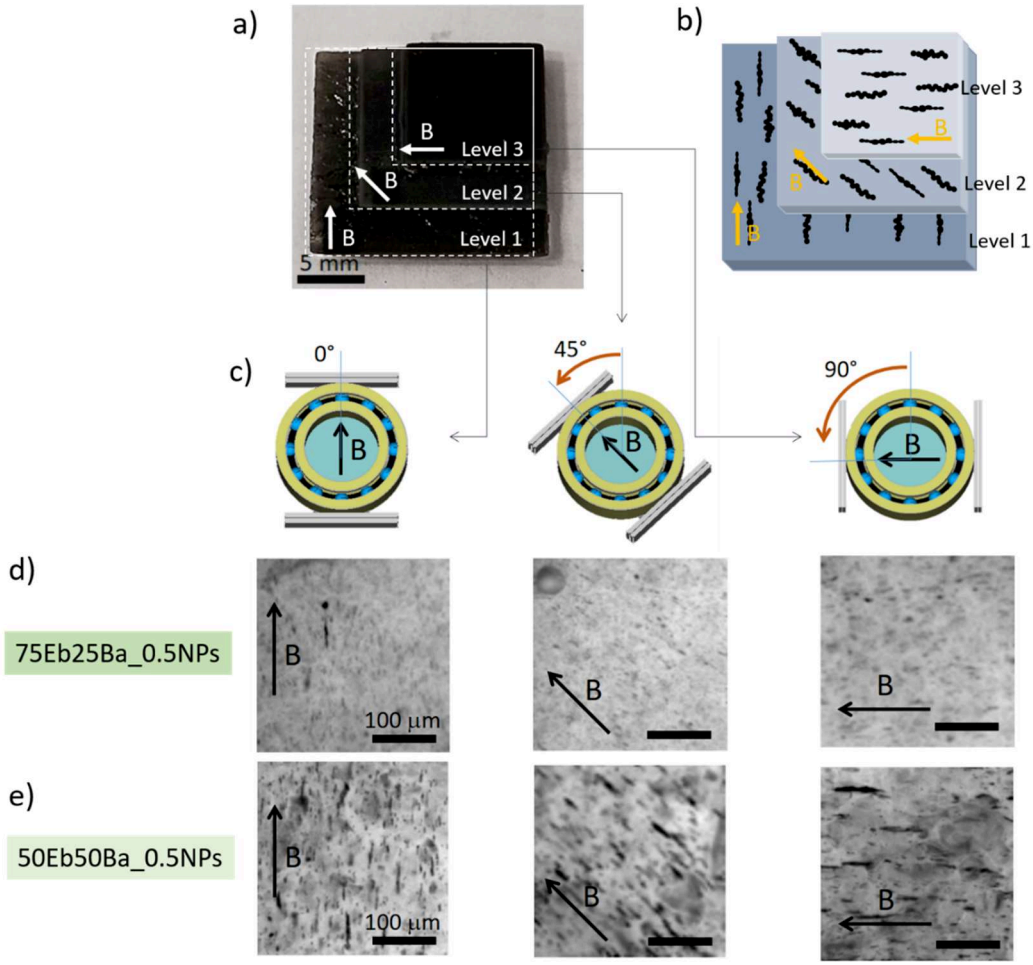

Figure 5.8: a) DLP 3D printed object containing three layers (500 □m each) with different orientations of nanoparticles chains. b) sketch showing the different orientations of the chains. c) sketch showing the orientation of the magnets to obtain the three-level structure with magnetic chains oriented at o°, 45°, and 90°. Optical images of the microstructures observed in the printed objects for d) 75Eb25BA_05NPs and for e) 50Eb50BA_05NPs formulations. The reported images are a collage of three different pictures taken at different focus points to maximize the contrast of the microstructure in the three different levels. The scale bar is 100 µm.

In Figures 5.8d and 5.8e are reported the microstructures observed in each planar floor (1,2, and 3) corresponding to the formulations 75Eb25BA and 50Eb50BA. The AA-AA magnet configuration was employed, measuring a magnetic field in the center of the printing region of 10 mT. Clearly, for both the formulations, optical images show that in each floor of the pyramid the chains of NPs are oriented following the direction of the applied magnetic field, which is indicated by the arrows in Fig. 5.8d-e. Nonetheless, some differences between the two formulations are visible. As observed in the previous chapter, the higher the viscosity of the formulation, the shorter the length of the chains. Indeed, the chains assembled in the more viscous formulation (75Eb25BA), Fig. 5.8d, are shorter than those embedded in the less viscous one (50Eb50BA), Fig 5.8e.

To conclude, these results validate the proposed set up to control the microstructure during the 3D printing process in the X-Y plane. Indeed, we demonstrated the possibility to print a pyramid-like object where each floor possesses distinct oriented microstructures.

In the next section is discussed how to control the direction of the chains in the three dimensions of the space, by adding a magnetic field in the Z direction.

5.3 Magnetic field in the Z direction

The control of the orientation of the magnetic chains' in the Z-axis is the last step to achieve the full programmability of the microstructures during the printing process. As for the orientation of the magnetic chains in the X-Y plane, some conditions must be satisfied. These are i) the necessity to minimize the magnetic gradient within the printing region to avoid depleted regions as shown in Fig. 5.6b. ii) the necessity to minimize the interaction with other magnetic elements e.g. the permanent magnets attached to the ball-bearing, and finally, iii) the necessity to avoid shadow-areas over the resin reservoir produced by any elements placed along the pathway of the light coming from the projector. This last point excludes the possibility to use permanent magnets, as they should be placed below, and above, the resin reservoir, or Helmholtz coils because of their dimension and the weakness of the delivered field. Thus, an alternative solution was developed.

5.3.1 Solenoid set-up

To produce a magnetic field in z-direction a solenoid has been used (Fig. 5.9). This is, an electromagnet, which generates a magnetic field through a coil allowing the production of a uniform magnetic field in a volume of space when an electric current is supplied.

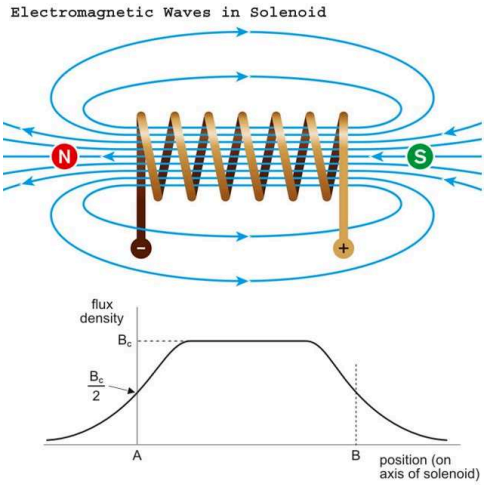

Figure 5.9: Sketch showing the magnetic field generated by a solenoid, and the magnetic field intensity along the solenoid axis.

The magnetic field produced at the center of an ideal solenoid is equal to:

$$B_{int} = \mu \frac{NI}{h} \qquad \text{(Eq 5.1)}$$

Where B_{int} is the magnetic induction produced at the center of the solenoid, μ is the magnetic permeability of the medium, N is the number of coils, I is the intensity of the electric current, and h is the height of the solenoid. One important advantage of using a solenoid consists of the large tunability of the produced magnetic field. Once fixed the structural parameters of the solenoid (h, and N), the intensity of the Z component of the magnetic field can be controlled by varying the voltage supplied to the solenoid.

For our purposes, we used an electromagnetic lens from an electron transmission microscope (Philips CM30) reported in Fig. 5.10. The internal diameter of the lens is 45 mm, the external one 130mm, whereas the height was measured to be 40 mm. When the maximum voltage and current were supplied (~25 V and 2.5 A) the magnetic field intensity measured at the top of the solenoid was about 50 mT, i.e. ten times larger than the value usually obtained using Helmholtz coils.

Figure 5.10: Electro-magnetic lens recuperated from a Philips CM30 transmission electron microscope (TEM) used as a solenoid

Using the "parallelogram" method sketched in Fig. 5.2, the coupling of the X-Y stage with the solenoid leads to the vectorial combination of the two components of B (X-Y and Z) allowing to tune the strength and the spatial direction of the magnetic field vector in the whole space.

Two possible configurations have been explored to couple X-Y setup and a solenoid into a DLP 3D printer:

1. **The reservoir plate and X-Y stage are placed in the middle of the central cavity of the solenoid** (Fig. 5.11a). The first designed option consists of positioning the set up for the orientation in the X-Y plane (the ball bearing and the magnets, Fig. 5.4) in the center of the cavity of the solenoid where the magnetic field is nearly constant. Although this configuration would exploit the homogeneity of the magnetic field and the presence of parallel field lines within the cavity, the small diameter of the solenoid does not allow the insertion of the X-Y stage. Moreover, magnetic interactions between the solenoid and the permanent magnets may occur, losing control of the resulting magnetic field vector. One alternative could consist of replacing the solenoid with a couple of Helmholtz coils, see e.g. Fig. 5.3. However, we discarded this option as the field produced by the Helmholtz coils is about 4 mT, which may be not sufficient to control the spatial directions of the chains, especially when viscous resins are used.

2. **The reservoir plate and X-Y stage is placed above the solenoid** (Fig. 5.11b). In this case, the X-Y stage, and thus the resin reservoir, will be placed on the

top of the solenoid. Thanks to this solution the interactions between the solenoid and permanent magnets are minimized, while the light path is not obstructed. However, working on the top surface of the solenoid, the divergence of the magnetic field lines must be taken into account, as shown in Fig. 5.9. Indeed, it is well-known that the magnetic field lines near the entrance and exit of the solenoid are subject to non-linear effects that are difficult to accurately predict, and that can have a significant impact on the homogeneity of the distribution of the filler. To minimize these effects, it is necessary to work on the constructive aspects of the solenoid preferring solenoids with an internal radius larger than the ball bearing, to minimize the fringe fields and the magnetic field lines deflection in the printing area [214].

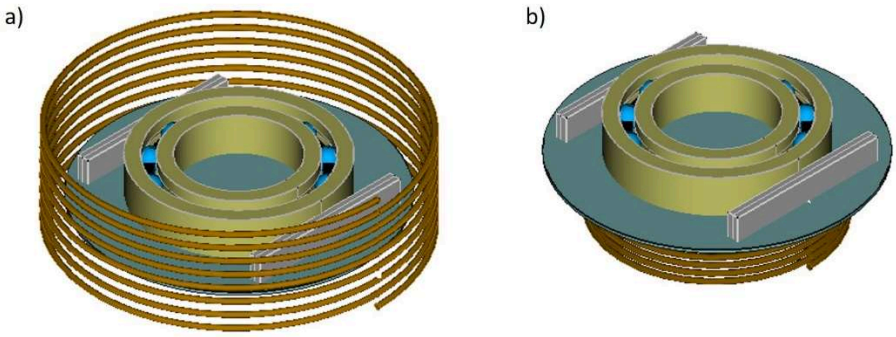

Figure 5.11: The two investigated solenoid positioning in the 3D printer: a) Solenoid centered to the resin reservoir, and b) Solenoid under the reservoir plate.

5.3.2 Control the orientation of magnetic chains in the whole space: a proof of concept

For our purposes, the second configuration was chosen, i.e. to put the reservoir plate above the electromagnetic lens. To check the feasibility of this choice, a prototypal experimental apparatus was built (Fig. 5.12a). The prototype has been tested in an optical microscope (Leica DFC295), where few drops of 50Eb50BA resin loaded with 0.5 wt% of Fe_3O_4 NPs were poured on the microscopy slide placed below the ball bearing.

The objective of this set up was to verify the effective control of the orientation of the self-assembled magnetic chains in the X-Y-Z space. The formation and the spatial evolution of the magnetic chains as a function of the orientation and the

intensity of the applied field **B** are shown in Figs. 5.12 b-h. Figure 5.12 b represents the as-deposited formulation, where neither permanent magnets nor the solenoid were used. In this case, fillers are homogeneously distributed within the resin. This corresponds to the initial configuration of the printable resin. First, self-assembled chains of vertically oriented NPs were obtained (Figs. 5.12 c). This was done by activating only the solenoid to generate a magnetic field of 10 mT using a current of 1.8 A and a tension of 10 V. Because the optical axis of the microscope coincides with the magnetic Z-axis produced by the solenoid, the image is composed by an ensemble of circular spots, each of which represents the projection of the vertically-aligned chain on the X-Y plane. Next, permanent magnets were introduced using the configuration A-A to add a magnetic field of 5 mT on the X-Y plane (Fig. 5.12 d). This results in the tilting of the magnetic vector from the Z-axis which is followed by the spatial rotation of the magnetic chains as shown in Fig. 5.11 c. The latter point is experimentally confirmed by the fact in the projected image of the chains is longer than in the previous case (Fig. 5.12 c). Then, the magnetic field in the X-Y plane was increased up to 10 mT by replacing the magnets from A-A to AA-AA configuration (Fig. 5.12e). Again, the magnetic chains appear longer, indicating that they were much more inclined on the X-Y plane. At this point, the field in the Z direction has been put to zero (B_z=0) by switching off the solenoid. In this configuration, magnetic chains are aligned in the X-Y plane (Fig. 5.12 f). To verify the reversibility of the process, the permanent magnets were removed, and the solenoid was again activated at 10 mT (1.8 A, 10V) to obtain vertically oriented chains (Fig. 5.12 g). To conclude, the horizontal configuration was again achieved by inserting the magnets and switching off the solenoid (Fig. 5.12 h).

The optical images validate our experimental approach demonstrating the good programmability of the microstructure within the photo-curable resin in the whole X-Y-Z space. Indeed, by varying the rotation of the ball bearing and controlling the voltage supplied to the solenoid, it was possible to tune the dimensions and direction of the magnetic chains. It is thus in principle possible to reproduce the same process in each printed layer and to fabricate a 3D printed material characterized by complex and spatially oriented microstructures. The magnetic forces and torques associated with the complex magnetic anisotropies would allow enhancing the actuation control on the 3D printed magnetic polymers exploiting

different types of movements within the same object. The final step will be thus the modification of the 3D printer to integrate this setup. This will be described in the next section.

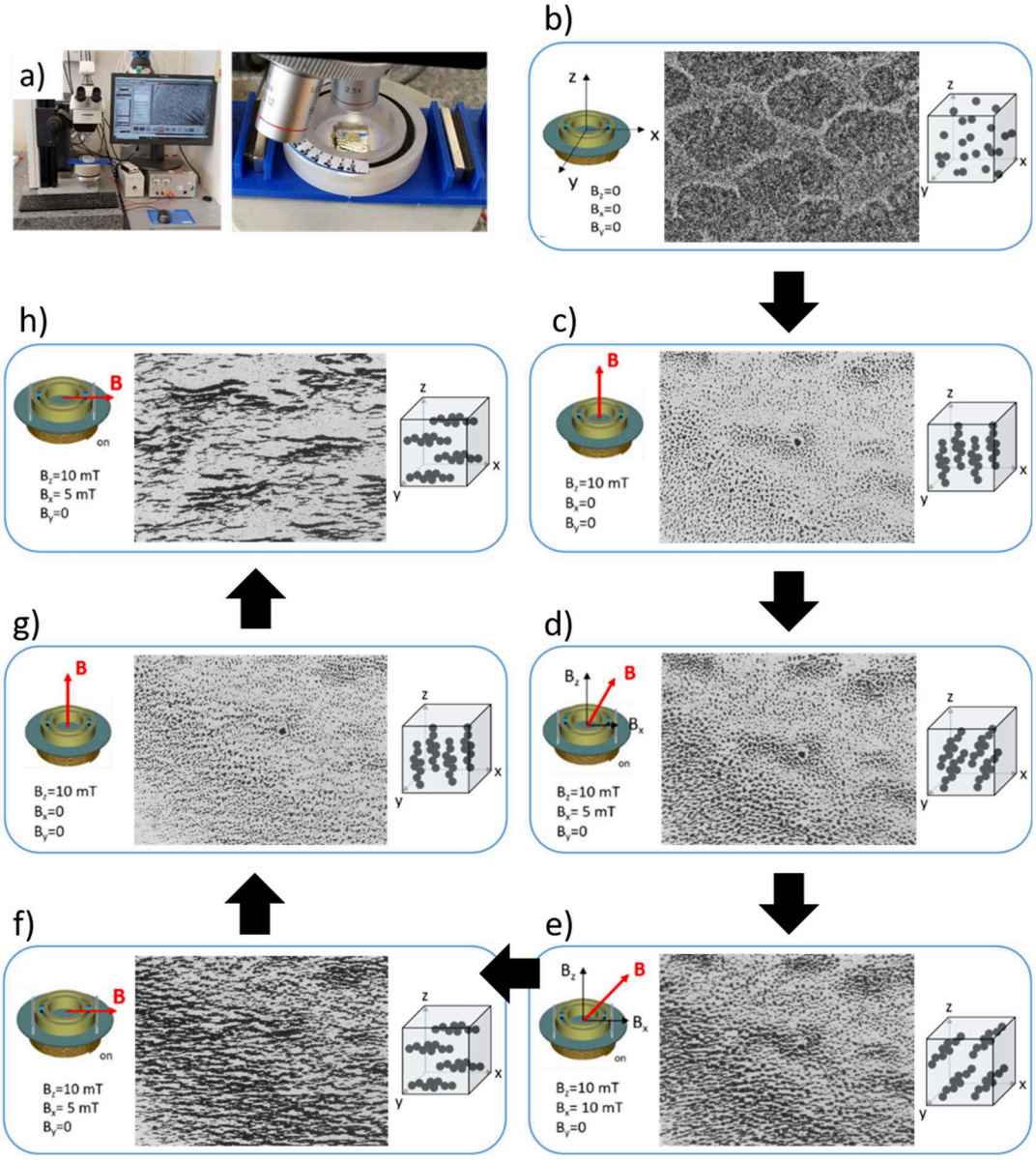

Figure 5.12: Programming of the spatial magnetic chains' orientation by tuning the magnetic field intensity generated by the solenoid and corresponding optical microscopy image.

5.4 Implementation of the set up into a DLP printer

Previous experiments validate the designed set up. The proper control of a magnetic field in the X-Y plane, obtained using permanent magnets, together with

the use of a solenoid to produce a magnetic field along the Z-axis, allows controlling the orientation of self-assembled magnetic nanochains. The implementation of this configuration in a DLP equipment will allow to program microstructures in magnetic composites during the printing process.

In the following, we will describe how, in principle, the DLP printer should be modified to include the magnetic setup. This is done by first describing the structure of a standard DLP printer, then showing which elements will be modified.

As shown in Fig. 5.13 a standard DLP printer can be divided into three different assemblies:

i) the **projector assembly** controls the optics of the 3D printer and allows to project the sliced images on the vat reservoir, where the photo-curing process sets in. The projector assembly is composed of the following elements: a light source, a digital mirror device (DMD), an optical lens. In some cases also a shutter can be present.
   - The illumination system can be either a high-pressure xenon lamp (e.g. bulb in projectors) with a broad emission range or a LED, with a narrower emission range.
   - The Digital Mirror Device (DMD) produces a pixelized image that is projected onto the resin tank where the selective curing process sets in. This is done by selectively reflecting the light produced by the illumination system using a matrix of microscopic mirrors arranged on a semiconductor chip. Here, each active mirror represents one pixel in the projected image, while the number of mirrors corresponds to the resolution of the image.
   - The lenses are used to focus the pixelized image onto the vat floor.
   - A shutter, when present, is activated by a servo motor, and it is used to stop the illumination between the printing of two successive layers.

ii) the **vat assembly** is responsible for the printing process and it is composed of two main elements: the resin reservoir and the vat actuator.
   - The resin reservoir contains the photocurable resin. Most DLP printers are in bottom-up configuration, thus the bottom of the vat is

transparent to UV or visible light. This allows the light to reach the photo-curable formulation and to activate the photopolymerization process. At the same time, it is important that the resin does not stick on the bottom of the vat, in order to avoid delamination of the objects or printing failure. For this reason, in most of the cases, the bottom of the vat is coated with a silicone or a fluorinated polymeric film, which prevents the adhesion of cured parts.

- A vat actuator motor is necessary to guarantee the correct printing of the different layers composing the object. Indeed, they must stick to the building platform, while detaching from the bottom window of the vat allowing the printer to renew the resin and the building of the next layer. There are several types of motions for the vat actuator motor that can be used for this purpose: tilt, horizontal translation, rotation, and contemporary tilt-and-shift. The last process is used in the Robotfactory HD 2.0+ printer.

iii) the **build platform assembly** allows the movement of the building platform along the Z-axis.

- The building platform is the element where the printed object is built on.
- the Z stage is composed of two sub-elements: an endless screw (or worm screw) where the build platform is fixed and a stepper motor. The latter controls the lifts and lowers of the build platform into the resin tank and allows to define the thickness of the printed layers. The displacements of the Z-stage are synchronized with the vat actuator motors, which tilt the tank to peel away successive layers before the next movement of the Z stage, and the servo motor, which closes the shutter between two successive printed layers.

iv) The **software** and the **micro-control unit**.

- From the software point of view, the object is first designed as a CAD file and then transformed into an STL file. The STL file describes an object by its external surface as defined by a series of

triangles (or facets). Using a slicing program the STL file is then converted into a series of thin layers producing a G-code file. The G-code (the positioning language of all CNC machines) typically contains all the printer parameters, such as speed and the illumination time, as well as the geometry of the 3D object.

- A micro control unit, such as Arduino or Raspberry pi, is finally used to distribute all the information contained in the G-code toward the different components of the DLP printer.

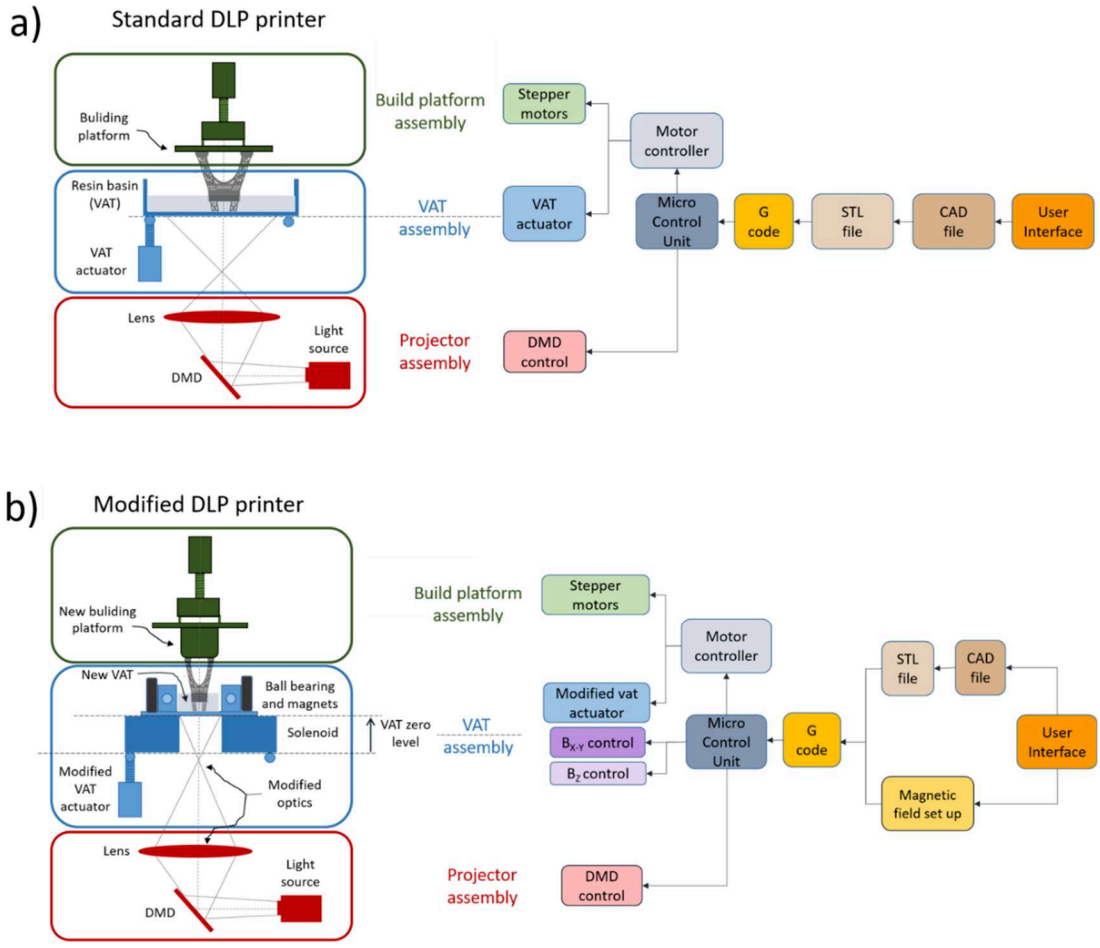

Figure 5.13: Sketches describing the different elements composing a) a standard DLP printer as well as the software control of the printing process, and b) a modified DLP printer.

After having described the elements composing a "standard" DLP printer, the schematics of Fig. 5.13b describes now how the printer should be modified to introduce the magnetic set-up. Fig. 5.14, shows the printing of magneto-responsive polymers with the control of the microstructures in the whole space.

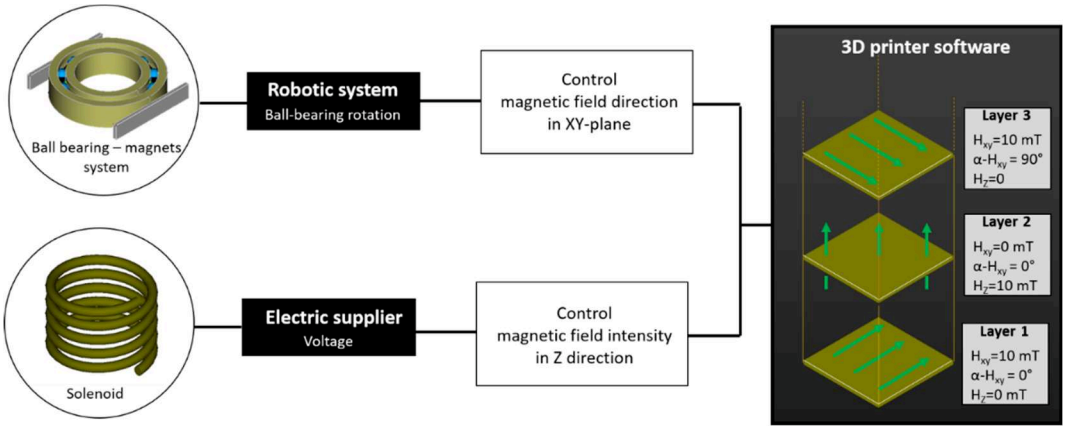

Figure 5.14: Schematics of the integrated system to control the magnetic field direction in the 3D printer.

The insertion of the ball-bearing system together with the solenoid leads to unavoidable modifications in all of the three levels of the 3D printer (Figs. 5.15a-b). For a better comprehension of the problem, here it is discussed firstly the implications of the ball-bearing, and later those of the solenoid.

As briefly mentioned before, the substitution of the original resin reservoir of the 3D printer with **the ball-bearing** produces a reduction of the printable area, which is now determined by the central cavity (Fig. 5.15c). Since the original building platform can no longer reach the resin due to its geometrical footprint, it is necessary to modify its shape. The simplest solution consists of adding a new stage that fits with the dimensions of the inner hole of the resin reservoir. This system alteration does not significantly change the 3D printing apparatus, since it is only necessary to modify the original zero level of the printer, which is easily accessible from the printer computer interface.

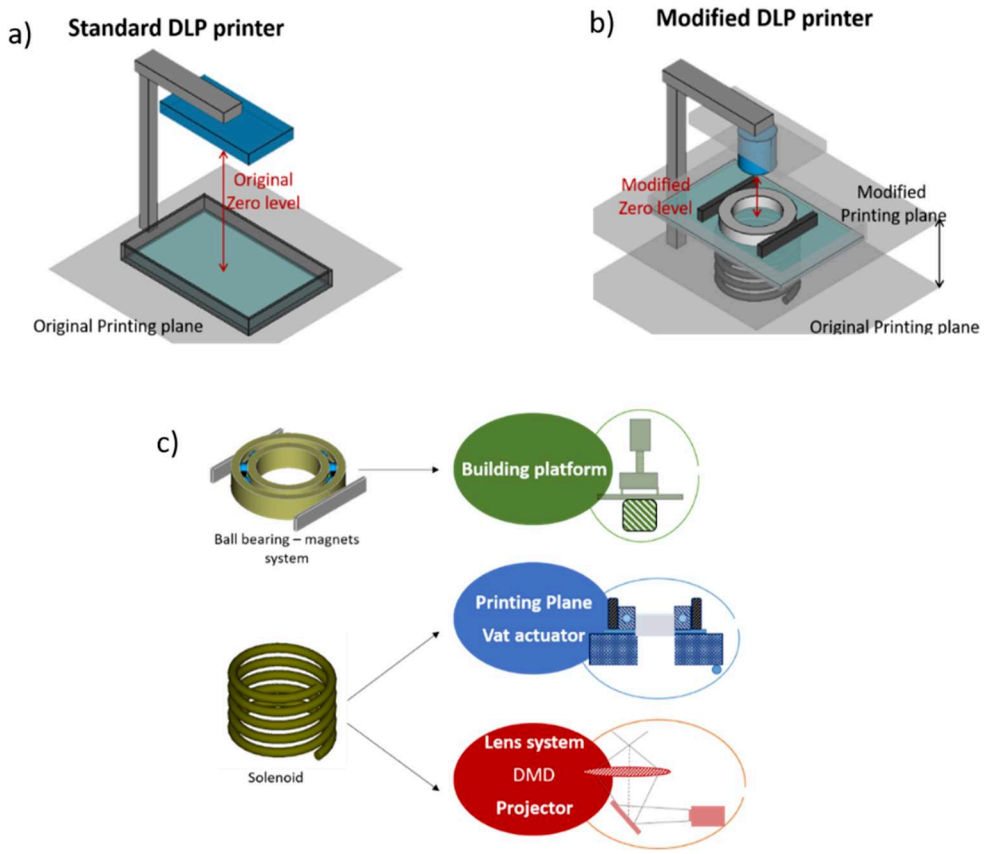

Figure 5.15: Sketch describing the modifications introduced by the ball bearing-magnets system and the solenoid

On the other hand, the addition of the **solenoid** significantly alters the initial configuration of the 3D printer and its components (Fig. 15.5b-c). For the correct operation of the solenoid, it is necessary to position it underneath the resin reservoir such that the magnetic field lines are perpendicular to the printing plane. Due to the compactness of commercial 3D printers, the space between the lenses and the resin reservoir is often limited, and it does not allow the easy insertion of the solenoid. In the case of HD 2.0+ Robotfactory, it is mandatory to raise the vat to include the solenoid in the 3D printer (see vat assembly module in Fig. 5.13). This apparent easy solution implies a series of modifications in cascade which profoundly alter the operating system of the 3D printer:

1. The lifting of the resin reservoir involves an equal raising of the **printing plane**.
2. Since the printing plane is changed, it is necessary to adapt the **vat actuator** to ensure the tilt motion of the resin reservoir.

3. Due to the shifting of the printing plane, the image of the layer projected is now out of focus. To re-modulate the focus on the new printing surface it is obligatory to intervene on the **lens system** of the 3D printer and eventually replace it (projector assembly in Fig. 5.13).
4. As the light intensity scales as $I \approx 1/r^2$, where r is the distance between the light source and the irradiated surface, the light intensity on the new printing plane is reduced because of the larger distance between the **projector** and the resin reservoir. This may lead to an increase in the printing times due to the lower light dose, which control the photopolymerization (see chap. 1). In the worst scenario, the light intensity at the printing plane is not sufficient to induce the photopolymerization reactions within the resin, thus the original projector must be replaced with a more powerful one.

The physical modifications of the 3D printer are reflected at the software level. As previously discussed, the impact of the ball bearing – magnets system on the printer software is very low, since the modification of the zero-level is a controlling parameter already provided by the 3D printer software in the user interface. However, the modification of the optic system induced by the solenoid drastically changed the printer informatics. Indeed, the further distance of the focal plane requires a readjustment of the original optical layout. This involves several aspects of the software such as the light intensity emitted by the projector, scaling the image of the projected layer, and the re-calculation of the focal plane. All of these controls are not available at the user-interface of the software, but on the contrary, it is necessary to operate in the g-code of the printer. Thus, it is necessary to modify the programming code of the 3D printer that is not a trivial operation.

Furthermore, to achieve complete control of the proposed magnetic-assisted 3D printer, it would be necessary to add new functionalities to the software in order to program the magnetic field generated in each printed layer (Fig. 5.14). To control the magnetic field in the XY-plane, the ball bearing must be connected to a mechanism that controls its rotation, and this system must be integrated into the 3D printer software to select the magnetic field direction layer by layer prior to the printing process. On the other hand, to control the magnetic field in the Z-direction, the voltage provided by the electric supplier to the solenoid must be programmable via the 3D printer software. The two controlling systems must be integrated and

coordinated with the 3D printer software, so that it will be possible to program the microstructure of each printed layer, before the 3D printing process, directly from the computer user-interface. Both the operations require a profound intervention at the informatic level of the 3D printer, but once it is accomplished, this will lead to a fully automated manufacturing process.

The integration of the solenoid in the 3D printer leads to many constructive issues as well as important software modifications. Here the efficacy of the proposed system was demonstrated, and a protocol for the remodeling of the 3D printer hardware and software was given. Due to the multidisciplinary and intensive work requested, the modifications on the 3D printer were not completed. Nevertheless, it was possible to install the ball-bearing system in the resin reservoir and manually control the magnetic field in the XY-plane which is not a minor achievement.

5.5 Conclusion

In this chapter, we demonstrated an easy approach to induce the self-assembling and the orientation of magnetic chains of fillers in the X-Y plane during the 3D printing process. Owing to its simplicity, this design can be easily implemented in any type of DLP or SLA 3D printers. Besides, we are working to further improve our set-up to introduce the magnetic field in the Z direction and thus to obtain control of the magnetic microstructures in all directions of space. The reported experimental results clearly show the efficiency of our set-up composed of a ball bearing and permanent magnets coupled with a solenoid. Its integration into a DLP printer was successfully achieved concerning the ball bearing device, but not for the solenoid due to constructive limitations. The aim of this work was to outline and investigate the constructive solutions to control a magnetic field during the 3D printing process, the proper modification and integration of the system in the DLP printer was beyond our purpose, and it will be divided into three parts.

i) Improving the homogeneity of the generated magnetic field to achieve higher intensities, by modifying the shape and spatial configuration of the magnetic components.

ii) developing a software that will be interfaced with the 3D printer software allowing to program the rotation of the ball bearing (and thus of the applied magnetic field) during the printing process.

iii) modifying the 3D printer software to subdivide each layer in voxels, allowing multiple chains' orientations in each printed layer, similar to other works reported in the literature[176].

6.

4D printing of magneto responsive composites with programmable microstructures

6.1 Introduction

In this chapter, we report on the 3D printing of several magneto-responsive objects and devices remotely activated and controlled. The results reported here summarizes the researches developed during the Ph.D.'s years, which are described in the previous chapters. These are the 3D printing by a vat-polymerization technique of nanocomposite polymers with dispersed magnetic fillers (Chap. 3), and the control of the self-assembly process of magnetic particles dispersed in viscous media (Chap. 4). Here, the Ebecryl8232-Buty acrylate-based formulations containing oriented magnetic microstructures have been 3D printed using a modified RobotFactory HD 2.0 DLP, as illustrated in Chapter 5.

First, the relationship between the microstructure and the mechanical properties of the printed magneto-responsive samples has been investigated. Then, the correlation between the microstructures and magnetic properties of the composites has been evaluated to determine the magnetic anisotropies of the materials.

By Scanning Electron Microscopy, the microstructure of the 3D printed samples was observed, investigating also the effect of NPs concentration on the average size of the magnetic chains. The mechanical properties of the materials were evaluated by measuring their elastic moduli for different microstructural organizations via stress-strain tests. Alternating Gradient Field Magnetometer was

used to magnetically characterize the printed samples and evaluate the effect of the embedded chains on the magnetic anisotropy of the materials. At last, programmable magnetic-driven hammer-like structures and magneto-responsive spur gears have been printed to investigate the rotation and bending movement of the actuators; those allowed to conceive several types of devices.

6.2 SEM investigations on the microstructure of the 3D printed samples

In chapter 5 we used an optical microscope (Leica DFC295) to demonstrate that the modified magnetic-assisted DLP printer was effective to control the microstructure of 75Eb25BA_0.5NPs and 50Eb50BA_0.5NPs samples (Fig. 5.8). This was achieved by applying the magnetic field in the vat resin to induce the self-assembly of the NPs into aligned chains. The arrangement of the embedded chains was controlled in each printed layer by rotating the magnetic field. However, when the concentration of embedded magnetic fillers was higher than 3 wt.% the image contrast resulted too low to use optical microscopy to characterize the microstructure of the printed objects. For this reason, the magnetic chains in highly NPs loaded samples were investigated with Scanning Electron Microscope using a Field Emission Zeiss Supra 40 FESEM. The characterizations were performed on 75Eb25BA samples at increasing NPs concentrations of Fe_3O_4 NPs (2%, 4%, 6%, and 8%) exposed to a magnetic field of 10 mT during the 3D printing process. A 75Eb25BA_8NPs sample with only dispersed NPs was also investigated and used as a reference. The samples were cryo-fractured to avoid plastic deformation in the nanocomposites to characterize the aggregates on the surface of the specimens as well as in the bulk.

Magnetic chains were observed in all the samples exposed to the magnetic field during the 3D printing process (Fig. 6.1a-d). On the other hand, in the reference sample, 75Eb25BA_8NPs, where no magnetic field was applied, no chains were observed, but only small aggregates (Fig. 6.1e). This confirmed that the application of the magnetic field induces the formation of magnetic chains during the 3D printing process and that the assembled chains were effectively incorporated within the polymeric matrix. Focusing on the samples containing organized

microstructures, as expected the dimension of the chains increases with the NPs concentration (Fig. 6.1a-d at the highest magnification). This result is coherent with the existing literature [168], [169], and in good agreement with the optical analyses described in chapter 4. In addition, SEM images show a good filler-matrix interface. Indeed, no voids or detachment areas were observed in the surroundings of the aggregates which is the primary condition for a good stress transfer between the matrix and the magnetic fillers [215]–[217].

These results confirm that the modified DLP printer allows to produce polymeric magnetic composites with programmable microstructures up to a load of 8 %wt. of NPs dispersed in the photocurable resins.

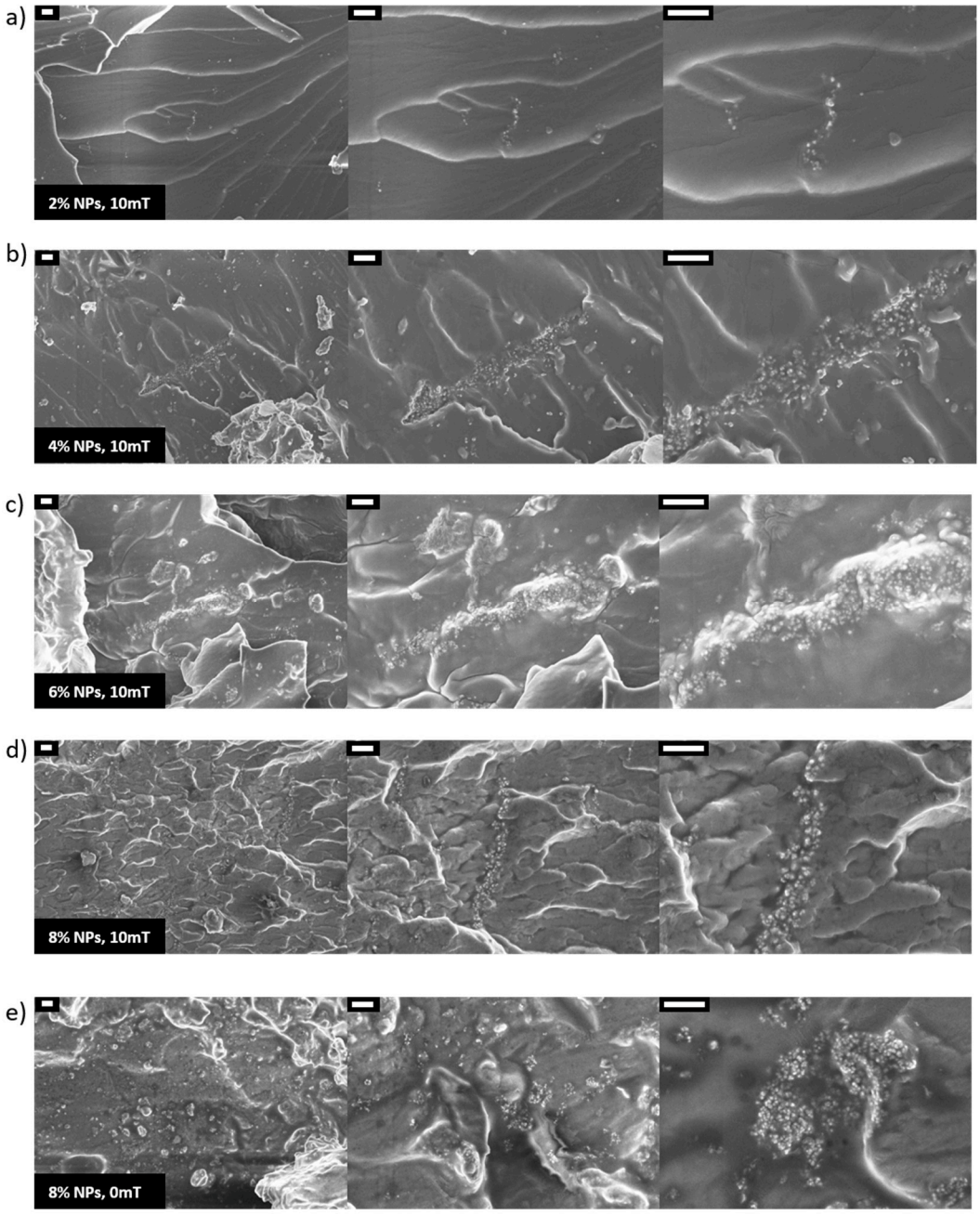

Figure 6.1: SEM images of cryo-fractured surfaces of 75Eb25BA samples 3D printed with the application of a magnetic field (10mT), for different NPs concentrations: a) 2%, b) 4%, c) 6%, d) 8% (the scale bar is 2 μm). In figure e) the images of 75Eb25BA_8NPs sample 3D printed without the assistance of a magnetic field and used as reference, (the scale bars are 2 μm).

6.3 Mechanical Properties

In the previous section, we have demonstrated that our magnetically-assisted DLP printer can effectively produce magnetic composite polymers with aligned chains of Fe_3O_4 NPs up to a load of 8 %wt. In this section, we investigate how the

presence of the embedded chains influences the mechanical properties of the printed material. This is done by studying the elastic moduli of the nanocomposites by stress vs strain tests performed using a Dynamic Mechanical Thermal Analysis (DMTA) apparatus in tensile configuration (Triton Technology TTDMA equipment). The details of the experimental technique have been already given in Chapter 3 (section 3.2.2). Elongation tests were run in load control (1N/min) at room temperature.

As described in Chapter 3 the optimum concentration of fillers for the printing process is 6 %wt. In addition, the stiffness of the printed composite can be tuned by varying the amount of butyl-acrylate (BA) in the Ebecryl (Eb) resin. For the aforementioned reasons, tests have been done on 75Eb25BA_6NPs and 50Eb50BA_6NPs formulations, giving rise to rigid and soft printed objects, respectively. Finally, as shown in chapter 4 (section 4.5) the application of a constant magnetic field of 10 mT allows the formation of the chains in a time which is compatible with the printing process.

As an example, the stress-strain curves measured for 75Eb25BA_6NPs samples obtained by applying a 10mT magnetic field during the printing process are reported in Fig. 6.2 The dimension of the tested specimens are 30x4x3 mm (length x width x thickness) and the chains have been oriented at 0°, 45°, and 90° respect to the length of the sample as shown in Figs. 6.2b-d. For comparison, the same formulations were also 3D printed with randomly dispersed NPs and used as a reference (Fig. 6.2a).

For each experimental configuration, four measurements have been performed (the red, green, blue, and black curves) and the elastic modulus has been obtained considering the slope of the curves in the elastic deformation region:

$$E = \left(\frac{Stress}{Strain}\right)_{elastic\ region} \qquad \text{(Eq. 6.1)}$$

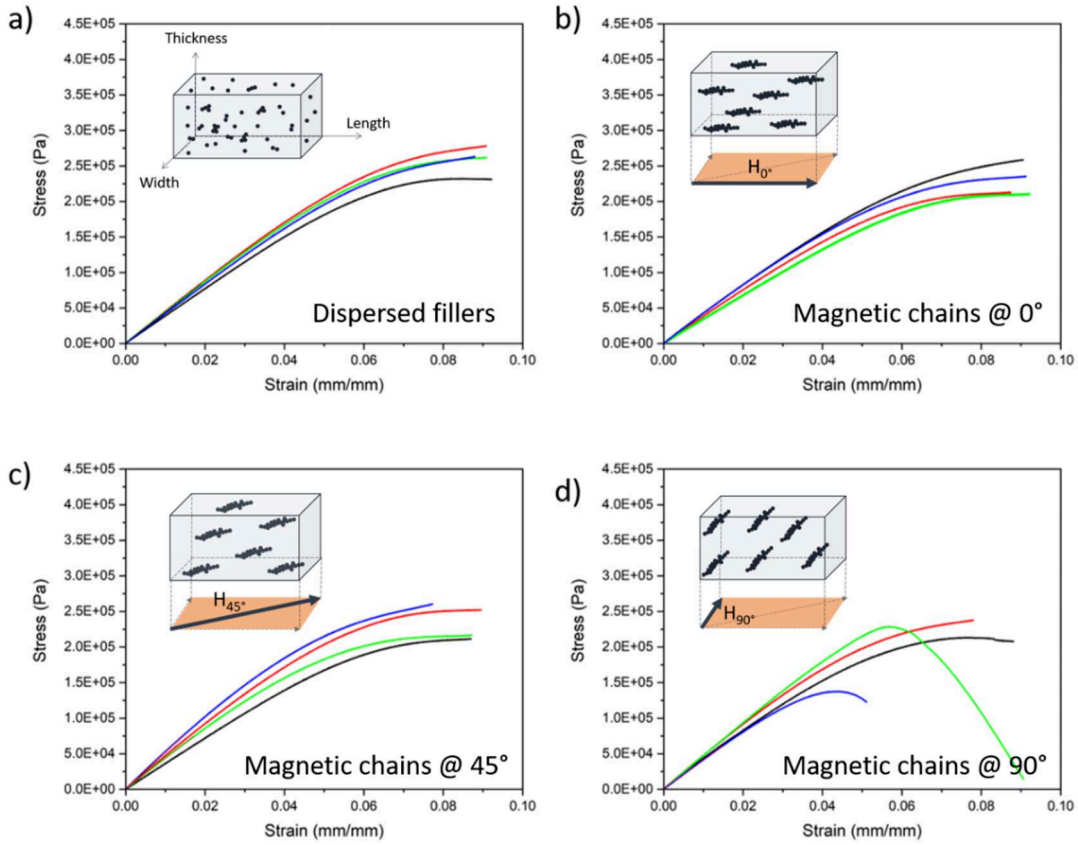

Figure 6.2: Stress-strain curves obtained for 3D printed 75Eb25BA_6NPs samples with a) dispersed NPs, b) magnetic chains at 0°, c)magnetic chains at 45°, and d) magnetic chains at 90°. The samples with organized microstructures were 3D printed applying a magnetic field of 10 mT during the printing process.

In Fig. 6.3 the elastic moduli measured for the different orientations of the chains (0°, 45°, and 90°), have been compared to the reference sample containing only dispersed NPs.

For the stiffer polymeric matrices (75Eb25BA_6NPs) the orientation of the chains does not modify the value of the elastic modulus which is, within the error bar, equivalent to those of the reference sample containing only dispersed NPs (~4.5 MPa). These results evidence that the microstructural organizations do not alter the mechanical response of the composites when subjected to tensile stress.

For the softer polymeric matrix (50Eb50BA_6NPs), again no difference in the mechanical response of the composites was observed for the different chains orientations and magnetization times (~3.4 MPa). However, a reduction of the elastic modulus of about 10 % is observed with respect to the reference sample containing only dispersed NPs (~3.75 MPa). Probably, the incorporation of large aggregates leads to the formation of defects in the material, and this effect is more remarkable in the softer material, i.e. 50Eb50BA polymeric matrix.

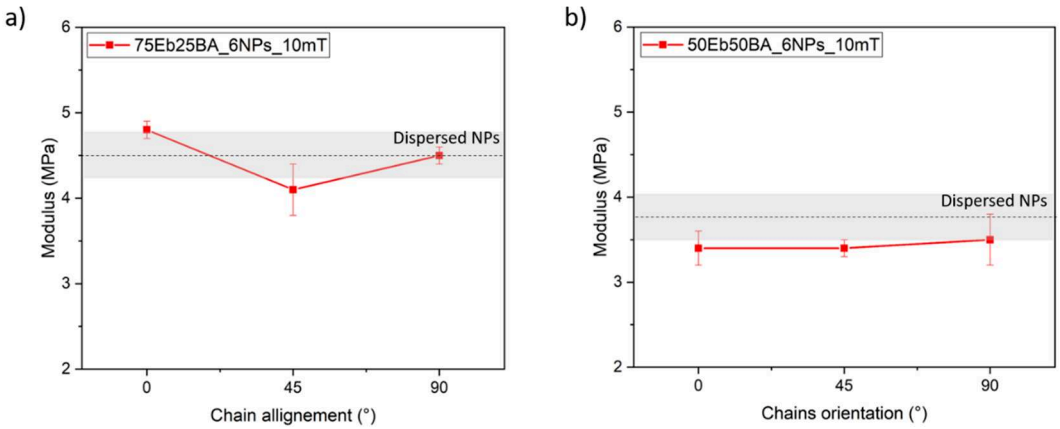

Figure 6.3: Elastic modulus vs chain alignment trends for a)75Eb25BA_6NPs, and b) 50Eb50BA_6NPs samples. The dot lines represent the elastic moduli measured for samples with only dispersed NPs.

In conclusion, the mechanical response of the printed composite materials is mainly driven by both the polymeric matrix (here expressed as the Ebecryl 8232 and BA ratio), and the amount of embedded nanoparticles. Moreover, as the mechanical response of the materials is not chain-orientation dependent, it can be supposed that in 3D printed composite materials with controlled microstructure the presence of the nanochains does not influence the mechanical properties.

6.4 Magnetic properties of the 3D printed samples

We have shown that the magnetically-assisted DLP printer is effective in both initiating the self-assembly process of the Fe_3O_4 NPs dispersed in the photocurable formulations into chains-like microstructures, and in controlling their spatial orientation during the printing process. In this section, magnetic characterizations have been performed to check whether the presence of oriented microstructures generates magnetic anisotropies in the 3D printed nanocomposite materials. This can be exploited to remotely control the movements of the printed objects.

The magnetic tests were performed in collaboration with Gabriele Barrera and Paola Tiberto from Istituto Nazionale di Ricerca Metrologica (INRIM).

First, we describe how to calculate the magnetic anisotropy in the case of a composite material. A hysteresis loop describes the magnetic response of a sample exposed to a magnetic field. Here, the hysteresis cycles have been recorded using an Alternating Gradient Field Magnetometer (AGFM) using 3D printed cubic samples (3x3x3 mm). Using the hysteresis cycle curve, it is possible to measure the

extent of magnetization in a material by an applied magnetic field. This quantity is known as the magnetic susceptibility, χ, and it is defined by the ratio of magnetization, M, to the applied field intensity, H. As χ is a tensor, it can be used to estimate the magnetization of the sample along different spatial directions. Thus, the magnetic susceptibility measured at the coercive field $\chi_c(H_c)$ has been selected as a physical indicator to estimate the degree of magnetic anisotropy in the material (Fig. 6.4).

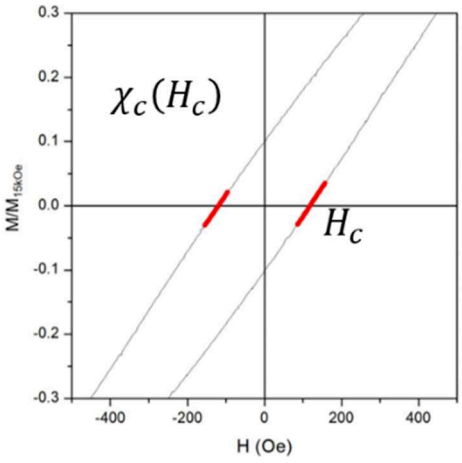

Figure 6.4: Example of a magnetic hysteresis cycle. In red the curve sections where the magnetic susceptibility at the coercive field was measured.

To investigate the magnetic anisotropy of the composite materials, three testing magnetic fields have been applied during the measurements, which are here named as parallel (x-direction), transversal (y-direction), and perpendicular (z-direction), and four different microstructural configurations have been considered: i) dispersed NPs, ii) magnetic chains at 0° (x-direction), iii) magnetic chains at 45° (in the x-y plane), and iv) magnetic chains at 90° (y-direction). For the sake of clarity, a sketch of the experimental set-up is reported in Fig. 6.5.

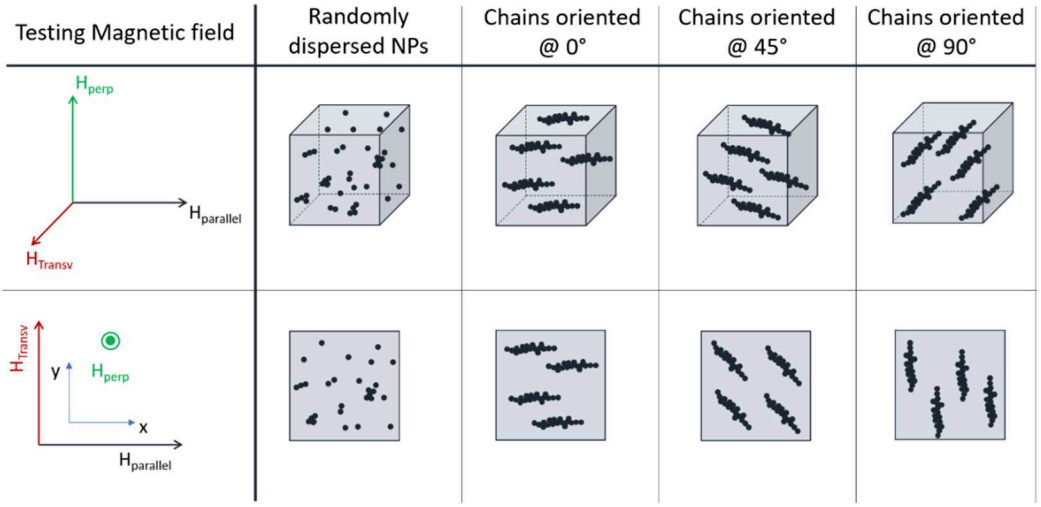

Figure 6.5: Experimental set-up used to test the cubic 3D printed 75Eb25BA_6NPs samples according to the organization of the magnetic chains and the direction of the testing fields.

6.4.1 Measuring the magnetic anisotropy varying the orientation of the microstructures

First, the magnetic anisotropy of 75Eb25BA-based samples has been analyzed as a function of the orientation of the microstructures, the fillers concentration, and the applied magnetic field. These results will be then compared to those obtained with the 50Eb50BA-based composites. Figure 6.6 shows the magnetic hysteresis cycles, normalized to the saturation magnetization (Ms), measured along three directions of the magnetic field: parallel (H_{parall}), transversal (H_{trans}), and perpendicular (H_{perp}) for the 75Eb25BA_6NPs samples in different configuration of the microstructures: a) dispersed NPs, b) chains oriented at 0°, c) chains oriented at 45°, d) chains oriented at 90°.

As expected, for the samples with dispersed NPs the hysteresis cycles measured along the three main axes are perfectly overlapping (Fig. 6.6a). Thus, the magnetic properties of the material are constant in the three directions of the space demonstrating the magnetic isotropy of the composite. On the contrary, when magnetic chains are formed, the hysteresis cycles are different along the three tested directions. In particular, for chains oriented at 0° (Fig. 6.6b) the hysteresis cycle measured along the parallel direction, coincident with the orientation of the chains and indicated by the black curve, shows a higher slope in the magnetization curve compared to the other two directions, which hysteresis curves overlap (green and

red curves). Therefore, the sample at 0° exhibits a preferable magnetization direction named *easy magnetic axis*; while the perpendicular and transversal directions are magnetically equivalent and they represent the hard magnetic axis of the material. For the sample with magnetic aggregates oriented at 45° (Fig. 6.6c), the parallel (H_{parall}) and the transversal (H_{trans}) hysteresis profiles i.e. the black and the red curves, are identical, and their slope is higher than the perpendicular (H_{perp}) hysteresis cycle, i.e. the green curve. Thus, the two directions are magnetically equivalent and the 45° orientation in the X-Y plane represents the easy magnetic axis of the material. When the chains were oriented at 90° (Fig. 6.6d), the magnetic chains are parallel to the transversal field (y-direction), and the latter constitutes the easy-magnetic axis of the material. Apart from this change of axis, the obtained results are similar to those previously discussed for the microstructure oriented at 0°.

These results demonstrate that the composite possesses a higher susceptibility when tested along the direction of the magnetic chains compared to the transversal and perpendicular ones which are magnetically equivalent. Because of this equivalence, in the next experiments the perpendicular magnetization cycle is no longer reported.

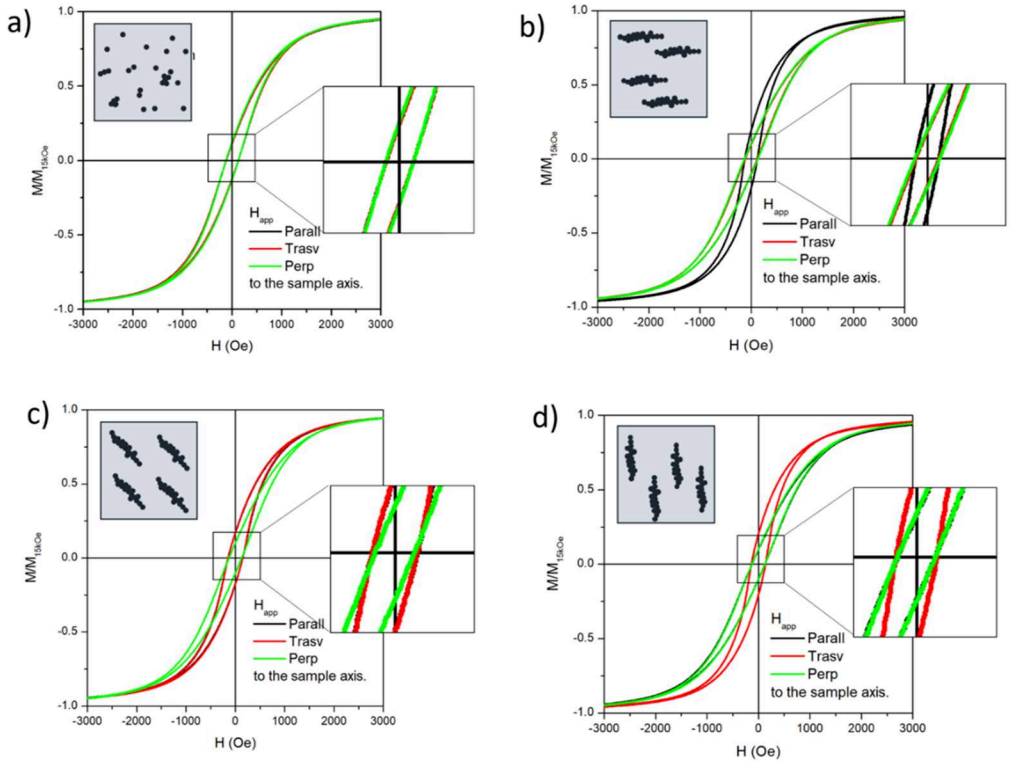

Figure 6.6: Magnetic hysteresis cycles measured along the three directions (parallel, transversal, and perpendicular) for the 75Eb25BA_6NPs samples differing by their microstructure: a) dispersed NPs, b) chains oriented at 0°, c) chains oriented at 45°, d) chains oriented at 90°.

The previous results indicate that the embedding of magnetic chains within the polymeric matrix induced magnetic anisotropy in the composite material. In order to develop soft polymers exploiting magnetic torques, it was necessary to have a numerical index describing the grade of magnetic anisotropy in the material.

6.4.2 Effect of NPs concentration

To investigate the influence of NPs concentration on the magnetic properties of the composite material, 75Eb25BA samples containing up to 8 wt.% of Fe_3O_4 NPs were 3D printed during the application of a constant magnetic field of 10mT. The magnetic susceptibility values reported in Fig. 6.7 were calculated for magnetic fields applied along and perpendicular to the easy axis of magnetization, i.e. the direction of the assembled chains (θ=0° and θ=90°, respectively).

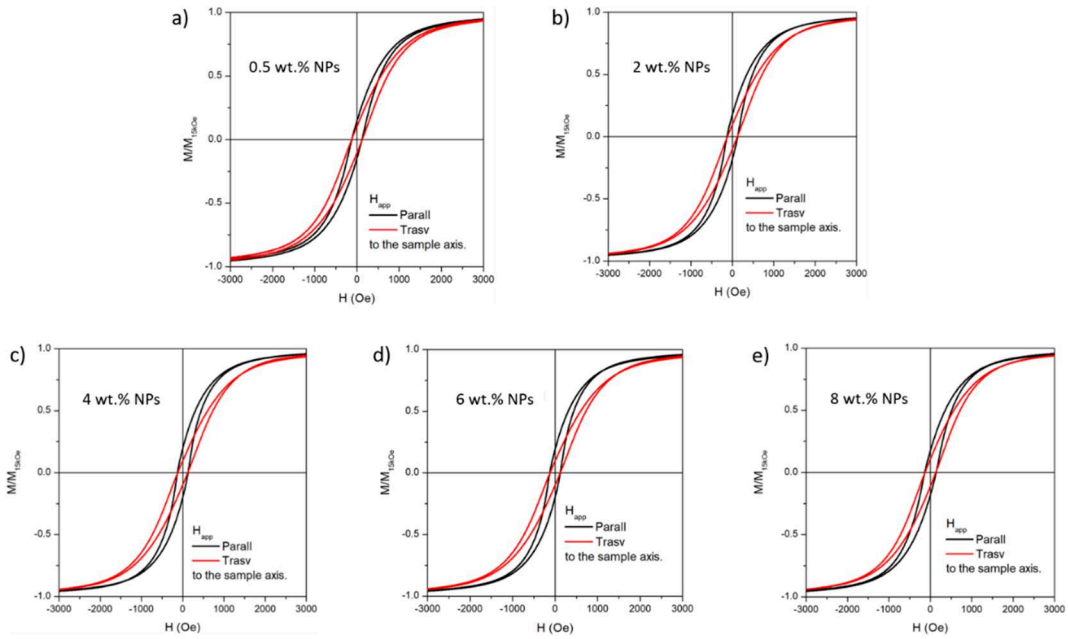

Figure 6.7: Magnetic hysteresis cycles measured parallel and transversal to the magnetic chains for a) 75Eb25BA_0.5NPs, b) 75Eb25BA_2NPs, c) 75Eb25BA_4NPs, d) 75Eb25BA_6NPs, and e) 75Eb25BA_8NPs samples. All the samples were 3D printed by applying a magnetic field of 10mT.

The evolution of magnetic susceptibility as a function of the concentration of the filler is shown in Fig. 6.8. The magnetic susceptibility of the sample containing only dispersed fillers is used as reference and it is reported on the figure by the grey dotted line. Experimental results show that when the probing field is normal to the direction of the chains (θ=90°), the magnetic susceptibility remains almost the same regardless of NPs concentration and lower than the magnetic susceptibility measured for the isotropic sample used as a reference. Thus, the hard-magnetic axis of the 3D printed composites is not affected by the load of the embedded particles. On the other hand, a more intriguing trend is observed when the field is applied along the easy axis of magnetization, i.e. the assembling direction of the chains (θ=0°). In this case, the χ_{HC} curve follows a bell-like profile. In particular, the magnetic susceptibility increases with the magnetic NPs concentration up to a load of 4 wt.%, remaining then nearly constant up to 6 wt.% of NPs. For larger NPs concentrations the value of χ_{HC} starts to decrease, reaching at 8 wt.% of NPs a value which is comparable with those obtained for samples loaded with 0.5 wt.% of NPs.

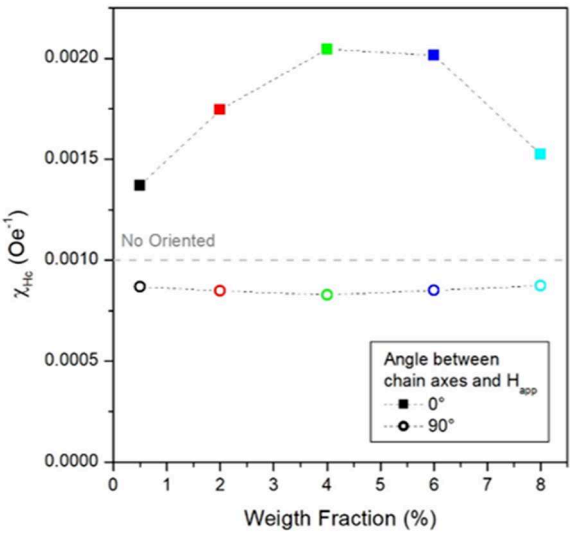

Figure 6.8: Magnetic susceptibility measured at 0° and 90° to the direction of the magnetic chains for 75Eb25BA-based samples at increasing NPs concentrations (0.5 – 8%).

As shown in Fig. 6.1 (SEM images), the NPs concentration strongly influences the dimension of the assembled chains, i.e. the higher the concentration of the fillers, the longer and larger the chains. This, in turn, modifies the magnetic response of the tested samples [195], [197], [218]. It is thus possible to explain the observed trend of χ_{HC} at 0°, by considering the relation between the dimension of the embedded chains and the magnetic anisotropy of the composite materials. For samples containing up to 4 wt.% of NPs the self-assembled chains can be considered as separate magnetic units, which contribution is added to those of the other chains.

However, when the amount of embedded NPs overcomes a threshold value, the self-assembly process leads to the formation of overlapping and interconnected magnetic chains. This is, for instance, shown in Fig. 6.9 for the formulation 75Eb25BA_6NPs exposed to a magnetic field of 10mT for 10 minutes. The magnetic behavior of the composite is strongly affected by the patterned chains configuration as here the magnetic chains do not longer act as "isolated magnetic units" but the whole interconnected microstructure act as a unique magnetic entity. Therefore, this microstructure may reduce the contribution to the magnetic anisotropy brought by the magnetic chains, which results in a decrease of the magnetic susceptibility of the composite material. This allows to define the optimum concentration of NPs in the printed object, that is 6 wt.% of Fe_3O_4 NPs.

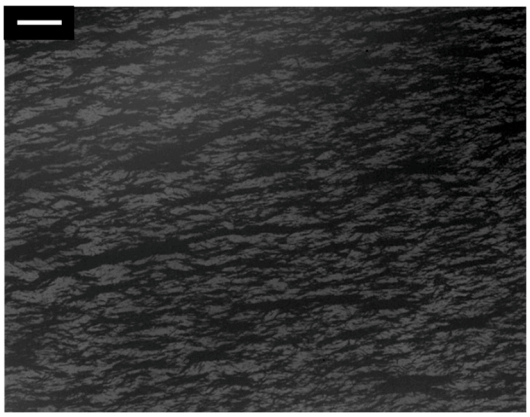

Figure 6.9: Optical microscopy image of liquid 75Eb25BA_8NPs formulation exposed to a magnetic field of 10mT for 10 minutes. Scale-bar is 200 μm.

6.4.3 Comparison with the 50Eb50BA_6NPs system

In the previous sections, we demonstrated that i) the magnetic anisotropy of the material is related to the arrangement direction of the magnetic chains, and ii) the magnitude of anisotropy, expressed as the magnetic susceptibility at the coercive field, is proportional to the load of magnetic particles in the material. An optimum concentration of fillers to enhance magnetic anisotropy was found to be equal to 6 wt.%. To investigate the effect of viscosity, 75Eb25BA_6NPs (≈0.18 Pa*s) and 50Eb50BA_6NPs (≈0.02 Pa*s) samples were fabricated applying a 10mT filed during the printing process, and their magnetic properties were compared. Fig. 6.10 shows the trend of χ_{HC} by varying the angle of the probing magnetic field (θ). 75Eb25BA_6NPs sample with dispersed NPs was used as a reference (gray dotted line). For both samples with oriented microstructures, χ_{HC} scales with the phase angle between the chains and the applied field: in particular, χ_{HC} is maximum when the field is applied parallel to the chains (θ=0°), minimum when the field is perpendicular (θ=90°), and intermediate for θ=45°. However, 50Eb50BA_6NPs sample has slightly lower magnetic susceptibility values compared to 75Eb25BA_6NPs formulation (0.00185 vs 0.002 Oe^{-1} respectively).

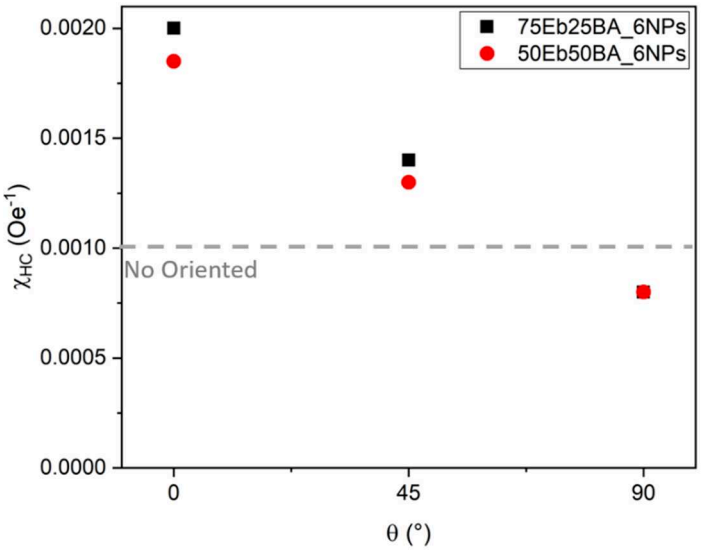

Figure 6.10: X_{HC} vs testing magnetic field angle measured for 75Eb25BA_6NPS and 50Eb50BA_6NPs samples. Both the specimens were 3D printed applying a constant magnetic field of 10 mT. The gray dotted line is the X_{HC} measured for 75Eb25BA_6NPs sample with dispersed NPs used as reference.

6.5 Exploiting the magnetic anisotropies of 3D printed polymers: the role of the magnetic torques

In the previous chapter, we demonstrated that the proposed modified printer is effective in programming the magnetic anisotropy of composite materials. Here, the effect of the magnetic anisotropy on the actuation mechanism of the 3D printed objects is investigated using 75Eb25BA_6NPs and 50Eb50BA_6NPs formulations. The former one will allow to print stiffer elements, whereas the latter one softer objects. The devices presented in the following have been developed exploiting the magnetic torques associated with the composite materials to induce the motion and/or the deformation of the printed objects. First, as a proof-of-concept, simple structures and easy types of motions are produced and tested. Then, multi-unit systems and devices are printed exhibiting complex actuation mechanisms.

The incorporation of the magnetic chains within the polymeric matrix allows to create a magnetic anisotropy in the composite material, where the easy magnetic axis of the object is parallel to the direction of the chains of aggregates. This allows the composite material, with all the chains aligned in the same direction, to be considered as a single magnetic unit [68], [190]. This is the magnetic anisotropies of each object are related to the orientation of the microstructures.

In the case of nanocomposite materials with oriented magnetic chains, the application of an external magnetic field produces a magnetic torque on the chains which would rotate to align their easy magnetic axis along the field direction [68], [175], [189], [190], [219], [220]. However, as the magnetic chains are embedded in the polymeric matrix, their rotation leads to the re-orientation (rotation) of the whole composite material (Fig. 6.11). However, when the magnetic torque associated with the chains overcomes the mechanical resistance of the material, the structured composite is deformed [175], [190]. These two remote-controlled actuation pathways will be used on printed objects presenting magnetic anisotropies, to undergo complex movements under spatially oriented magnetic fields.

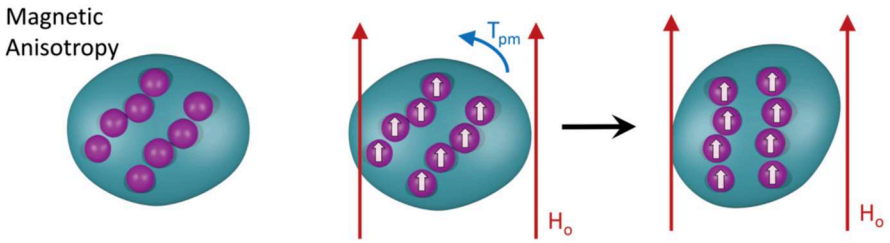

Figure 6.11: Description of the rotation induced by the presence of embedded magnetic chains in materials.

In general, the magnetic torque ($\boldsymbol{\tau_m}$) associated with a magnetic unit can be expressed as follows [190]:

$$\boldsymbol{\tau_m} = dU_m/d\theta \qquad \text{(Eq. 6.2)}$$

Where U_m is the magnetic energy of the material and θ is the rotation angle.

Chains of magnetic fillers dispersed within the photo-cured matrix can be approximated to prolate ellipsoids with *a* and *b*, the long the short dimensions, respectively. In this case, the magnetic energy U_m can be written as [190]:

$$U_m(\theta) = \frac{2\pi ab^2}{3}\frac{\bar{\chi}^2}{\bar{\chi}+2}\mu_0 H^2 \sin^2\theta \qquad \text{(Eq. 6.3)}$$

Where $\bar{\chi} = 3\chi/(\chi+3)$ is the shaped corrected susceptibility of the magnetic unit and H is the applied magnetic field.

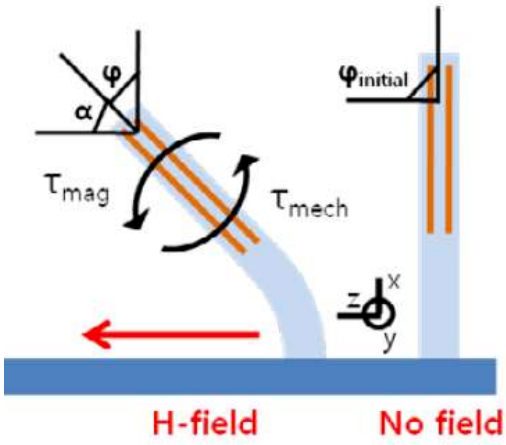

Figure 6.12: Effect of the magnetic torque on the bending of composite materials [175].

The total torque depends on the angle between the magnetic field and chain directions, the induced magnetic moment of the magnetic fillers as well as their number in a chain and, the number of the chains in the specimen. Substituting Eq. 6.2 in Eq. 6.1, the magnetic torque exerted on a sample composed of N magnetic chains can be expressed as [175]:

$$\tau_m = \mathrm{N} \times \frac{2\pi ab^2}{3} \frac{\bar{\chi}^2}{\bar{\chi}+2} \mu_0 H^2 \sin 2\theta \qquad \text{(Eq. 6.4)}$$

On the other hand, the mechanical torque deriving from the resistance of the material depends on the geometry and the elastic modulus of the sample:

$$\tau_{mech} = -\frac{wD^3}{12} E_y \varphi \qquad \text{(Eq. 6.5)}$$

the bending of the sample is possible whenever the magnetic torque overcomes the mechanical torque of the specimen:

$$\tau_{Magnetic} > \tau_{Mechanic} \qquad \text{(Eq. 6.6)}$$

When the magnetic torque is larger than the mechanical resistance of the materials, i.e. the mechanical torque, the sample bends in the direction of the magnetic field direction as shown in Fig. 6.12.

The equilibrium angle for the mechanical deflection is found when the mechanical restoring and the magnetic torque compensate one another and writes [175]:

$$\theta = \frac{K_m}{K_\varphi} Sin2(\varphi_{initial} - \varphi) \qquad \text{(Eq. 6.7)}$$

Where K_m is the mechanical stiffness of the sample and K_φ the magnetic factor of the chains.

6.6 Programmable magnetic-driven hammer-like actuators

Taking advantage of the microstructural control allowed by the modified DLP printer, several magnetic-driven actuators were produced. In this section, we fabricated nanocomposite hammer-like structures that are driven by programmable heterogeneous magnetic anisotropy. By programming the rotational axis of each element, and exploiting the magnetic torque as remote-control force, we demonstrate that the polymeric hammers actuators can undergo predesigned complex rotations.

The printed hammers are composed of a 5x9x3 mm parallelepipedal head, and a 14x2x1.5. mm, long perpendicular arm terminating with a cylindrical structure used to anchor the object (Fig. 6.13a). The actuators are 3D printed using 75Eb25BA_6NPs formulation, and each printed object presents a peculiar microstructure depending on the direction of the magnetic field (10mT) used during the printing process. Here five types of magneto-responsive hammers have been studied, each of which has a defined orientation of the microstructures (as indicated by the arrow): 0°, 45°, 90°, 135°, and 180° (Fig. 6.13b).

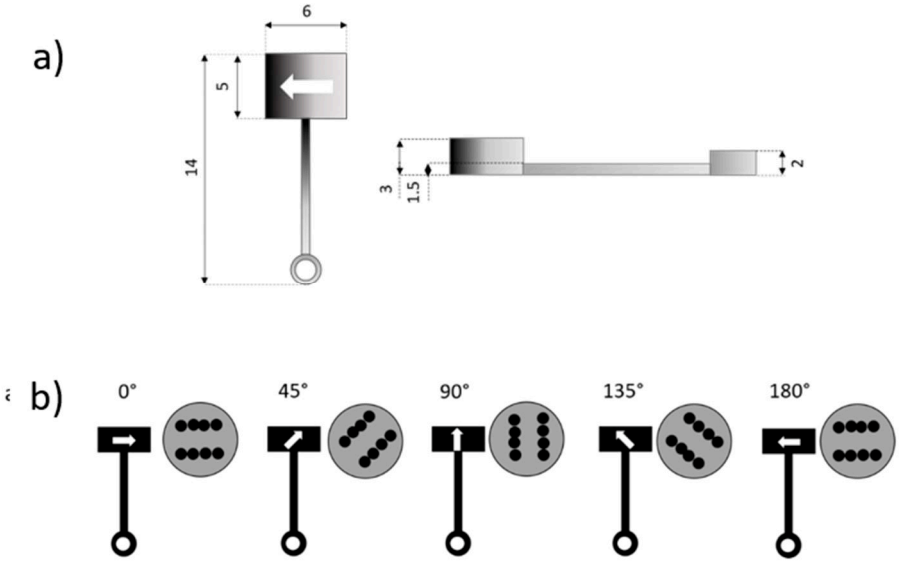

Figure 6.13: A) Dimensions of the printed magnetic hammers and b) their microstructural organizations.

To minimize friction effects, the hammers were placed in a petri dish filled with water and anchored to a printed system composed of five plastic pinions. Their rotations were studied by using a pair of Helmholtz coils generating a magnetic field in the X-Y plane up to 4 mT, whose direction is defined by using an Arduino microcontroller (Fig.6.14).

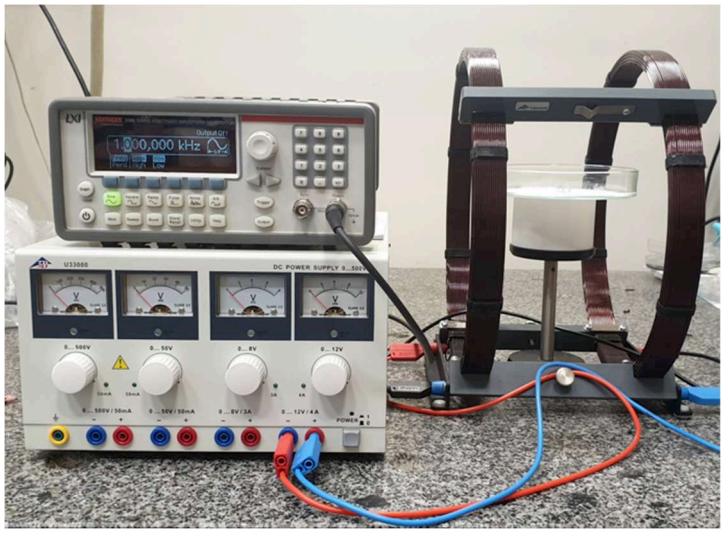

Figure 6.14: Experimental set-up used to test the magnetic hammers.

In the initial configuration, where the magnetic field is not applied (H=0), all the hammers are put parallel one to another as shown in Fig. 6.15a. The white arrows indicate the orientation of the embedded microstructure. As soon as the field is applied in the direction indicated in Fig. 6.15b-c, the hammers start to pivot around their anchoring point and to diverge from each other. The final (equilibrium) configuration is reached when all the arrows become parallel to the direction of the applied field (Fig. 6.15c). Correspondingly, responding to the homogeneous external magnetic field, hammers rotate at a different angle. This demonstrates that by controlling the microstructure of the printed objects it is possible to program the final orientation of the printed object. By reversing the direction of the applied field, it is possible to reverse the process in such a way all the hammers start to tilt in the opposite direction. However, the initial configuration cannot be precisely reached as it is not an equilibrium one, i.e. the direction of the microstructure is not parallel

to the direction of the field (Fig. 6.15d). Finally, the reversibility of the process is shown in Figs. 6.15e-f, where the actuators return to their equilibrium positions.

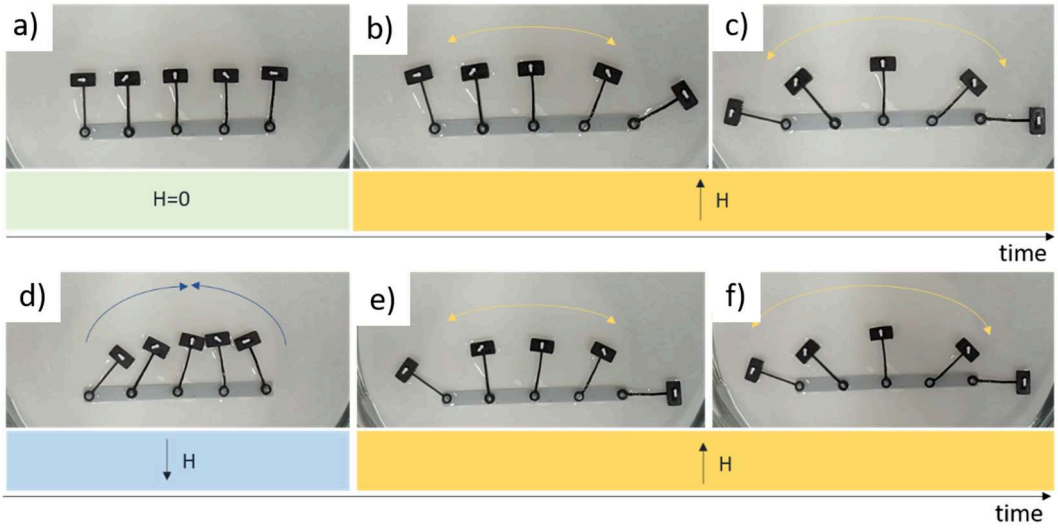

Figure 6.15: a) microstructural organization of the 3D printed magnetic arrows. b-g) Temporary evolution of the arrangement of the arrows depending on the magnetic field application.

6.6.1 Magnetic-responsive hammers flexible actuators

As described in section 6.5 the bending of a specimen is possible whenever the magnetic torque overcomes the mechanical torque of the specimen:

$$\tau_{Magnetic} > \tau_{Mechanic}$$

Thus, to print magneto-responsive flexible actuators it is possible either to increase the intensity of the applied magnetic field or to reduce the mechanical restoring force of the sample. The latter option can be obtained by two strategies: i) by regulating the stiffness of the matrix and/or ii) by changing the geometry of the sample by decreasing its length, thickness, or width.

In the previous section, we used the 75Eb25BA_6NPs formulation to print rigid magneto-responsive hammers. Here, to obtain more flexible structures that can be bent upon the application of the magnetic field, we use the 50Eb50BA_6NPs formulation. On the other hand, the elastic contribution of the torque was reduced by inserting a weak point in the object. This is was obtained by decreasing the width of one portion of the arm's hammer from 1mm to 0.8mm (Fig. 6.16).

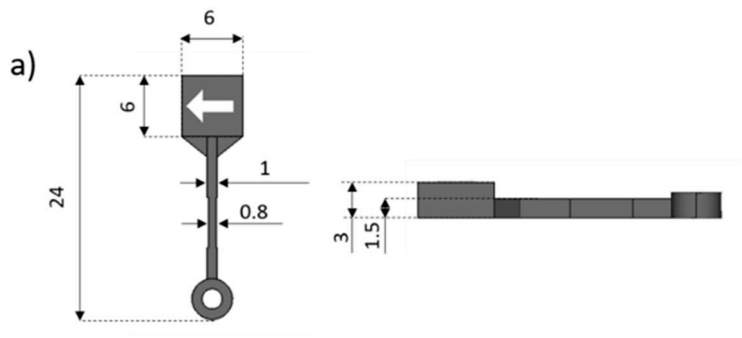

Figure 6.16: Shape and dimensions of the modified magnetic hammer designed to test bending motion.

The bending of a millimeter size actuator necessitates an intensity of the magnetic field larger than the one that can be obtained using standard Helmholtz coils. For this reason, a couple of NdFeB permanent magnets have been used to activate the actuation process.

First, the initial distance of the magnets from the magneto-responsive hammer has been chosen such that the magnetic torque is much smaller than the mechanic torque: $\tau_{mag} \ll \tau_{mech}$. In this configuration, the initial shape of the object is maintained (Fig. 6.17a). Then, we progressively reduced the relative distance between the two magnets. Correspondingly, the magnetic torque increases till it becomes larger than the mechanical restoring force of the sample: $\tau_{mag} > \tau_{mech}$. Magneto-responsive hammer starts then to bend to align the embedded microstructures along the field direction (Fig. 6.17b). Increasing again the distance between the magnets allows the system to come back to the initial configuration (Fig. 6.17c). At this point, the polarity of the magnets is inversed by applying a rotation of 180° along their long axis as shown in Fig. 6.17d. In this novel magnetic configuration, the approaching of the two magnets induces the bending of the hammer in the other direction (Fig. 6.17e).

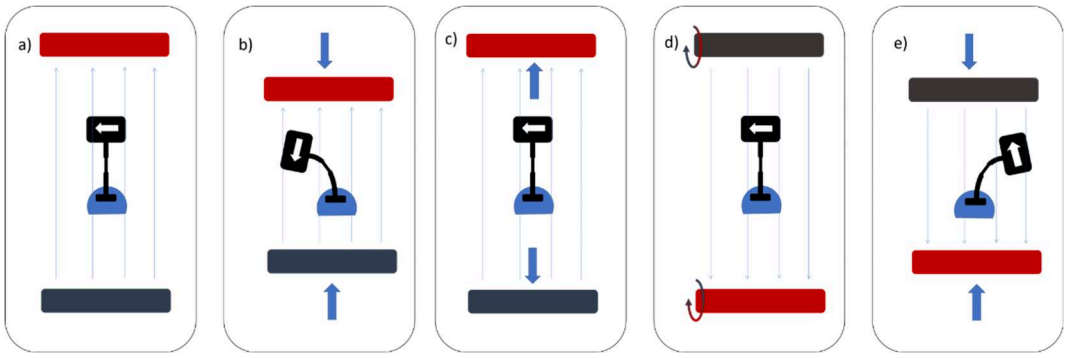

Figure 6.17: Sketch of the experimental set-up adopted to control the magnetic field intensity and test the bending motion of the soft magnetic hammer.

Fig. 6.18 shows the time evolution of the flexible hammer when the magnetic field is applied following the idea developed above. Contrary to the rigid hammers, the extremity of the flexible hammer was fixed to a support for preventing the object to rotate. Starting from the initial configuration where the microstructure of the specimen (indicated by the arrow) is perpendicular to the applied field (Fig. 6.18a). Here, the permanents magnets are too part apart to induce any bending of the hammer. When the magnets are approached below a critical distance, i.e. when the magnetic torque becomes larger than the mechanical torque, the hammer starts to bend to align its microstructure in the direction of the magnetic field (Fig. 6.18b). As expected, when the polarity of the magnets is reversed, the bending is observed in the opposite direction (Fig. 6.18c).

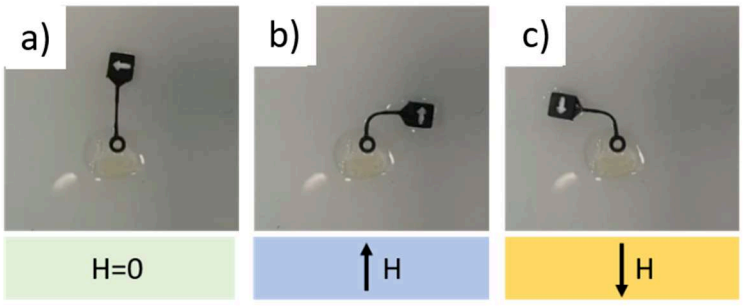

Figure 6.18: a) Flexible arrow design and its dimensions. b) Magnetic arrow in absence of magnetic field, c) Magnetic arrow bending for a 90° magnetic field, d) magnetic arrow bending for a -90° magnetic field.

These observations demonstrate that by controlling the microstructure of the 3D printed objects, it was possible to predict the material rotation upon magnetic field exposure. Moreover, by accurately tuning the stiffness of the polymeric matrix and

by applying the proper design of the shape of the device, it is also possible to introduce bending motion with predictable bending direction and the bending angle.

6.7 3D printed magneto-responsive polymeric devices

6.7.1 Magnetic-driven spur gears

As a first example, the efficiency of the magnetic control has been investigated by comparing the torque-induced rotation in two geometrically identic 3D printed *spur gears* but presenting different microstructures (Fig. 6.19).

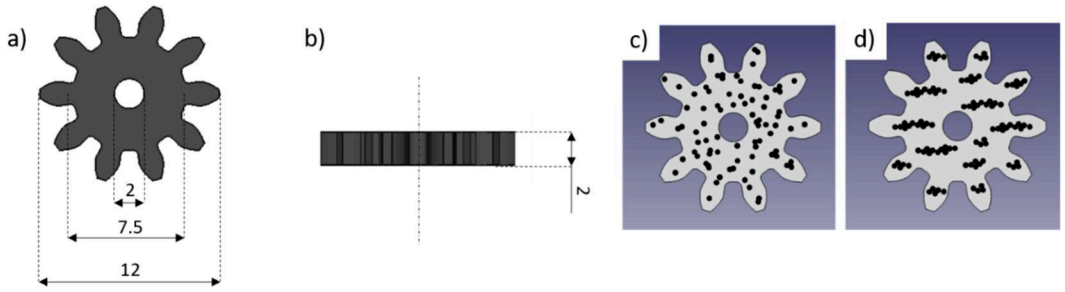

Figure 6.19: a-b) Geometrical dimensions of the 3D printed spur gears. C) Microstructure of the spur gear with randomly dispersed NPs. D) Microstructure of the spur gear with oriented magnetic chains.

Indeed, both gears have been printed using the same formulation (75Eb25BA_6NPs) and have the same design characteristics (10 teeth, 1 mm module, and a pressure angle of 20°) [221] (Fig. 6.19a-b). Conversely, one of the gear was printed with randomly dispersed NPs, and used as a reference (Fig. 6.19c), while the second one was printed by applying a magnetic field of 10 mT during the manufacturing process to assemble the magnetic chains along the field direction (Fig. 6.19d). To minimize friction effects, the two spur gears were placed in a petri dish filled with water and anchored to a printed system composed of two diamagnetic pinions. Their rotations have been observed by using a pair of Helmholtz coils generating a magnetic field in the X-Y plane up to 4 mT, whose direction is modified by using an Arduino microcontroller (Fig. 6.14).

The initial orientation of the two gears, in the absence of a magnetic field, is indicated by the white spots and the blue arrows in Fig. 6.20a. A magnetic field (4mT) is then applied as indicated in Fig. 6.20b. As expected, the spur gear

containing the oriented chains undergoes a rotation to align the embedded chains with the direction of the applied field. Conversely, the spur gear containing dispersed NPs remains nearly at the initial position as indicated by the arrows in Fig. 6.20b. Once the orientation is achieved, the process has been reversed by inverting the magnetic field (Fig. 6.20c). Again, the spur gear with dispersed NPs does not rotate, whereas the one containing the oriented chains flips of about 180° to align itself along the new direction of the applied magnetic field. The reversibility of the process has been checked by switching the magnetic field several times as shown in Figs. 6.20d-e.

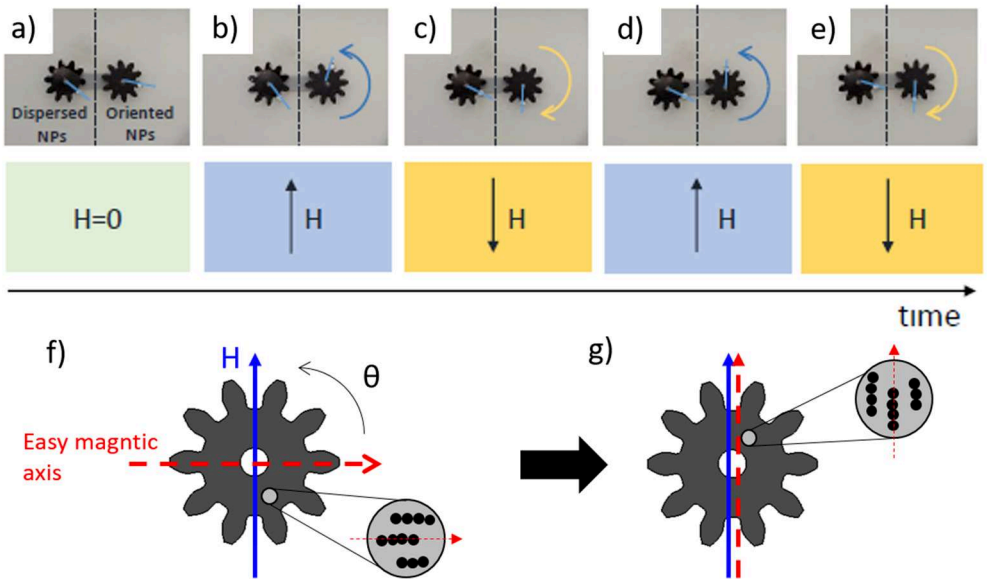

Figure 6.20: a-e) Different behaviors upon the application of a magnetic field according to the microstructure of the 3D printed spur gears. F-g) Graphical explanation of the rotation of the spur-gear containing an oriented microstructure. When the magnetic field is applied, the gear rotates to align its easy magnetic axis to the field lines.

The interpretation of these experimental results is quite straightforward, and it is clearly related to the different microstructure of the two objects. On one hand, hysteresis cycles measured for the samples with dispersed NPs indicate that the magnetic properties of the material are the same in the three directions of the space, i.e. the composite is magnetically isotropic. Thus, the application of a uniform magnetic field does not induce a magnetic torque in the object, and the rotation of the sample is nearly absent. On the other hand, the controlled microstructure in the gear-wheel induces magnetic anisotropy in the object and the formation of a macroscopic easy magnetic axis, M_{easy}. When the magnetic field is applied, the

object is exposed to a magnetic torque ($\sim M_{easy} \times H$) which forces the spur gear to rotate to align the magnetic chains along the field lines (Fig. 6.20 b-e). For the sake of clarity, a graphical representation of the rotation induced by magnetic anisotropy is reported in Fig. 6.20f,g. In addition, these experiments demonstrate that the magnetic anisotropy of the 3D printed gears is strong enough to allow remote control even employing low magnetic field intensities, i.e. 4 mT.

6.7.2 Magnetic-driven gear-trains

In the previous section, the possibility to program the magnetic anisotropy during the printing process has been tested to remotely control the rotation of a gear-wheel. In this section, this result will be used to develop more complex devices based on the rotation of a gear-wheel.

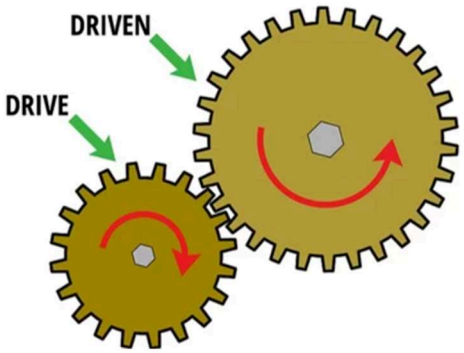

Figure 6.21: Example of a conventional gear train.

The first structure we tested is composed of two gears. When two or more gears are linked together the ensemble is considered a *gear train* where the "input gear" (also known as drive gear) transmits the power to the "output gear" (also known as driven gear) (Fig.6.21). In a standard *gear train*, the input gear is typically connected to a power source, such as a motor or engine. However, in our case, it will be remotely controlled by an external magnetic field. The rotational speed from the output (driven) gear depend on the gear ratio, i.e. the ratio of the dimensions of the two gears [221]:

$$Gear\ ratio = \frac{\text{Number of teeth on the } \mathbf{driven\ gear}}{\text{Number of the teeth on the } \mathbf{driver\ gear}} = \frac{Angular\ velcity\ of\ the\ \mathbf{driver\ gear}}{Angular\ velcity\ of\ the\ \mathbf{driven\ gear}}$$

(Eq. 6.8)

For gear ratio<1 the driver gear is smaller than the driven gear, and the latter rotate slower, but it also generates a higher torque. On the contrary, if the driver gear is larger than the driven one, the gear ratio is >1, and the driven gear rotates faster but with a lower torque. The concept of *gear train* has been applied to investigate the possibility to build more complex devices. In our case, the drive gear is a magnetic-responsive gear-wheel composed of 10 teeth, while the driven gear is a 20 teeth polymeric gear-wheel 3D printed using an ASIGA DLP apparatus with a commercial resin (Asiga Plasgray V.2). In particular, the driven gear contains hexagonal holes to both lighten the structure and to enhance the transfer of the torque. The rotational speed for our *gear train* is 2 meaning that that the rotation's angular velocity of the driven gear is two times smaller than that of the magneto-responsive drive gear. The *gear train* system was placed in a petri dish filled with water and anchored to a printed system composed of two plastic pinions and exposed to a rotating magnetic field. Fig. 6.22 shows that the drive wheel successfully transfers the momentum to the driven wheel demonstrating the possibility to develop more magnetic driven-devices.

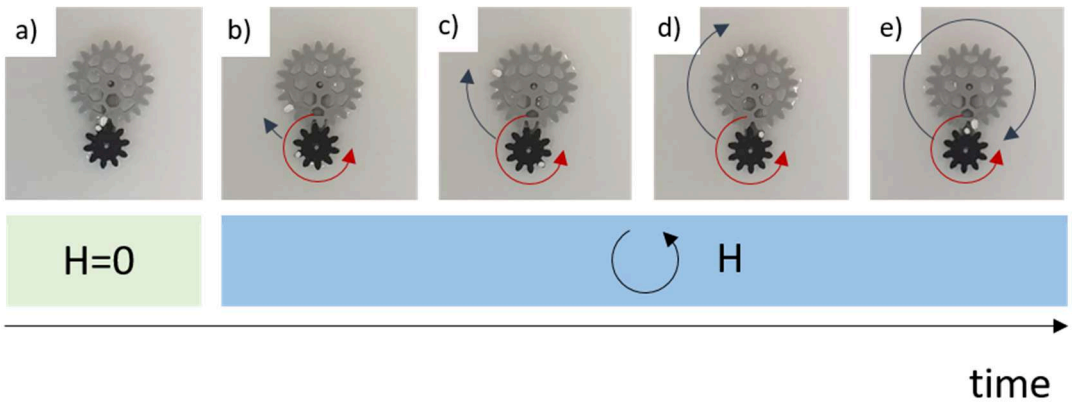

Figure 6.22: Operating principle of the a magnetic-driven train-gear mechanism.

6.7.3 Spur gear coupled with a rack

A simple example of a linear actuator is the one composed of a spur gear and a linear rack coupled together through the meshing of their respective teeth. If the spur gear rotates on a fixed axis, while the rack can move, the actuator is used to transform a rotational motion into linear motion as shown in Fig. 6.23.

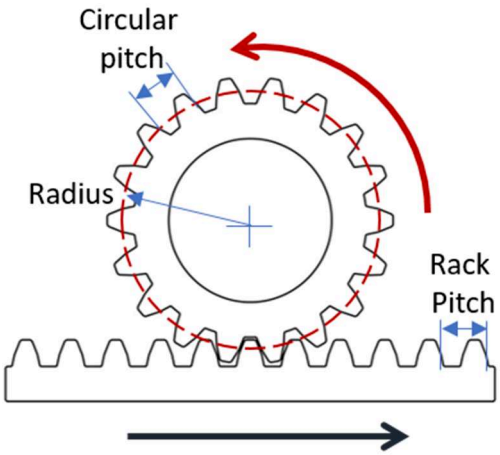

Figure 6.23: Example of conventional spur gear – rack mechanics.

Our linear actuator is composed of two spur gears and a double-side rack, as shown in Fig. 6.24. The *linear actuator* is placed in a petri dish filled with water and anchored to a printed system composed of four pinions allowing the spur gears to rotate and the rack to move in the plane (Fig. 6.24). Both the spur gears have the same characteristics (15 teeth, 1mm module, and 2mm thick). However, one is magneto-responsive and printed using the 75Eb25BA_6NPs formulation and applying a 10mT field to organize the magnetic chains along the field direction, while the second one is 3D printed using a commercial acrylic resin (Asiga Plasgray V.2). If the role of the magneto-responsive spur gear is to transfer the torque to the rack, that of the non-magnetic one is to stabilize the system and facilitate the linear movement of the double-side rack. This one (15 teeth, 1mm module, 1mm thick, and 47mm long) has been printed using the same acrylic resin (Asiga Plasgray V.2).

Figure Fig. 6.24a shows the system before the application of the magnetic field. Once the field is applied, the direction is indicated by the arrow in Fig. 6.24b, the clockwise rotation of the magneto-responsive spur gear induces the displacement of the rack upward. The inversion of the field reverses the direction of rotation of the gear, which becomes anti-clockwise. In this case, the rack moves downward

(Fig. 6.24c). Thus, the linear movement of the rack can be remotely controlled by the direction of the applied field.

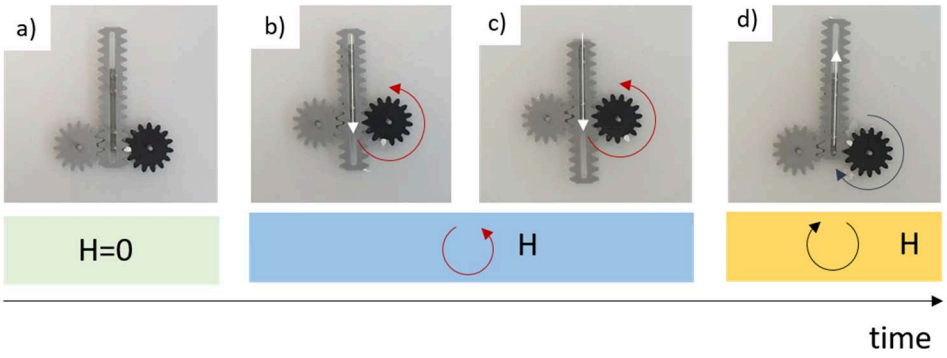

Figure 6.24: a) Composition of the tested linear actuator. B-d) Operating principles of the spur gear – rack mechanism.

6.7.4 Magneto-responsive gripper

Generally speaking, grasping is the ability to pick up and hold an object, while manipulation is the ability to produce its rotation and displacement. Grasping and manipulation are two functions that are of paramount importance in robotics as they allow the machine to mimic the behavior of human beings and animals. In this section, we will use the knowledge developed so far to build a magneto-responsive gripper. A gripper indicates a robotic device that can exploit one or more of the aforementioned functionalities. This device will be composed of two clamping arms activated by a magneto-responsive spur gear and it will serve as a proof-of-concept for the development of devices with more advanced functionalities.

The actuation mechanism is activated by a permanent NdFeB fixed at the extremity of a servo motor whose rotation angle is controlled by an Arduino microcontroller (Fig. 6.25). The torque applied to the magnetic chains forces the spur gear to rotate to align the chains along the field of the permanent magnet. Thus, the servomotor can be used to precisely control the angular direction of the permanent magnet and in turn the spinning of the spur gear.

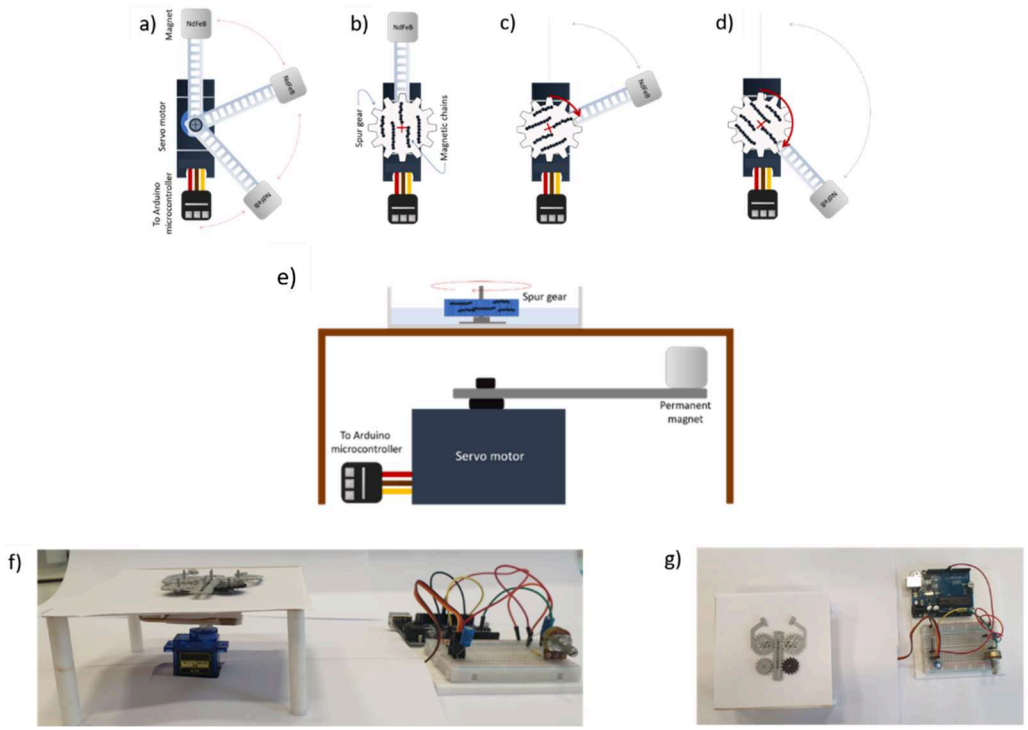

Figure 6.25: Sketch of the operating principles of magneto-responsive mechanics. A-d) the rotation of the spur gear with magnetic chains is controlled by the positioning of the NdFeB magnet. E-g) The Arduino system is used to control the rotation direction of the magnet.

The effectiveness and versatility of the magnetically driven gears led to the design of more complex systems that involved several moving parts. An example is the claw mechanism reported in Fig. 6.26 where different components are used to transform rotary motion into translating motion and vice versa to control the opening and closing of a vise.

The operation of the magneto-responsive gripper is illustrated in Fig. 6.26a-g. In the initial configuration, the two arms of the grippers are in the open position, i.e. they are far from each other. Then the servomotor is activated such that the magneto-responsive spur gear stars to rotate clockwise. This rotary motion then is transmitted to the rack and transformed into a translating motion and then again into a rotary motion thanks to the second (polymeric) spur gear. The latter has been printed with an arm and a clamp. As there are two identical structures of this type, they act as a gripper upon the rotation of the magneto-responsive spur gear in the clockwise direction. Inversing the rotation of the servomotor, allows the magneto-responsive spur gear to rotate anti-clockwise, and the arms of the gripper to open up and to return to the initial configuration.

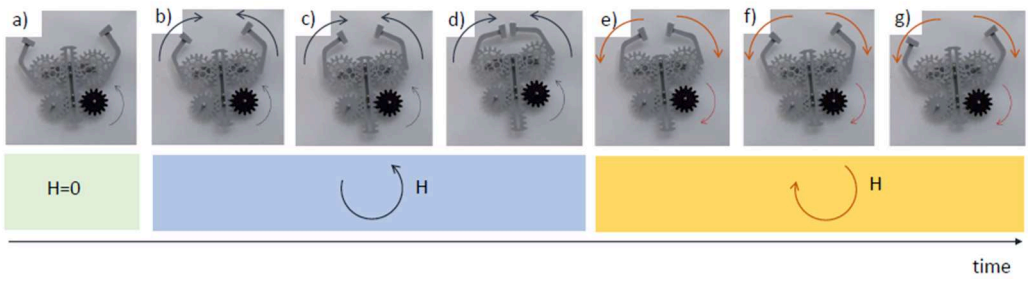

Figure 6.26: Operating principles of the mechanical clamp developed using a magneto-driven drive wheel.

Here, the magnetic-driven rotation of gears and racks was exploited to produce a gripper composed of several elements that are remotely controlled and that can work in closed environments.

6.8 Conclusions

Urethane acrylated resins loaded with Fe_3O_4 NPs were 3D printed upon the application of a magnetic field in the developed modified DLP printer. The applied field induced the self-assembly of the magnetic particles in the printing resins. SEM observations performed on the printed samples confirmed that by controlling the magnetic field during the 3D printing process it was possible to program the arrangement of the assembled magnetic chains in each layer of the composite. Therefore, we demonstrated that the proposed strategy allowed the precise micro-structuration of the material during the 3D printing process. After, the effect of the controlled microstructures on the macroscopic mechanical and magnetic behavior of the materials was evaluated. While the mechanical properties resulted not affect by controlled microstructuration, the 3D printed objects show magnetic anisotropy exhibiting an easy-magnetic axis coincident with the alignment direction of the embedded chains. These results indicated that by controlling the microstructure of the materials it was also possible to program their magnetic properties. Finally, we took advantage of the control of the magnetic properties to produce devices undergoing programmed rotation and bending via magnetic torques application. We demonstrated that 3D printed objects were easily activated by the application of uniform magnetic fields, proving also their remote control in closed environments. The proposed devices are good candidates for several application fields such as

biomedical, sensing, and robotics where direct contact between the motion source and the object is not allowed.

General Conclusions and Perspectives

Through the pages of this manuscript, a novel 3D printing method was designed to fabricate polymeric nanocomposite materials with programmable microstructures exploiting the self-assembly process of magnetic nanoparticles. This approach was also effective in inducing magnetic anisotropy in the fabricated materials, and in programming the easy-magnetic axis in different parts of the 3D printed objects. The produced devices exhibited complex actuation mechanisms, and they were remotely controlled by low-intense magnetic fields, paving the way for several application fields such as robotics, sensing, biomedicine, and drug delivery.

In the first chapter of this thesis, an introduction to the 3D printing field was given focusing on the potential impact of this innovative manufacturing technique in our society. After describing the recent economical and industrial trends of additive manufacturing, we introduced the smart materials and 4D printing concepts, illustrating also the different investigated approaches to control the shape and properties of the materials by external stimuli. Finally, we described in detail the 3D printing technology used in this work, i.e. Digital Light Processing (DLP).

Hereafter, in the second chapter, we presented a consistent overview of magneto-responsive polymers. After a brief introduction to the magnetic properties of materials, we presented the most common ways to magnetize polymers consisting of the incorporation of magnetic fillers in the matrices. This was followed by several examples of industrial applications of magneto-responsive polymer composites. As the main topic of the work, particular attention was given to magneto-driven soft actuators and the common strategies to enhance their actuation mechanisms. Both the strategies of magnetic polarization control, and self-assembly exploitation were discussed, and the latter was the procedure applied in this work.

At the beginning of the experimental work, the fabrication of magneto-responsive polymers with randomly dispersed magnetic fillers via a DLP 3D

printing technique was demonstrated in chapter 3. After selecting a good combination of acrylic monomers in terms of photo-reactivity and mechanical properties, Fe_3O_4 nanoparticles (NPs) were added to magnetize the printed polymers. The mechanical response of the polymers was tailored from stiff to soft, by adding a different ratio of Butyl acrylate as a reactive diluent. The magnetic properties of the materials were not affected by the polymeric matrix, but the magnetization of the composites was simply proportional to the Fe_3O_4 NPs load in the resins. The prepared formulations witnessed good printability up to 6 wt.% of fillers, and the printed objects exhibited high-resolution details and a good fidelity to the CAD file. For higher nanomagnetite concentrations, the light absorption competition between the photoinitiator and the fillers results in low photo-reactive formulations and poor mechanical stability of the objects, preventing an adequate 3D printing process. Taking advantage of the design-freedom allowed by the 3D printing technology, several devices with complex shapes were fabricated to probe different kinds of magneto-induced motions such as rolling, translation, bending, and folding/unfolding processes.

In the second experimental contribution (chapter 4), we investigate the self-assembly process of magnetite nanoparticles dispersed in photocurable formulations films for later program the microstructure of the nanocomposite materials during the 3D printing process. The spontaneous formation of chains-like structure by the application of external magnetic fields was experimentally studied in-situ at the micro and the nanoscale by optical microscopy and scanning transmission X-ray microscopy. Moreover, a simplified physical model describing both the self-assembly process and the rotation of the magnetic chains was developed. The dimension of the assembled chains was regulated by varying the external magnetic field intensity, and by controlling the NPs concentration and the viscosity of the formulations. We also demonstrated the chance to control the alignment direction of the assembled structures by varying the direction of the applied magnetic fields. Above a critical angle of 40°, the parallel magnetic interactions between particles became negative leading to the breaking of the magnetic chains. Below the critical rotation angle, the magnetic chains rotated solidly with the magnetic field maintaining their dimensions. Lately, the knowledge

acquired in the self-assembly process of magnetite nanoparticles has allowed us to estimate the microstructural evolution in 2D polymeric films.

Because 3D printing is a layer by layer technology, the control on the microstructure of the printed composites was achieved by replicating in each layer the aforementioned 2D control on the size and direction of the assembled magnetic chains. In chapter 5 we described a DLP modification-set up to produce controlled magnetic fields during the printing process. By inserting a ball bearing – permanent magnets set-up in the resin reservoir of the 3D Printer, we demonstrated an easy approach to control the microstructure of each printed layer paving the way to fabricate nanocomposite polymers with programmable microstructures. As a proof of concept, a three-level structure was 3D printed programming the size and arrangement of the magnetic chains in each printed layer by controlling the application of the printing magnetic field.

In the last section of this thesis (chapter 6), we took advantage of the modified 3D printer to fabricate nanocomposite materials with programmed microstructures and magnetic properties. A controlled magnetic anisotropy was induced by programming the microstructures of the printed objects, and the easy-magnetic axis of the materials was coinciding with the alignment direction of the embedded magnetic chains. The grade of anisotropy in the materials was tailored by controlling the intensity of the printing magnetic field and the Fe_3O_4 NPs load in the resin. The fabricated objects behaved as magnetic compasses, and by the application of a uniform magnetic field, they endured a magnetic torque which forced their rotation to align their easy magnetic axis along the field lines. Therefore, by programming the microstructure and the magnetic anisotropy, it was possible to predict the rotation of the objects. This approach was exploited to developed different types of devices such as magneto-driven gears and mechanics, rigid and soft magnetic arrows undergoing controlled rotation and bending respectively, and remotely controlled electric connectors.

The proposed magneto-assisted 3D printers allowed the production of several magneto-responsive devices undergoing controlled motion mechanism owned to their programmed microstructure. Owing to its simplicity, the designed printing method can be easily implemented in any type of vat-polymerization 3D printing techniques boosting the development of magneto-responsive polymers. Since these

materials can be remotely activated by low-intense magnetic fields and work in closed environments, they are of great interest for several application fields. In the "La chaire Art & Science" framework, which promote collaborations between scientific, human, and social expertise, two events were organized during the Ph.D. work: the "Behavioral Matter" workshop organized at Centre Pompidou in Paris in 2018, and "Useful fictions" workshop organized in Ecole Polytechnique in 2019. At both events, our research group was involved as an organizer of a studio in the 4D printing field. Magneto-responsive materials turned out to be of great interest also for designers and artists, and the synergies created during the working days were of help also for the realization of the thesis work. Another interesting application field for the developed materials is doubtless biomedicine as magnetic fields are body-harmless and allow remote control of the devices once inserted in the body. However, the devices designed for biomedical applications must fulfill several requirements both in terms of cytocompatibility and dimension of the objects. In the next future, an accessible route to boost the production of magneto-driven biomedical devices would consist of downscaling the 3D printing process to produce microdevices remotely controlled when inserted in the human body. This can be achieved by replicating the control on the microstructure in a two-photon polymerization (2PP) 3D printing technique. Likewise stereolithography and DLP technologies, two-photons polymerization 2PP 3D printers are based on photopolymerization and they work with materials in the liquid state. Therefore, for all the three printing technology it is possible to take advantage of the self-assembly processes of magnetic particles to control the microstructure of the fabricated composite materials. In particular, 2PP 3D printing exploits the non-linear two-photon absorption phenomenon to produce micrometric objects with a resolution in the order of hundreds of nm. Combining the programming of the microstructure with the fabrication of micro-objects will lead to the productions of magneto-responsive devices satisfying the dimensional restrictions intrinsic to biomedical applications.

Appendices

A1 – Composition of the 3D printed formulations

To 3D print the commercial resins provided by Allnex, phenylbis(2,4,6-trimethylbenzoyl)phosphine oxide (BAPO, Merck) was added as radical photoinitiator, and Reactive Orange16 (RO16, Allnex) was added as a dye. The composition of the tested formulations is reported in Tab. A1.1.

Table A1.1: Composition of the 3D printed formulations based on pristine commercial resins

Formulations	Ebecryl 8254 (wt.%)	Ebecryl 82328 (wt.%)	Ebecryl 4740 (wt.%)	BAPO (wt.%)*	RO16 (wt.%)*
100Eb 8254	100	/	/	1	0.2
100Eb 8232	/	100	/	1	0.2
100Eb 4740	/	/	100	1	0.2

*percentage referred to the amount of resin

The formulations containing Fe_3O_4 NPs (Merck) as fillers were prepared by mixing two different ratios of Ebecryl 8232 resin and Butyl acrylate (BA, Merck). BAPO was used as the radical photoinitiator. For the pristine 75Eb25BA and 50Eb50BA formulations, RO16 was added as the dye. The composition of the magnetic formulations is reported in Tab. A1.2.

Table A1.2: Composition of the 3D printed formulations with magnetic nanoparticles.

Formulations	Ebecryl 8254 (wt.%)	Butyl Acrylate (wt.%)	BAPO (wt. %)*	Fe_3O_4 NPs (wt.%)*	RO16 (wt.%)*
75Eb25BA	75	25	1	/	0.2
75Eb25BA_2NPs	75	25	1	2	/
75Eb25BA_4NPs	75	25	1	4	/
75Eb25BA_6NPs	75	25	1	6	/
75Eb25BA_8NPs	75	25	1	8	/
50Eb50BA	50	50	1	/	0.2
50Eb50BA_2NPs	50	50	1	2	/
50Eb50BA_4NPs	50	50	1	4	/
50Eb50BA_6NPs	50	50	1	6	/

*percentage referred to the amount of resin

A2 – Analysis of the optical microscopy images

Optical microscopy was used to follow the self-assembly process of Fe_3O_4 NPs dispersed photocurable formulations upon the application of a magnetic field. The same technique was also applied to investigate the rotation of the assembled magnetic chains when the magnetic field direction was varied. For a quantitative evaluation of the two processes, it was essential to develop a consistent method to process the images and to characterize the observed aggregates.

This was achieved by processing the microscopy pictures with ImageJ software. As for several image analysis softwares, ImageJ allows to manually measure every single object present in a picture. Nevertheless, due to the large number and the wide size-range of the chains, this analysis route was not directly practicable. Therefore, a multi-step procedure was developed to automatically measure the sizes and the angles of all the aggregates present in a picture. To give a more detailed description of the image analysis method, here the process is subdivided into 5 consecutive passages. As an example, the microscopy picture taken for 60Eb40BA_3NPs formulation after 10 minutes of exposure to an external magnetic field of 30mT is used as a case-study (Fig. A2.1).

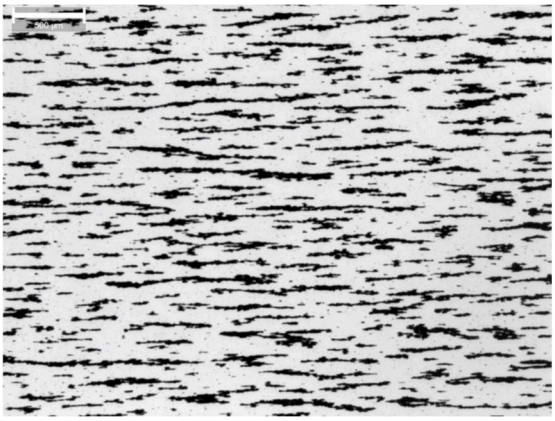

Figure A2.1: Original optical image of 60Eb40BA_3NPs formulation after 10 minutes of exposure to an external magnetic field of 30mT

1) To proper measure the aggregates, it was necessary to find the correlation between a single pixel of the picture and the physical unit of length of the image (μm). Therefore, by measuring the length of the scale-bar in pixels and by dividing this to its actual dimension, it was possible to find the number of pixels composing the unit of length (μm in this case). Once pixels/unit of length ratio was settled in Image J, all the following measurements were reported in the scale-unit.

2) In order to perform automatic measurements of the chains, it was fundamental to improve the resolution and to maximize the contrast of the image to well distinguish the magnetic chains from the background. In particular, ImageJ can process only images in black and white. This was achieved firstly converting the full-colors image into a grey-scale picture, and then the contrast and the brightness was adjusted to transform the picture into a black and white one (Fig. A2.2). It is important to note that, for a correct comparison of the results, the parameters used to maximize the contrast have to be the same for all the pictures taken in a single experimental series.

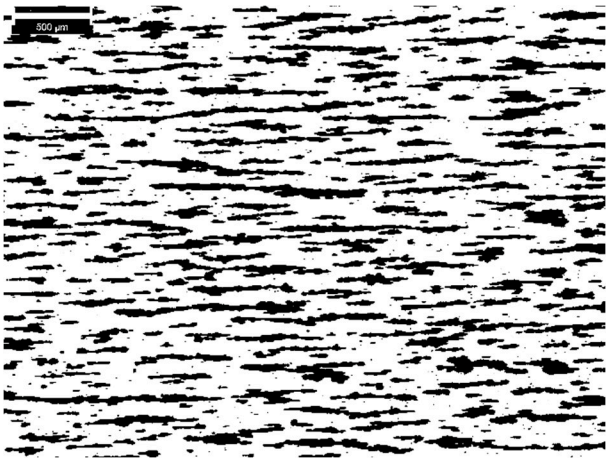

Figure A2.2: Resulting image after contrast maximization.

3) Thanks to the maximization of the contrast, the software was able to perfectly distinguish the aggregates (in black) from the photocurable resin (in white), and thus it was possible to perform automatic measurements of

the dimensions of the magnetic chains. Indeed, the software was now able to measure the geometrical characteristics of each isolated aggregate. For our tests, we excluded from the analysis all the aggregates placed at the edges of the picture as it is not possible to determine their effective size. We selected to fit the remaining aggregates as ellipses, measuring their diagonals and angles (Fig. A2.3). The major and the minor diagonals of the fitted ellipses have been matched to the length and width of the chains respectively.

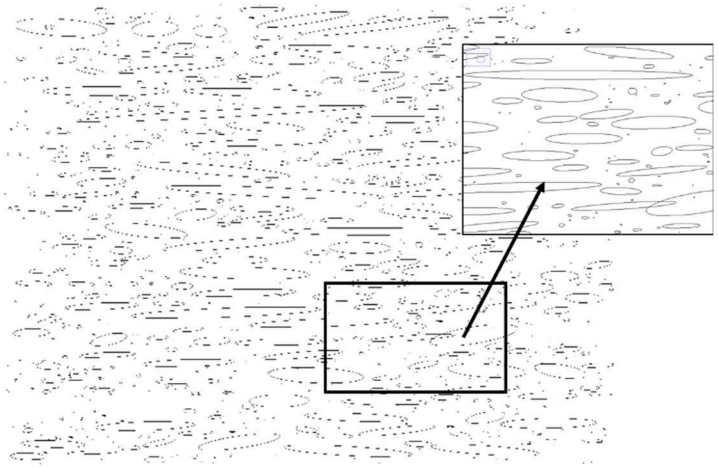

Figure A2.3: Image after ellipses fitting.

4) The collected data were then exported on a spreadsheet and filtered to eliminate distortions coming from the treatment of the image. In particular, the maximization of the contrast may generate groups of isolated pixels that alter the measures since they may be considered as particles by the software. To avoid this issue, the data collected were filtered by excluding all the aggregates shorter than 4 pixels.

5) Also, the data regarding the angle of the chains were processed as ImageJ does not return negative values on angles, but it returns the corresponding positive angles. For instance, a chain oriented at -10° was computed with an angle of 170°. If an angle of -10° and 170° are geometrically equivalent, this led to a strong overestimation of the average angle of the magnetic chains. To overcome this issue an if-function was applied to convert all the angles

larger than 90° into negative angles and to maintain unaltered the angles lower than 90°. In a common Excel spread-sheet this can be achieved by typing the following function:

=IF(A1<90;A1;A1-180)

Where A1 is the cell containing the raw angle value.

Finally, the collected results were analyzed by Origin Pro software calculating the average length, width, and the angles of the observed magnetic chains. For some images, also the length distribution of the aggregates was calculated. This was performed by dividing the chains into several length-intervals of 5μm, and by calculating the relative frequency of each group.

A3 – List of tables

Chapter 1

Chapter 3

Appendix 1

A4 – List of figures

Chapter 1

Chapter 2

Chapter 3

Chapter 4

Figure 4.18: A) Images obtained by the simulations of the theoretical model for $\Delta\theta_B$ =30° and $\Delta\theta_B$ =45°. B) θ/θ_B trends obtained by the simulations based on the physical model for several values of $\Delta\theta_B$: 15°, 30°, 45°, 60°, and 60°. F) L/L_0 trends obtained by the simulations based on the physical model for $\Delta\theta_B$= 30°, and $\Delta\theta_B$= 45°.

Figure 4.19: a) Chains angle vs time kinetics curve $\Delta\theta_B$ = 5°, 10°, 15°, and 30°. B) Angular gap vs $\Delta\theta_B$ at 120s. Inset: representation of the angular gap.

Figure 4.20: A) Experimental set-up: single rotation of 40° versus two subsequent rotations of 20°. B) evolution of the angle in the two systems. C) evolution of the length in the two systems.

Figure 4.21: Comparison of the rotation kinetics between the 75Eb15BA_3NPs and 60Eb40BA_3NPs formulations for $\Delta\theta_B$ =10°, and 30°.

Chapter 5

Figure 5.1: a) Maskless lithography set-up. The set-up is composed of an ultraviolet light source, a digital micromirror device (DMD) modulator, and objective lenses. The light is patterned through a DMD modulator and focused on the microfluidic channel, polymerizing the resin. B) Actuation of a simple magnetic cantilever. Under a homogeneous magnetic field the magnetic cantilever, which contains self-assembled magnetic nanoparticles (MNs), only bends towards the field line. (Scale bar 50 _m). [175]

Figure 5.2: sketch of the parallelogram method allowing the decomposition of a three-dimensional vector, B, into two sub-vectors, the first one in the X-Y plane, BX-Y, and the second one in the Z direction, BZ.

Figure 5.3: a) Helmholtz coils showing the homogeneity of the magnetic field in the center of the system. b) Set up composed of three sets of Helmholtz coils to vectorial control the magnetic field in the X-Y-Z space (https://www.3bscientific.fr).

Figure 5.4: a) Non-metallic ball bearing and used NdFeB permanents magnets. b) Geometries and magnetic field of the tested magnets. c) The designed set-up of magnets and ball bearing allowing the rotation of the magnetic field. d) The adopted ball bearing and its geometrical dimension. The inner hole of the ball bearing acts as a resin reservoir. e) this set up allows the passage of the light emitted by the light projector of the DLP 3D printer.

Figure 5.5: a) DLP Robotfactory (HD 2.0+), b) detail of the growth platform, and the vat resin. c) Ensemble of the modifies and added pieces, d) detail of the glass cylinder used as a new growth platform. E) Modified Robotfactory 3DL HD 2.0+ to control the magnetic chains assembling and direction in the X-Y plane.

Figure 5.6: Distribution of the magnetic fillers dispersed in the photocurable resin according to the configuration of the permanent magnets: a) AA-AA, and b) BB-BB. In the latter, remarkable inhomogeneities are observed as well as depleted areas.

Figure 5.7: Magnetic field distribution tested for different magnets couples: a) A-A, b) AA-AA, c) B-B, d) BB-BB, and e) BA-AB.

Chapter 6

Figure 6.24: a) Composition of the tested linear actuator. B-d) Operating principles of the spur gear – rack mechanism.

Figure 6.25: Sketch of the operating principles of magneto-responsive mechanics. A-d) the rotation of the spur gear with magnetic chains is controlled by the positioning of the NdFeB magnet. E-g) The Arduino system used to control the rotation direction of the magnet.

Figure 6.26: Operating principles of the mechanical clamp developed using a magneto-driven drive wheel.

Appendix 2

Figure A2.1: Original optical image of 60Eb40BA_3NPs formulation after 10 minutes of exposure to an external magnetic field of 30mT.

Figure A2.2: Resulting image after contrast maximization.

Figure A2.3: Image after ellipses fitting.

References

[1] N. Spaldin, “Fundamental Materials Research and the Course of Human Civilization,” 2017.

[2] J. Diamond, *Guns, germs, and Steel: The fates of Human Societies*. W. W. Norton &CO Inc, 1999.

[3] M. Blaug, A. Klamer, D. N. McCloskey, and R. M. Solow, “The Consequences of Economic Rhetoric.,” *Econ. J.*, 1989, doi: 10.2307/2233777.

[4] American Chemical Society, “Bakelite: The World’s First Synthetic Plastic,” *A Natl. Hist. Chem. Landmarks*, 1993.

[5] ACS, “The Establishment of Modern Polymer Science By Wallace H. Carothers,” *An Int. Hist. Chem. Landmark*, 2000.

[6] D. W. Van Krevelen and K. Te Nijenhuis, *Properties of polymers: their correlation with chemical structure; their numerical estimation and prediction from additive group contributions*. Elsevier Science, 2009.

[7] R. L. Park and S. W. Leslie, “The Cold War and American Science: The Military-Industrial-Academic Complex at MIT and Stanford,” *Academe*, 1994, doi: 10.2307/40250622.

[8] M. Stanisz, Ł. Klapiszewski, and T. Jesionowski, “Recent advances in the fabrication and application of biopolymer-based micro- and nanostructures: A comprehensive review,” *Chemical Engineering Journal*. 2020, doi: 10.1016/j.cej.2020.125409.

[9] S. Kee, P. Zhang, and J. Travas-Sejdic, “Direct writing of 3D conjugated polymer micro/nanostructures for organic electronics and bioelectronics,” *Polym. Chem.*, vol. 11, no. 28, pp. 4530–4541, 2020, doi: 10.1039/D0PY00719F.

[10] E. Umaras and M. S. G. Tsuzuki, “Additive Manufacturing - Considerations on Geometric Accuracy and Factors of Influence,” *IFAC-PapersOnLine*, 2017, doi: 10.1016/j.ifacol.2017.08.2545.

[11] B. Kelechava, “Is it 3D Printing or Additive Manufacturing?” https://blog.ansi.org/2016/11/3d-printing-additive-manufacturing-difference/#gref.

[12] A. Savini and G. G. Savini, “A short history of 3D printing, a technological revolution just started,” 2015, doi: 10.1109/HISTELCON.2015.7307314.

[13] J. Horvath, “A brief history of 3D printing,” in *Mastering 3D Printing*, Springer, 2014, pp. 3–10.

[14] R. D. Farahani, M. Dubé, and D. Therriault, “Three-Dimensional Printing of Multifunctional Nanocomposites: Manufacturing Techniques and Applications,” *Advanced Materials*. 2016, doi: 10.1002/adma.201506215.

[15] K. V. Wong and A. Hernandez, “A Review of Additive Manufacturing,” *ISRN Mech. Eng.*, 2012, doi: 10.5402/2012/208760.

[16] T. Wohlers, “3D Printing and Additive Manufacturing State of the Industry. Annual Worldwide Progress Report.,” *Wohlers Report, Executive summary*. 2017.

[17] J. Coykendall, M. Cotteleer, J. Holdowsky, and M. Mahto, “3D opportunity

in aerospace and defense: Additive manufacturing takes flight," *Deloitte Univ. Press*, 2014.
[18] B. C. Gross, J. L. Erkal, S. Y. Lockwood, C. Chen, and D. M. Spence, "Evaluation of 3D printing and its potential impact on biotechnology and the chemical sciences," *Anal. Chem.*, 2014, doi: 10.1021/ac403397r.
[19] R. D'Aveni, "The 3D Printing revolution," *Harvard Business Review*, 2015.
[20] "The economist," *The Economist Newspaper Limited*, 2011.
[21] B. Berman, "3-D printing: The new industrial revolution," *Bus. Horiz.*, 2012, doi: 10.1016/j.bushor.2011.11.003.
[22] A. Ben-Ner and E. Siemsen, "Decentralization and Localization of Production: The Organizational and Economic Consequences of Additive Manufacturing (3D Printing)," *Calif. Manage. Rev.*, 2017, doi: 10.1177/0008125617695284.
[23] Z. X. Khoo *et al.*, "3D printing of smart materials: A review on recent progresses in 4D printing," *Virtual Phys. Prototyp.*, 2015, doi: 10.1080/17452759.2015.1097054.
[24] R. Bogue, "Smart materials: A review of recent developments," *Assem. Autom.*, 2012, doi: 10.1108/01445151211198674.
[25] S. Tibbits, "The emergence of 4D Printing," *TED*, 2013. .
[26] A. Mitchell, U. Lafont, M. Hołyńska, and C. Semprimoschnig, "Additive manufacturing — A review of 4D printing and future applications," *Additive Manufacturing*. 2018, doi: 10.1016/j.addma.2018.10.038.
[27] J. Choi, O. C. Kwon, W. Jo, H. J. Lee, and M. W. Moon, "4D printing technology: A review," *3D Printing and Additive Manufacturing*. 2015, doi: 10.1089/3dp.2015.0039.
[28] D. G. Shin, T. H. Kim, and D. E. Kim, "Review of 4D printing materials and their properties," *International Journal of Precision Engineering and Manufacturing - Green Technology*. 2017, doi: 10.1007/s40684-017-0040-z.
[29] P. Ravinder Reddy and P. Anjani Devi, "Review on the advancements to additive manufacturing-4D and 5D printing," *Int. J. Mech. Prod. Eng. Res. Dev.*, 2018, doi: 10.24247/ijmperdaug201841.
[30] J. Mohd Jani, M. Leary, A. Subic, and M. A. Gibson, "A review of shape memory alloy research, applications and opportunities," *Materials and Design*. 2014, doi: 10.1016/j.matdes.2013.11.084.
[31] J. Wu *et al.*, "Multi-shape active composites by 3D printing of digital shape memory polymers," *Sci. Rep.*, 2016, doi: 10.1038/srep24224.
[32] K. Yu, A. Ritchie, Y. Mao, M. L. Dunn, and H. J. Qi, "Controlled Sequential Shape Changing Components by 3D Printing of Shape Memory Polymer Multimaterials," 2015, doi: 10.1016/j.piutam.2014.12.021.
[33] Y. Mao, K. Yu, M. S. Isakov, J. Wu, M. L. Dunn, and H. Jerry Qi, "Sequential Self-Folding Structures by 3D Printed Digital Shape Memory Polymers," *Sci. Rep.*, 2015, doi: 10.1038/srep13616.
[34] S. E. Bakarich, R. Gorkin, M. In Het Panhuis, and G. M. Spinks, "4D printing with mechanically robust, thermally actuating hydrogels," *Macromol. Rapid Commun.*, 2015, doi: 10.1002/marc.201500079.
[35] H. Meng and G. Li, "A review of stimuli-responsive shape memory polymer composites," *Polymer*. 2013, doi: 10.1016/j.polymer.2013.02.023.
[36] D. Raviv *et al.*, "Active printed materials for complex self-evolving deformations," *Sci. Rep.*, 2014, doi: 10.1038/srep07422.

[37] S. Bose, S. Vahabzadeh, and A. Bandyopadhyay, “Bone tissue engineering using 3D printing,” *Materials Today*. 2013, doi: 10.1016/j.mattod.2013.11.017.
[38] X. Zhang *et al.*, “Multifunctional up-converting nanocomposites with smart polymer brushes gated mesopores for cell imaging and thermo/pH dual-responsive drug controlled release,” *Adv. Funct. Mater.*, 2013, doi: 10.1002/adfm.201300136.
[39] H. Yang *et al.*, “3D Printed Photoresponsive Devices Based on Shape Memory Composites,” *Adv. Mater.*, 2017, doi: 10.1002/adma.201701627.
[40] H. Jiang, S. Kelch, and A. Lendlein, “Polymers move in response to light,” *Adv. Mater.*, 2006, doi: 10.1002/adma.200502266.
[41] M. Layani, X. Wang, and S. Magdassi, “Novel Materials for 3D Printing by Photopolymerization,” *Advanced Materials*. 2018, doi: 10.1002/adma.201706344.
[42] Y. Bar-Cohen, “Electroactive polymers as artificial muscles: A review,” *J. Spacecr. Rockets*, 2002, doi: 10.2514/2.3902.
[43] T. Mirfakhrai, J. D. W. Madden, and R. H. Baughman, “Polymer artificial muscles,” *Mater. Today*, 2007, doi: 10.1016/S1369-7021(07)70048-2.
[44] S. Ashley, “Rapid prototyping systems,” *Mech. Eng.*, vol. 113, no. 4, p. 34, 1991.
[45] N. Mohan, P. Senthil, S. Vinodh, and N. Jayanth, “A review on composite materials and process parameters optimisation for the fused deposition modelling process,” *Virtual and Physical Prototyping*. 2017, doi: 10.1080/17452759.2016.1274490.
[46] J. A. Lewis, J. E. Smay, J. Stuecker, and J. Cesarano, “Direct ink writing of three-dimensional ceramic structures,” *J. Am. Ceram. Soc.*, 2006, doi: 10.1111/j.1551-2916.2006.01382.x.
[47] P. Jiang, Z. Ji, X. Zhang, Z. Liu, and X. Wang, “Recent advances in direct ink writing of electronic components and functional devices,” *Progress in Additive Manufacturing*. 2018, doi: 10.1007/s40964-017-0035-x.
[48] S. Abbasi, P. J. Carreau, and A. Derdouri, “Flow induced orientation of multiwalled carbon nanotubes in polycarbonate nanocomposites: Rheology, conductivity and mechanical properties,” *Polymer (Guildf).*, 2010, doi: 10.1016/j.polymer.2009.12.041.
[49] E. T. Thostenson and T. W. Chou, “Processing-structure-multi-functional property relationship in carbon nanotube/epoxy composites,” *Carbon N. Y.*, 2006, doi: 10.1016/j.carbon.2006.05.014.
[50] M. Kaur and A. K. Srivastava, “Photopolymerization: A review,” *J. Macromol. Sci. Part C Polym. Rev.*, vol. 42, no. 4, pp. 481–512, 2002.
[51] M. Tehfe, F. Louradour, J. Lalevée, and J.-P. Fouassier, “Photopolymerization Reactions: On the Way to a Green and Sustainable Chemistry,” *Appl. Sci.*, 2013, doi: 10.3390/app3020490.
[52] K. D. Jandt and R. W. Mills, “A brief history of LED photopolymerization,” *Dental Materials*. 2013, doi: 10.1016/j.dental.2013.02.003.
[53] J. P. Fouassier, X. Allonas, and D. Burget, “Photopolymerization reactions under visible lights: Principle, mechanisms and examples of applications,” *Prog. Org. Coatings*, 2003, doi: 10.1016/S0300-9440(03)00011-0.
[54] I. Gibson, D. W. Rosen, and B. Stucker, *Additive manufacturing technologies: Rapid prototyping to direct digital manufacturing*. 2010.
[55] A. Bertsch, S. Jiguet, P. Bernhard, and P. Renaud, “Microstereolithography:

A review," 2003, doi: 10.1557/proc-758-ll1.1.
[56] R. F. Pereira and P. J. Bártolo, "3D Photo-Fabrication for Tissue Engineering and Drug Delivery," *Engineering*. 2015, doi: 10.15302/J-ENG-2015015.
[57] F. P. W. Melchels, J. Feijen, and D. W. Grijpma, "A review on stereolithography and its applications in biomedical engineering," *Biomaterials*. 2010, doi: 10.1016/j.biomaterials.2010.04.050.
[58] A. Medellin, W. Du, G. Miao, J. Zou, Z. Pei, and C. Ma, "Vat photopolymerization 3d printing of nanocomposites: A literature review," *Journal of Micro and Nano-Manufacturing*. 2019, doi: 10.1115/1.4044288.
[59] M. Nadgorny and A. Ameli, "Functional Polymers and Nanocomposites for 3D Printing of Smart Structures and Devices," *ACS Applied Materials and Interfaces*. 2018, doi: 10.1021/acsami.8b01786.
[60] X. Wang, M. Jiang, Z. Zhou, J. Gou, and D. Hui, "3D printing of polymer matrix composites: A review and prospective," *Composites Part B: Engineering*. 2017, doi: 10.1016/j.compositesb.2016.11.034.
[61] G. Gonzalez *et al.*, "Development of 3D printable formulations containing CNT with enhanced electrical properties," *Polymer (Guildf).*, 2017, doi: 10.1016/j.polymer.2016.12.051.
[62] D. Lin *et al.*, "3D stereolithography printing of graphene oxide reinforced complex architectures," *Nanotechnology*, 2015, doi: 10.1088/0957-4484/26/43/434003.
[63] A. Chiappone *et al.*, "3D Printed PEG-Based Hybrid Nanocomposites Obtained by Sol-Gel Technique," *ACS Appl. Mater. Interfaces*, 2016, doi: 10.1021/acsami.5b12578.
[64] A. Chiappone *et al.*, "Study of graphene oxide-based 3D printable composites: Effect of the in situ reduction," *Compos. Part B Eng.*, 2017, doi: 10.1016/j.compositesb.2017.05.049.
[65] E. Fantino *et al.*, "3D Printing of Conductive Complex Structures with in Situ Generation of Silver Nanoparticles," *Adv. Mater.*, 2016, doi: 10.1002/adma.201505109.
[66] J. G. Kim, J. E. Park, S. Won, J. Jeon, and J. J. Wie, "Contactless manipulation of soft robots," *Materials*. 2019, doi: 10.3390/ma12193065.
[67] S. Palagi and P. Fischer, "Bioinspired microrobots," *Nature Reviews Materials*. 2018, doi: 10.1038/s41578-018-0016-9.
[68] Z. Li, F. Yang, and Y. Yin, "Smart Materials by Nanoscale Magnetic Assembly," *Advanced Functional Materials*. 2020, doi: 10.1002/adfm.201903467.
[69] M. Falahati *et al.*, "Smart polymers and nanocomposites for 3D and 4D printing," *Materials Today*. 2020, doi: 10.1016/j.mattod.2020.06.001.
[70] S. Blundell and D. Thouless, " Magnetism in Condensed Matter ," *Am. J. Phys.*, 2003, doi: 10.1119/1.1522704.
[71] N. A. Spaldin, *Magnetic materials: Fundamentals and applications*. 2010.
[72] O. H. Wyatt and D. Dew-Hughes, "Metals, ceramics and polymers: An introduction to the structure and properties of engineering materials(Book)," *London New York, Cambridge Univ. Press. 1974. 650 p*, 1974.
[73] N. A. Yefimov, *Handbook of non-ferrous metal powders: technologies and applications*. Elsevier, 2009.
[74] S. Mørup, M. F. Hansen, and C. Frandsen, "1.04 Magnetic Nanoparticles☆," *Compr. Nanosci. Nanotechnol.*, pp. 89–140, 2019.
[75] J. Jeevanandam, A. Barhoum, Y. S. Chan, A. Dufresne, and M. K. Danquah,

"Review on nanoparticles and nanostructured materials: History, sources, toxicity and regulations," *Beilstein Journal of Nanotechnology*. 2018, doi: 10.3762/bjnano.9.98.

[76] F. Bødker, M. F. Hansen, and C. B. Koch, "Magnetic properties of hematite nanoparticles," *Phys. Rev. B - Condens. Matter Mater. Phys.*, 2000, doi: 10.1103/PhysRevB.61.6826.

[77] H. Shokrollahi, "A review of the magnetic properties, synthesis methods and applications of maghemite," *Journal of Magnetism and Magnetic Materials*. 2017, doi: 10.1016/j.jmmm.2016.11.033.

[78] L. Blaney, "Magnetite (Fe3O4): Properties, synthesis, and applications," 2007.

[79] J. Lucas, P. Lucas, T. Le Mercier, A. Rollat, and W. Davenport, *Rare Earths: Science, Technology, Production and Use*. 2014.

[80] M. Sagawa, S. Fujimura, N. Togawa, H. Yamamoto, and Y. Matsuura, "New material for permanent magnets on a base of Nd and Fe (invited)," *J. Appl. Phys.*, 1984, doi: 10.1063/1.333572.

[81] U. S. Deshpande, "Recent advances in materials for use in permanent magnet machines-a review," in *IEEE International Electric Machines and Drives Conference, 2003. IEMDC'03.*, 2003, vol. 1, pp. 509–515.

[82] J. E. Mark, *Physical properties of polymers handbook*, vol. 1076. Springer, 2007.

[83] R. J. Young and P. A. Lovell, *Introduction to polymers*. CRC press, 2011.

[84] I. M. Ward and J. Sweeney, *Mechanical properties of solid polymers*. John Wiley & Sons, 2012.

[85] P. C. Hiemenz and T. P. Lodge, *Polymer chemistry*. CRC press, 2007.

[86] D. Mileva, D. Tranchida, and M. Gahleitner, "Designing polymer crystallinity: An industrial perspective," *Polymer Crystallization*. 2018, doi: 10.1002/pcr2.10009.

[87] M. Puttegowda, S. M. Rangappa, M. Jawaid, P. Shivanna, Y. Basavegowda, and N. Saba, "Potential of natural/synthetic hybrid composites for aerospace applications," in *Sustainable Composites for Aerospace Applications*, 2018.

[88] V. V. Sorokin, G. V. Stepanov, M. Shamonin, G. J. Monkman, A. R. Khokhlov, and E. Y. Kramarenko, "Hysteresis of the viscoelastic properties and the normal force in magnetically and mechanically soft magnetoactive elastomers: Effects of filler composition, strain amplitude and magnetic field," *Polymer (Guildf).*, 2015, doi: 10.1016/j.polymer.2015.08.040.

[89] J. Winger, M. Schümann, A. Kupka, and S. Odenbach, "Influence of the particle size on the magnetorheological effect of magnetorheological elastomers," *J. Magn. Magn. Mater.*, 2019, doi: 10.1016/j.jmmm.2019.03.027.

[90] H. Fu *et al.*, "Morphable 3D mesostructures and microelectronic devices by multistable buckling mechanics," *Nat. Mater.*, 2018, doi: 10.1038/s41563-017-0011-3.

[91] R. L. Snyder, V. Q. Nguyen, and R. V. Ramanujan, "Design parameters for magneto-elastic soft actuators," *Smart Mater. Struct.*, 2010, doi: 10.1088/0964-1726/19/5/055017.

[92] A. R. Khokhlov and Y. Osada, *Polymer gels and networks*. Marcel Dekker, 2002.

[93] D. G. Bekas, Y. Hou, Y. Liu, and A. Panesar, "3D printing to enable multifunctionality in polymer-based composites: A review," *Composites*

Part B: Engineering. 2019, doi: 10.1016/j.compositesb.2019.107540.
[94] J. P. Pelteret and P. Steinmann, *Magneto-active polymers: Fabrication, characterisation, modelling and simulation at the micro- and macro-scale*. 2020.
[95] C. de Marco *et al.*, "Indirect 3D and 4D Printing of Soft Robotic Microstructures," *Adv. Mater. Technol.*, 2019, doi: 10.1002/admt.201900332.
[96] B. Khatri, K. Lappe, D. Noetzel, K. Pursche, and T. Hanemann, "A 3D-printable polymer-metal soft-magnetic functional composite-development and characterization," *Materials (Basel).*, 2018, doi: 10.3390/ma11020189.
[97] Lu, P. Guo, and Y. Pan, "Magnetic-Field-Assisted Projection Stereolithography for Three-Dimensional Printing of Smart Structures," *J. Manuf. Sci. Eng. Trans. ASME*, 2017, doi: 10.1115/1.4035964.
[98] A. K. Bastola, M. Paudel, and L. Li, "Development of hybrid magnetorheological elastomers by 3D printing," *Polymer (Guildf).*, 2018, doi: 10.1016/j.polymer.2018.06.076.
[99] A. Hodaei *et al.*, "Single Additive Enables 3D Printing of Highly Loaded Iron Oxide Suspensions," *ACS Appl. Mater. Interfaces*, 2018, doi: 10.1021/acsami.8b00551.
[100] J. H. Kim *et al.*, "Three-Dimensional Printing of Highly Conductive Carbon Nanotube Microarchitectures with Fluid Ink," *ACS Nano*, 2016, doi: 10.1021/acsnano.6b04771.
[101] J. A. Cuenca *et al.*, "Study of the magnetite to maghemite transition using microwave permittivity and permeability measurements," *J. Phys. Condens. Matter*, 2016, doi: 10.1088/0953-8984/28/10/106002.
[102] M. Hofmann, "3D printing gets a boost and opportunities with polymer materials," *ACS Macro Letters*. 2014, doi: 10.1021/mz4006556.
[103] F. Frascella *et al.*, "Three-Dimensional Printed Photoluminescent Polymeric Waveguides," *ACS Appl. Mater. Interfaces*, 2018, doi: 10.1021/acsami.8b16036.
[104] Z. Ji, C. Yan, B. Yu, X. Wang, and F. Zhou, "Multimaterials 3D Printing for Free Assembly Manufacturing of Magnetic Driving Soft Actuator," *Adv. Mater. Interfaces*, 2017, doi: 10.1002/admi.201700629.
[105] E. B. Joyee and Y. Pan, "A fully three-dimensional printed inchworm-inspired soft robot with magnetic actuation," *Soft Robot.*, 2019, doi: 10.1089/soro.2018.0082.
[106] M. Yalcintas and H. Dai, "Magnetorheological and electrorheological materials in adaptive structures and their performance comparison," *Smart Mater. Struct.*, 1999, doi: 10.1088/0964-1726/8/5/306.
[107] C. Ruddy, E. Ahearne, and G. Byrne, "A review of Magnetorheological Elastomers: Properties and Applications," 2012.
[108] F. D. Goncalves, J. H. Koo, and M. Ahmadian, "A review of the state of the art in magnetorheological fluid technologies - Part I: MR fluid and MR fluid models," *Shock and Vibration Digest*. 2006, doi: 10.1177/0583102406065099.
[109] N. H. Rajhan, H. A. Hamid, I. Azmi, and R. Ismail, "Magnetorheological Elastomers: A Review," *Appl. Mech. Mater.*, 2014, doi: 10.4028/www.scientific.net/amm.695.255.
[110] T. Liu and Y. Xu, "Magnetorheological Elastomers: Materials and Applications," in *Smart and Functional Soft Materials*, 2019.

[111] J.-T. Zhu, Z.-D. Xu, and Y.-Q. Guo, “Experimental and Modeling Study on Magnetorheological Elastomers with Different Matrices,” *J. Mater. Civ. Eng.*, 2013, doi: 10.1061/(asce)mt.1943-5533.0000727.
[112] A. K. Bastola, M. Paudel, and L. Li, “3D printed magnetorheological elastomers,” in *Smart Materials, Adaptive Structures and Intelligent Systems*, 2017, vol. 58257, p. V001T01A001.
[113] M. R. Jolly, J. D. Carlson, and B. C. Muñoz, “A model of the behaviour of magnetorheological materials,” *Smart Mater. Struct.*, 1996, doi: 10.1088/0964-1726/5/5/009.
[114] H. Krueger, M. Vaezi, and S. Yang, “3D printing of magnetorheological elastomers(MREs)smart materials,” 2014, doi: 10.3850/978-981-09-0446-3_088.
[115] D. P. Arnold, “Review of microscale magnetic power generation,” *IEEE Transactions on Magnetics*. 2007, doi: 10.1109/TMAG.2007.906150.
[116] S. Sugimoto, “Current status and recent topics of rare-earth permanent magnets,” *J. Phys. D. Appl. Phys.*, 2011, doi: 10.1088/0022-3727/44/6/064001.
[117] P. Glynne-Jones, M. J. Tudor, S. P. Beeby, and N. M. White, “An electromagnetic, vibration-powered generator for intelligent sensor systems,” 2004, doi: 10.1016/j.sna.2003.09.045.
[118] X. Jiang, G. Shen, Y. Lai, and J. Tian, “Development of an open 0.3 T NdFeB MRI magnet,” 2004, doi: 10.1109/TASC.2004.831015.
[119] J. Jaćimović *et al.*, “Net Shape 3D Printed NdFeB Permanent Magnet,” *Adv. Eng. Mater.*, 2017, doi: 10.1002/adem.201700098.
[120] C. Huber *et al.*, “3D print of polymer bonded rare-earth magnets, and 3D magnetic field scanning with an end-user 3D printer,” *Appl. Phys. Lett.*, 2016, doi: 10.1063/1.4964856.
[121] C. Huber *et al.*, “3D Printing of Polymer-Bonded Rare-Earth Magnets with a Variable Magnetic Compound Fraction for a Predefined Stray Field,” *Sci. Rep.*, 2017, doi: 10.1038/s41598-017-09864-0.
[122] Y. Yang *et al.*, “Design and Comparison of Interior Permanent Magnet Motor Topologies for Traction Applications,” *IEEE Trans. Transp. Electrif.*, 2017, doi: 10.1109/TTE.2016.2614972.
[123] J. F. Bell, “Advances in Bonded Magnet Materials Theory and Practice,” 2016.
[124] C. Huber, S. Cano, I. Teliban, S. Schuschnigg, M. Groenefeld, and D. Suess, “Polymer-bonded anisotropic SrFe12O19 filaments for fused filament fabrication,” *J. Appl. Phys.*, 2020, doi: 10.1063/1.5139493.
[125] E. M. Palmero *et al.*, “Development of permanent magnet MnAlC/polymer composites and flexible filament for bonding and 3D-printing technologies,” *Sci. Technol. Adv. Mater.*, 2018, doi: 10.1080/14686996.2018.1471321.
[126] B. Slusarek and K. Zakrzewski, “Magnetic properties of permanent magnets for magnetic sensors working in wide range of temperature,” *Przeglad Elektrotechniczny*. 2012.
[127] “A mechanism of magnetic hysteresis in heterogeneous alloys,” *Philos. Trans. R. Soc. London. Ser. A, Math. Phys. Sci.*, 1948, doi: 10.1098/rsta.1948.0007.
[128] N. Hamada, C. Mishima, H. Mitarai, and Y. Honkura, “Development of Nd-Fe-B Anisotropic Bonded Magnet With 27 MGOe,” 2003, doi: 10.1109/TMAG.2003.815757.

[129] X. Chen, C. Cen, L. Zhou, R. Cao, Z. Yi, and Y. Tang, “Magnetic properties and reverse magnetization process of anisotropic nanocomposite permanent magnet,” *J. Magn. Magn. Mater.*, 2019, doi: 10.1016/j.jmmm.2019.03.104.
[130] W. Bin Cui, Y. K. Takahashi, and K. Hono, “Nd2Fe14B/FeCo anisotropic nanocomposite films with a large maximum energy product,” *Adv. Mater.*, 2012, doi: 10.1002/adma.201202328.
[131] V. Q. Nguyen, A. S. Ahmed, and R. V. Ramanujan, “Morphing soft magnetic composites,” *Adv. Mater.*, 2012, doi: 10.1002/adma.201104994.
[132] S. Tasoglu, E. Diller, S. Guven, M. Sitti, and U. Demirci, “Untethered micro-robotic coding of three-dimensional material composition,” *Nat. Commun.*, 2014, doi: 10.1038/ncomms4124.
[133] E. Diller, S. Miyashita, and M. Sitti, “Remotely addressable magnetic composite micropumps,” *RSC Adv.*, 2012, doi: 10.1039/c2ra01318e.
[134] B. J. Nelson, I. K. Kaliakatsos, and J. J. Abbott, “Microrobots for minimally invasive medicine,” *Annual Review of Biomedical Engineering*. 2010, doi: 10.1146/annurev-bioeng-010510-103409.
[135] M. Sitti *et al.*, “Biomedical Applications of Untethered Mobile Milli/Microrobots,” *Proceedings of the IEEE*. 2015, doi: 10.1109/JPROC.2014.2385105.
[136] P. R. Buckley *et al.*, “Inductively heated shape memory polymer for the magnetic actuation of medical devices,” *IEEE Trans. Biomed. Eng.*, 2006, doi: 10.1109/TBME.2006.877113.
[137] I. Willner, B. Basnar, and B. Willner, “From molecular machines to microscale motility of objects: Application as ‘smart materials’, sensors, and nanodevices,” *Adv. Funct. Mater.*, 2007, doi: 10.1002/adfm.200601154.
[138] Y. Bar-Cohen and C. Breazeal, “Biologically inspired intelligent robots,” 2003, doi: 10.1117/12.484379.
[139] S. Fusco *et al.*, “Shape-switching microrobots for medical applications: The influence of shape in drug delivery and locomotion,” *ACS Appl. Mater. Interfaces*, 2015, doi: 10.1021/acsami.5b00181.
[140] M. P. Kummer, J. J. Abbott, B. E. Kratochvil, R. Borer, A. Sengul, and B. J. Nelson, “Octomag: An electromagnetic system for 5-DOF wireless micromanipulation,” *IEEE Trans. Robot.*, 2010, doi: 10.1109/TRO.2010.2073030.
[141] L. Hines, K. Petersen, G. Z. Lum, and M. Sitti, “Soft Actuators for Small-Scale Robotics,” *Advanced Materials*. 2017, doi: 10.1002/adma.201603483.
[142] L. Chen, X. L. Gong, W. Q. Jiang, J. J. Yao, H. X. Deng, and W. H. Li, “Investigation on magnetorheological elastomers based on natural rubber,” *J. Mater. Sci.*, 2007, doi: 10.1007/s10853-006-0975-x.
[143] H. S. Jung, S. H. Kwon, H. J. Choi, J. H. Jung, and Y. G. Kim, “Magnetic carbonyl iron/natural rubber composite elastomer and its magnetorheology,” *Compos. Struct.*, 2016, doi: 10.1016/j.compstruct.2015.10.008.
[144] N. A. Yunus, S. A. Mazlan, Ubaidillah, S. A. Abdul Aziz, S. T. Shilan, and N. A. Abdul Wahab, “Thermal stability and rheological properties of epoxidized natural rubber-based magnetorheological elastomer,” *Int. J. Mol. Sci.*, 2019, doi: 10.3390/ijms20030746.
[145] J. G. Puente-Córdova, M. E. Reyes-Melo, L. M. Palacios-Pineda, I. A. Martínez-Perales, O. Martínez-Romero, and A. Elías-Zúñiga, “Fabrication and characterization of isotropic and anisotropic magnetorheological elastomers, based on silicone rubber and carbonyl iron microparticles,”

Polymers (Basel)., 2018, doi: 10.3390/polym10121343.
[146] I. A. Perales-Martínez, L. M. Palacios-Pineda, L. M. Lozano-Sánchez, O. Martínez-Romero, J. G. Puente-Cordova, and A. Elías-Zúñiga, "Enhancement of a magnetorheological PDMS elastomer with carbonyl iron particles," *Polym. Test.*, 2017, doi: 10.1016/j.polymertesting.2016.10.029.
[147] C. Lian, K. H. Lee, and C. H. Lee, "Effect of Temperature and Relative Humidity on Friction and Wear Properties of Silicone-Based Magnetorheological Elastomer," *Tribol. Trans.*, 2018, doi: 10.1080/10402004.2017.1306636.
[148] B. Ju *et al.*, "Dynamic mechanical properties of magnetorheological elastomers based on polyurethane matrix," *Polym. Compos.*, 2016, doi: 10.1002/pc.23330.
[149] I. Bica, E. M. Anitas, L. M. E. Averis, S. H. Kwon, and H. J. Choi, "Magnetostrictive and viscoelastic characteristics of polyurethane-based magnetorheological elastomer," *J. Ind. Eng. Chem.*, 2019, doi: 10.1016/j.jiec.2019.01.015.
[150] T. L. Sun, X. L. Gong, W. Q. Jiang, J. F. Li, Z. B. Xu, and W. H. Li, "Study on the damping properties of magnetorheological elastomers based on cis-polybutadiene rubber," *Polym. Test.*, 2008, doi: 10.1016/j.polymertesting.2008.02.008.
[151] Y. Lei, Z. Sheng, J. Zhang, J. Liu, W. Lv, and X. Hou, "Building Magnetoresponsive Composite Elastomers for Bionic Locomotion Applications," *J. Bionic Eng.*, 2020, doi: 10.1007/s42235-020-0033-4.
[152] K. Kim, S. Y. Ko, J. O. Park, and S. Park, "Development of a cantilever-type ferro-actuator using a porous PVDF membrane," *Proc. Inst. Mech. Eng. Part C J. Mech. Eng. Sci.*, 2016, doi: 10.1177/0954406215616143.
[153] R. T. Olsson *et al.*, "Making flexible magnetic aerogels and stiff magnetic nanopaper using cellulose nanofibrils as templates," *Nat. Nanotechnol.*, 2010, doi: 10.1038/nnano.2010.155.
[154] Q. Zhao, W. Zou, Y. Luo, and T. Xie, "Shape memory polymer network with thermally distinct elasticity and plasticity," *Sci. Adv.*, 2016, doi: 10.1126/sciadv.1501297.
[155] J. Diani, P. Gilormini, C. Frédy, and I. Rousseau, "Predicting thermal shape memory of crosslinked polymer networks from linear viscoelasticity," *Int. J. Solids Struct.*, 2012, doi: 10.1016/j.ijsolstr.2011.11.019.
[156] A. M. Schmidt, "Electromagnetic activation of shape memory polymer networks containing magnetic nanoparticles," *Macromol. Rapid Commun.*, 2006, doi: 10.1002/marc.200600225.
[157] T. Xie, "Tunable polymer multi-shape memory effect," *Nature*, 2010, doi: 10.1038/nature08863.
[158] Q. Ze *et al.*, "Magnetic Shape Memory Polymers with Integrated Multifunctional Shape Manipulation," *Adv. Mater.*, 2020, doi: 10.1002/adma.201906657.
[159] W. Hu, G. Z. Lum, M. Mastrangeli, and M. Sitti, "Small-scale soft-bodied robot with multimodal locomotion," *Nature*, 2018, doi: 10.1038/nature25443.
[160] H. Lu *et al.*, "A bioinspired multilegged soft millirobot that functions in both dry and wet conditions," *Nat. Commun.*, 2018, doi: 10.1038/s41467-018-06491-9.
[161] Y. Kim, H. Yuk, R. Zhao, S. A. Chester, and X. Zhao, "Printing

ferromagnetic domains for untethered fast-transforming soft materials," *Nature*, 2018, doi: 10.1038/s41586-018-0185-0.
[162] M. Grzelczak, J. Vermant, E. M. Furst, and L. M. Liz-Marzán, "Directed self-assembly of nanoparticles," *ACS Nano*. 2010, doi: 10.1021/nn100869j.
[163] A. K. Boal, F. Ilhan, J. E. Derouchey, T. Thurn-Albrecht, T. P. Russell, and V. M. Rotello, "Self-assembly of nanoparticles into structured spherical and network aggregates," *Nature*, 2000, doi: 10.1038/35008037.
[164] Y. Hu, L. He, and Y. Yin, "Magnetically responsive photonic nanochains," *Angew. Chemie - Int. Ed.*, 2011, doi: 10.1002/anie.201100290.
[165] M. Ma *et al.*, "Fabrication of one-dimensional Fe 3O 4/P(GMA-DVB) nanochains by magnetic-field-induced precipitation polymerization," *J. Colloid Interface Sci.*, 2012, doi: 10.1016/j.jcis.2012.02.015.
[166] H. Wang, Y. Yu, Y. Sun, and Q. Chen, "Magnetic nanochains: A review," *Nano*, 2011, doi: 10.1142/S1793292011002305.
[167] G. Bertoni, B. Torre, A. Falqui, D. Fragouli, A. Athanassiou, and R. Cingolani, "Nanochains formation of superparamagnetic nanoparticles," *J. Phys. Chem. C*, 2011, doi: 10.1021/jp111235n.
[168] D. Lorenzo *et al.*, "Formation and magnetic manipulation of periodically aligned microchains in thin plastic membranes," *J. Appl. Phys.*, 2012, doi: 10.1063/1.4759328.
[169] Y. Men *et al.*, "Controlled evaporative self-assembly of Fe3O4 nanoparticles assisted by an external magnetic field," *RSC Adv.*, 2015, doi: 10.1039/c5ra02160j.
[170] Y. Nagaoka, H. Morimoto, and T. Maekawa, "Ordered complex structures formed by paramagnetic particles via self-assembly under an ac/dc combined magnetic field," *Langmuir*, 2011, doi: 10.1021/la201156q.
[171] A. Snezhko, I. S. Aranson, and W. K. Kwok, "Structure formation in electromagnetically driven granular media," *Phys. Rev. Lett.*, 2005, doi: 10.1103/PhysRevLett.94.108002.
[172] D. Fragouli *et al.*, "Dynamical formation of spatially localized arrays of aligned nanowires in plastic films with magnetic anisotropy," *ACS Nano*, 2010, doi: 10.1021/nn901597a.
[173] A. Darras, E. Opsomer, N. Vandewalle, and G. Lumay, "Superparamagnetic colloids in viscous fluids," *Sci. Rep.*, 2017, doi: 10.1038/s41598-017-07917-y.
[174] E. Myrovali *et al.*, "Arrangement at the nanoscale: Effect on magnetic particle hyperthermia," *Sci. Rep.*, 2016, doi: 10.1038/srep37934.
[175] J. Kim, S. E. Chung, S. E. Choi, H. Lee, J. Kim, and S. Kwon, "Programming magnetic anisotropy in polymeric microactuators," *Nat. Mater.*, 2011, doi: 10.1038/nmat3090.
[176] J. J. Martin, B. E. Fiore, and R. M. Erb, "Designing bioinspired composite reinforcement architectures via 3D magnetic printing," *Nat. Commun.*, 2015, doi: 10.1038/ncomms9641.
[177] S. Lantean *et al.*, "3D Printing of Magnetoresponsive Polymeric Materials with Tunable Mechanical and Magnetic Properties by Digital Light Processing," *Adv. Mater. Technol.*, 2019, doi: 10.1002/admt.201900505.
[178] Z. Zhao, X. Tian, and X. Song, "Engineering materials with light: Recent progress in digital light processing based 3D printing," *Journal of Materials Chemistry C*. 2020, doi: 10.1039/d0tc03548c.
[179] S. Stassi *et al.*, "Polymeric 3D Printed Functional Microcantilevers for

Biosensing Applications," *ACS Appl. Mater. Interfaces*, 2017, doi: 10.1021/acsami.7b04030.
[180] S. Lantean, I. Roppolo, M. Sangermano, C. F. Pirri, and A. Chiappone, "Development of new hybrid acrylic/epoxy DLP-3D printable materials," *Inventions*, 2018, doi: 10.3390/inventions3020029.
[181] J. Herzberger, J. M. Sirrine, C. B. Williams, and T. E. Long, "Polymer Design for 3D Printing Elastomers: Recent Advances in Structure, Properties, and Printing," *Progress in Polymer Science*. 2019, doi: 10.1016/j.progpolymsci.2019.101144.
[182] Y. Deng, J. Li, Z. He, J. Hong, and J. Bao, "Urethane acrylate-based photosensitive resin for three-dimensional printing of stereolithographic elastomer," *J. Appl. Polym. Sci.*, 2020, doi: 10.1002/app.49294.
[183] "UV/EB curable resins industrial coatings." https://allnex.com/getattachment/ee16af66-460d-45e9-9250-4049efe344eb/730AL_222-Industrial-Coatings-Radcure-spreads.pdf.aspx?lang=en-US.
[184] I. Roppolo *et al.*, "3D printable light-responsive polymers," *Mater. Horizons*, 2017, doi: 10.1039/c7mh00072c.
[185] M. Sangermano, W. Carbonaro, G. Malucelli, and A. Priola, "UV-cured interpenetrating acrylic-epoxy polymer networks: Preparation and characterization," *Macromol. Mater. Eng.*, 2008, doi: 10.1002/mame.200800020.
[186] A. Schlegel, S. F. Alvarado, and P. Wachter, "Optical properties of magnetite (Fe3O4)," *J. Phys. C Solid State Phys.*, 1979, doi: 10.1088/0022-3719/12/6/027.
[187] G. Herzer, "Grain Size Dependence of Coercivity and Permeability in Nanocrystalline Ferromagnets," *IEEE Trans. Magn.*, 1990, doi: 10.1109/20.104389.
[188] S. Ahmed *et al.*, "Multi-field responsive origami structures: Preliminary modeling and experiments," 2013, doi: 10.1115/DETC2013-12405.
[189] P. Von Lockette, "Fabrication and performance of magneto-active elastomer composite structures," 2014, doi: 10.1115/SMASIS20147590.
[190] R. M. Erb, J. J. Martin, R. Soheilian, C. Pan, and J. R. Barber, "Actuating Soft Matter with Magnetic Torque," *Advanced Functional Materials*. 2016, doi: 10.1002/adfm.201504699.
[191] H. Kim *et al.*, "Shape morphing smart 3D actuator materials for micro soft robot," *Materials Today*. 2020, doi: 10.1016/j.mattod.2020.06.005.
[192] L. K. Lagorce, O. Brand, and M. G. Allen, "Magnetic microactuators based on polymer magnets," *J. Microelectromechanical Syst.*, 1999, doi: 10.1109/84.749396.
[193] G. I. Peterson, S. Yang, and T.-L. Choi, "Polymers producing hydrogen," *Nat. Chem.*, vol. 12, no. 12, pp. 1093–1095, 2020.
[194] J. Tian *et al.*, "Tailored self-assembled photocatalytic nanofibres for visible-light-driven hydrogen production," *Nat. Chem.*, 2020, doi: 10.1038/s41557-020-00580-3.
[195] M. Varón *et al.*, "Dipolar magnetism in ordered and disordered low-dimensional nanoparticle assemblies," *Sci. Rep.*, 2013, doi: 10.1038/srep01234.
[196] H. Wang *et al.*, "Magnetic-field-induced formation of one-dimensional magnetite nanochains," *Langmuir*, 2009, doi: 10.1021/la900234n.

[197] Y. Zhang *et al.*, "The shape anisotropy in the magnetic field-assisted self-assembly chain-like structure of magnetite," *J. Phys. Chem. C*, 2009, doi: 10.1021/jp807937d.
[198] Y. Sahoo, M. Cheon, S. Wang, H. Luo, E. P. Furlani, and P. N. Prasad, "Field-directed self-assembly of magnetic nanoparticles," *Journal of Physical Chemistry B*. 2004, doi: 10.1021/jp031148i.
[199] V. S. Andreev and A. E. Luk'yanov, "Concentration dependence of the average distance between particles in disperse systems," *Colloid J. USSR*, vol. 51, no. 4, pp. 643–645, 1990.
[200] B. M. Smirnov, E. E. Son, and D. V Tereshonok, "Diffusion and mobility of atomic particles in a liquid," *J. Exp. Theor. Phys.*, vol. 125, no. 5, pp. 906–912, 2017.
[201] V. Germain and M. P. Pileni, "Size distribution of cobalt nanocrystals: A key parameter in formation of columns and labyrinths in mesoscopic structures," *Adv. Mater.*, 2005, doi: 10.1002/adma.200401559.
[202] J. Ge, Y. Hu, M. Biasini, W. P. Beyermann, and Y. Yin, "Superparamagnetic magnetite colloidal nanocrystal clusters," *Angew. Chemie - Int. Ed.*, 2007, doi: 10.1002/anie.200700197.
[203] M. H. DeGroot, M. J. Schervish, X. Fang, L. Lu, and D. Li, *Probability and statistics*, vol. 2. Addison-Wesley Reading, MA, 1986.
[204] J. H. E. Promislow, A. P. Gast, and M. Fermigier, "Aggregation kinetics of paramagnetic colloidal particles," *J. Chem. Phys.*, 1995, doi: 10.1063/1.469278.
[205] M. A. M. Gijs, "Magnetic bead handling on-chip: New opportunities for analytical applications," *Microfluidics and Nanofluidics*. 2004, doi: 10.1007/s10404-004-0010-y.
[206] N. Pamme, "Magnetism and microfluidics," *Lab on a Chip*. 2006, doi: 10.1039/b513005k.
[207] S. Melle, O. G. Calderón, M. A. Rubio, and G. G. Fuller, "Rotational dynamics in dipolar colloidal suspensions: Video microscopy experiments and simulations results," *J. Nonnewton. Fluid Mech.*, 2002, doi: 10.1016/S0377-0257(01)00174-4.
[208] S. Melle and J. E. Martin, "Chain model of a magnetorheological suspension in a rotating field," *J. Chem. Phys.*, 2003, doi: 10.1063/1.1570817.
[209] A. K. Vuppu, A. A. Garcia, and M. A. Hayes, "Video Microscopy of Dynamically Aggregated Paramagnetic Particle Chains in an Applied Rotating Magnetic Field," *Langmuir*, 2003, doi: 10.1021/la034195a.
[210] S. Melle, O. G. Calderón, M. A. Rubio, and G. G. Fuller, "Microstructure evolution in magnetorheological suspensions governed by Mason number," *Phys. Rev. E - Stat. Physics, Plasmas, Fluids, Relat. Interdiscip. Top.*, 2003, doi: 10.1103/PhysRevE.68.041503.
[211] M. Khoo and C. Liu, "Micro magnetic silicone elastomer membrane actuator," *Sensors Actuators, A Phys.*, 2001, doi: 10.1016/S0924-4247(00)00559-8.
[212] L. Zhang, J. J. Abbott, L. Dong, B. E. Kratochvil, D. Bell, and B. J. Nelson, "Artificial bacterial flagella: Fabrication and magnetic control," *Appl. Phys. Lett.*, 2009, doi: 10.1063/1.3079655.
[213] S. H. Kim, J. Y. Sim, J. M. Lim, and S. M. Yang, "Magnetoresponsive microparticles with nanoscopic surface structures for remote-controlled locomotion," *Angew. Chemie - Int. Ed.*, 2010, doi: 10.1002/anie.201001031.

[214] C. Baumgärtel, R. T. Smith, and S. Maher, “Accurately predicting electron beam deflections in fringing fields of a solenoid,” *Sci. Rep.*, 2020, doi: 10.1038/s41598-020-67596-0.
[215] D. A. Jesson and J. F. Watts, “The interface and interphase in polymer matrix composites: Effect on mechanical properties and methods for identification,” *Polymer Reviews*. 2012, doi: 10.1080/15583724.2012.710288.
[216] S. Y. Fu, X. Q. Feng, B. Lauke, and Y. W. Mai, “Effects of particle size, particle/matrix interface adhesion and particle loading on mechanical properties of particulate-polymer composites,” *Compos. Part B Eng.*, 2008, doi: 10.1016/j.compositesb.2008.01.002.
[217] B. L. Zhu, J. Wang, H. Zheng, J. Ma, J. Wu, and R. Wu, “Investigation of thermal conductivity and dielectric properties of LDPE-matrix composites filled with hybrid filler of hollow glass microspheres and nitride particles,” *Compos. Part B Eng.*, 2015, doi: 10.1016/j.compositesb.2014.10.035.
[218] B. D. Cullity and C. D. Graham, *Introduction to Magnetic Materials*. 2008.
[219] H. W. Huang, M. S. Sakar, A. J. Petruska, S. Pané, and B. J. Nelson, “Soft micromachines with programmable motility and morphology,” *Nat. Commun.*, 2016, doi: 10.1038/ncomms12263.
[220] T. Li *et al.*, “Highly efficient freestyle magnetic nanoswimmer,” *Nano Lett.*, 2017, doi: 10.1021/acs.nanolett.7b02383.
[221] R. K. Mobley, “Vibration Fundamentals,” in *Plant Engineer’s Handbook*, 2001.

ECOLE DOCTORALE

Titre : Fabrication d'une imprimante 3D magnétique pour la conception de micro-actionneurs nanocomposites polymères renforcés avec des architectures 3D bio-inspirées

Mots clés : photo-polymerisation, Microscopie, Fabrication additive, nanoparticules magnétiques, Impression 4D

Résumé : L'objectif de cette thèse est d'imprimer en 4D des polymères magnéto-actifs utilisant la technique du traitement numérique de la lumière (DLP). Pour atteindre notre objectif, nous avons d'abord développé des résines photo-réticulables contenant des nanoparticules (NPs) de magnétite (Fe_3O_4). Ces résines ont ensuite été utilisées pour imprimer des polymères magnéto-actifs contenant des NP dispersées de manière aléatoire. En faisant varier leurs propriétés mécaniques, nous avons réussi à programmer plusieurs mouvements : roulement et translation pour les matrices rigides et pliage et dépliage pour les matrices souples. L'auto-assemblage des NPs, la formation de configurations en chaîne lorsqu'un champ magnétique externe est appliqué, a été étudié par microscopie optique et microscopie à rayons X à balayage, et interprété à l'aide d'un modèle théorique simplifié et de simulations numériques.Pour contrôler la microstructure d'un objet imprimé en 3D, notre stratégie a consisté à reproduire le contrôle 2D de la microstructure magnétique pour toutes les couches imprimées de l'objet. Pour ce faire, nous avons modifié une imprimante DLP afin d'appliquer des champs magnétiques d'intensité et de direction accordables pendant le processus d'impression. Enfin, comme preuve de concept, des dispositifs magnéto-actifs consistant en des actionneurs linéaires, des engrenages, des pinces magnéto-actives ou des interrupteurs électroniques ont été imprimés.

Title : A novel approach to fabricate bioinspired programmable composite materials: the 3D Printing way

Keywords : photocuring, microscopy, additive manufacturing, magnetic nanoparticles, 4D printing

Abstract : The objective of this thesis is to 4D printing magneto-responsive polymers using Digital Light Processing (DLP) technique. For reaching our goal, we first developed photocurable resins containing magnetite (Fe3O4) nanoparticles (NPs). These resins were then used to print magneto-responsive polymers containing randomly dispersed NPs. By varying their mechanical properties, we succeeded in programming several movements: rolling and translation for rigid matrices and folding and unfolding for soft polymers. The self-assembly of NPs, the formation of chain-like configurations when an external magnetic field is applied, was studied by optical and scanning X-ray microscopies, and interpreted using a simplified theoretical model and numerical simulations. To control the microstructure of a 3D printed object, our strategy consists in reproducing the 2D control on the magnetic microstructure in each printed layer of the object. This was done by modifying a DLP printer to apply magnetic fields of tunable intensity and direction during the printing process. Finally, as a proof of concept, magneto-active devices consisting of linear actuators, gears, magneto-active clamps or electronic switches have been printed.

Institut Polytechnique de Paris
91120 Palaiseau, France